JOHANNES GUTENBERG UNIVERSITÄT MAINZ

MAGNESIUM HOMEOSTASIS AND CHANNELS IN THE CYANOBACTERIUM *SYNECHOCYSTIS* SP. PCC 6803

Dissertation
zur Erlangung des Grades
"Doktorin der Naturwissenschaften"
im Promotionsfach Chemie

am Fachbereich Chemie, Pharmazie, Geographie und Geowissenschaften
der Johannes Gutenberg-Universität
in Mainz

Anne-Christin Pohland
geb. in Gießen

Mainz, 2023

Dekanin: [redacted]
1. Gutachter: [redacted]
2. Gutachterin: [redacted]

Tag der mündlichen Prüfung: 22.06.2023

Die vorliegende Arbeit wurde in der Zeit von April 2018 bis April 2023 am Department für Chemie der Johannes Gutenberg-Universität Mainz unter Betreuung von [redacted] angefertigt. Hiermit versichere ich, dass ich diese Arbeit selbständig verfasst habe und keine anderen als die angegebenen Quellen und Hilfsmittel verwendet habe.

Contents

List of Figures

List of Tables

List of Abbreviations

H	high (300 µM) Mg^{2+} concentration
L	low (50 µM) Mg^{2+} concentration
E. coli	*Escherichia coli*
S. elongatus	*Synechococcus elongatus*
S. typhimurium	*Salmonella typhimurium*
Synechocystis	*Synechocystis* sp. PCC 6803
ADP	adenosine diphosphate
ANS	8-anilinonaphthalene-1-sulfonic acid
AO	N,N,N',N'-tetramethylacridine-3,6-diamine
APC	allophycocyanin
APS	Ammonium persulfate
ARTO	alternative respiratory terminal oxidase
ATP	adenosine triphosphate
BSA	bovine serum albumin
Car	carotenoids
CBB	Calvin–Benson–Bassham
CBS	cystathionine β-synthase
CD	circular dichroism
CEF	cyclic electron flow
Chaps	3-[(3-cholamidopropyl)dimethylammonio]-1-propanesulfonate
Chl *a*	chlorophyll *a*
Cm	chloramphenicol
cmc	critical micelle concentration
CNNM	cyclinM
CorA	cobalt resistance A
Cox	aa_3-type cytochrome *c*
CV	column volume
Cyd	cytochrome *bd*-type quinol oxidase
Cyt b_6f	cytochrome b_6f
Cyt c_6	cytochrome c_6
cytMgtE	cytoplamic domain of MgtE
DBMIB	2,5-dibromo-6-isopropyl-3-methyl-1,4-benzoquinone
DCMU	3-(3,4-dichlorophenyl)-1,1-dimethylurea
DDM	N-dodecyl-β-D-maltopyranoside
DOPC	1,2-dioleoyl-sn-glycero-3-phosphocholine
DTT	dithiothreitol
ECFP	enhanced cyan fluorescent protein
EPL	*E. coli* Polar Lipids
EPS	exopolysaccharides
ETC	electron transport chain
$F_{m'}$	maximal fluorescence when the PQ pool is reduced
F_m	maximal fluorescence when the PQ pool is oxidised
$F_{o'}$	minimal fluorescence when the PQ pool is reduced
F_o	minimal fluorescence when the PQ pool is oxidised
F_s	steady-state fluorescence
F_v	F_m-F_o
F_v/F_m	maximum quantum yield of PSII
Fd	ferredoxin
FNR	ferredoxin-$NADP^+$ reductase
FRET	Förster resonance energy transfer
FTSA	fluorescence-based thermal shift assay
ICTCC	intermediate-conductance thylakoid cation channel
IsiA	iron stress-induced protein
Kan	kanamycin
KO	knock out
LAHG	light-activated heterotrophic growth
LDAO	lauryldimethylamine oxide
LEF	linear electron flow
MGR	Mg^{2+} Release
MgtE	magnesium transporter E

mt	mutant
MV	methyl viologen
NADH	nicotinamide adenine dinucleotide hydrogen
NADPH	nicotinamide adenine dinucleotide phosphate hydrogen
NDH-1	type I NADPH:plastoquinone oxidoreductase
NDH-2	type II NADH:quinone oxidoreductase
Ni-NTA	nickel nitriloacetic acid
OCP	orange carotenoid protein
OEC	oxygen-evolving complex
OG	N-octyl-β-D-glucoside
OM	outer membrane
ORF	open reading frame
P680	reaction centre of PSII
P700	reaction centre of PSI
PAM	pulse amplitude-modulated
PBS	phycobilisomes
PC	phycocyanin
PGR5	proton gradient regulation 5
PGRL1	PGR5-like photosynthetic phenotype 1
PLC	plastocyanin
pLDDT	predicted local-distance difference test
PM	plasma membrane
PMF	proton motive force
PQ	plastoquinone
PQH_2	plastoquinol
PSI	photosystem I
PSII	photosystem II
PTOX	plastid terminal oxidase
PxcA	proton-extrusion-protein A
Q_o site	quinol oxidation site
RT	room temperature
RuBisCO	ribulose-1,5-bisphosphate carboxylase
SD	standard deviation
SDH	succinate dehydrogenase
SDS	sodium dodecyl sulphate
SDS-PAGE	sodium dodecyl sulphate-polyacrylamide gel electrophoresis
Sp	spectinomycin
TEMED	tetramethylethylenediamine
TM	thylakoid membrane
TO	terminal oxidase
VDE	violaxanthin de-epoxidase
WB	Western blot
wt	wild type
Y(I)	effective quantum yield of PSI
Y(II)	effective quantum yield of PSII

I. Summary

Mg^{2+} is the central ion of chlorophyll *a* (Chl *a*) and, as a counter ion, it is essential for proton translocation across the thylakoid membranes (TMs). Moreover, several enzymes involved in carbon fixation rely on Mg^{2+} ions. The bacterial Mg^{2+} channels cobalt resistance A (CorA) and magnesium transporter E (MgtE) have already been studied in some detail. Their homologs were also found in eukaryotes. Cyanobacteria are often used to study photosynthetic processes. The model organism *Synechocystis* sp. PCC 6803 (*Synechocystis*) was chosen to study the function of cyanobacterial MgtE and (two) CorA homologs. The corresponding single or double knock out (KO) strains were generated. Studies of these strains suggested that all three channels are involved in Mg^{2+} homeostasis. When grown under standard growth conditions, all mutants (mts) showed impaired respiration, while the respiration of the wild type (wt) was only affected when Mg^{2+} was limiting. Lower respiration rates appeared to be a major reason for the observed lowered pH gradient across *Synechocystis*' membranes. Under Mg^{2+} limitation, all *ΔcorA* mts showed a prolonged lag phase. In addition, altered photosynthetic performance was observed in the *ΔcorA1* mt, even under standard growth conditions. The same photosynthetic parameters were changed in the wt under Mg^{2+} limitation. Deletion of the *mgtE* gene resulted in Co^{2+} resistance. All putative Mg^{2+} channels were expressed in *Synechocystis* cells with an N-terminal yellow fluorescent protein (YFP)-tag. While YFP-tagged MgtE was observed in the plasma membrane (PM) and the TM, YFP-tagged CorA1 was mainly observed in the TM, and YFP-tagged CorA2 was only observed in the PM. Direct proof for (a decreased) Mg^{2+} flux across membranes, is still needed. Preliminary *in vitro* studies with heterologously expressed and purified CorA2 protein incorporated into liposomes seemed to confirm Mg^{2+} transport across (artificial) membranes. Studies with the heterologously expressed and purified cytoplasmic domain of MgtE revealed Mg^{2+}-dependent differences in the protein stability, which indicates a regulatory role of the MgtE channel in *Synechocystis* by putative ligand (Mg^{2+})-binding. In summary, the described analysis provides new insight into the potential roles of Mg^{2+} channels in *Synechocystis*, including bioenergetic processes.

II. Zusammenfassung

Mg^{2+} ist das Zentralion von Chlorophyll *a* (Chl *a*) und als Gegenion ist es essentiell für den Protonentransport über die Thylakoidmembranen (TMn). Darüber hinaus sind mehrere Enzyme, die an der Kohlenstofffixierung beteiligt sind, auf Mg^{2+}-Ionen angewiesen. Die bakteriellen Mg^{2+}-Kanäle cobalt resistance A (CorA) und magnesium transporter E (MgtE) wurden bereits ausführlich untersucht. Ihre Homologe wurden auch in Eukaryoten gefunden. Cyanobakterien werden häufig verwendet, um photosynthetische Prozesse zu untersuchen. Der Modellorganismus *Synechocystis* sp. PCC 6803 (*Synechocystis*) wurde ausgewählt, um die Funktion von cyanobakteriellen MgtE- und (zwei) CorA-Homologen zu untersuchen. Die entsprechenden Einzel- oder Doppel-Knockout (KO)-Stämme wurden generiert. Studien dieser Stämme legten nahe, dass alle drei Kanäle an der Mg^{2+}-Homöostase beteiligt sind. Bei Wachstum unter Standardbedingungen, zeigten alle Mutanten (Mtn) eine beeinträchtigte Atmung, während diese beim Wildtyp (Wt) nur bei niedrigen Mg^{2+}-Konzentrationen beeinträchtigt war. Niedrigere Atmungsraten schienen ein Hauptgrund für die schwächere Ausbildung eines pH-Gradienten über den *Synechocystis*-Membranen zu sein. Bei Mg^{2+}-Limitierung, zeigten alle *ΔcorA*-Mtn eine verlängerte Lag-Phase. Darüber hinaus wurde bei der *ΔcorA1*-Mt auch unter Standardwachstumsbedingungen eine veränderte Photosyntheseleistung beobachtet. Die gleichen photosynthetischen Parameter waren bei Mg^{2+}-Limitierung im Wt verändert. Die Deletion des *mgtE*-Gens führte zu einer Co^{2+}-Resistenz. Alle vorhergesagten Mg^{2+}-Kanäle wurden mit einem N-terminalen gelb fluoreszierenden Protein (YFP)-Tag in *Synechocystis*-Zellen exprimiert. Während YFP markiertes MgtE in der Plasmamembran (PM) und der TM beobachtet wurde, wurde YFP markiertes CorA1 hauptsächlich in der TM und YFP markierte CorA2 nur in der PM beobachtet. Ein direkter Nachweis von (einem verringerten) Mg^{2+}-Fluss über die Membranen wird noch benötigt. Vorläufige *In-vitro*-Studien mit heterolog exprimiertem und gereinigtem, in Liposomen eingebautem CorA2-Protein schienen einen CorA2-vermittelten Mg^{2+}-Transport über (künstliche) Membranen zu bestätigen. Studien mit der heterolog exprimierten und gereinigten zytoplasmatischen Domäne von MgtE zeigten Mg^{2+}-abhängige Unterschiede in der Proteinstabilität, was auf eine regulatorische Rolle des MgtE-Kanals in *Synechocystis* durch mutmaßliche Ligandenbindung (Mg^{2+}-Bindung) hindeutet. Zusammenfassend erlauben die Studien neue Einblicke in die mögliche Rolle von Mg^{2+}-Kanälen in *Synechocystis*, einschließlich bioenergetischer Prozesse.

1. Introduction

1.1. Magnesium in the environment and living cells

Magnesium (Mg) is a highly abundant element in the earth's crusts as well as in aquatic environments. It is the fifth most commonly occurring element in the earth's crusts (Jokinen 1990), and Mg^{2+} is the third most abundant ion in seawater after Cl^- and Na^+ (R. B. Martin 1990). While seawater contains about 50 mM Mg^{2+} (Lehigh University 2011; Mewes *et al.* 2014), freshwater habitats are in contrast often characterised by very low Mg^{2+} concentrations with approximately 0.2-2 mM (Lehigh University 2011). In living cells, Mg^{2+} is the second most abundant cation after K^+ (Wacker 1969), and it is believed that it has already been used in biological systems very early during evolution (Birch 1990). Mg^{2+} is of great importance for cell metabolism as it is involved in numerous enzymatic reactions (Heaton 1990). Since about 50% of cells' Mg^{2+} is bound to adenosine triphosphate (ATP) forming MgATP (Maguire *et al.* 2002), it is a key player and regulator of cellular bioenergetics. As a counterion for the negatively charged phosphate groups, Mg^{2+} is also important for the stability of other nucleotides (Moncany *et al.* 1981; Anastassopoulou 2003). Additionally, Mg^{2+} stabilises membranes (Brock 1962), and ribosomes (Tissières *et al.* 1958), and can even be used for osmoregulation in marine bacteria (Fagerbakke *et al.* 1999). The majority of the metals in metalloenzymes are Mg^{2+} (Waldron *et al.* 2009). However, it forms weak complexes with some organic molecules (Waldron *et al.* 2009). Metal ions that are more tightly bound to apoproteins are generally recruited by metalloproteins (Irving *et al.* 1948; Foster *et al.* 2014). Therefore, Mg^{2+} can bind to an apoprotein only at higher intracellular Mg^{2+} concentrations, showing the importance of tightly controlled concentration. The amount of free cellular Mg^{2+} in the bacterium *Escherichia coli* (*E. coli*) was estimated to be between 1 and 2 mM (Alatossava *et al.* 1985), while total Mg^{2+} concentrations up to 100 mM were reported (Moncany *et al.* 1981).

1.2. Chl *a* and the model organism *Synechocystis* sp. PCC 6803

Serving as the central ion of the chlorin ring of Chl, Mg^{2+} is of particular importance for all oxygenic photoautotrophs. In 1817, the name chlorophyll was proposed by Pierre Joseph Pelletier and Joseph Bienaimé Caventou, referring to the leaf (green) colour (Pelletier *et al.* 1818). It took almost 100 years until the correct molecular formula was established by Richard Wilstätter (Willstätter *et al.* 1913). The photosynthetic pigment Chl *a* (Figure 1.1) is the only Chl in the cyanobacterium *Synechocys-*

tis, the strain used in this study. As gram-negative bacteria, *Synechocystis* contains

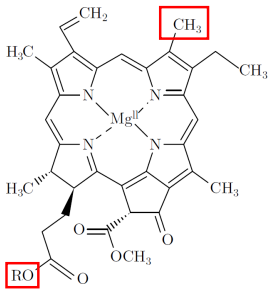

Figure 1.1: Chemical structure of Chl *a*
Chl *a* is the only chlorophyll found in *Synechocystis*. In the Chl *a* molecule, like in other chlorophyll forms a Mg^{2+} ion is located at the centre of the chlorin ring. The central ion is coordinated by four nitrogen atoms of the chlorin ring. Chl *a* is defined by its methyl group at position C-7 and R in the structure stands for the phytol ester a hydrocarbon tail (R = $C_{20}H_{39}$) that enables interaction with a hydrophobic environment. (The chemical structure was generated using EasyChem (Version 0.6).)

an outer membrane (OM). The peptidoglycan layer lies in between the OM and a PM. Like most cyanobacteria, *Synechocystis* contains an additional internal membrane system. These thylakoid membranes, surround an intracellular space called lumen and harbour all of the photosynthetic pigment-protein complexes (Lea-Smith *et al.* 2016; L. N. Liu 2016). Not surprisingly, membrane systems corresponding to the PM and TMs of cyanobacteria are also found in chloroplasts of higher plants and algae (J. F. Allen *et al.* 2011), given that more than 1.5 billion years ago, algal and higher plant plastids evolved from a cyanobacterial ancestor through an endosymbiotic event (Schimper 1883; Mereschkowsky 1905; Lynn 1967; Gray 1989; McFadden 2001; De Clerck *et al.* 2012). As organisms performing oxygenic photosynthesis, cyanobacteria clearly have an Mg^{2+} requirement. TMs of cyanobacteria and chloroplasts show a similar lipid content with two lipids carrying a negatively charged head group (Sakurai *et al.* 2006). This negative membrane surface is mostly screened by loosely bound Mg^{2+} ions (Barber 1980) and Mg^{2+} is even stored within the thylakoid lumen (Kaňa *et al.* 2016; Pottosin *et al.* 2016). The unicellular freshwater strain *Synechocystis* is a widely used model to study photosynthesis. The original strain ("Berkeley strain no. 6803") was already isolated in 1968 by R. Kunisawa (Stanier *et al.* 1971). When studying photosynthetic organisms, the use of *Synechocystis* has several advantages: *Synechocystis* can grow both in a liquid medium and on agar plates, and since it can take up glucose from the environment, it can grow mixotrophically or even heterotrophically under light-activated heterotrophic growth (LAHG) (daily brief light pulse (10-20 s) (S. L. Anderson *et al.* 1991). *Syne-*

chocystis can furthermore be easily transformed because it is naturally competent (Barten *et al.* 1995) and DNA uptake requires only incubation at a high cell density (Eaton-Rye 2011). Compared to other oxygenic photosynthetic organisms, it has a relatively short doubling time of $\sim$ 12 h (Vermass *et al.* 1988). Additionally, it was the first genome of a phototrophic organism to be fully sequenced in 1996 (Kaneko *et al.* 1996) and the extensively studied nucleotide sequence has been deposited at the public CyanoBase server (Nakamura *et al.* 2000; Nakao *et al.* 2010; Fujisawa *et al.* 2017) and has been extensively studied. As stated above, the endosymbiont theory suggests that chloroplasts originated from cyanobacteria, and, in fact, about $\sim$ 18% of the *Arabidopsis thaliana* genome has cyanobacterial origin (W. Martin *et al.* 2002). *Synechocystis'* natural competence, ease of maintenance, relatedness to chloroplasts, and the availability of literature data make it a very important model organism for studying photosynthesis and/or photosynthesis related processes.

1.3. Photosynthesis in plant chloroplasts and cyanobacteria

1.3.1. Linear electron flow

Oxygenic photosynthesis is the process by which plant chloroplasts and their progenitors, the cyanobacteria (Schimper 1883; Mereschkowsky 1905; Lynn 1967; Gray 1989; McFadden 2001; De Clerck *et al.* 2012) absorb energy from sunlight, convert it into electrochemical energy, and produce oxygen and organic compounds from carbon dioxide and water. Photosynthesis is regarded as one of the most important biological processes on earth. The overall equation of the photosynthesis reaction is:

$$6\,CO_2 + 6\,H_2O \xrightarrow{\text{light}} C_6H_{12}O_6 + 6\,O_2$$

Photosynthesis can be divided into two major processes. The so-called light reaction, which produces ATP and nicotinamide adenine dinucleotide phosphate hydrogen (NADPH), and the light-independent reaction, which uses these energy equivalents to fix CO_2 and produce organic compounds in the Calvin–Benson–Bassham (CBB) cycle. The light reaction takes place in/close to the TMs. When the light is captured by light-harvesting protein complexes, either inserted into the TM as in chloroplasts antenna complexes (Chl *a*) or attached to the TMs' surface, as are phycobilisomes (PBS) (containing phycobilins) in cyanobacteria (Grossman *et al.* 1995), the energy is channelled along a path and eventually reaches special reaction centre Chl *a* molecules (Mirkovic *et al.* 2017) within either P680 in photosystem II (PSII) (surrounded by the core antenna proteins CP43 and CP47 (Dekker *et al.* 2005; Nickelsen

et al. 2013)) or P700 in photosystem I (PSI). There, charge separation can occur, and the generated electrons are transferred along the so-called electron transport chain (ETC), consisting of a series of redox-active components of photosynthesis. The electron donor of this chain is water (see above), which is oxidised into molecular O_2 at the oxygen-evolving complex (OEC) of PSII (Joliot 1968; Joliot *et al.* 1969). The electron is transferred *via* plastoquinone Q_A to plastoquinone Q_B. Q_B can accept two electrons and two protons. When Q_B is fully reduced and protonated it forms plastoquinol (PQH_2), which then is released from PSII and diffuses into the membranes' plastoquinone (PQ) pool (Barber *et al.* 2001). PQH_2 reduces the cytochrome b_6f (Cyt b_6f) complex and, afterwards, the electrons are transferred *via* water-soluble proteins (PLC (plastocyanin) in chloroplasts/cyanobacteria and/or cytochrome c_6 in cyanobacteria) (J. F. Allen *et al.* 2011; Lea-Smith *et al.* 2016) on the luminal side to the donor side of PSI. There, the electron donor is neutralised by a positive charge generated by charge separation. The electron from PSI is transferred to ferredoxin (Fd) and reduces $NADP^+$ to NADPH, catalysed by the ferredoxin-$NADP^+$ reductase (FNR) (Carrillo *et al.* 2003). This electron transport route is called linear electron flow (LEF) (Figure 1.2). The electrons carried by NADPH can be further used for carbon fixation or donated to the cyclic electron flow (CEF) around PSI (Figure 1.3). A key difference between chloroplast and cyanobacterial ETC is that in cyanobacteria protein complexes of the photosynthetic and respiratory electron transfer chains are co-localised whithin the TMs (Vermaas 2001; Mullineaux 2014), and thus, the PQ pool can be reduced even in the dark *via* respiratory protein complexes: type II NADH:quinone oxidoreductase (NDH-2), and succinate dehydrogenase (SDH), with SDH having the greater capacity to feed electrons into the PQ pool than the NDH complexes (Cooley *et al.* 2001). Furthermore, PQH_2 can also donate electrons to terminal oxidases (TOs). Both chloroplasts and cyanobacteria contain such a terminal oxidase pathway to relax a reduced PQ pool (Pils *et al.* 2001; McDonald *et al.* 2011). Cyanobacteria possess a cytochrome *bd*-type quinol oxidase (Cyd) and an aa_3-type cytochrome *c* oxidase (Cox) in the TM (Howitt *et al.* 1998; Pils *et al.* 2001; Berry *et al.* 2002). Whereas in chloroplasts the plastid terminal oxidase (PTOX) can oxidise the PQ-pool (McDonald *et al.* 2011).

1.3.2. Cyclic electron flow

Since linear electron flow results in an ATP:NADPH ratio of 9:7 and CBB requires a fixed 3:2 ratio, cyclic electron flow, resulting solely in ATP, is needed to adjust the ATP:NADPH ratio (J. F. Allen 2003). During cyclic electron flow, the

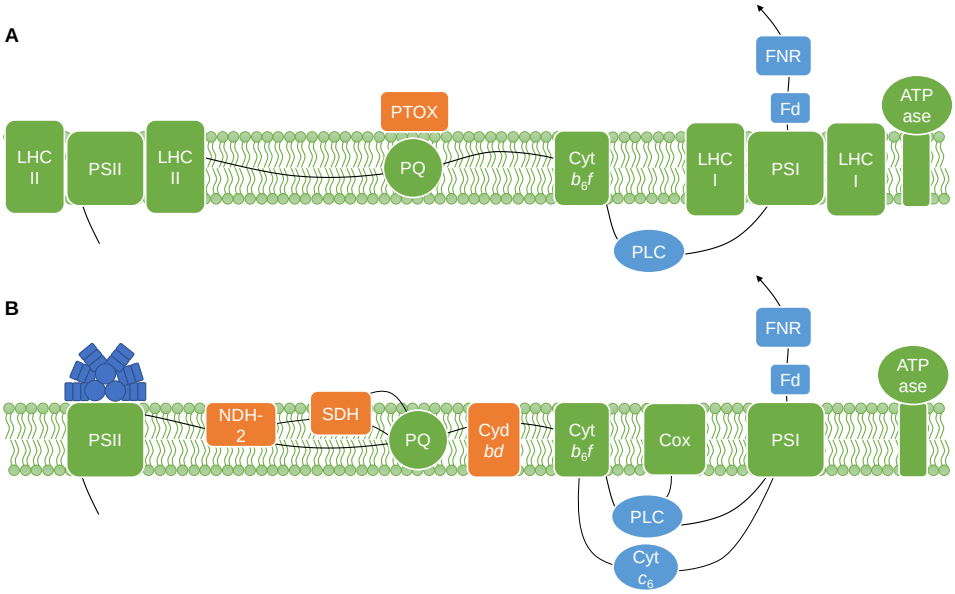

Figure 1.2: Linear electron flow in chloroplasts and cyanobacteria.
Schematic model of linear electron flow in chloroplasts (A) and cyanobacteria (B). After charge separation, the electron is carried from PSII *via* the PQ pool to the Cyt b_6f complex and from there to PSI by soluble proteins at the luminal side (PLC and/or Cyt c_6). PSI donates the electron after excitation to Fd and $NADP^+$ is reduced to NADPH at the FNR. Cyanobacteria have an additional electron input at the PQ pool from respiratory proteins (NDH-2, SDH). The TOs Cyd and Cox in cyanobacteria and PTOX in chloroplasts, can relax a reduced PQ pool.

electrons are transferred back to the PQ pool *via* NADPH/Fd reduction at the type I NADPH:plastoquinone oxidoreductase (NDH-1) complex (Mi *et al.* 1992b; Battchikova *et al.* 2011a; Battchikova *et al.* 2011b; Strand *et al.* 2017; Takahashi 2022) resulting in a higher ATP:NADPH ratio compared to linear electron flow alone. Besides these routes, an additional pathway was proposed. This involves the proton gradient regulation 5 (PGR5) and the PGR5-like photosynthetic phenotype 1 (PGRL1) in plants (DalCorso *et al.* 2008). In an *in vitro* assay the reduction of PQ by Fd was catalysed by PGR5 protein and the PGRL1 protein as a complex (Hertle *et al.* 2013). A PGR5 homolog has also been suggested to play a role in CEF in cyanobacteria (Yeremenko *et al.* 2005; Nikkanen *et al.* 2021). There are

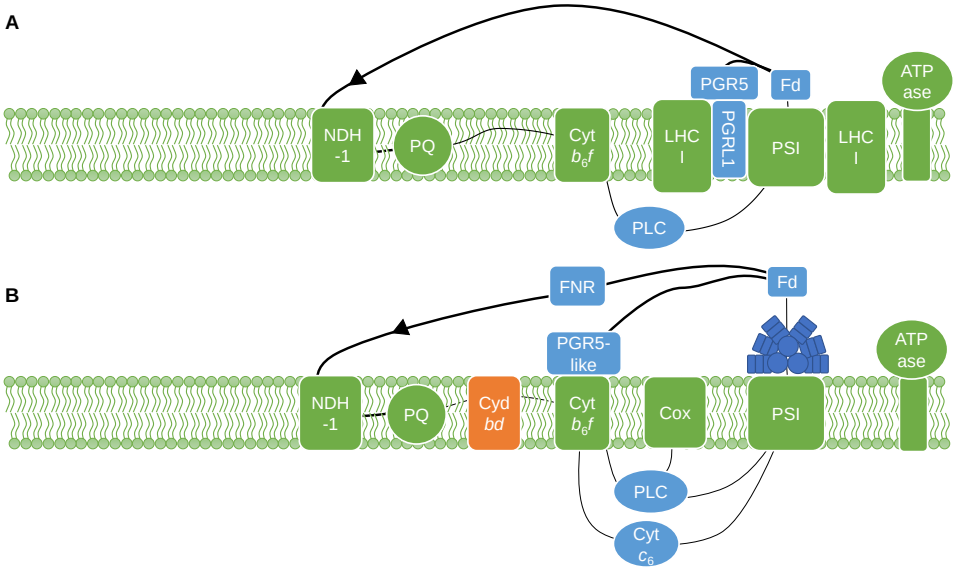

Figure 1.3: Cyclic electron flow in chloroplasts and cyanobacteria.
Schematic model of cyclic electron flow in chloroplasts (A) and cyanobacteria (B). During cyclic electron flow, either NADPH can reduce the PQ pool or the electron that arrives at Fd is not transferred onto $NADP^+$ *via* FNR but instead transferred back to the PQ pool. These transfers can be mediated by NDH-1 or the PGR5/PGR5like protein (Nikkanen *et al.* 2021; Takahashi 2022). This results in a higher ATP:NADPH ratio.

several sites of action for inhibitors along the ETC. The well-known algaecide and herbicide 3-(3,4-dichlorophenyl)-1,1-dimethylurea (DCMU) binds to the Q_B site at PSII, thereby blocking electron flow from PSII to the PQ pool (Metz *et al.* 1986; Mackay *et al.* 1993), while 2,5-dibromo-6-isopropyl-3-methyl-1,4-benzoquinone (DBMIB) binds at the Cyt b_6f, and thus, blocks the elctron flow from the PQ pool to the Cyt b_6f complex (Riedel *et al.* 1995). Since the cyanobacterial PQ pool in the TM is reduced by the activity of photosynthetic as well as respiratory protein complexes

(Vermaas 2001; Mullineaux 2014), inhibitors like malonate influence the electron transfer and thus also the proton pumping at both membranes when applicated. KCN is an inhibitor of TOs (Keilin 1929; Way 1984) and blocks electron transfer in the PM while electron transfer in the TM remains functional in the light. Methyl viologen (MV) and $HgCl_2$ predominantly block electron transport to NDH-1 (Patrick Fuerst *et al.* 1991; Mi *et al.* 1992a; Mi *et al.* 1992b; Mi *et al.* 2000; Sétif 2015). Further details will be discussed in section 4.2.

1.4. Formation of pH gradients across cyanobacterial membranes

During photosynthesis, electron transport is accompanied by the translocation of protons across the TM. Products of water oxidation at the PSII OEC are O_2 and protons, which are released into the lumen and where the latter acidify the lumen. While the electron is passed through the ETC, there is additional proton transfer from the cytoplasm into the lumen during both linear and cyclic electron flow. The formed pH gradient is the driving force of ATP synthesis from adenosine diphosphate (ADP) and phosphate at an F-type ATPase. Electron transfer coupled proton translocation takes place at the PQ pool. PQ is reduced to PQH_2 at the Q_B site of PSII. The PQH_2 diffuses through the TM to the Cyt b_6f complex (Barber *et al.* 2001). The ratio of translocated protons per transported electrons is doubled by the so-called Q-cycle (Mitchell 1976) where 2 H^+ are translocated into the thylakoid lumen while one electron is donated to PLC. As already mentioned above, respiratory and photosynthetic electron transfer take place in cyanobacterial TMs (Vermaas 2001; Mullineaux 2014). SDH and NDH-2 only transfer electrons to the PQ pool and are not involved in proton translocation despite its induced proton translocation by the formation of PQH_2 (Ermakova *et al.* 2016). Upon oxidation of NADPH to $NADP^+$ at the NDH-1 complex, electrons are transferred to the PQ pool which has a central role in proton translocation. Furthermore, NDH-1 itself can also pump protons across the membrane (Battchikova *et al.* 2011a; Strand *et al.* 2017). The TOs localised at the TM are also involved in the generation of a ΔpH. While Cyd is only involved in accepting electrons from the PQ pool and transferring them to oxygen and thus alkalises the cytoplasm, Cox oxidases can pump protons across the TM while transferring electrons to oxygen (Brändén *et al.* 2006; Ermakova *et al.* 2016). These processes in cyanobacteria allow establishing a proton motive force (PMF) and, therefore, ATP synthesis even in the dark (Mullineaux 2014). In addition to light-dependent linear and light-independent electron flow and proton translocation at the TMs, there is proton translocation at the plasma membrane when electrons

are fed into the PQ pool *via* NDH-2 and SDH. In the PM, electron transfer from the PQ pool to either Cyd or an alternative respiratory terminal oxidase (ARTO) releases protons into the periplasm (Lea-Smith *et al.* 2016). ARTO additionally pumps protons across the PM (Pils *et al.* 2001; Doello *et al.* 2021) while transferring electrons onto molecular oxygen. In addition to these processes directly involved in establishing a proton driving force along the TM and the PM, other processes also affect the cytoplasmic pH, such as the bidirectional functioning [NiFe]- hydrogenase (H_2ase), which can use or release H^+ (De Rosa *et al.* 2015), and flavodiiron proteins that reduce molecular oxygen to water and are involved in photoprotection (Vicente *et al.* 2002; Santana-Sanchez *et al.* 2019) (Figure 1.4). Besides light-independent

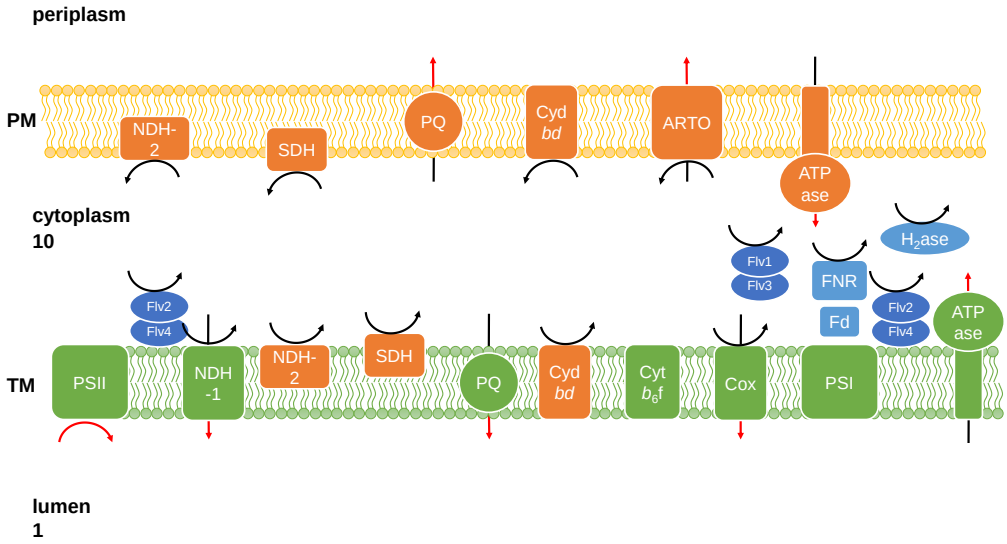

Figure 1.4: Proton transport across *Synechocystis* membranes.
Arrow colours indicate the alkalisation (black) or acidification (red) of the compartment. The numbers below cytoplasm and lumen indicate the approximate volume ratio from 10:1 of these two compartment, (M. M. Allen 1968; Belkin *et al.* 1987; Van De Meene *et al.* 2012). In the PM, NDH-2, SDH, and Cyd cannot pump protons across the membrane and thus only contribute to the alkalisation of the cytoplasm. In contrast, ARTO can translocate protons across the PM. Electron transfer from the PQ pool to downstream electron acceptors leads to the alkalisation of the cytoplasm and simultaneous acidification of the periplasm and the lumen. ATPases acidify the cytoplasm and with this alkalise either the periplasm or the thylakoid lumen. Water splitting at PSII releases protons, and hence acidifies the thylakoid lumen. Electron transfer through NDH-1 and Cox alkalises the cytoplasm and acidifies the thylakoid lumen by pumping protons across the TMs. Reduction of $NADP^+$ to NADPH at the FNR alkalises the cytoplasm. Reduction of flavodiiron proteins (Flv 1-4) and H_2ase by accepting electrons from PSII and/or Fd alkalise the cytoplasm.

proton translocation, there is also light-dependent proton pumping across the PM. During the photosynthetic light reactions, the alkalisation of the cytoplasm is not

caused only by protons being pumped into the thylakoid lumen, but also by simultaneous proton extrusion into the surrounding medium (Nitschmann *et al.* 1985; Peschek *et al.* 1985). Several different mechanisms can be involved in proton extrusion at the PM. In *Synechocystis*, proton extrusion into the surrounding medium can be driven by either ATP hydrolysis at the ATPase or mediated by the respiratory electron transport chain of the PM (Teuber *et al.* 2001). However, additional proteins have been identified that regulate light-dependent proton translocation at the PM. The *pxcA* gene (proton-extrusion-protein A) (formerly *cotA*) and the *pxcL* gene (*pxcA*-like) of *Synechocystis* encode two homologs of the chloroplast *ycf10* gene (also termed chloroplast envelope membrane protein A (CemA)) and the *dldg1* gene (Day-Length-dependent Delayed-Greening1) both of which are localised at the inner chloroplast envelope membrane (Sasaki *et al.* 1993; Harada *et al.* 2019). It was suggested that the two gene products of *dldg1* and *ycf10* interact with each other to regulate proton homeostasis in chloroplasts, which is important during light acclimation (Harada *et al.* 2019). A *pxcA* gene deletion mutant did not show light-induced sodium-dependent proton extrusion (Katoh *et al.* 1996; Sonoda *et al.* 1998). During the first 30 s of illumination the PxcA protein extrudes H^+ from the inside to the outside of the cells. This results in a rapid formation of the H^+ concentration gradient across the membranes. After 30 s, the process is converted and PxcA and PxcL take up H^+ from the extracellular environment. Thus, *Synechocystis* cells first extrude H^+ and subsequently take them up during the light exposure (Inago *et al.* 2020). Light-dependent proton extrusion seemed to be influenced by sodium concentrations of the surrounding medium (Kaplan *et al.* 1989; Katoh *et al.* 1996; Sonoda *et al.* 1998). *Synechocystis* possesses six Na^+/H^+ antiporters (Tsujii *et al.* 2020) which are involved in the proton translocation across the TM (NhaS3 (Na^+/H^++ antiporter) (Tsunekawa *et al.* 2009) and PM (NhaS4 (Na^+ influx (Mikkat *et al.* 2000); Na^+/H^+ antiporter (Billini *et al.* 2008))). Overall, the cytoplasmic pH of cyanobacteria is approximately at pH 7 while the luminal pH in the dark ranges from $\sim$ pH 5.0 - 5.5 (Falkner *et al.* 1976; Peschek *et al.* 1985; Belkin *et al.* 1987). Upon light exposure, the cytoplasmic pH rises about 0.5 units while the luminal pH decreases by the same amount when cells are illuminated (Falkner *et al.* 1976; Belkin *et al.* 1987). Coupling of an electrochemical gradient of protons across membranes with the generation of ATP was first postulated in 1961 by Peter Mitchell (Mitchell 1961). However, alkalisation of the cytoplasm is also important for a fully functional CBB cycle. In the chloroplast stroma, light-dependent alkalisation activates fructose biphosphatase and ribulose-1,5-bisphosphate carboxylase (RuBisCO) (Lorimer *et al.*

1976; Flügge *et al.* 1980; Mott *et al.* 1986) and a decrease in the degree of alkalinity in the chloroplast stroma downregulates CO_2 fixation (Werdan *et al.* 1975).

1.5. Diversity of TM localisation and architecture

Although light-dependent reaction is always localised at the TM, the TM architecture is highly divers (Rast *et al.* 2015). There are even cyanobacteria, *e.g. Gloeobacter violaceus* that do not possess an additional inner membrane system (Rippka *et al.* 1974) but where the complexes of the photosynthetic light reaction are localised within defined PM regions (Rexroth *et al.* 2011). While TMs in cyanobacteria may vary in their spatial arrangement (Mareš *et al.* 2019), plant chloroplasts contain TMs with distinct areas: The grana and the stroma lamellae, that differ in protein composition. While PSII and the Light Harvesting Complex II (LHCII) are mainly localised in the stacked grana, PSI and the ATPase reside predominantly in the stroma and the Cyt b_6f complex is evenly distributed (Andersson *et al.* 1980; Dekker *et al.* 2005). It has been suggested that the separation of the proteins is preventing excess energy dissipation towards PSII (J. M. Anderson *et al.* 1994). Although the cyanobacterial TMs do not show such a structural separation, there appears to be a local accumulation of different populations of protein complexes within the membrane, forming segregated domains of both PSII and PSI (Casella *et al.* 2017; Strašková *et al.* 2019; Mullineaux *et al.* 2020).

1.6. Excess energy dissipation

1.6.1. Non-photochemical quenching (NPQ) in chloroplasts and cyanobacteria

In chloroplasts, formation of a trans-thylakoid proton gradient is an prerequisite for energy dissipation under high light conditions, which is important to ensure the proper function of the photosynthetic apparatus. The mechanism involves activation of the xanthophyll cycle (Yamamoto *et al.* 1962; Latowski *et al.* 2004). During the xanthophyll cycle, the low pH activates violaxanthin de-epoxidase (VDE), which converts violaxanthin into zeaxanthin (Latowski *et al.* 2004). In addition, low luminal pH leads to protonation of the PSII subunit PsbS (X. P. Li *et al.* 2000), which alters the interaction between PSII and LHCII (Ruban 2018). Cyanobacteria lack such mechanisms, in which low luminal pH plays a central role. Cyanobacteria have another regulatory process, in which strong blue light activates a soluble protein, the orange carotenoid protein (OCP) (Wilson *et al.* 2006). This protein harbours a single 3-hydroxyechinenone (Kerfeld *et al.* 2003) and its interaction with the PBS,

increases energy dissipation in the form of heat (Wilson *et al.* 2006) (Figure 1.5). Additionally, like in plants carotenoids play an important role in the protection of the photosynthetic apparatus from photodamage under high light (Young *et al.* 1996; Steiger *et al.* 1999).

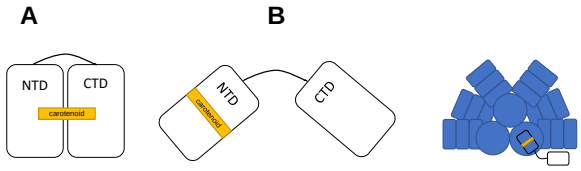

Figure 1.5: Schematic representation of the OCP quenching mechanism.
The proposed schematic model is based on Cogdell and Gardiner (Cogdell *et al.* 2015). (A) The OCP protein consists of an N-terminal domain (NTD) and a C-terminal domain (CTD) domain connected by a linker and a carotenoid. (B) Upon exposure to strong blue light, the carotenoid moves into the NTD domain, binds to the allophycocyanin (APC) protein of the PBS complex and induces NPQ (Cogdell *et al.* 2015).

1.6.2. Light acclimation and regulation of the electron flow by state transitions

Both chloroplasts and cyanobacteria can adjust the energy input to their PSs. Whether this is achieved by positional changes of the antenna complexes or is simply a redistribution of the excitation energy between the two PSs, regardless of its exact manner, is still under debate. These so-called state transitions are triggered by changes in the redox state of the PQ pool and were first described in algae (Bonaventura *et al.* 1969; Murata 1969). In chloroplasts with their membrane-integrated antenna complexes, changes in the redox level are sensed by the Cyt b_6f complex (Wollman *et al.* 1988). The phosphorylation of a specific kinase triggers the movement of the main PSII (LHCII) antenna (Depège *et al.* 2003), and the antenna becomes associated with the PSI-enriched stroma lamellae (J. F. Allen 1992). Cyanobacterial PBS regulate their energy distribution to the two PSs by redistributing the energy by their soluble antenna systems, the PBS, between the two PSs (Calzadilla *et al.* 2020). PBSs consist of six rods formed by phycocyanin (PC) and a core formed by allophycocyanin (APC) (Kirilovsky *et al.* 2014). They are mainly associated with PSII when the PQ pool is oxidised (state I) and predominantly associated with PSI when the PQ pool is reduced (state II) (Mullineaux *et al.* 1990). Although cyanobacterial state transitions have been studied extensively, there is still an ongoing debate about how state transitions are regulated on the molecular level.

1.7. Mg^{2+} fluxes across TMs

During the formation of a pH gradient generated by the photosynthetic electron transport chain in the light, the electric potential is balanced by the release of Mg^{2+} and K^+ from the lumen and a reverse uptake of Cl^- (Dilley *et al.* 1965; Hind *et al.* 1974; Chow *et al.* 1976; Lyu *et al.* 2017). It has recently been shown that the $MgATP^{2-}$ complex pool increases upon illumination in the chloroplast stroma, and thus Mg^{2+} is required for ATP generation as well as for the activity of enzyme involved in carbon fixation (Elsässer *et al.* 2020). While a K^+ channel has already been identified in the *Synechocystis* TM, which partially dissipates the electrical component of PMF $\Delta\Psi$ (Checchetto *et al.* 2012), there is still a lack of knowledge on Mg^{2+} channels in TMs. Although it has long been known that Mg^{2+} fluxes across TMs occur in the light (Dilley *et al.* 1965; Barber *et al.* 1974; Hind *et al.* 1974; Chow *et al.* 1976; Portis *et al.* 1976) and a channel transferring several cations (Ca^{2+}, Mg^{2+}, K^+) (ICTCC (intermediate-conductance thylakoid cation channel)) across the chloroplast TM has been identified in patch clamp studies (Pottosin *et al.* 1996), the role of Mg^{2+} fluxes across TMs and the involved channels remain little understood.

1.8. Channel-mediated Mg^{2+} transport in bacteria

In recent years, channels have been identified that mediate Mg^{2+} flux across bacterial membranes. As discussed later, homologs of these channels are also encoded in the *Synechocystis* genome. The chemistry of Mg^{2+} is very special amongst the biologically relevant cations. It has a small ionic radius, but a large hydration shell compared to other cations with the first hydration shell bound tightly (R. B. Martin 1990; Maguire *et al.* 2002). This requires a rather unique transport mechanism (Niegowski *et al.* 2007). Two distinct channels have been identified in bacteria that facilitate Mg^{2+} flux in prokaryotes (Maguire 2006; Moomaw *et al.* 2008). Although structurally different, MgtE and CorA have revealed potential common mechanisms of Mg^{2+}-based regulation as they both function as ligand-gated ion channels with Mg^{2+} as a negative regulator that leads to channel closure (Payandeh *et al.* 2008).

1.8.1. Mg^{2+} transport mediated by the CorA channel protein

Uptake and efflux of Mg^{2+} in metabolically active *E. coli* cells were first described in 1969 (Silver 1969). In 1971 Nelson and Kennedy observed that mutants with higher resistance to cobalt ions showed decreased transmembrane flux of both Co^{2+}

and Mg^{2+} ions (Nelson *et al.* 1971). Later, the responsible gene for the observed resistance, *corA* was identified in *Salmonella typhimurium* (*S. typhimurium*) and the protein was biochemically characterised (Hmiel *et al.* 1986). CorA is widely distributed amongst bacteria and often serves as the primary Mg^{2+} channel (Smith *et al.* 1995; Niegowski *et al.* 2007). Mg^{2+} transport by CorA follows the membrane potential, and thus, CorA is a true Mg^{2+} channel (Maguire 2006). Although CorA is mainly an Mg^{2+} channel it also facilitates the flux of Co^{2+} and Ni^{2+} (Nelson *et al.* 1971; Maguire 2006). Measured affinities (Co^{2+} and Ni^{2+}) in *E. coli* and *S. typhimurium* are in the toxic range for bacteria (Maguire 2006). The functional channel is a homo-pentamer with a large N-terminal cytoplasmic domain (Lunin *et al.* 2006). The monomer has a large cytoplasmic domain at the N-terminus that has a α/β-structure and a C-terminal domain with two transmembrane helices. A central funnel that opens to the cytoplasm is formed by all of the five innermost helices. The ion-conducting pore is formed by this funnel as it extends into the membrane (Eshaghi *et al.* 2006; Lunin *et al.* 2006; Payandeh *et al.* 2006). All CorA proteins are characterised by a conserved Gly-Met-Asn (GMN) motif sandwiched between two conserved transmembrane helices at the C-terminus (Knoop *et al.* 2005) (Figure 1.6). Based on Cryo EM studies it has been sug-

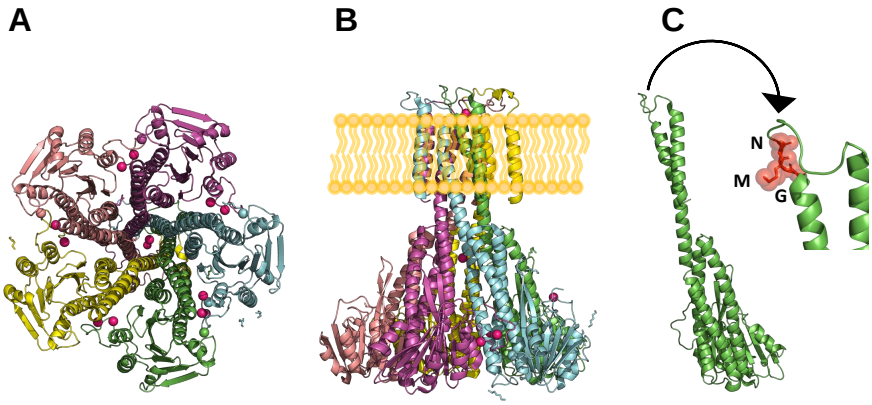

Figure 1.6: X-ray structure of the CorA protein from *Thermotoga maritima* (PDB 4I0U) (Nordin *et al.* 2013).
(A) Bottom view of CorA with bound Mg^{2+} ions (pink). Each monomer is shown in a different colour. (B) Side view of CorA with bound Mg^{2+} ions. (C) CorA monomer with the conserved GMN motif (red) in the loop region between the two transmembrane helices.

gested that Mg^{2+} ions stabilise a 5-fold symmetric closed state and that Mg^{2+} release leads to large-range cytoplasmic domain rearrangements (Matthies *et al.* 2016) (Figure 1.7). These conformational changes have been further addressed by atomic

force microscopy studies. Here, the opening mechanism was described as a three-phase process: The Mg^{2+} bound, 5-fold symmetric state is followed by a highly mobile state when the bound Mg^{2+} ions are subsequently released. This transiently ends up in asymmetric architectures where different sub-structures can be distinguished and which is characterised by an elevated cytoplasmic domain (Rangl *et al.* 2019). It has been shown that cobalt(III)hexaammine is a potent inhibitor of the

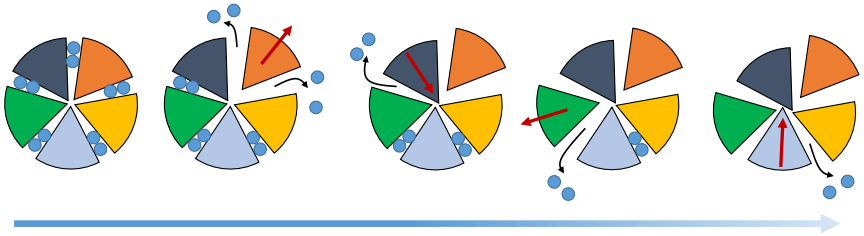

Figure 1.7: Schematic view of Mg^{2+}-induced conformational changes of CorA.
The proposed schematic model of the CorA opening is based on Matthies *et al.* (Matthies *et al.* 2016). At high Mg^{2+} (blue circles) concentrations, all 10 binding sites are occupied, and the channel is in a closed conformation (left). A transient opening occurs when the Mg^{2+} concentration falls (from left to right) and there is a subsequent release of Mg^{2+} ions accompanied by movements of the monomers (indicated by red arrows).

bacterial CorA channel (Kucharski *et al.* 2000). As cobalt(III)hexaammine is almost exactly the size of a hydrated Mg^{2+} it has been concluded that a completely hydrated Mg^{2+} binds to the channel and that the strongly bound water molecules have to be removed when Mg^{2+} is transferred across the membrane (Maguire *et al.* 2002). For influx, a hydrated Mg^{2+} ion binds at the pore entrance to the conserved GMN motif, and the Mg^{2+} ion is subsequently dehydrated for transport (Lunin *et al.* 2006; Pfoh *et al.* 2012).

1.8.2. CorA homologs in plants

CorA homologs have been also identified in eukaryotes (Moomaw *et al.* 2008). The CorA channel belongs to the CorA-Mrs2-Alr1 superfamily of Mg^{2+} channel proteins and distant relatives of CorA in eukaryotes are mostly termed Alr1p and Mrs2p (Schweyen *et al.* 2007). The Mrs2 family was first identified in *Arabidopsis thaliana* (Schock *et al.* 2000; L. Li *et al.* 2001), has nine members (Saito *et al.* 2013), and AtMRS2-7 allows the plant to grow at low Mg^{2+} conditions (Gebert *et al.* 2009). In plant chloroplasts, a CorA homologue AtMRS2-11/AtMGT10 is probably localised to the inner envelope membrane and is essential for chloroplast development as well

as photosynthetic function (Drummond *et al.* 2006). Since Mg^{2+} is required for grana stacking, this agrees well with the AtMGT10 mutant showing abnormal TM stacking (Sun *et al.* 2017). Members of the Mrs2 proteins (OsMRS2-5 and OsMRS2-6) have also been found to be localised in the chloroplast in rice (*Oryza sativa*) (Saito *et al.* 2013). In this work, the two CorA homologues that were identified *via* gene analysis in *Synechocystis* using CyanoBase (Nakamura *et al.* 2000; Nakao *et al.* 2010; Fujisawa *et al.* 2017) were investigated. It is not uncommon for cyanobacteria to encode two possible CorA homologs (Pohland *et al.* 2019). The open reading frames (ORFs) *sll0507* (*corA1*) and *sll0671* (*corA2*) code for two possible CorA channels and have already been postulated to be Mg^{2+} channels and termed CorA1 (Sll0507) and CorA2 (Sll0671) (Pakrasi *et al.* 2006). Both proteins harbour the conserved GMN within their sequence. The CorA1 protein was found to be localised in the cyanobacterial PM (Liberton *et al.* 2016). The expression of the *sll0507* gene was upregulated under salt stress, nitrogen starvation (Krasikov 2012) or when cells were grown at fluctuating light conditions under low CO_2 (Mustila *et al.* 2021). Expression of the *sll0671* gene, coding for the second CorA homolog, was found to be connected to salt stress in *Synechocystis* (Qiao *et al.* 2013). It is important to note that in rice the transporter OsHKT1;5a, which is responsible for removing Na^+ from the xylem, requires transmembrane Mg^{2+} flux mediated by the CorA homolog OsMGT1 (Z. C. Chen *et al.* 2017). Nonetheless, knocking out the *sll0671-0672* *Synechocystis* genes did not induce any salt sensitivity (Z. Wang *et al.* 2002). The expression of the *sll0671* gene was also upregulated under conditions of nitrogen starvation (S. Huang *et al.* 2013).

1.8.3. Mg^{2+} transport mediated by the MgtE channel protein

MgtE, a second type of Mg^{2+} channels, was identified using the MM281 strain of *S. typhimurium*, which possesses mutations in each Mg^{2+} uptake system. This mutant was used to screen a *Bacillus subtilis* plasmid library (Smith *et al.* 1995). A bacterium typically expresses either CorA or MgtE, with a few exceptions in which both *corA* and a *mgtE* genes are expressed (Moomaw *et al.* 2008). Nevertheless, as in case of CorA, Mg^{2+} import by MgtE is also controlled by the membrane potential (Maguire 2006). A C-terminal transmembrane domain and a cytoplasmically localised soluble N-terminal domain make up each monomer of the homodimeric MgtE channel. Each monomer has five membrane-spanning helices in its transmembrane domain, and the dimer's ion-conducting pore is made up of all 10 transmembrane helices (Hattori *et al.* 2007). In the cytoplasmic domain a superhelical N-terminal

subdomain is linked by a single (connecting) helix to a tandemly repeated cystathionine β-synthase (CBS) domain (Hattori *et al.* 2007) (Figure 1.8). Alexander Bateman was the first to identify CBS domains in the human cystathionine β-synthase and several other bacterial proteins (Bateman 1997). CBS pairs form a tight structure also known as Bateman domain (Baykov *et al.* 2011). CBS domains are involved in a variety of cellular processes, including energy sensing and the regulation of ion-conducting channels, and they can be found in all kingdoms of life either as separate proteins or fused to other proteins (Scott *et al.* 2004; Ereño-Orbea *et al.* 2013). Mg^{2+} flux through the conductive pore is controlled by the release of Mg^{2+} ions bound to six putative Mg^{2+} binding sites within the cytoplasmic MgtE domains and the binding of Mg^{2+} to these intracellular domains depends on the intracellular Mg^{2+} level (Hattori *et al.* 2009). Overall, the MgtE dimer has 13 Mg^{2+} binding sites, six per monomer in each cytoplasmic domain, plus one Mg^{2+} ion bound in the channel pore, formed by 10 transmembrane α helices, in the closed state (Hattori *et al.* 2007; Payandeh *et al.* 2013; Maruyama *et al.* 2018). The negatively charged Asp432 in the centre of the transmembrane pore is optimised to bind a hydrated Mg^{2+} ion (Takeda *et al.* 2014; Kimura *et al.* 2018). When the intracellular Mg^{2+} concentration increases above ∼ 5-10 mM, all of MgtE's binding sites are occupied and the channel is in its closed conformation. It re-opens when the Mg^{2+} concentration falls below that value (Hattori *et al.* 2009; Tomita *et al.* 2017; Maruyama *et al.* 2018).

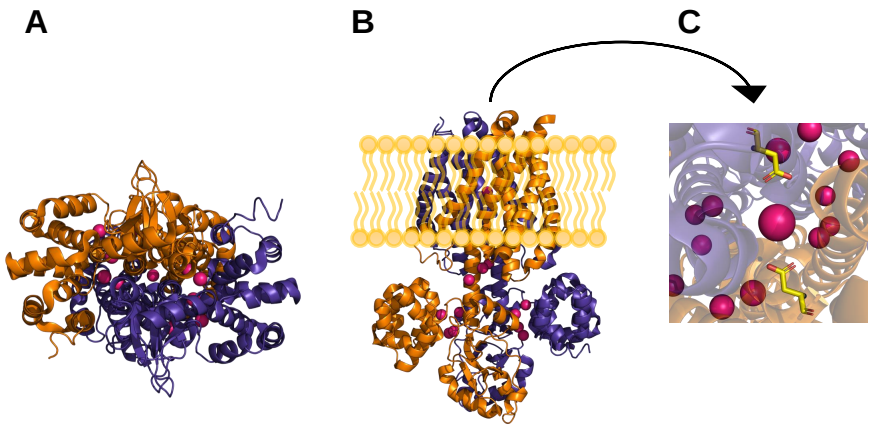

Figure 1.8: X-ray structure of the MgtE protein from *Thermus thermophilus* (PDB 2ZY9) (Hattori *et al.* 2009).
(A) Bottom view of MgtE with bound Mg^{2+} ions (pink). Each monomer is marked by a different colour. (B) Side view of membrane integrated MgtE with bound Mg^{2+} ions. (C) Top view of the MgtE dimer with both Asp432 (sticks, coloured by element) that bind a hydrated Mg^{2+}.

The opening and closing are accompanied by large changes in the orientation of the N-terminal cytoplasmic domains, which exhibit a high degree of flexibility (Hattori *et al.* 2007; Moomaw *et al.* 2008; Hattori *et al.* 2009; Maruyama *et al.* 2018; Jin *et al.* 2021). The CBS domains dimerise when Mg^{2+} is present, and Mg-mediated interactions between the connecting helices and the cytosolic and transmembrane domains result in channel closure. The CBS domains' dimeric interface becomes looser as the concentration of Mg^{2+} decreases, allowing the connecting helices to rotate and swing apart, and the N domain also moves away from the CBS domain (Hattori *et al.* 2007) (Figure 1.9). Nucleotides can be recognised by the CBS domain (Kemp 2004; Ereño-Orbea *et al.* 2013). For example, the Cl^- channel (ClC) family proteins also contain CBS domains that have been shown to bind ATP (Scott *et al.* 2004), and in patch clamp studies a heterologously expressed hClC-4 channel supported Cl^- current when ATP was present (Vanoye *et al.* 2002). Also for MgtE, ATP has been shown to affect the channel properties by inducing complete channel closure already at a lower Mg^{2+} concentration of ∼1-2 mM (Tomita *et al.* 2017). In some bacteria,

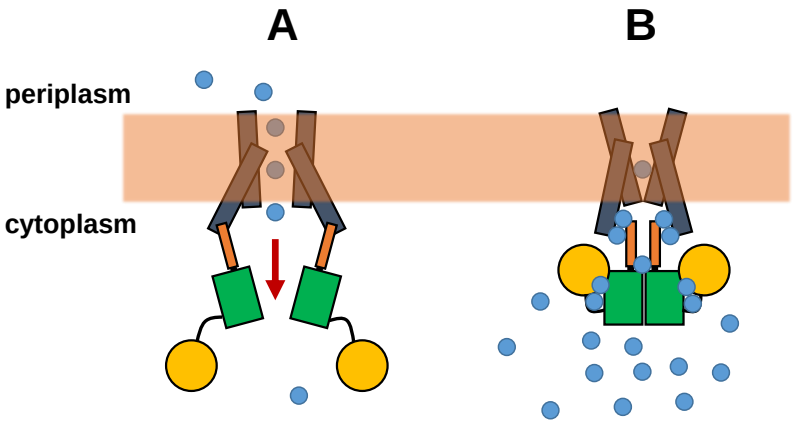

Figure 1.9: Schematic view of Mg^{2+}-induced conformational changes of MgtE.
The proposed schematic model of MgtE closure is based on Hattori *et al.* (Hattori *et al.* 2007)/Tomita *et al.* (Tomita *et al.* 2017). (A) At low Mg^{2+} (blue circles) concentrations, MgtE facilitates Mg^{2+} fluxes across the membrane (brown, red arrow: direction of Mg^{2+} influx). (B) At concentrations of ∼ 5-10 mM, the channel undergoes a conformational change and closes (Hattori *et al.* 2007; Hattori *et al.* 2009; Tomita *et al.* 2017). The binding of ATP to the CBS domain (green) leads to channel closure at already ∼ 1-2 mM Mg^{2+} (Tomita *et al.* 2017).

also expression of MgtE protein is controlled by Mg^{2+} ions through a riboswitch (M-box) (Dann *et al.* 2007). Typically this RNA motif is located upstream of the Mg^{2+} transport genes in gram-positive bacteria (Barrick *et al.* 2004). However, the M-box is not present in all bacteria that encode the *mgtE* gene (Franken *et al.* 2022).

1.8.4. MgtE homologs

While MgtE is abundant in bacteria and homologs can be found also in eukarya (Moomaw *et al.* 2008), no close homologs have been identified in higher plants thus far (Yan *et al.* 2018). Eukaryotic homologs belong to the solute carrier SLC41 subfamily (Wabakken *et al.* 2003; Goytain *et al.* 2005; Sahni *et al.* 2007; De Baaij *et al.* 2016). BLAST searches revealed the existence of single MgtE domain proteins in both green and red algae, and an SLC41 family homolog has been found to be involved in the circadian timekeeping of the unicellular green algae *Ostreococcus tauri* (Feord *et al.* 2019). While MgtE functions as an Mg^{2+} influx system in bacteria, SLC41 proteins have been reported to function as Na^{+}/Mg^{2+} exchangers (Wabakken *et al.* 2003; Kolisek *et al.* 2012). The ORF *slr1216* (*mgtE*) in *Synechocystis* encodes a possible MgtE channel (Kaneko *et al.* 1996; Pakrasi *et al.* 2006), which is localised in the PM, according to proteomic analyses (Pisareva *et al.* 2011; Liberton *et al.* 2016; Baers *et al.* 2019). It has been suggested that the gene product of *slr1216* serves as the main Mg^{2+} import system in *Synechocystis* (Pakrasi *et al.* 2006) and a deletion mutant had less Chl *a* when grown under salt stress conditions (T. Li *et al.* 2016). Furthermore, the *slr1216* gene product was identified being a cyclic di-adenosine monophosphate binding protein (Selim *et al.* 2021).

1.8.5. Mg^{2+} efflux mediated by the CorB/C channel protein

In *S. typhimurium*, three additional genes, *corB*, *corC*, and *corD* were identified to be involved in Mg^{2+} efflux (M. M. Gibson *et al.* 1991). CorB/C are prokaryotic members of the cyclinM (CNNM)(formerly known as ancient conseved domain proteins (ACDP) (C. Y. Wang *et al.* 2003; Giménez-Mascarell *et al.* 2019))/CorC family of proteins widely distributed in all domains of life (C. Y. Wang *et al.* 2003; Funato *et al.* 2019; Giménez-Mascarell *et al.* 2019; Y. Huang *et al.* 2021). Mg^{2+} transport through CorB from *Methanoculleus thermophilus* was demonstrated in a liposome-based *in vitro* assay (Y. S. Chen *et al.* 2021). Like MgtE, CorB/C proteins also contain CBS domains that can bind MgATP (Y. S. Chen *et al.* 2021; Franken *et al.* 2022) (Figure 1.10). In *Staphylococcus aureus*, loss of the *corC* homolog gene *mpfA* resulted in hypersensitivity to high Mg^{2+} concentrations (Armitano *et al.* 2016; Trachsel *et al.* 2019). It has been suggested that the YhdP (a CorC homolog) protein is an important efflux pump in *Bacillus subtilis* (Akanuma *et al.* 2014). CorC expression in human embryonic kidney (HEK)293 cells showed Na^{+} gradient-dependent Mg^{2+} extrusion (Y. Huang *et al.* 2021). In addition, two members of the Mg^{2+} Re-

lease (MGR) family, which are homologs of the ACDP/CNNM family, are localised in the chloroplast inner envelope membrane and are responsible for chloroplast Mg^{2+} uptake (B. Zhang *et al.* 2022). These results indicate the importance of the CorB/C proteins in maintaining Mg^{2+} balance in bacteria.

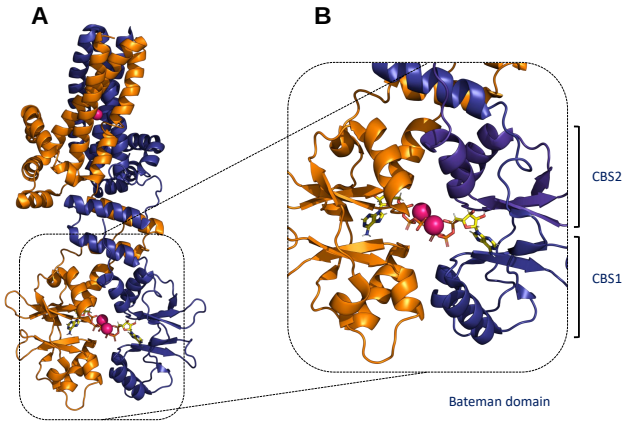

Figure 1.10: X-ray structure of the CorB protein of *Methanoculleus thermophilus* (PDB 7M1T) (Y. S. Chen *et al.* 2021).
(A) Side view of CorB with each monomer coloured differently and with two bound MgATP complexes (Mg^{2+}: pink spheres; ATP: yellow sticks coloured by element). (B) Side view of the cytoplasmic domain of CorB with the two CBS pairs each forming a Bateman domain.

2. Objectives of this thesis

Mg^{2+} is a crucial ion for cell viability and of particular importance in organisms performing oxygenic photosynthesis as it serves as the central ion of the light-harvesting pigment chlorophyll. The cytoplasmic Mg^{2+} concentration in chloroplasts rises during light exposure, and Mg^{2+} has been proposed to serve as a counterion for protons being pumped across thylakoid membranes (Dilley *et al.* 1965; Barber *et al.* 1974; Hind *et al.* 1974; Chow *et al.* 1976; Portis *et al.* 1976; Lyu *et al.* 2017). Bacterial Mg^{2+} channels and transporters have been identified in recent years, and homologs are also found in eukaryotes. However, although a non-selective cation channel was identified in chloroplast thylakoid membranes that appears to mediate Mg^{2+} fluxes (Pottosin *et al.* 1996), the exact identity of Mg^{2+} channels translocating Mg^{2+} across thylakoid membranes is still enigmatic. Understanding the Mg^{2+} transport across membranes in the model organism *Synechocystis* will help to better understand the physiological "need" of Mg^{2+} flux across the membranes in oxygenic photosynthetic organisms and Mg^{2+} homeostasis.
I have studied the requirement of Mg^{2+} for the cell growth of *Synechocystis* and the function (and localisation) of its predicted Mg^{2+} channel homologs *in vivo* and *in vitro*. The dissertation is divided into four main chapters, all describing a certain project aspect.

1. **The influence of low Mg^{2+} availability on *Synechocystis* wt.**

   Mg^{2+} deficiency has already been shown to alter Chl *a* content in plants (Balakrishnan *et al.* 2000; Hermans *et al.* 2004; Hermans *et al.* 2005; Yang *et al.* 2012) and cyanobacteria (Utkilen 1982) as well as their photosynthetic activities (Hermans *et al.* 2004; Tang *et al.* 2012; Yang *et al.* 2012; Urek *et al.* 2019). To determine Mg^{2+} requirements for *Synechocystis*' growth, wt cells were grown in the presence of replete and different low Mg^{2+} concentrations. To examine the changes generated by Mg^{2+} limitation, distinct cellular responses of *Synechocystis* cells were monitored under Mg^{2+} replete and low Mg^{2+} concentrations. Besides cell growth, the cell morphology was examined by electron microscopy. The amounts of pigments and their ratios were studied with spectroscopic methods. The activity of the photosynthetic machinery was studied using pulse amplitude-modulated fluorescence spectroscopy (PAM).

2. **The influence of various electron transport chain inhibitors on the pH gradient build-up in intact *Synechocystis* cells.**

   The fluorescent dye acridine orange has proven in the past to be useful in the analysis of pH gradient build-up in whole *Synechocystis* cells (Teuber *et al.* 2001; Berry *et al.* 2003; Checchetto *et al.* 2012; Miller *et al.* 2021). That dye allows observing both luminal and cytoplasmic pH changes during dark-light transitions (Teuber *et al.* 2001). *Synechocystis* cytoplasmic pH is influenced by proton translocation across both the PM and the TM. To better understand the AO signal transitions and the underlying processes involved in proton translocation during dark-light-dark transitions, site-specific inhibitors of the electron transport chain were applied during the measurements. This was a prerequisite to interpreting the observed differences between the wt and the generated knock-out mutants.

3. **Function and localisation of predicted Mg^{2+} channels in *Synechocystis*.**

   Two bacterial Mg^{2+} channel classes, the CorA and the MgtE channels, have been studied to some extent in bacteria. Homologs of these bacterial Mg^{2+} channels are also encoded in the *Synechocystis* genome (Kaneko *et al.* 1996). The respective *Synechocystis* single and double knock-out mutants were generated and analysed. Special attention was paid to cell morphology and physiology and photosynthetic performance under Mg^{2+} replete and low Mg^{2+} concentrations. Moreover, the localisation of the predicted Mg^{2+} channels was visualised using fluorescence microscopy on mutant strains carrying a YFP-tag fused to the N-terminus of the corresponding polypeptides.

4. ***In vitro* studies of the predicted Mg^{2+} channels.**

   The predicted structures of the *Synechocystis* Mg^{2+} channel homologs were compared with already resolved structures from other microorganisms, and their ability to interact with Mg^{2+} ions was analysed. For this purpose, the corresponding proteins were expressed heterologously (full-length protein/soluble domain) in *E. coli*. After successfully purifying a CorA homolog, the protein was reconstituted in proteoliposomes, and a fluorescence assay was developed to test Mg^{2+} transport abilities. In addition, the secondary structure of the soluble domain of the MgtE homolog with and without Mg^{2+} and possible conformational changes upon binding of Mg^{2+} were investigated using CD

spectroscopy and ANS-FTSA measurements.

3. Material and Methods

3.1. Materials

3.1.1. Instruments

Table 3.1: Used instruments in this study.

Instrument	Name	Manufacturer
Biological Safety Cabinets	Microflow (5/242/2)	MDH Ltd. (Hampshire, GB)
	Safe2020	Thermo Scienific (Langenselbold, GER)
CD spectrometer	Jasco J-1500	Jasco (Pfungstadt, GER)
	6-sample Peltier Turret Cell Changer (Model MPTC-490S/15)	
Centrifuges	5810 R	Eppendorf (Hamburg, GER)
	5415 R	Eppendorf (Hamburg, GER)
	5424	Eppendorf (Hamburg, GER)
	Allegra X-15R	Beckmann Coulter (Krefeld, GER)
	Avanti J-26XP	Beckmann Coulter (Krefeld, GER)
	Optima Max XP UC	Beckmann Coulter (Krefeld, GER)
	Optima L-100K	Beckmann Coulter (Krefeld, GER)
Centrifuge Rotors	A-4-81	Eppendorf (Hamburg, GER)
	F45-24-11	Eppendorf (Hamburg, GER)
	FA-45-24-11	Eppendorf (Hamburg, GER)
	SX4750	Beckmann Coulter (Krefeld, GER)
	JA-25.50	Beckmann Coulter (Krefeld, GER)
	JLA 8.1000	Beckmann Coulter (Krefeld, GER)
	JLA 16.250	Beckmann Coulter (Krefeld, GER)
	70 Ti	Beckmann Coulter (Krefeld, GER)
	90 Ti	Beckmann Coulter (Krefeld, GER)
	MLA-130	Beckmann Coulter (Krefeld, GER)
	TLA-100	Beckmann Coulter (Krefeld, GER)
Chemoluminescene detection system	Stella	Raytest (Straubenhardt, GER)
	Fusion FX	Vilber (Marne-la Vallée cedex 3, FRA)
Cold Light Source	KL 2500 LCD	Schott (Mainz, GER)
Cooling unit	AC-710 Cooling Unit	Photon Systems Instruments (Drásov, CZE)
	Alpha RA 8	Lauda (Lauda-Königshofen, GER)
	Julabo F10 with UC thermostat	Julabo (Seelbach, GER)
Counting chamber	Counting chambers, Thoma pattern	Brand (Wertheim, GER)
Electron microscope	JEM-1400Plus	JEOL (Tokyo, JAP)
	JEOL Ruby CCD-camera	
Electrophoresis chamber	Mini-Protean Tetra Cell	Bio-Rad (Hercules, USA)
	PerfectBlue Gelsystem S, M	PeqLab (Erlangen, GER)
Electrophoresis power supply	PowerPac Basic	Bio-Rad (Hercules, USA)
	PowerPac HC	Bio-Rad (Hercules, USA)
	PowerPac 300	Bio-Rad (Hercules, USA)

Table 3.1 Used instruments in this study.

Instrument	Name	Manufacturer
Fluorescence microscope	Axio Observer.Z1	Carl Zeiss Microscopy GmbH (Jena, GER)
	Axiocam 503 mono	
	Colibri 7	
	ApoTome.2	
Fluorescence spectrometer	FluoroMax-4	Horiba Scientific (Bensheim, GER)
	Aminco Bowman Series 2	Thermo Electron Corporation (Waltham, USA)
	FP-8500	Jasco (Pfungstadt, GER)
Gel documentation	Quantum-ST4 1100/26MX	PeqLab (Erlangen, GER)
Gel scanner	ViewPix700	Biostep (Burkhardtsdorf, GER)
Heating block	HBT -2 131	HLC-Biotech (Pforzheim, GER)
Heating plate/magnetic stirrer	MR Hei-Standard	Heidolph (Schwabach, GER)
Heating bath	Thermomix 1420	Braun (Melsungen, GER)
Horizontal shaker	Duomax 1030	Heidolph (Schwabach, GER)
Incubator *E. coli*	Binder Inkubator Serie BF	Binder (Tuttlingen, GER)
Incubator *Synechocystis*	Economic Delux, ECD01E	Snijders Scientific (Tilburg, NLD)
Incubator shaker	Multitron HT	Infors (Bottmingen, CHE)
Inverse laboratory microscope	Leica DM IL LED	Leica (Wetzlar, GER)
Microplate Spectrophotometer	BioTek PowerWave XS	BioTek (Winooski, USA)
Microscope camera	OXM901	Kern & Sohn (Balingen-Frommern, GER)
Microtome	Ultracut EM UCT ultramicrotome	Leica Microsystems (Wetzlar, GER)
	diamond knife Type Ultra 45°	Diatome (Biel, CHE)
Multi-Cultivator	Multi-Cultivator MC 1000-OD	Photon Systems Instruments (Drásov, CZE)
Overhead shaker	Rollenmischer CMV- ROM	Fröbel (Lindau, GER)
Oxygen sensor	fibre-optic oxygen meter	PreSens (Regensburg, GER)
PAM fluorimeter	Dual-PAM-100	Walz GmbH (Effeltrich, GER)
pH-meter	pH211 Microprocessor	Hanna Instruments (Vöhringen, GER)
Thermocycler	Thermocycler Primus 25	PeqLab (Erlangen, GER)
	TGradient 96	Biometra (Göttingen, GER)
Thermomixer	Thermomixer comfort	Eppendorf (Hamburg, GER)
Turbidostatic Module	Turbidostat TS-1000	Photon Systems Instruments (Drásov, CZE)
Ultrasonic cell homogeniser	Branson Sonifier 250	Branson, (Danbury, USA)
UV/Vis spectrometer	Lambda 35	PerkinElmer (Rodgau, GER)
	Lambda 465	PerkinElmer (Rodgau, GER)
	NanoDrop	Thermo Scientific (Darmstadt, GER)
Vacuum pump	High Vacuum Pump	Edwards (Crawley, GBR)
Visible spectrometer	Novaspec Plus	Amersham Biosciences (Little Chalfont, GBR)
Vortex mixer	Vortex Mixer	VWR (Radnor, USA)
Western Blot system	Trans-Blot Turbo Transfer System	Bio-Rad (Hercules, USA)

3.1.2. Consumables and Kits

Table 3.2: Consumables and Kits used during this study.

Consumables	Name	Manufacturer
Antibody	His-Tag Monoclonal Antibody	Novagen, (Darmstadt, GER)
Bio-BeadsTM SM-2	Bio-BeadsTM SM-2	Bio-Rad (Hercules, USA)
Blotting paper	Thick Blot Paper	Bio-Rad (Hercules, USA)
Chemiluminescent	ECL Prime	GE Healthcare (Munich, GER)
Western Blot Reagents	Western Blotting Detection Reagent	
Cuvettes	10 mm polystyrene cuvettes	Sarstedt (Nümbrecht, GER)
Dialysis membrane tubing	Spectra/Por^{TM} 6000-8000 Da MWCO	Roth (Karlsruhe, GER)
DNA Ladder	GeneRulerTM 1kb	Thermo Scientific (Darmstadt, GER)
DNA-Loading dye	TriTrack DNA-Loading dye (6x)	Thermo Scientific (Darmstadt, GER)
Fluorescence indicator	FluoZin™-3, Tetrapotassium Salt, cell impermeant	Thermo Fisher Scientific (Darmstadt, GER)
Immunoblotmembrane	Roti-PVDF	Roth (Karlsruhe, GER)
PD-10 column	PD-Minitrap G-25	Cytiva (Marlborough, USA)
Protein Ladder	PageRulerTM Prestained PageRulerTM Unstained	Thermo Scientific (Darmstadt, GER) Thermo Scientific (Darmstadt, GER)
Kits		
Agarose gel extraction	Gel/PCR DNA Fragments Kit NucleoSpin Gel and PCR Clean-up	Geneaid Biotech (Taipei, TWN) Macherey-Nagel GmbH & Co. KG (Düren, GER)
BCA assay	BCA Protein Assay Kit	Thermo Scientific (Darmstadt, GER)
Plasmid preparation	PrestoTM Mini Plasmid Kit NucleoSpin Plasmid Kit	Geneaid Biotech (Taipei, TWN) Machery Nagel (Düren, GER)

3.1.3. Software

Table 3.3: Software used during this study.

Application	Software
Protein structure	PyMOL 2.5.0 (Schrödinger, LLC 2021)
Data analysis	Origin 2019b Excel Microsoft 365 Fityk 1.3.1 (©2001–2016 Marcin Wojdyr)(Wojdyr 2010)
Figure editing	Adobe Photoshop 2020 ImageJ 1.53c PowerPoint Microsoft 365
Sequence analysis	BioEdit 7.2.5 SnapGene Viewer 6.1.2
Text editing	Word Microsoft 365 Kile 2.9.93
Reference management	Mendeley 1.19.8

All statistical analyses were performed using Origin 2019b.

3.1.4. Bacterial Strains

Table 3.4 lists the *E. coli* strains used for cloning and protein expression. The bacteria were grown in LB-Medium (Table 3.8).

Table 3.4: *E. coli* strains used during this study.

E. coli	**genotype**	**Reference**
cloning		
XL1-Blue	*recA1 endA1 gyrA96 thi-1 hsdR17 supE44 relA1 lac* [F' *proAB lacI*^{q}*ZΔM15*Tn*10*(Tet^{r})]	Agilent, Santa Clara, USA
expression		
BL21 (DE3)	F- *ompT hsd*S_B($r_B$$^-$$m_B$$^-$) *gal dcm* (DE3)	Novagen, Darmstadt, GER
HMS174 (DE3) pLysS	F- *recA1 hsdR*($r_{K12}$$^-$ $m_{K12}$$^+$) (DE3) pLysS ($Cam^R$, Rif^R)	Novagen, Darmstadt, GER
OverExpress™ 41(DE3)	F- *ompT hsd*S_B(r_B-m_B-) *gal dcm* (DE3)	Lucigen, Middleton, USA
OverExpress™ 43(DE3)	F- *ompT hsd*S_B(r_B-m_B-) *gal dcm* (DE3)	Lucigen, Middleton, USA
RosettaTM 2(DE3)	F- *ompT hsd*S_B(r_B-m_B-) *gal dcm* (DE3) pRARE2 (Cam^R)	Novagen, Darmstadt, GER
Tuner (DE3) pLysS	F- *ompT hsd*S_B(r_B-m_B-) *gal dcm lacY1* (DE3) pLysS (Cam^R)	Novagen, Darmstadt, GER

The cyanobacteria used in the described projects are listed in Table 3.5. *Synechocystis* cells were grown in modified BG11-Medium (modified from standard BG11 (Rippka *et al.* 1979)) (Table 3.10).

Table 3.5: *Synechocystis* strains used during this study.

Synechocystis	**genotype**	**Reference**
wt	*wt*	Pasteur Culture Collection of Cyanobacteria
Δslr1216	*Δslr1216*::Cm^R	this study
Δsll0507	*Δsll0507*:: Kan^R	this study
Δsll0671	*Δsll0671*::Sp^R	this study
Δslr1216Δsll0507	*Δslr1216Δsll0507*::Cm^R Kan^R	this study
Δsll0671Δslr1216	*Δsll0671Δslr1216*::Sp^R Cm^R	this study
Δsll0671Δsll0507	*Δsll0671Δsll0507*::Sp^R Kan^R	this study
Δsll1254	*Δsll1254*::Sp^R	this study
wt_yfp	*yfp*::Kan^R	this study
Δslr1216_yfp-slr1216	*Δslr1216_yfp-slr1216*::Cm^R Kan^R	this study
Δsll0507_yfp-sll0507	*Δsll0507_yfp-sll0507*::Kan^R Cm^R	this study
Δsll0671_yfp-sll0671	*Δsll0671_yfp-sll0671*::Sp^R Kan^R	this study
slr1216-mTurquoise2	*slr1216-mTurquoise2*::Kan^R	this study
sll0671-gfp	*sll0671-gfp*::Cm^R	this study
wt mario	*mario*::Kan^R	this study
Δslr1216 mario	*Δslr1216 mario*::Cm^R Kan^R	this study
Δsll0671 mario	*Δsll0671 mario*:: Sp^R Kan^R	this study

3.1.5. Plasmids

Table 3.6: Plasmids used in this study.

Plasmid	Resistance	Properties	Reference
pET30b-5M SrtA with TEV site	Kan^R	TEV-His6 (C-term.)	pET30b-5M SrtA with TEV site was a gift from Ron Bose (Addgene plasmid # 86962 http://n2t.net/addgene:86962 RRID:Addgene_86962) (Sarpong *et al.* 2017)
pET30b-sll0507 with TEV site	Kan^R	expression of sll0507-His	this study
pET30b-sll0671 with TEV site	Kan^R	expression of sll0671-His	this study
pET His6 StrepII TEV LIC cloning vector (2HR-T)	Amp^R	His6-StrepII-TEV (N-term.)	pET His6 StrepII TEV LIC cloning vector (2HR-T) was a gift from Scott Gradia (Addgene plasmid # 29718 http://n2t.net/addgene:29718 RRID:Addgene_29718)
pET His6 StrepII TEV slr1216 LIC cloning vector	Amp^R	expression of His-slr1216	this study
pET His6 StrepII TEV sll0671 LIC cloning vector	Amp^R	expression of His-sll0671	this study
pBluescript II KS+	Amp^R	Standard cloning vector	Stratagene (La Jolla, USA)
pACYC184	Cm^R	Cm^R	ATCC (Manassas, USA)
pBluescript II KS+Δslr1216	Amp^R Cm^R	upstreamslr1216-Cm^R -downstreamslr1216 KO construct	this study
pBSL15	Kan^R	Kan^R	ATCC (Manassas, USA)
pBluescript II KS+Δsll0507	Amp^R Kan^R	upstreamsll0507-Kan^R -downstreamsll0507 KO construct (Kan^R pBSL15; PstI excised)	this study
pSpec	Sp^R	Sp^R on an omega fragment	WG Schneider Ω-fragment from pHP45Ω Prentki and Krisch, 1984 (Prentki *et al.* 1984)
pBluescript II KS+Δsll0671	Amp^R Sp^R	upstreamsll0671-Sp^R -downstreamsll0671 KO construct	this study
pBluescript II KS+Δsll1254	Amp^R Sp^R	upstreamsll1254-Sp^R -downstreamsll1254 KO construct	this study
pAGH23	Amp^R Gm^R	curT-mTurquoise2 construct used to replace the native *curT* in *Synechocystis via* homologous recombination	pAGH23 was a gift from Erin O'Shea (Addgene plasmid # 107262 http://n2t.net/addgene:107262 RRID:Addgene_107262) (Gutu *et al.* 2018)
pBSL14	Kan^R	Kan^R	ATCC (Manassas, USA)

Table 3.6 Plasmids used during this study.

Plasmids	Resistance	Properties	Reference
pBluescript II KS+ slr1216-mTurquoise2	Amp^R Kan^R	upstreamslr1216-slr1216 -GS-mTurquoise2 (from pAHG23) -Kan^R (from pBSL14) -downstreamslr1216 construct to replace slr1216 in *Synechocystis via* homologous recombination	this study
pWaldo	Amp^R	GFP	Waldo *et al.*, 1999 (Waldo *et al.* 1999)
pBluescript II KS+ sll0671-gfp	Amp^R Cm^R	upstreamsll0671-sll0671 -GS-gfp (from pWaldo) -Cm^R (from pACYK184) -downstreamsll0671 construct to replace sll0671 in *Synechocystis* *via* homologous recombination	this study
pCK306	Kan^R	an *E. coli-Synechocystis* shuttle vector for chromosomal integration that allows regulated gene expression in cyanobacteria	pCK306 was a gift from John Heap (Addgene plasmid # 110544 http://n2t.net/addgene:110544 RRID:Addgene_110544) (C. L. Kelly *et al.* 2018)
pCK306_yfp-slr1216	Kan^R	rhamnose-inducible N-term. YFP-Slr1216	this study
pCK306_yfp-sll0507	Cm^R	rhamnose-inducible N-term. YFP-Sll0507	this study
pCK306_yfp-sll0671	Kan^R	rhamnose-inducible N-term. YFP-Sll0671	this study
pcDNA3/MARIO	Amp^R Neo^R/Kan^R	expression of MARIO, a genetically-encoded fluorescent Mg^{2+} sensor	MARIO/pcDNA3 was a gift from Takeharu Nagai (Addgene plasmid # 124838 http://n2t.net/addgene:124838 RRID:Addgene_124838) (Maeshima *et al.* 2018)
pCK306MARIO	Kan^R	rhamnose inducible MARIO	this study

3.1.6. Oligonucleotides

Oligonucleotides were purchased from Sigma Aldrich / Merck.

Table 3.7: Oligonucleotides used in this study.

Name	Sequence 5'-3'	DNA source
	Forward primer	
	Reverse primer	
Cloning of the channels for Expression in *E. coli*		
Gene and plasmid backbone amplification for Gibson Assembly		
fslr1216_2HRT	cgccgaaaacctgtacttccaatccatgacagaggtcactacgactgttc	*Synechocystis wt*
rslr1216_2HRT	ggatccgttatccacttccaatattttaaattcccaataaagagcgggca	
f2HRT_slr1216	tgcccgctctttattgggaatttaaaatattggaagtggataacggatcc	2HR-T
r2HRT_slr1216	gaacagtcgtagtgacctctgtcatggattggaagtacaggttttcggcg	
fmgtE1_271pET30b	gaaataattttgtttaactttaagaaggagatatacatatgacagaggtcactacgactgttcgact	*Synechocystis wt*
rmgtE1_271pBlue	gtggtggtgaccttgaaaatagagattctcttccgtggcttcttcctccaaaatgtcgat	
fpET30bmgtE1_271	atcgacattttggaggaagaagccacggaagagaatctctattttcaaggtcaccaccac	pET30b
rpET30bmgtE1_271	agtcgaacagtcgtagtgacctctgtcatatgtatatctccttcttaaagttaaacaaaattatttc	
fsll0507pET30b	aatctttgtagctacagaagtcaaactcgagatgccccaaacccaacccggcattgagga	*Synechocystis wt*
rsll0507pET30b	ggtggtgaccttgaaaatagagattctccttttctcccaaatcataggagggacta	
fpET30bsll0507	tagtccctcctatgatttgggagaaaaggagaatctctattttcaaggtcaccacc	pET30b
rpET30bsll0507	tcctcaatgccgggttgggtttggggcatctcgagtttgacttctgtagctacaaagatt	
fsll0671pET30b	actttaagaaggagatatacatatgcccaacaagcctcagtttc	*Synechocystis wt*
rsll0671pET30b	accttgaaaatagagattctctctatttccttttcaacatc	
fpET30bsll0671	gatgttgaaaaaggaaatagagagaatctctattttcaaggt	pET30b
rpET30bsll0671	gaaactgaggcttgttgggcatatgtatatctccttcttaaagt	
fsll0671_2HR-T	cgccgaaaacctgtacttccaatccatgcccaacaagcctcagtttcgac	*Synechocystis wt*
rsll0671_2HR-T	ggatccgttatccacttccaatattttatctatttccttttcaacatca	
f2HR-T_sll0671	tgatgttgaaaaaggaaatagataaaatattggaagtggataacggatcc	2HR-T
r2HR-T_sll0671	gtcgaaactgaggcttgttgggcatggattggaagtacaggttttcggcg	
Cloning of the KO constructs for *Synechocystis* and XFP-tagged protein versions for expression in *Synechocystis*.		
Amplification of upstream and downstream regions for restriction ligation		
fHindIIIslr1216up	tatc aagctt caaggctcagaatgtatgag	*Synechocystis wt*
rPstIslr1216up	tatg ctgcag cgaaacgacacccccaatat	
fPstIslr1216down	tatg ctgcag tggcggcttttgctgga	
rBamHIslr1216down	tagt ggatcc agtaggaaaatagtaaaaggcttt	
fEcoRVsll0507up	tatc gatatc gctacttttctcccaaatc	*Synechocystis wt*
rPstIsll0507up	tatg ctgcag atgaaatttttgaccgtcat	
fPstIsll0507down	tatg ctgcag cttcttcttcctcttcttcttg	
rSacIsll0507down	tagc gagctc cccagaaattaaatttgactgg	
fEcoRVsll0671up	tatc gatatc agcttaaattactgacgttaga	*Synechocystis wt*
rPstIsll0671up	tatg ctgcag actgagcaacgaggcga	
fPstIsll0671down	tatg ctgcag gcattgggggaaagatttaa	
rBamHIsll0671down	tagt ggatcc aatttattgtgtaatctggcat	
Amplification of antibiotics resistance cassette for restriction ligation		
fPstICmR	tatg ctgcag ttacgccccgccctgcc	pACYC184
rPstICmR_pr	tatg ctgcag tgatcggcacgtaagag	
Kan^R was gained by digestion of pBSL15 with PstI by [redacted]		pBSL15

Table 3.7 Oligonucleotides used in this study.

Name	Sequence 5'-3'	DNA source
frPstISmR_2	tatg ctgcag tgattgattgagcaagctttatg	pSpec
Amplification of upstream and downstream regions for Gibson Assembly combined with restriction ligation		
fsll1254upPstsll1254down	cggttgcggagatcaagaaattctgcaggcataaaattccgaaaccaact	*Synechocystis wt*
rsll1254uppBlue	ccctcactaaagggaacaaaagctgacgtcccactgcatcagcaacaggc	
fsll1254downpBlue	atacgactcactatagggcgaattgtcatctttaggaaaattagatagat	*Synechocystis wt*
rsll1254downPstsll1254up	agttggtttcggaattttatgcctgcagaatttcttgatctccgcaaccg	
Amplification of plasmid backbone for Gibson Assembly combined with restriction ligation		
fpBluesll1254up	gcctgttgctgatgcagtgggacgtcagcttttgttccctttagtgaggg	pBluescript II KS+
rpBluesll1254down	atctatctaattttcctaaagatgacaattcgccctatagtgagtcgtat	
Primer used for the amplification of the antibiotic resistance cassette for restriction ligation was frPstISmR_2		
Genes, Ant. resistance cassettes and plasmid backbones for amplification for XFP tagged protein versions using Gibson assembly		
fmgtE	ctagtggatcccccgggctgcaggaaaatgtatgaggggctagggaaat	*Synechocystis wt*
rmgtE	aaccataccactgccgcttccaattcccaataaagagcgggc	
fGS_mtur	gcccgctctttattgggaattggaagcggcagtggtatggtt	pAGH23
rGS_mtur	tagcggaattcgagctcggtacccggggactacttatacaattcatccatcccgag	
fKan	ctcgggatggatgaattgtataagtagtccccgggtaccgagctcgaattccgcta	pBSL14
rKan	gtcccaggttgtggagccaaagcccccatccccgggtaccgagctcgaattccgcgaa	
fmgtE_down	ttcgcggaattcgagctcggtacccggggatgggggctttggctccacaacctgggac	*Synechocystis wt*
rmgtE_down	atcgataagcttgatatcgaagcccacggcattttggaaatt	
fpBlue	aatttccaaaatgccgtgggcttcgatatcaagcttatcgat	pBluescript II KS+
rpBlue	atttccctagccccctcatacattttcctgcagcccgggggatccactag	
fsll0671_pBLue	ggatcccccgggctgcaggaattttatttggtcaaatttatc	*Synechocystis wt*
rsll0671_GFP	gaaaagttcttctcctttgctaccactgccgcttcctctatttccttttttcaacatca	
fGFP_sll0671	tgatgttgaaaaaggaaatagaggaagcggcagtggtagcaaaggagaagaactttttc	pWaldo
rGFP_CmR	gaacctcttacgtgccgatcactatttgtagagctcatccat	
fCmR_GFP	atggatgagctctacaaatagtgatcggcacgtaagaggttc	pACYC184
rCmR_ sll0671down	ttagcggacaagaaaaataatttacgccccgccctgccactc	
fsll0671down_CmR	gagtggcagggcggggcgtaaattatttttcttgtccgctaa	*Synechocystis wt*
rsll0671down_pBlue	atcgataagcttgatatcgaatttttatttattaattcattg	
fpBlue_sll0671down	caatgaattaataaataaaaattcgatatcaagcttatcgat	pBluescript II KS+
rpBlue_sll0671	gataaatttgaccaaataaaattcctgcagcccgggggatcc	
fslr1216pCK306YFP	tctcggcatggacgagctgtacaagggaagcggcagtggtatgacagaggtcactacgactgttc	*Synechocystis wt*
rslr1216pCK306YFP	tgagacacaacgtggctttggatccttaaattcccaataaagagcgggca	
fpCK306YFPslr1216	tgcccgctctttattgggaatttaaggatccaaagccacgttgtgtctca	pCK306
rpCK306YFPslr1216	gaacagtcgtagtgacctctgtcataccactgccgcttcccttgtacagctcgtccatgccgaga	
fsll0507pCK306YFP	tctcggcatggacgagctgtacaagggaagcggcagtggtatgccccaaacccaacccggcattg	*Synechocystis wt*
rsll0507CmR	ttggaacctcttacgtgccgatcattacttttctcccaaatcataggagg	
fCmRsll0507	cctcctatgatttgggagaaaagtaatgatcggcacgtaagaggttccaa	pACYC184
rCmRpCK306YFP	tcgtcaacacggcgaaatattacgccccgccctgccactc	
fpCK306YFPCmR	cgatgagtggcagggcggggcgtaatatttcgccgtgttgacgacatcag	pCK306
rpCK306YFPsll0507	caatgccgggttgggtttggggcataccactgccgcttcccttgtacagctcgtccatgccgaga	
fsll0671_pCK306	gcatggacgagctgtacaagggaagcggcagtggtatgcccaacaagcctcag	*Synechocystis wt*
rsll0671_pCK306	acaacgtggctttggatccttatctatttccttttttcaacatcattaagatttct	
fpCK306_sll0671	agaaatcttaatgatgttgaaaaaggaaatagataaggatccaaagccacgttgt	pCK306
rpCK306_sll0671	ctgaggcttgttgggcataccactgccgcttcccttgtacagctcgtccatgc	

Table 3.7 Oligonucleotides used in this study.

Name	Sequence 5'-3'	DNA source
fpCK306_EcoRI	tccgaattcaaagccacgttgtgtct	pCK306
rpCK306_BamHI	tcggatccttctacctcctttgtatattataaact	
Sequencing primers to confer insertion into *Synechocytis*		
Knock out strains		
seq0671	gttcaccatagacttccatc	
seq0507	gattggtgcgaattctttc	
seq1216	gacaaattatggtgcctg	
pCK306 insertion site		
f-hom-left-pCK306	ggcaggtattctggcta	
r-hom-right-pCK306	gcaccaaggtggtaatt	

The primers marked in red (Table 3.7) were those that resulted in an in-frame cloning of *sll0507* with the *srtA* gene encoded by the pET30b vector, which later had to be excised.

3.1.7. Chemicals

Chemicals used in this study were purchased from Merck (Darmstadt, GER), Roth (Karlsruhe, GER), Serva (Heidelberg, GER), Sigma Aldrich (Munich, GER), AppliChem (Darmstadt, GER), VWR (Darmstadt, GER), Fluka (Buchs, CHE) and Fisher Scientific (Hampton, USA). Lipids were purchased from Avanti Polar Lipids (Alabaster, USA). Enzymes were purchased from New England Bio Labs (Frankfurt, GER). Buffers and solutions were prepared using deionised water and filtered if necessary. The buffers used for cyanobacterial growth were prepared using ultrapure water.

3.1.8. Growth media

E. coli cells were grown in liquid Lysogeny broth (LB) medium (Table 3.8) at 37°C in a shaking incubator or on LB agar plates in an incubator.

Table 3.8: Composition of LB medium.

LB medium pH 7.0 ±0.2	
Substance	**Amount [g/L]**
Tryptone	10
Yeast extract	5
NaCl	10

Table 3.9: Additives for *E. coli* grown in liquid LB medium or on agar plates.

Additive	**Stock**	**Final concentration**	**Solvent**
Ampicillin	100 mg/ml	100 µg/mL	50% EtOH / 50% ultrapure H_2O
Chloramphenicol	30 mg/mL	30 µg/mL	100% EtOH
Kanamycin	30 mg/mL	30 µg/mL	ultrapure H_2O
Isopropyl β-D-1-thiogalactopyranoside (IPTG)	1 M	0.1-1 mM	ultrapure H_2O
Agar	Powder	1.5 g/L	LB medium

Liquid LB medium was supplemented with the required antibiotics (Table 3.9). For LB agar plates, agar powder was added before autoclaving. The required antibiotics were added after autoclaving just prior pouring the plates. Liquid LB medium for protein expression was prepared by diluting a ten-fold concentrated and autoclaved stock with deionised water, the required antibiotics were added and IPTG (sterile filtered) was added to induce protein expression.
Synechocystis strains were grown in a modified liquid blue green medium (BG11) (Table 3.10) supplemented with 5 mM HEPES/KOH pH 8 (from now on BG11) or on BG11 agar plates. BG11 agar plates were supplemented with 5 mM glucose, and 50 µg/mL of the appropriate antibiotics and cells were grown in an incubator with the temperature set to 30°C under 30 µmol photons * m^{-2} * s^{-1} cold white light. To confirm gene knock out, *Synechocystis* strains were grown in liquid BG11 in Erlenmeyer flasks under photomixotrophic conditions (5 mM glucose) without antibiotics for two weeks. Cultures were grown in a shaking incubator at 130 rpm with the illumination adjusted to 120 µmol photons * m^{-2} * s^{-1} of cold white light.

Table 3.10: Composition of BG11 medium.

standard BG-FPC (100x)			**BG-FPC (100x) without $MgSO_4$**		
Substance	**g**	**mmol/L**		**g**	**mmol/L**
$NaNO_3$	149.58	1.76			
Citric acid	0.66	3.44			
$CaCl_2x2H_2O$	3.6	24.49			
$MgSO_4$	7.49	30.39	Na_2SO_4 instead of $MgSO_4$	4.32	30.41
NaEDTA pH 8	1.12 mL (250 mM)	0.28			
Add 1 L of ultrapure H_2O and filter sterile					
Trace minerals					
H_3BO_3	1.43	46.26			
$MnCl_2x4H_2O$	0.905	9.15			
$Na_2MoO_4x2H_2O$	0.111	0.92			
$Co(NO_3)2x6H_2O$	0.195	1.34			
$CuSO_4x5H_2O$	0.04	0.32			
Add 0.5 L of ultrapure H_2O and filter sterile					

preparation of 1 L BG11	
Substance	**mL**
Autoclaved ultrapure H_2O	981
BG-FPC (100x)	10
1M HEPES-KOH pH 8.2	5
Trace minerals	1
6 mg/ml Ammonium ferric citrate in ultrapure H_2O	1
190 mM Na_2CO_3 in ultrapure H_2O	1
175 mM K_2HPO_4 in ultrapure H_2O	1

Table 3.11: Additives for *Synechocystis* growth in BG11 medium or on agar plates.

Substance	**Stock**	**Final concentration**	**Solvent**
Chloramphenicol	50 mg/mL	10-200 µg/mL	100 % EtOH
Kanamycin	50 mg/ml	10-200 µg/mL	H_2O
Spectinomycin	50 mg/mL	10-200 µg/mL	H_2O
Glucose	1 M	5 mM	H_2O
Rhamnose	100 mg/mL	1 mg/mL	H_2O
Difco Bacto Agar	powder	1.5 g/L	BG11 medium
Sodium thiosulfate	powder	3 g/L	BG11 medium
$MgCl_2$	1 mM	10 – 300 µM	BG11 medium
$CoCl_2$	powder	12-13 µM	BG11 medium

BG11 medium was prepared from autoclaved ultrapure water by adding the sterile filtered components listed in Table 3.11. Sterile glucose was added to a final concentration of 5 mM when needed. The BG11 agar plates contained 1.5% Difco Bacto Agar, and 3 g/L $Na_2S_2O_2$, and 5 mM glucose. $Na_2S_2O_2$ is known to be a reactive oxygen species (ROS) scavenger (Stewart *et al.* 1999; Z. Wang *et al.* 2002). The required antibiotics were added. When defined Mg^{2+} concentrations were required, the BG11 medium was prepared without $MgSO_4$, and the amount of sterile $MgCl_2$ was added.

3.2. Methods

3.2.1. Molecular biology

3.2.1.1. Preparation of genomic DNA (gDNA) from *Synechocystis*

Synechocystis was grown in liquid BG11 to an OD_{750} between 1-2. 30 mL of the culture were centrifuged (10-15 min; RT; ∼5000 g). The supernatant was discarded, and the cyanobacterial pellet was washed 3-4 times with 30 mL TES buffer (Table 3.12).

Table 3.12: Composition of TES buffer.

TES buffer pH 8.5	
Substance	**Amount [mM]**
Tris(hydroxymethyl)aminomethane (Tris)	5
EDTA	5
NaCl	50

After resuspension of the cyanobacterial pellet in 2 mL TES buffer, the solution was centrifuged (16000 g; 4°C; 1 min) and resuspended in 495 µL TES buffer. 5 µL of lysozyme [200 mg/mL] was added, followed by incubation at 37°C for 30 min. The following steps were performed in a fume hood. Here, 50 µL of 10% sodium lauryl sarcosinate and 600 µL of ROTI®Phenol (lower phase) were added and the sample was incubated for 15 min at room temperature (RT) with gentle shaking. The sample was centrifuged (16000 g; 4°C; 10 min), and the upper phase was transferred to a new 1.5 mL reaction tube with a cut pipette tip. 5 µL RNase (10 mg/mL) was added and incubated for 15 min at 37°C. Then 100 µL of a NaCl solution (5 mol/L), 80 µL 10% CTAB in 0.7 mol/L NaCl and 600 µL chloroform/isoamyl alcohol (24:1) were added and the sample was incubated for 15 min at RT with gentle shaking. The sample was centrifuged (16000 g; 4°C; 5 min), and the upper phase was transferred to a new 1.5 mL reaction tube with a cut pipette tip. 600 µL of isopropanol was mixed with the sample (no vortexing) and the sample was immediately centrifuged (16000 g; 4°C; 10 min) to precipitate the DNA. The supernatant was discarded and the pellet was washed with 70% EtOH and centrifuged (16000 g; 4°C; 5 min). The supernatant was discarded, and the pellet was air-dried overnight. The DNA pellet was dissolved in TE buffer (Table 3.13), and the DNA concentration was measured with a NanoDrop.

Table 3.13: Composition of TE buffer.

TE buffer pH 7.5	
Substance	**Amount [mM]**
Tris	10
EDTA	0.1

When DNA was needed for a rapid check of the segregation process, 1-2 mL *Synechocystis* culture was heated to 95°C for 5 min and centrifuged for 2 min at 2000 g at RT. 28 µL of the supernatant was used for the PCR (Table 3.14).

3.2.1.2. Preparation of plasmid DNA from *E. coli*

According to the manufacturer's instructions, the plasmid DNA was extracted using a miniprep kit (Table 3.2). The DNA concentration was measured with a NanoDrop. The DNA was frozen at -20°C until use.

3.2.1.3. PCR

The polymerase chain reaction (PCR) was used to amplify DNA from *Synechocystis* or plasmid DNA isolated from *E. coli* (Table 3.14).

Table 3.14: Components of a PCR reaction.

Substance	**Volume [µL]**
DMSO 100 %	1.5
dNTP's 2 or 10 mM	5 or 1
Phusion GC Buffer 5x	10
Phusion DNA Polymerase 1 unit 50 µL	0.5
fPrimer 10 µM	2.5
rPrimer 10 µM	2.5
DNA template	Variable volumes gDNA *Synechocystis* ∼200 ng Plasmid 2 – 100 ng
Autoclaved ultrapure H_2O	fill up to 50 µL

The annealing temperature was set according to the melting temperature of the DNA calculated using the SnapGene viewer (SnapGene 2022). Finally, the elongation time was calculated by estimating a reaction time of 30 s per kb.

Table 3.15: Protocol of a PCR reaction.

Temperature [°C]	**Time [sec]**	
110 (Lid)	∞	
98	120	
98	30	
52-70	30 - 240	25 - 30x
72	30 - 60	
72	600	
4-8	∞	

The PCR products were digested with DpnI at 37°C for one hour or at 4°C overnight.

3.2.1.4. PCR purification

PCR products were purified using a kit (Table 3.2) following the manufacturer's instructions. The DNA concentration was measured with a NanoDrop. The DNA was frozen at -20°C until use.

3.2.1.5. Agarose gel electrophoresis

Agarose gel electrophoresis was used for the analytical and preparative separation of DNA. Therefore, 1% (w/v) agarose was dissolved in TAE buffer (Table 3.16) using a microwave, and the agarose solution was poured into a gel tray with the well comb in place. When the gel was cooled down and cured, the DNA samples were mixed with Loading Dye (6x) and filled into the wells. The DNA was separated at a constant voltage (140 V) for 40 min. Next, the DNA was stained with 1 µg/mL ethidium bromide in water for 15-30 min, visualised under UV light and photographed. For preparative gel electrophoresis, the gel portion containing the DNA fragment was excised from the gel on a UV table, and the DNA was extracted using a gel/PCR DNA fragment kit (Table 3.2).

Table 3.16: Composition of TAE buffer.

TAE buffer pH 8.5	
Substance	**Amount [mM]**
Tris	40
acetic acid	20
EDTA	1

3.2.1.6. Restriction digestion of plasmids and amplified gene products

PCR products and plasmid backbones were restriction digested with an appropriate enzyme (indicated by the primers' names (Table 3.7)) before ligation, and obtained plasmids were restriction digested to check for their correct length after ligation (Table 3.17). The DNA coding for the genetically encoded Mg^{2+} sensor MARIO was cut out of the pcDNA3/MARIO (Maeshima *et al.* 2018) plasmid.

Table 3.17: Protocol for DNA restriction digestion.

Substance	**Amount**
	40-50 µL
PCR-product/Plasmid	1 µg DNA (preparative)
	500 ng DNA (analytical)
For restriction enzyme/s, see primers	1/20 of the reaction volume
NEB Buffer 10x (manufacturer's instructions)	1/10 of the reaction volume

The protocol used for DNA restriction digestion is listed in Table 3.17, and the sample was incubated at 37°C for 30 min to 2 hours.

3.2.1.7. Ligation of DNA fragments

Restriction and ligation was used for the construction of the *ΔmgtE* (frame *slr1216*), *ΔcorA1* (frame *sll0507*), *ΔcorA2* (frame *sll0671*) KO constructs, the insertion of the antibiotic cassette into the *Δsll1254* KO construct and the insertion of the DNA coding for the genetically encoded Mg^{2+} sensor MARIO into the pCK306 plasmid under the control of a rhamnose inducible promoter. The antibiotic cassettes used to replace the genes were those which give resistance to chloramphenicol (Cm) (*ΔmgtE*), kanamycin (Kan) (*ΔcorA1*) and spectinomycin (Sp) (*ΔcorA2*, *Δsll1254*). The DNA region upstream and downstream of the encoding genes was amplified by PCR (for primers see Table 3.7), cloned *via* Gibson assembly into pBluescript II KS+ (*Δsll1254*), or digested with the appropriate restriction enzyme, and ligated with pBluescript II KS + (*ΔmgtE*, *ΔcorA1*, *ΔcorA2*). Afterwards, the digested PCR products containing the antibiotic cassettes were ligated to restriction digested pBluescript II KS + containing the upstream and downstream fragments. Generated gene products were sequenced and used for transformation. For the generation of double mutants, the genes were knocked out individually in the order of the strains' names. The DNA coding for the Mg^{2+} sensitive Förster resonance energy transfer (FRET) sensor MARIO was excised from the pcDNA/MARIO (Maeshima *et al.* 2018) plasmid (Table 3.6) and ligated into restriction digested pCK306 (C. L. Kelly *et al.* 2018).

Table 3.18: Protocol for DNA ligation.

Substance	Amount
Plasmid	x µL (100 ng)
Insert	y µL (plasmid:insert Ratio 4:1)
T4-Ligase (5 Weiss Units)	0.4 µL
T4-Ligase Buffer	1.6 µL
Autoclaved ultrapure H_2O	fill up to 16 µL

Reactions were incubated overnight at 4-16°C.

3.2.1.8. DNA Gibson assembly

Gibson assembly (D. G. Gibson *et al.* 2009) was used to construct the plasmids harbouring the predicted Mg^{2+} channels/domains for expression in *E. coli*, the XFP-tagged predicted Mg^{2+} channels in *Synechocystis*, and the *sll1254* KO construct. For this purpose, the DNA was mixed in a molar ratio of 3/4:1 (insert:backbone) with

a final volume of 15 µL. Next, an equal amount of Gibson Assembly Mastermix (modified from (Samuel Miller Lab 2011)) (Table 3.19) was added, and the sample was incubated at 50°C for 1-1.5 hours in a thermomixer. Next, the obtained products were chilled on ice for 2 min. Finally, the entire assembled product was added to chemically competent XL1-blue cells and transformed according to the protocol (see section 3.2.1.10).

Table 3.19: Gibson Assembly Mastermix.

Substance	**Volume [µL]**		
		Substance	**Amount**
		PEG-8000	25%
		Tris-HCl pH 7.5	500 mM
		$MgCl_2$	50 mM
5x Isothermal reaction buffer	320	DTT	50 mM
		each of the 4 dNTPs	1 mM
		NAD	5 mM
T5 exonuclease (10 U/µL)	0.64		
Phusion DNA polymerase (2 U/µL)	20		
Taq ligase (40 U/µL)	0.16		
fill up with H2O to 1.2 mL			

3.2.1.9. Sequencing of constructs

Correct cloning was confirmed by restriction digestion of the penerated plasmids and DNA sequencing (Eurofins Genomics, Ebersberg, GER).

3.2.1.10. Transformation of chemically competent *E. coli*

Chemically competent *E. coli* cells were produced using the method described in Chung *et al.* (Chung *et al.* 1989). Therefore, 50 mL of LB medium was inoculated with an overnight culture of *E. coli*, resulting in an OD_{600} of ∼0.2. Cells were grown until they reached an OD_{600} of ∼0.8. Then they were centrifuged (5000 g; 4°C; 10 min), the pellet was resuspended in ice-cold transformation and storage solution (TSS), and 150 µL aliquots were frozen in liquid N_2 and stored at -80°C until further use.

Table 3.20: Composition of TSS.

Substance	**Amount [%]**
PEG 4000	10 (w/v)
DMSO	5 (v/v)
1 M $MgCl_2$	2 (v/v)
Tryptone	1 (w/v)
Yeast extract	0.5 (w/v)
NaCl	0.5 (w/v)

For transformation, chemically competent cells (100-200 µL) were removed from the

-80°C freezer and thawed on ice for 30 min. Next, DNA (all assembled product) was added to the cells, and the cells were incubated for 15-30 min on ice. Afterwards, the cells were either kept in a water bath or a thermomixer at 42°C for 45-60 s. The cells were then cooled on ice for a further 2 min. Next, 300-900 µL of LB medium was added, and the transformed cells were incubated in a thermomixer at 37°C and 300 rpm for 1-1.5 hours. Afterwards, cells were sedimented (2000 g; 4°C; 2 min) and resuspended in ∼100 µL LB medium. Finally, cells were plated on LB agar plates containing the required antibiotics and incubated overnight at 37°C, and those containing the plasmid were selected.

3.2.1.11. Plasmid transformation into *Synechocystis* and segregation of mutant cells

Synechocystis is naturally competent (Barten *et al.* 1995) and can efficiently take up DNA without additional treatment. For transformation, wt or mt cells were grown photomixotrophically in a shaker until they reached an OD_{750} ∼1. Next, 30-50 mL cells were centrifuged (3000 g; 15 min; RT) and resuspended to an OD_{750} of 2.5 in fresh BG11 medium containing 5 mM glucose. Thereafter, 400 µL of the cells were transferred to a sterile glass culture tube, and 1-5 µL of plasmid DNA was added. The cyanobacterial cells were left in an incubator overnight at 30°C and 30 µmol photons * m^{-2} * s^{-1}. The next day, the sample was plated onto BG11 agar plates containing 5 mM glucose and initially 10 µg/mL of the appropriate antibiotics. After ∼10 days, small *Synechocystis* colonies were visible on the plates, 3-4 colonies were selected and transferred to BG11 agar plates with antibiotic concentrations of 30 µg/mL. Subsequently, the colonies were transferred weekly to agar plates with increased antibiotic concentrations of up to 200 µg/mL. Then the colonies were transferred to BG11 liquid medium containing 5 mM glucose and the penultimate concentration of antibiotics. The DNA was extracted for a rapid ckeck (see section 3.2.1.1). When PCR confirmed the insertion of the DNA, the cells were grown for at least two weeks without antibiotics. The gDNA was prepared (see section 3.2.1.1) and used for PCR to verify complete segregation without antibiotic pressure. Strains showing complete KO were maintained on 50 µg/mL antibiotics when grown on BG11 agar plates. The KOs were confirmed by PCR (Tables 3.14, 3.15) using the outer primer of the construct and a primer that binds within the initial gene in combination with an outer primer.

3.2.2. Biochemical methods

3.2.2.1. Heterologous protein expression

An *E. coli* overnight culture was used to inoculate fresh LB medium for protein overexpression. *E. coli* were grown with one drop of sigma antifoam 204 at 37 °C and 80 rpm in 100/200/1000 mL LB (1/5/5 L Erlenmeyer baffled flasks) until they reached an optical density of OD_{600} ∼0.6. Protein expression was induced with addition of IPTG at the indicated growth conditions (Table 3.21).

Table 3.21: Conditions of protein expression.

Expression	IPTG [mM]	temp [°C]	time after IPTG addition
CorA1	1	30/32/37	4h/5h/overnight
CorA2	0.1	37	4 h
MgtE	1	37	5 h
cytMgtE	1	37	4 h or overnight

3.2.2.2. Protein purification

The bacterial cultures were centrifuged (5000 g; RT; 10 min), and the pellets were resuspended in 40/200 mL buffer (Table 3.23) followed by 2-3 times 6 min of sonication on ice (output control 4-5 duty cycle 40-50%). Next, the disrupted bacterial cells were centrifuged (10000 g; RT; 10 min). For isolation of membranes, the supernatant was centrifuged (117000 g; 4°C; 1 h) to precipitate the membrane fraction. Several detergents were tested for their respective ability to solubilise a given membrane protein (Table 3.20).

Table 3.22: Detergents tested for membrane solubilisation.

Detergent	% (w:v)	temp [°C]
Sodium dodecyl sulphate (SDS) (control)	3	RT
Triton X-100	1	4
3-[(3-cholamidopropyl)dimethylammonio]-1-propanesulfonate(Chaps)	2	4
N-dodecyl-β-D-maltopyranoside (DDM)	1	4
Lauryldimethylamine oxide (LDAO)	1	4
N-octyl-β-D-glucoside (OG)	3	4

Next, the obtained membrane pellets were solubilised in a solubilisation buffer (Table 3.23) overnight at 4°C. The solubilised membranes were centrifuged for one hour at 117000 g (protein purification) or 99100 g (detergent test). The supernatant of the solubilised membrane fraction, or in case of the cytoplamic domain of MgtE (cytMgtE), the disrupted cells, were loaded twice in a row onto a nickel nitriloacetic acid (Ni-NTA) column (250 µL/2 mL/2.5 mL) and washed with 10 column volumes (CV) of washing buffer with increasing imidazole concentrations (Table 3.23). Finally, proteins were eluted with a buffer containing 300 mM imidazole (Table 3.23).

Table 3.23: Buffers for protein purification.

	HEPES/KOH pH 7.6 [mM]	NaCl [mM]	detergent [%]	glycerol [%]	imidazole [mM]	sigma-protease inhibitor (P8849) [%] (v/v)
CorA1						
Lysis buffer	20	150	-	10	-	0.1
Solubilisation buffer	20	150	1 DDM or 4 Chaps	10	-	0.1
CorA2						
Lysis buffer	50	300	-	10	-	0.1
Solubilisation buffer	50	300	3 LDAO	10	-	0.1
Washing buffer	50	300	0.3 LDAO	10	20, 40, 70	-
Elution buffer	50	300	0.3 LDAO	10	-	-
Storage buffer	50	300	0.5 Triton-X 100	10	-	-
MgtE						
Lysis buffer	50	300	-	10	-	0.1
Solubilisation buffer	50	300	1 DDM	10	-	0.1
Washing buffer	50	300	0.1 DDM	10	20, 40, 60	-
Elution buffer	50	300	0.1 DDM	10	300	-
Storage buffer	50	300	0.1 DDM	10	-	-
cytMgtE						
Lysis buffer	20	150	-	10	-	0.1
Washing buffer	20	150	-	10	20, 30, 40, 60, and 1 CV 80	-
Elution buffer	20	150	-	10	300	-
Storage buffer	20	150	-	10	-	-

3.2.2.3. Determining the protein concentration

The protein concentration was determined using the BCA assay following the manufacturer's instructions (Table 3.2).

3.2.2.4. Desalting of protein by dialysis or using a PD10 desalting column

After protein elution, the buffer was exchanged for storage buffer (Table 3.23) by dialysis in a 250/500 mL beaker against 1/2 L with constant stirring in the cold room at 4°C. The dialyse buffer was changed hourly (3 times), followed by one dialysis step overnight. The next day, the dialyse buffer was changed and the sample was dialysed for another hour. Alternatively, the buffer was exchanged using a PD10 column according to the manufacturer's instructions (Table 3.2).

3.2.2.5. SDS-PAGE

To follow purification of a protein and determine the purity of the protein samples, these were separated according to their molecular mass on sodium dodecyl sulphate-polyacrylamide gel electrophoresis (SDS-PAGE) (Laemmli 1970). The exact compositions of the SDS gels are shown in Table 3.24.

Table 3.24: Buffers and substances for SDS-PAGE.

Substance	Separation gel		Stacking gel
	8%	12%	6%
H_2O	5.5 mL	4.5 mL	3 mL
acrylamide	2 mL	2 mL	0.75 mL
Separating buffer (1.5 M Tris, 0.4 % (w/v) SDS, pH 8.8)	2.5 mL	3.5 mL	
Stacking buffer (0.5 M Tris, 0.4 % (w/v) SDS, pH 6.8)			1.25 mL
10 % (w/v) Ammonium persulfate (APS)	50 µL	50 µL	25 µL
Tetramethylethylenediamine (TEMED)	20 µL	20 µL	10 µL
SDS running buffer			
Tris	25 mM		
glycine	192 mM		
SDS (w/v)	0.10%		
5x SDS sample buffer			
Tris	250 mM		
bromophenol blue (w/v)	0.20%		
glycerol (w/v)	50%		
SDS (w/v)	10%		
Dithiothreitol (DTT)	500 mM		

20 µL of the sample were mixed with 5 µL of a 5x SDS sample buffer (Table 3.24) and heated to 95 °C for 5 min. For the semi-native PAGE used to monitor the oligomeric states of the liposome-integrated protein, 5x sample buffer without SDS and DTT was used, and the samples were not heated. Electrophoresis was performed for 40 min at 230 V in SDS running buffer (Table 3.24). For subsequent staining, the gel was incubated in Coomassie Brilliant Blue (CBB) staining solution (Table 3.25) on a horizontal shaker for 60 min and then destained in destaining solution (Table 3.25) with changing the solution several times.

Table 3.25: Solutions for protein staining and destaining.

Staining solution	
Coomassie Brilliant Blue G-250 (w/v)	0.125%
EtOH (v/v)	40%
Phosphoric acid (v/v)	2%
Destaining solution	
EtOH (v/v)	30%
Phosphoric acid (v/v)	2%

3.2.2.6. Western blotting

Western blots (WBs) were used to identify the overexpressed protein by the fused His-Tag after transfer of the proteins from an SDS-PAGE gel to a nitrocellulose membrane. The membrane was activated in 100% methanol and equilibrated in a transfer buffer (Table 3.26). The filter paper was equilibrated in a transfer buffer (Table 3.26). The membrane was placed on a wet filter paper and covered with the gel and another wet filter paper. The proteins were transferred to the membrane by applying an electric field of 25 V for 30 min. Subsequently the membrane was

blocked with 5% milk powder dissolved in TBST buffer (Table 3.26) for at least one hour with gentle shaking. The membrane was washed three times in TBST buffer for 5-10 min. Next, the membrane was incubated with Anti-His-Tag-HRP conjugate antibody (1:5000 in TBST buffer) for at least one hour. After three 5–10-minute washes in TBST buffer, the blot was transferred to a transparent film and developed using Prime Western Blotting Detection Reagent according to the manufacturer's instructions. After four min of incubation, a second transparent film was carefully placed over the membrane, the liquid was squeezed out, and chemiluminescence was detected.

Table 3.26: Buffers for Western blotting.

Transfer buffer pH 7.6	
Tris	25 mM
EtOH (v/v)	20%
glycine	192 mM
TBST buffer pH 7.8	
Tris	20 mM
NaCl	150 mM
TWEEN 20 (v/v)	0.05%

3.2.2.7. Preparation of proteoliposomes

To prepare liposomes, 60 µL *E. coli* Polar Lipids (EPL) (25 mg/mL) and 20 µL 1,2-dioleoyl-sn-glycero-3-phosphocholine (DOPC) (25 mg/mL) solved in chloroform were mixed. The chloroform was evaporated under a stream of N_2, and the lipid film was completely dried in a vacuum desiccator overnight. Next, 497.5 µL 50 mM KPi pH 7.5 and 2.5 µL FluoZin™-3 (1 mM in deionised water) were added to the lipid film. The sample was vortexed rapidly and the membrane completely rehydrated for 45 min at 37°C and 1400 rpm in a thermomixer. The obtained multilamellar liposomes were frozen in liquid N_2, followed by thawing in a 37°C water bath (five cycles) to obtain unilamellar liposomes. The sample was divided into two portions of 250 µL. Protein was added to one portion at a ratio of 1:500 (w/w). The final volume was 500 µL with a detergent concentration of 0.1%, and the volume was adjusted with 50 mM HEPES/KOH, pH 7.6. The control contained the same amounts of storage buffer, 50 mM HEPES/KOH pH 7.6 and Triton X-100. The samples were incubated on a horizontal shaker for 30 min to allow membrane destabilisation. Next each sample was pipetted to 50 µL of a 1:1 (v:v) mixture of BioBeads in 50 mM HEPES/KOH pH 7.6. The BioBeads were exchanged after 30 min, one hour, two hours, overnight and an additional hour to remove Triton X-100. Samples were loaded onto a PD10 column to remove most of the unincorporated fluorophore. The

samples were then centrifuged (285000 g; 4°C; 30 min), and the resulting pellet was washed thoroughly five times with 250 µL 50 mM HEPES/KOH pH 7.6. The pellet was resuspended in 250 µL 50 mM HEPES/KOH pH 7.6 and used for the transport assay.

3.2.3. Biophysical methods

3.2.3.1. Mg^{2+} transport assay

Mg^{2+} transport was monitored using a Mg^{2+}-sensitive fluorescent dye incorporated into the proteo-/liposomes. Therefore, FluoZin™-3, a zinc sensor that binds Mg^{2+}, was used. First, spectra of the liposomes were taken to ensure proper encapsulation of the fluorescent dye. The spectra were recorded in a quartz cuvette (3 mm, Hellma Analytics, Jena, GER) at 25°C on an FP-8500. The excitation wavelength was set to 494 nm with a slit width of 2.5 nm. Emission spectra were recorded between 510 and 550 nm with a slit width of 2.5 nm. To measure Mg^{2+} transfer across the proteoliposomal membrane, the prepared samples were quickly mixed with 0.8-6 mM $MgCl_2$ or $MgSO_4$, and changes in the FluoZin™-3 fluorescence emission were immediately measured . The excitation wavelength was set to 494 nm with a slit width of 2.5 nm. Emission was recorded at 516 nm with a slit width of 10 nm for 400 s.

3.2.3.2. CD-spectroscopy

Circular dichroism (CD) refers to the differential absorption of counter-clockwise and clockwise circularly polarised light. The different types of regular secondary structures in proteins result in characteristic CD spectra between 260 and 180 nm that can be analysed (S. M. Kelly *et al.* 2005). Prior CD spectroscopy cytMgtE was dialysed overnight against 10 mM HEPES/KOH pH 7.6. The spectra were recorded in a quartz cuvette (1 mm, Hellma Analytics, Jena, GER) at 25°C from 200 nm to 260 nm, a scan rate of 200 nm/min, 0.5 nm steps, 2 s data integration time with a six-time accumulation. The protein concentration was 5 µM. To gain further information on thermal-induced changes in the secondary structure, samples were heated from 25-99°C in 2°C steps. The thermal transition was monitored by following the signal changes at 222 nm (mdeg). The spectra were recorded in a quartz cuvette (1 mm, Hellma Analytics, Jena, GER) from 200 nm to 250 nm, with a scan rate of 100 nm/min, 1 nm steps, and 1 s data integration time. The protein concentration was 5.8 µM. Spectra of the thermal denaturation were taken for multiple spectra analysis using the online tool BeStSel (Micsonai *et al.* 2015;

Micsonai *et al.* 2018; Micsonai *et al.* 2021).

3.2.3.3. ANS measurements

A thermal shift assay with the fluorescence dye 8-anilinonaphthalene-1-sulfonic acid (ANS) was used to analyse changes in the surface polarity of cytMgtE upon thermal denaturation. ANS binds to hydrophobic and hydrophilic parts of the protein. An increase in fluorescence and a blue shift of the emission maximum result from the restricted mobility of ANS bound to a hydrophilic part of the protein (Gasymov *et al.* 2007; Cimmperman *et al.* 2011; Guliyeva *et al.* 2020; Ota *et al.* 2021). For the measurements, 7.6 µM of the protein was mixed with 50 µM ANS and 5 mM $MgCl_2$. The measurements were performed in a quartz cuvette (3 mm; Hellma Analytics, Jena, GER) on an FP-8500. The excitation wavelength was set at 370 nm with a slit width of 2.5 nm. Emission spectra were recorded between 400 and 600 nm with a slit width of 2.5 nm from 20-95°C in 1°C steps. The wavelength at 470 nm was monitored to gain information on changes in the surface polarity of cytMgtE. The midpoint of the normalised (0;1) denaturation curve was obtained *via* fitting the data with an adjusted Boltzmann fit.

$$F_{meas}(T) = \frac{(T * m_N + F_N) - (T * m_D + F_D)}{1 + e^{\frac{T - T_m}{dT}}} + (T * m_D + F_D) \qquad (1)$$

F_{meas}	=	fluorescence intensity at 470 nm
T	=	Temperature
F_N/F_D	=	fluorescence intensity of the native/denatured protein at the plateaus
m_N/m_D	=	slopes of the corresponding plateaus

3.2.4. Characterisation of Synechocystis cultures

3.2.4.1. Growth curves and spot assay

For growth curves, 20-25 mL *Synechocystis* wt and mts were grown in 50 mL Erlenmeyer flasks in an orbital shaker at 130 rpm, 30°C and constant illumination of 120 µmol photons * m^{-2} * s^{-1}. Each curve represents three biological replicates where the OD_{750} was measured, and the error bars represent the standard deviation (SD). Growth was monitored under various conditions (Table 3.27) until saturation was reached. To analyse the growth on BG11 agar plates, the cultures were adjusted to an OD_{750} of 0.2, and a dilution series (1:10 steps) was spotted (5 µL) on plates (Dörrich *et al.* 2015). Plates were grown in an incubator at 30°C with 30 µmol * m^{-2} * s^{-1} irradiation.

Table 3.27: Conditions for growth curves and the spot assay.

Growth curve	**Condition**
BG11	photoautotrophically
BG11 + 5 mM glucose	photomixotrophically
BG11 + 5 mM glucose + 5 µM DCMU	photoheterotrophically
BG11 10,20,30,40,50,60,70 mM Mg^{2+}	photoautotrophically, low Mg^{2+}
BG11 + 12 µM $CoCl_2$	Co^{2+} stress
BG11 + 13 µM $CoCl_2$ + 10 mM $MgCl_2$	Co^{2+} stress and Mg^{2+} complementation
Spot assay	
BG11 10 µM Mg^{2+}	photoautotrophically, low Mg^{2+}

3.2.4.2. Fluorescent micrographs to determine the protein localisation in living cells

The pCK306 plasmid encoding the gene to express a YFP protein (C. L. Kelly *et al.* 2018) or the corresponding N-terminal YFP-tagged channel was transformed into *Synechocytis wt*, *ΔcorA1*, *ΔcorA2* and *ΔmgtE*. Cells were grown in liquid BG11 containing 5 mM glucose to an OD_{750} of ∼1. Expression of YFP or the YFP-tagged channel was induced overnight with 1 mg/mL rhamnose. Fluorescence images were acquired the next day using whole cells immobilised on 2% agarose on a slide. A brightfield image with the cells was taken. Chl *a* was excited to image the thylakoid membrane, and YFP was excited to image the overexpressed protein. All images were captured with a ZEISS Axio Observer.Z1 equipped with a ZEISS ApoTome.2 to remove out-of-focus light. A 63x/1.4 oil objective was used. Image processing was carried out with the ZEN software (Version 2.3.64.0). See Table 3.28 for details. The three obtained images were overlayed, and light intensities were adjusted using Adobe Photoshop 2020.

Table 3.28: Settings of the fluorescence microscope.

	Chl *a*	**YFP**
tag method	mRF12(FS63)	TaYFP
filter	559-585 600-690	450-490 500-550
reflector	63HERedFluores.Protein	38HEGFP
beam splitter	590	495
excitation	559-585	450-490
emission	600-690	500-550
wavelength light source	577-604	450-488
Intensity	100%	50%

3.2.4.3. FRET measurements with MARIO

The gene coding for the genetically encoded FRET sensor MARIO (FRET pair: enhanced cyan fluorescent protein (ECFP), Venus) (Maeshima *et al.* 2018) was inserted into the pCK306 plasmid where gene expression is under the control of a rhamnose inducible promoter (C. L. Kelly *et al.* 2018). The plasmid was transformed into *Synechocystis wt*, and the *ΔcorA2* and *ΔmgtE* single mutant strains and segregation was performed as described above (see section 3.2.1.11). Cells were grown in liquid BG11 medium containing the appropriate antibiotics and 5 mM glucose until an OD_{750} ∼1 was reached. Expression of *mario* was induced with 1 mg/mL rhamnose (w/v) and cells were grown overnight. Fluorescence measurements were performed using whole cells with an OD_{750} ∼1-2. At first, measurements were performed to confirm protein expression. Therefore, Venus was excited after dark adaption and a 10 min light exposure at 490 nm (slit 5 nm), and emission (slit 10 nm) was observed from 510-580 nm. Expression from pCK306 has a basal expression rate (D. Liu *et al.* 2020), which was also observed in the generated constructs. Spectra of uninduced cells were subtracted from spectra after induction with rhamnose and corrected with a linear baseline subtraction. Three technical replicates were performed.

3.2.4.4. Cell analysis under maintained optical density in the same growth state

For the following measurements, cyanobacterial cells were grown photoautotrophically in turbidostate mode (OD_{750} = 1) in a multicultivator and purged with (v/v) 5% CO_2 in air at 30°C. The intensity of the warm white light was set at 30 µmol photons * m^{-2} * s^{-1}. Cells were grown either in standard BG11 or under Mg^{2+} limitation in BG11 medium with 50 µM Mg^{2+}. Before the measurements, the cells were centrifuged at 1800 g at RT for 10 min and solubilised in fresh medium with the OD_{750} adjusted to 2.

3.2.4.5. EM micrographs

EM images were acquired in cooperation with [redacted] & [redacted]. Images were taken from whole cells grown under high and low Mg^{2+} concentrations. To do this, 20 mL of the cells grown in the multicultivator (see above) were centrifuged at 1800 g for 10 min at RT. The supernatant was removed, and the cells were washed with 20 mM HEPES/KOH pH 7.0. After further centrifugation, the cells were resuspended in 20 mM HEPES/KOH pH 7.0 to obtain an OD_{750} of 5. They were then mixed 1:1 with 10% glutaraldehyde (25% solution in water from SERVA Electrophoresis GmbH, Heidelberg, GER). Thus, the cells were finally fixed in a 5% glutaraldehyde solution with an OD_{750} of 2.5. [redacted] and [redacted] performed the following sample preparation and imaging in [redacted]. The fixed samples were centrifuged at 3300 g for 10 min, washed with bidistilled water at RT for 10 min and then centrifuged again. A 2% solution of OsO_4 (w/v in bidestilled water) was used for fixation, and the samples were incubated for 120 min at 4°C. The samples were centrifuged for 10 min at 6600 g and washed with bidestilled water. Centrifugation and washing were repeated twice more. The cells grown under Mg^{2+} limitation had an additional step to obtain a dense cell pellet. Therefore, they were infiltrated with 20% bovine serum albumin (BSA) for 120 min at 4°C, centrifugated for 10 min and fixed in 5% glutaraldehyde in 0.05 M phosphate buffer pH 7.5. All samples were then taken up in 2% agar, cut into small blocks and washed in bidestilled water for 5 min. The samples were dehydrated in ethanol of increasing concentration for 15 min at 4°C (30, 50%) or -20°C (70, 95%). Then three times in 100% ethanol for 20 min at -20°C, 15 min at -20 °C in ethanol + propylene oxide (1:1) and twice for 15 min at -20°C in 2x propylene oxide. After dehydration, the solvent was replaced with a gradually increasing concentration of epon resin (epon + propylene oxide 1:3, 3-4 h at -20 °C; epon + propylene oxide 1:1, overnight at -20 °C; epon + propylene oxide 3:1, 3-4 h at RT, epon, 3-4 h at RT and twice epon overnight at RT). After that, the samples were polymerised in an embedding capsule for 2-3 days at 60°C. Ultrathin sections were cut with an Ultracut EM UCT ultramicrotome using a diamond knife (Type Ultra 45°). Sections were collected on pioloform-coated copper slotted grids (Plano,Wetzlar, GER) and stained with uranyl acetate and lead citrate (Reynolds 1963). The samples were viewed with a JEM-1400Plus transmission electron microscope operated at 80 kV. The recordings were made with a JEOL Ruby CCD camera (3,296 x 2,472 pixels).

3.2.4.6. Pigment extraction and determination

Chl *a* and carotenoids (Car) were extracted and their concentration determined in the dark. For this purpose, 500 µL of culture with the OD_{750} set to 2 was harvested (16000 g; 10 min; RT). The supernatant was discarded thoroughly. Then, 1 mL of 100% methanol (MeOH) was added to the samples. The samples were vortexed quickly and left on an orbital shaker at RT for 15 min. After further centrifugation (16000 g; 10 min; 4°C), the pellet was checked visually. If it was blue with no green colour, the supernatant was used for absorbance (A) measurements at 665.2 nm, 652 nm (Chl *a*), 470 nm and 720 nm (Car) in a polystyrene cuvette (10 mm) using a Perkin Elmer, Lamda 435 photometer. The Chl *a* concentration was (taking the dilution into account) determined according to Porra *et al.* (Porra *et al.* 1989) using the following equation:

$$Chl\,a\,\left[\frac{\mu g}{ml}\right] = 16.26 * A_{665.2} - 8.54 * A_{652} \tag{2}$$

Chl *a* = chlorophyll *a*
A = absorption at X nm

The Car concentration was determined according to Zavřel *et al.* 2015 (Zavřel *et al.* 2015):

$$Car\,\left[\frac{\mu g}{ml}\right] = \left[\frac{1000 * (A_{470} - A_{720}) - 2.86(Chl\,a\,[\frac{\mu g}{ml}])}{221}\right] \tag{3}$$

Car = carotenoids
A = absorption at X nm

The pellet was frozen at -20°C and further used to estimate total carbohydrates (see section 3.2.4.10).

3.2.4.7. Room temperature absorption spectra

Whole-cell spectra were recorded with a Perkin-Elmer Lambda 25 spectrophotometer equipped with an integrated sphere. Spectra accumulation was set to three, and spectra were recorded between 300-800 nm. The spectra were baseline corrected for minimum absorbance at 800 nm and normalised to Chl *a* absorbance at 678 nm. The molar ratio of phycocyanin (PC) to Chl *a* was calculated according to Rakhimberdieva *et al.* (2001) (Rakhimberdieva *et al.* 2007).

$$PC : Chl\,a = \frac{4.9 * A_{625} - 2.1 * A_{652} - 0.8 * A_{678}}{0.1 * A_{625} - 0.7 * A_{652} + 15.8 * A_{678}} \tag{4}$$

PC = phycocyanin
Chl *a* = chlorophyll *a*
A = absorption at X nm

The Car to Chl *a* ratio was estimated from the Chl *a* peak maximum at 437 nm and the 480 nm value representing the Car shoulder (Zlenko *et al.* 2019).

3.2.4.8. Cell counting in a Thoma chamber

The number of cyanobacterial cells per mL at an $OD_{750} = 2$ was counted. For this purpose, the cells were diluted to an OD_{750} of 0.1, and 10 µL were pipetted into a counting chamber (Thoma scale). After the cells had settled to the ground, they were visualised using a microscope with a 40x objective and counted from images taken with a microscope camera using ImageJ (Version 1.53c). The counted number of four large squares was averaged, and the number of cells was calculated as follows:

$$N * 16 * 20 * 10^4 = \frac{cells}{mL} \tag{5}$$

N = average of the counted cells
16 = number of small squares
20 = dilution factor
10^4 = the chamber volume is 1 mm * 1 mm * 0.1 mm = 0.1 mm^3 = 10^{-4} mL

3.2.4.9. 77K fluorescence emission spectra

Low-temperature spectra were recorded using an Aminco Bowman Series 2 fluorimeter equipped with a 77K accessory. One mL of the culture was frozen in liquid N_2. Chl *a* was excited at 435 nm, and phycobilisomes (PBS) at 580 nm. Spectra were recorded between 630-760/800 nm with an accumulation of three. After correcting with a linear baseline subtraction, the spectra were normalised to 695 nm (Chl *a* excitation) or 669 nm (PBS excitation). For further evaluation, the two peak areas of Chl *a* excitation with their height centred at 695 nm (photosystem II (PSII)) and 725 nm (photosystem I (PSI)) were fitted with a Gaussian curve using Fityk. The areas under the curves were integrated as the ratio of the surface areas of the PSI and PSII peaks in the 77K fluorescence emission spectra which correspond to the molar PSI:PSII ratio (Murakami 1997). To obtain an estimate of the PSI and PSII contents [mol/cell] they were calculated as previously described by Luimstra *et al.* (Luimstra *et al.* 2019) using the estimated PSI:PSII ratios, the Chl *a* amount in

mol/cell ($M_{Chl\ a}$ 893.5 g/mol) and assuming that PSI contains ∼100 (Jordan *et al.* 2001) and PSII ∼35 (Umena *et al.* 2011) Chl *a* molecules:

$$PSI_{cell} = \frac{Chl\,a[\frac{mol}{cell}]}{100 + 35/(PSI:PSII)} \tag{6}$$

$$PSII_{cell} = \frac{Chl\,a[\frac{mol}{cell}]}{100 * (PSI:PSII) + 35} \tag{7}$$

PSI = photosystem I
PSII = photosystem II
Chl *a* = chlorophyll *a*
100 = chlorophyll *a* molecules in PSII
35 = chlorophyll *a* molecules in PSI

3.2.4.10. Determining the total carbohydrate content per cells

The cellular content of total carbohydrates was estimated according to Zavřel *et al.* 2018 (Zavřel *et al.* 2018). Briefly, the pellet obtained after Chl *a* extraction (see section 3.2.4.6) was dissolved in 500 µL of deionised water. A 5% phenol solution (v/v) was prepared by mixing 500 µL of ROTI®Phenol solution with 9.5 mL of deionised water. Next, 500 µL of the solution was added to the pre-dissolved pellet and each glucose standard (glucose concentration µg/mL: 25, 50, 75, 100, 300, 500). After mixing and incubation for 15 min, 60 µL were transferred to a 96-well plate. Next, 150 µL of 96% sulfuric acid was added to each well containing the calibration solution (4 technical replicants) or sample (8 technical replicants) and gently mixed by pipetting up and down. After an additional 5 min of incubation, the absorbance at 490 nm was measured with a microplate reader.

3.2.4.11. O_2 evolution and consumption

O_2 measurements were performed in cooperation with [redacted]. O_2 evolution was measured in a 1000 or 600 µL chamber with a fibre-optic oxygen meter at ∼30°C (circulating water). The electrode was calibrated with air saturated water (100% oxygen), and oxygen-free water was obtained by adding sodium dithionite (0% oxygen). Samples were incubated under light exclusion for 15 min before measurement. Sodium bicarbonate ($NaHCO_3$ 10 mM final concentration) was added to prevent CO_2 limitation. The measurement started with measuring the samples for at least 2 min in the dark with subsequent strong light exposure

(3000 K; cold light source). The data were evaluated by comparing the slope of the signal during the min in the dark (respiration) and the slope of the subsequent signal rise (oxygen evolution due to water splitting at PSII). The O_2 consumption, the O_2 production and the net O_2 production were calculated.

3.2.4.12. Pulse amplitude modulation (PAM) fluorometry

PAM measurements were performed in cooperation with [redacted]. The Dual-PAM-100 measuring system (Dual-PAM-100 2006) (Software: DualPAM Version 1.9k) enables separate or combined pulse amplitude modulated (PAM) measurement of PSII (*i.e.* Chl *a* fluorescence) and PSI signals (*i.e.* P_{700} absorption changes). As a sample (*i.e.* cuvette) holder, the system possessed an ED-101US/MS optical unit for suspensions. The fluorimeter was equipped with a DUAL-DR measuring head for excitation of Chl *a* (with red measuring light, red saturating pulses, and red or blue actinic light) and for simultaneous detection of Chl *a* fluorescence. Simultaneously it detects the light transmitted by a DUAL-E emitter, which also provides actinic light and also 830 nm/870 nm P_{700} measuring and reference lights, respectively for P_{700} measurements. (In this latter case, a 180° arrangement between Dual-DR and Dual-E is needed, while at Chl *a* measurements both 90° and 180° arrangement can be used). Two more units, DUAL-EAY and DUAL-DAY (at 90° arrangement), enabled the detection of acridine orange (N,N,N',N'-tetramethylacridine-3,6-diamine, AO) fluorescence (alone or combined with Chl *a* fluorescence). All measurements were performed using a 1.5 mL sample volume in a 10 mm quartz cuvette (Hellma Analytics, Jena, GER) at RT.

3.2.4.13. Fluorescence induction (Kautzky) curves and determination of the maximal PSII quantum yield (F_v/F_m)

While F_v/F_m in higher plants and green algae is established as a measure to determine the maximal photochemical efficiency of PSII and, in turn, to characterise their fitness (Murchie *et al.* 2013), it should be evaluated with more care in cyanobacteria due to its complex dependence, *e.g.* on pigment composition and antenna systems. Nevertheless, it can serve as useful information about PSII-mediated electron transport also in cyanobacteria (Campbell *et al.* 1998). The minimum fluorescence, F_o is commonly probed by low intensity modulated measuring light (ML) whose intensity is too weak to induce charge separation (Campbell *et al.* 1998). Upon applying

a saturating light pulse (SP), all PSII centres transiently close due to charge separation and the maximal fluorescence yield, F_m, is reached. Cyanobacterial cells are usually in state II in darkness, which is characterised by a decreased PSII light absorption compared to state I, due to a partially reduced PQ pool by metabolic electron flow (Mullineaux 2014). Hence, the initial (minimum) fluorescence signal is reduced to $F_{o'}$ (Ogawa *et al.* 2016). Weak blue light, which is mainly absorbed by PSI (where most of the Chl *a* are bound), results in PQ oxidation (Schreiber *et al.* 1995) and, since state transition are most likely triggered by the redox state of the PQ pool (Mullineaux *et al.* 1990), a so-called state I transition and, thus, a higher fluorescence yield, F_o (Ogawa *et al.* 2017). To achieve a complete reaction centre closure and maximal fluorescence yield, an effective PSII-specific electron transfer inhibitor, DCMU (1.5 µl of 10 mM stock (100% EtOH) mixed quickly with a 1 ml pipette), was added (Campbell *et al.* 1998) and F_m was determined. Fluorescence induction curves were recorded according to a protocol adapted from a procedure described in Ogawa *et al.*, 2017 (Ogawa *et al.* 2017) and Ogawa & Sonoike, 2016 (Ogawa *et al.* 2016). This protocol considers the influence of the "basal fluorescence" (f) originated from Chl *a* bound to PSI and phycobilins within the external antenna complexes, and the obtained signals are defined as follows:

F_m	=	maximal fluorescence when the PQ is oxidised
$F_{m'}$	=	maximal fluorescence when the PQ pool is reduced
$F_{o'}$	=	minimal fluorescence when the PQ pool is reduced
F_o	=	minimal fluorescence when the PQ pool is oxidised
F_v	=	F_m-F_o
F_v/F_m	=	maximum quantum yield of PSII (in plants)
$((F_m\text{-}f)\text{-}(F_o\text{-}f))/(F_m\text{ -}f)$	=	maximum quantum yield of PSII in cyanobacteria
f	=	basal fluorescence from phycobilisomes and/or PSI Chl *a*

$$f = \frac{F_{o'}F_m - F_oF_{m'} - \sqrt{(F_m - Fo)(F_{m'} - F_{o'})(F_o - F_{o'})(F_m - F_{m'})}}{(F_m - F_{m'}) - (F_o - F_{o'})} \quad (8)$$

(Ogawa *et al.* 2016)

Table 3.29: Protocol for measuring induction curves.

Step		Time [ms]	intensity [µmol photons * m^{-2} * s^{-1}]	
1	F-ML on	0	2	F_o, used as F_o (lowest signal in the dark)
2	BL on	14900	31	F_o
3	BL off	316010	2	F_o'
4	AL on + DCMU	664000	218	F_m
5	AL/F-ML off	766000	0	
	saturation pulse	width		F_m'
		600 ms	10000	

Since the determination of F_o with weak blue light was inappropriate after the cells were grown under low Mg^{2+} conditions, the lowest fluorescence signal in the dark (defined as F_o (Campbell *et al.* 1998)) was used to determine F_v/F_m (marked in red Table 3.29).

3.2.4.14. Estimation of the effective quantum yield of PSI Y(I) and PSII Y(II)

As mentioned above, the effective quantum yields of the two photosystems are an indirect indicator (proxy) for cellular fitness, *e.g.* during acclimation to different light conditions (Genty *et al.* 1989). The efficiency of the light energy utilisation at PSI and PSII was measured simultaneously using a Dual-PAM-100 routine for recording the rapid light curves (Klughammer *et al.* 2008; Pfündel *et al.* 2008). During that protocol, the actinic light intensity was increased stepwise from 0 to 827 µmol photons * m^{-2} * s^{-1}. Steady-state (F_s) and maximal (F_m') fluorescence levels were determined after 30 s adaptation periods at each light intensity. F_s levels were determined right before the corresponding light pulse, while F_m' levels were obtained by applying 300 ms saturating pulses with an intensity of 10000 µmol photons * m^{-2} * s^{-1}. During the same routine P_{700} parameters were also measured. The maximal P_{700} (P_{700} fully oxidised) signal intensity (P_m) was determined by applying an SP after far-red preillumination. Minimum P_{700} signal intensities, P_o (P_{700} fully reduced) was determined after each SP. The maximal amplitude between the maximal P_{700} and P_o is P_m. The (steady-state) P_{700} signal P and P_m' were recorded just before and after the onset of an SP, respectively. Determined parameters:

$Y(I) = (P_m'-P)/P_m$ (Pfündel *et al.* 2008)
$Y(ND) = (P-P_o)/P_m$ (Pfündel *et al.* 2008)
$Y(NA) = (P_m-P_m')/P_m$ (Pfündel *et al.* 2008)
$Y(II) = (F_m'-F_s)/F_m'$ (Genty *et al.* 1989)

3.2.4.15. P_{700}^+ re-reduction kinetics

P_{700}^+ re-reduction kinetics are used to gain information on the electron transport through PSI (Klughammer *et al.* 1994) and were measured with a Dual-PAM-100 measuring system as described above (see section 3.2.4.12). The activity of PSI can be investigated by recording specific light absorption signals in the near-infrared (875-830 nm) (Klughammer *et al.* 2008). Normally, complete P_{700} oxidation was achieved by a 100-ms saturation pulse (I = 10000 µmol photons * m^{-2} * s^{-1}). Traces were recorded after 5 min of dark incubation without any addition as well as in the presence of 10 mM DCMU. In the case of KCN addition, the samples were incubated in the dark for 15 min with 4.6 mM KCN. Three technical replicates were averaged, and P_{700}^+ decay kinetics were fitted with single or double exponential (DCMU) functions to determine the corresponding rate constants (k).

3.2.4.16. ΔpH measurements with the pH-sensitive fluorescence dye acridine orange (AO)

Similar to the Chl *a* and P_{700} measurements, pH changes in *Synechocystis* were determined in the Dual-PAM-100 measuring system using intact cells with the pH-sensitive fluorescent dye AO. Using AO as a fluorescent dye enables to follow pH changes in both the cyanobacterial thylakoid lumen and the cytoplasm (Teuber *et al.* 2001). The applied protocol is summarised in Table 3.30, while the used chemicals are listed in Table 3.31. Samples were incubated in darkness for 15 min prior to measurements.

Table 3.30: Measuring protocol for AO measurements.

Step		Time [ms]	intensity [µmol photons * m^{-2} * s^{-1}]
1	F-ML and AO on	0	24
2	AL on	180000	216
3	AL off	480000	24
4	F-ML and AO off	600000	0

Table 3.31: Sample composition for the AO measurements.

	Tricin pH 8	AO	DCMU	DBMIB Na ascorbate	MV	KCN	Malonate pH 8	$HgCl_2$
solvent	H_2O	DMSO	EtOH	EtOH H_2O	H_2O	BG11	H_2O	H_2O
c stock	1 M	10 mM	10 mM	10 mM 1 M	10 mM	0.5 M	0.5 M	10 mM
volume [mL]	0.1	0.001	0.0015	0.0075	0.015	0.015	0.015	0.005
c final	without inhibitors							
	62.5 mM	6.3 µM						
	DCMU							
	62.4 mM	6.2 µM	9.4 µM					
	DBMIB							
	62.0 mM	6.2 µM		46.4 µM 4.6 mM				
	MV							
	61.9 mM	6.2 µM			92.8 µM			
	KCN							
	61.9 mM	6.2 µM				4.6 mM		
	Malonate							
	61.9 mM	6.2 µM					4.6 mM	
	HgCl2							
	62.3 mM	6.2 µM						31 µM

The obtained curves were corrected with a linear baseline subtraction and normalised to their initial intensity.

4. Results and Discussion

4.1. Mg^{2+} limitation in *Synechocystis* sp. PCC 6803 cells

Mg^{2+} is a micronutrient essential for plant growth (Merhaut 2007), and during the early 20th century, Mg^{2+} was identified as part of the Chl molecule (Willstätter 1906). Not only does Mg^{2+} serve as the central ion of the light-harvesting pigment Chl, but during the formation of a ΔpH across the TM in the light, the electric potential generated by the photosynthetic electron transfer chain is balanced by the release of Mg^{2+} (Barber *et al.* 1974; Portis *et al.* 1976) and K^+ from the lumen and uptake of Cl^- into the TM lumen (Dilley *et al.* 1965; Hind *et al.* 1974; Chow *et al.* 1976; Lyu *et al.* 2017). As Chl-containing organisms, cyanobacteria require Mg^{2+} for growth, and it has been shown that the lower limit for the growth of cyanobacteria is around 5 µM Mg^{2+} (Utkilen 1982). In contrast, a concentration above 45 mM Mg^{2+} leads to the formation of an irreversible scum (Dervaux *et al.* 2015). Therefore, to investigate the possible effects of Mg^{2+} limitation on the physiology of *Synechocystis* wt cells, cell growth at various Mg^{2+} concentrations was first measured using medium with concentrations ranging from 10–70 µM, as well as at 300 µM Mg^{2+}, *i.e.*, the Mg^{2+} concentration in BG11 medium (Rippka *et al.* 1979). To investigate the effects on the photosynthetic machinery, the physiology of *Synechocystis* cells was analysed after photoautotrophic growth in a multicultivator in the presence of high (300 µM (**H**)) and low (50 µM (**L**)) Mg^{2+} concentrations.

4.1.1. Results

4.1.1.1. Growth of *Synechocystis* under Mg^{2+}-limiting conditions

To elucidate the requirement for Mg^{2+}, first, *Synechocystis* cell growth was monitored at different Mg^{2+} concentrations. It was observed for the cyanobacterium *Anacystis nidulans* ((*Synechococcus elongatus*)(*S. elongatus*)), which can grow with as little as 5 µM Mg^{2+}, that at Mg^{2+} concentrations below 7.5 µM, Mg^{2+} was the only growth limiting factor (Utkilen 1982). Since a low Mg^{2+} concentration was targeted without inhibiting cellular growth, concentrations not lower than 10 µM Mg^{2+} were used for measuring growth curves. According to the results, *Synechocystis* can grow at an Mg^{2+} concentration as low as 10 µM (Figure 4.1.1). Growth was almost identical from 40 - 70 µM Mg^{2+}, yet at concentrations below 30 µM Mg^{2+}, *Synechocystis* growth was significantly impaired with decreasing Mg^{2+} concentrations. In addition, at very low Mg^{2+} concentrations, the reached maximum OD_{750} was decreased, whereas an expanded lag phase was observed,

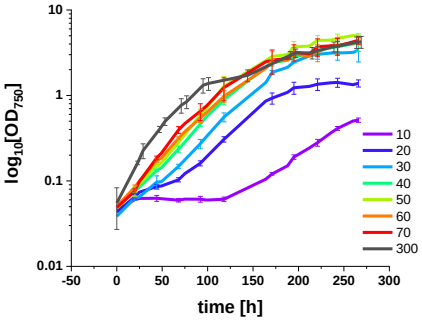

Figure 4.1.1: Growth curve of *Synechocystis* in the presence of different Mg^{2+} concentrations.
Growth curve of *Synechocystis* over 250 h. Numbers next to the colour bars indicate the Mg^{2+} concentration in µM. Lower Mg^{2+} concentrations led to a more extended lag phase. At Mg^{2+} concentrations lower than 30 µM, cells did not reach saturation levels of cells grown at 300 µM conditions during the time of observation. Experimental error bars are shown for n=3.

as most evident at 10 µM Mg^{2+}. Starting at an Mg^{2+} concentration of 40 µM and higher, growth appeared not to be affected. Thus, it was decided to use 50 µM Mg^{2+} (**L**) in the culture medium to further investigate the effects of low Mg^{2+} availability on *Synechocystis* physiology without inducing unintended side effects and compare the observations with measurements at 300 µM Mg^{2+} (**H**) in the growth medium.

4.1.1.2. Cell appearance and cell number

It is known that low Mg^{2+} concentrations impair cell division of several non-photosynthetic bacteria (Webb 1951; Brock 1962) as well as of the cyanobacterium *S. elongatus* (Utkilen 1982). When *S. elongatus* was grown at 5 µM Mg^{2+}, cells appeared filamentous with three to four times the "normal" cell length. When transferred to higher Mg^{2+} concentrations, cells reverted to "normal" size but not if Mg^{2+} concentrations were below 10 µM (Utkilen 1982). EM images were recorded to analyse how low Mg^{2+} (50 µM) concentrations affect cell division and cellular morphology. *Synechocystis* cells did not show bigger or elongated cells that formed filaments at **L** conditions. While *Synechocystis* cultures grew well under **L** conditions, cells displayed a considerable layer of exopolysaccharides (EPS) surrounding the cell. In addition, the cells appeared less densely packed under **L** conditions (Figure 4.1.2). Although cellular size appeared to be the same at both growth conditions, cell counting revealed slightly increased cell numbers in BG11 media with low Mg^{2+} concentrations compared to those with high Mg^{2+} concentrations when culture densities were set to the same OD_{750} (Figure 4.1.3). This is in line with the observed less densely packed cells under **L** conditions, albeit in the EM images, no apparent differences in the amount and stacking of TMs were observed.

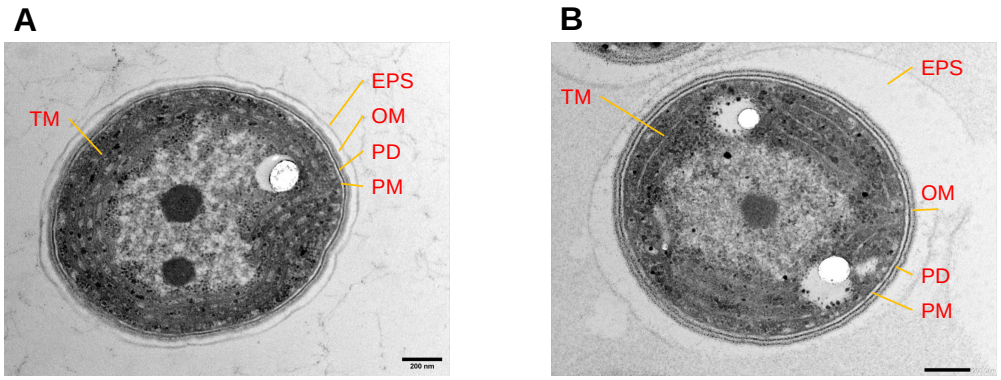

Figure 4.1.2: EM images of *Synechocystis* grown at high or low Mg^{2+} concentrations.
Images of whole cells were taken after growth under **H** or **L** conditions. Whole-cell images showed less densely packed cells and a much bigger EPS layer when cells were grown under Mg^{2+} limiting conditions. OM, outer membrane; PD, Peptidoglycan; PM, plasma membrane; TM, thylakoid membrane. Scales bars = 200 nm. Images were taken by [redacted] and [redacted], [redacted].

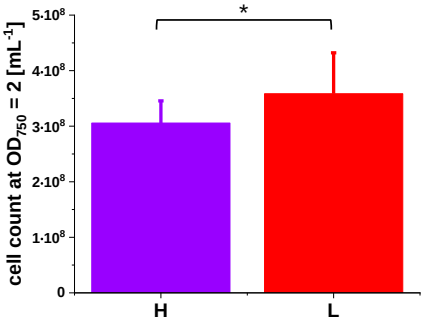

Figure 4.1.3: Cell count at OD_{750} = 2 per mL cell culture.
Cell count when cells were set to an OD_{750} of 2 revealed slightly higher cell numbers under **L** conditions. Experimental error bars indicate the means ±SDs for n=13 (**H**) and n=8 (**L**) biological replicates. Significant differences (two-sample t-test) are indicated as: * $p < 0.05$; ** $p < 0.01$; *** $p < 0.001$.

4.1.1.3. The cellular amount of total carbohydrates was unaltered

In several bacterial strains, Mg^{2+} limitation led to an increased synthesis of polysaccharides (Webb 1951). It is also known that carbohydrates accumulate in plant chloroplasts under Mg^{2+} deficiency (Cakmak *et al.* 1994). Yet, this appears not to be directly related to the photosynthetic activity of the cells but to the Mg^{2+} requirement for the export of glucose from the chloroplasts (Cakmak *et al.* 1994). Nevertheless, Mg^{2+} limitation caused a decrease in the total carbohydrate content in the algae *Botryococcus braunii* (Giraldo *et al.* 2021). The observation of an enlarged EPS layer in EM images could be accompanied by an increased amount of carbohydrates, but the appearance of less densely packed cells could argue for a lower amount of total carbohydrates. Therefore, the number of total carbohydrates was determined with a phenol-sulfuric acid method (Zavřel *et al.* 2018). Considering the higher number of cells under Mg^{2+} deficiency, the amount of total carbohydrates per cell hardly changed. The amount of total carbohydrates in pg per cell was 0.24 ±0.06 (SD) under **H** and 0.32 ±0.20 SD under **L** conditions. Thus, it appeared that *Synechocystis* cells grown under **H** conditions could produce a sufficient amount of carbohydrates and did not appear to be impaired in their ability to fix CO_2. Therefore, the content and composition of pigment-containing protein complexes involved in photosynthesis were examined for possible changes.

4.1.1.4. Content and composition of pigment-containing protein complexes involved in photosynthesis

First, whole-cell absorption spectra were recorded to determine the ratios of all *Synechocystis* pigments. *Synechocystis* absorption spectra are dominated by three different types of pigments: phycocyanin (PC), which is bound to the antenna proteins (absorbance maximum at around 625 nm), carotenoids (Car) (480 nm shoulder), and Chl *a* (437 nm and 678 nm). All cultures were adjusted to the same OD_{750}, and absorbance was analysed from 400 nm to 800 nm using an integrated sphere to reduce light scatter. The absorption spectra of cultures grown under **H** or **L** conditions differed significantly: a low Chl *a* content was visible after growth in medium containing low Mg^{2+} concentrations since both typical absorbance maxima were severely reduced (Figure 4.1.4 A). A reduced Chl *a*:Car ratio in the cells grown under **L** conditions was also observed (Figure 4.1.4 B). In addition, the low Chl *a* content of the cells after growth at Mg^{2+} limiting conditions resulted in a relatively increased PC peak at 625 nm. Consequently, the estimated PC:Chl *a* ratio increased by about half under Mg^{2+}-limited conditions (Figure 4.1.4 C).

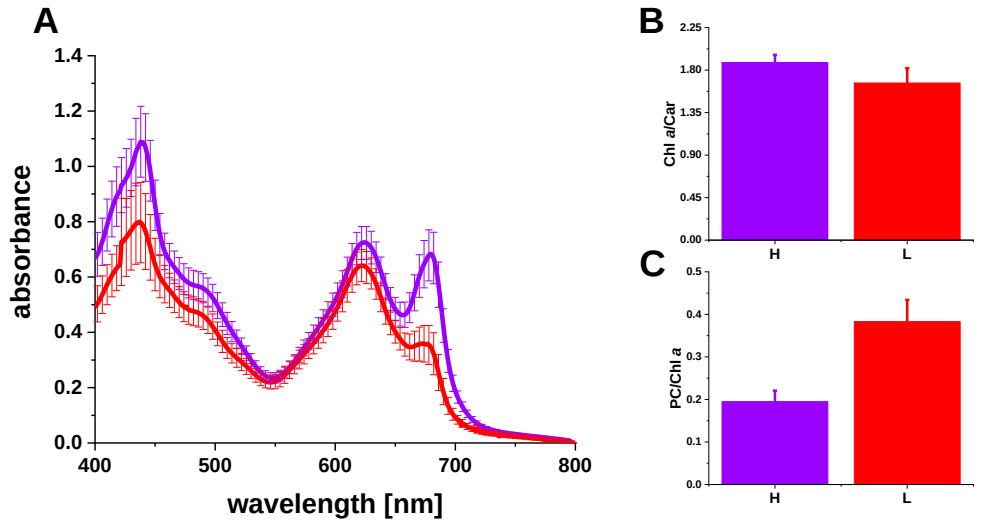

Figure 4.1.4: Absorption spectra of whole cells.
Absorption spectra (A) were recorded under **H** (purple) and **L** (red) conditions. The loss of Chl *a* can be seen from a decrease in the peaks at 437 nm and 678 nm. The changed Chl *a* to Car ratio can be calculated based on the spectra (A, B). The increase in the PC:Chl *a* ratio is evident from the spectrum (A, C). Experimental error bars indicate the means ±SDs of n=6 (**H**) and n=3 (**L**) biological replicates.

Thus, in **L**-grown cells, the PBS content per cell is high compared to the Chl-containing PSs. The reduced Chl *a* content, indicated by lowered peak maxima at 437 nm and 678 nm in the absorption spectra, was confirmed by calculating the Chl *a* concentration after methanolic pigment extraction. The Chl *a* content of *Synechocystis* cells was significantly lowered when cells were grown in an Mg^{2+}-limiting medium (Figure 4.1.5 A). Since the absorption spectra showed an altered Chl *a*:Car ratio, the number of carotenoids was also examined. *Synechocystis* carotenoids are mainly composed of β-carotene (26%), myxoxanthophyll (36%), zeaxanthin (14%) and echinenone (18%) (Takaichi *et al.* 2001). They are required for proper assembly of the PSII complex (Zakar *et al.* 2016) as well as the trimerisation of PSI complexes (Vajravel *et al.* 2017), plus carotenes may take part in light harvesting at PSI (Stamatakis *et al.* 2014). Furthermore, they are important for stress response as the expression of carotenoid biosynthesis genes is upregulated by illumination (Fernández-González *et al.* 1998). Myxoxanthophyll, which has the highest photoprotective properties (Steiger *et al.* 1999), has high amounts in the PM (Takaichi *et al.* 2007; Zhu *et al.* 2010) and OM (Jürgens *et al.* 1985). Additionally, myxoxanthophyll is important for stabilising TMs (Mohamed *et al.* 2005), while zeaxanthin plays a role in photoprotection at high light conditions (Steiger *et al.* 1999).

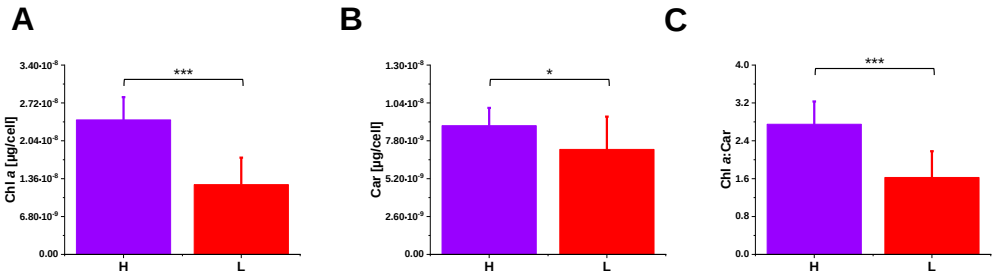

Figure 4.1.5: Cellular pigment content.
Methanolic pigment extraction revealed a reduced amount of Chl *a* per cell (A), only small changes in the amount of Car per cell (B), and thus a lower Chl *a* to Car ratio (C). Experimental error bars indicate the means ±SDs of (A) n=13 (**H**) and n=7 (**L**), (B) n=12 (**H**) and n=8 (**L**) and (C) n=12 (**H**) and n=7 (**L**) biological replicates. Significant differences (two-sample t-test) are indicated as: * $p < 0.05$; ** $p < 0.01$; *** $p < 0.001$.

Although Chl *a* levels were reduced when the amount of available Mg^{2+} was limited, cells retained almost the same number of Car (Figure 4.1.5 B) under Mg^{2+} limiting conditions, so the total Chl *a*:Car ratio was lower (Figure 4.1.5 C). The ratios calculated from the methanolic extract (Figure 4.1.5) and the absorption spectra (Figure 4.1.4) slightly differed, but showed the same trend.

4.1.1.5. Reduction in Chl *a* under Mg^{2+} deficiency was accompanied by altered PSI:PSII ratios

The reduced Chl *a* content suggested a greatly reduced content of Chl-containing protein complexes per cell when cells were grown under **L** conditions. Since reduced Chl *a* levels often result in reduced PSI levels (Shen *et al.* 1993), it was investigated whether the relative PSI content per cell changed when cells were grown under **L** conditions. Therefore, fluorescence emission spectra were measured at 77K after freezing whole *Synechocystis* cells in liquid nitrogen. These conditions allow the evaluation of the PSI:PSII ratio (Murakami 1997) and, since no positional changes of the antenna complexes (state transition) can occur, the evaluation of the energy transfer between the PBS and the two PSs. The Chl *a* fluorescence emission from PSI has a maximum at 725 nm (Shen *et al.* 1993), and PSII core antennas (CP43, CP47) have peaks at 685 nm (CP43, CP47) and 695 nm (CP47) (Andrizhiyevskaya *et al.* 2005). Normalised spectra after Chl *a* excitation at 435 nm clearly showed a decreased PSI:PSII ratio when compared to cells grown under **H** conditions (Figure 4.1.6 A). Furthermore, with a simultaneously high PBS content per cell in the case of **L**-grown cells, the energy transfer between the light-harvesting

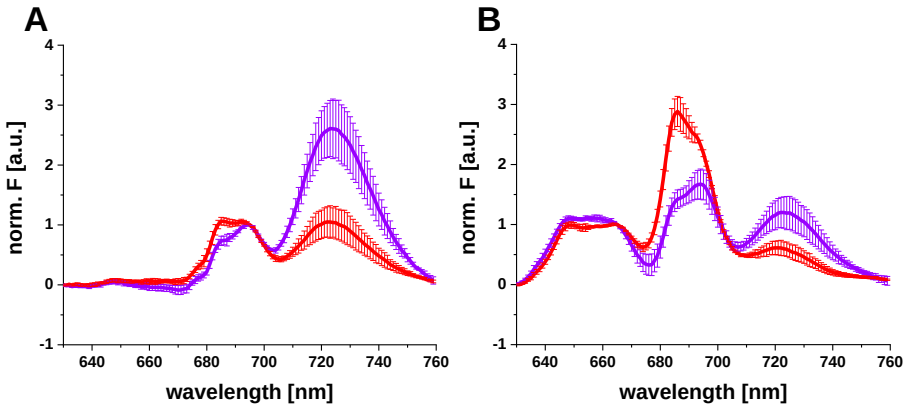

Figure 4.1.6: 77K spectra recorded with whole cells.
Fluorescence emission spectra were recorded under **H** (purple) and **L** (red) conditions. (A) Cells were excited at 435 nm, and spectra were analysed from 630 nm to 760 nm and normalised at 695 nm. Mg^{2+} limitation resulted in an altered PSI:PSII ratio and a slightly altered ratio of 685 nm:695 nm. (B) Cells were excited at 580 nm, and spectra were analysed from 630 nm to 760 nm and normalised at 665 nm. Mg^{2+} limitation resulted in an altered PC:PSI and PC:PSII and a slightly altered ratio of 685 nm:695 nm as previously observed with Chl *a* excitation Experimental error bars indicate the means ±SDs of n=5 (**H**) and n=3 (**L**) biological replicates.

antenna pigments and the two PSs might be altered. To analyse the energy coupling of the PBS to the two PSs, the samples were excited at 580 nm, which mainly excites PBS antenna complexes. When cells were grown under **L** conditions, energy transfer to PSI was reduced, whereas energy transfer to PSII increased (Figure 4.1.6 B). Thus, an increased amount of PBSs' appeared to bind to PSII complexes compared to **H** conditions. Additionally, the ratio between the 685 nm (CP43, CP47) and the 695 nm (CP47) fluorescence emission signal was changed. Next, the total amounts of PSI and PSII were calculated by integrating the areas under the 695 nm peak (PSII) and the 725 nm peak (PSI) using the spectra obtained upon Chl *a* excitation. Based on the combined results, the number of PSII complexes hardly changed under **L** conditions, while the number of PSI decreased significantly (calculated as described in (Luimstra *et al.* 2019)). Although the total number of PCs was lower, the PC:Chl *a* ratio was higher since the Chl *a* content decreased more dramatically than the PC content (Table 4.1.1).

Table 4.1.1: Cellular pigment contents and ratios.
Contents [10^{-18} mol/cell] and ratios of Chl *a*, PSI, PSII and PC of wt grown under high (**H**) and low (**L**) Mg^{2+} conditions. Numbers were obtained as described in Luimstra *et al.* (Luimstra *et al.* 2019). Arrows indicate the direction of cell content change and n indicates the number of biological replicates.

	H	**n**	**L**	**n**	**units**
Chl *a* content	28.7 ±4.8	8	↓ 11.0 ±2.4	3	10^{-18} mol/cell
PSI content	0.27 ±0.03	4	↓ 0.10 ±0.02	3	10^{-18} mol/cell
PSII content	0.031 ±0.002	4	= 0.030 ±0.002	3	10-18 mol/cell
PSI:PSII ratio	8.8 ±0.9	4	↓ 3.4 ±1.0	3	-
PC content	5.8 ±1.1	3	↓ 4.1 ±0.7	3	10^{-18} mol/cell
PC:Chl *a* ratio	0.19 ±0.03	6	↑ 0.38 ±0.05	3	-
PC:PSII ratio	182.8 ±26.5	3	↓ 140.4 ±22.6	3	-

4.1.1.6. The activity of photosynthetic complexes

The above-described analyses have indicated that the PSI content per cell is significantly reduced under **L** conditions, whereas PSII remained unchanged. To analyse and quantify the PSII activity, oxygen evolution rates of intact *Synechocystis* cells grown under **L** or **H** conditions were measured. To avoid overestimating O_2 production at Mg^{2+} limitation, O_2 yields were expressed as µmol/L/min at $OD_{750} = 2$ and not normalised to Chl concentrations, as typically done (Figure 4.1.7). Under **L**

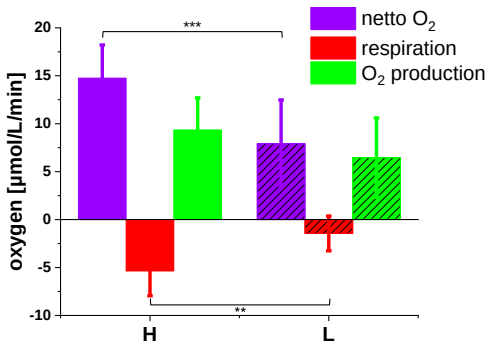

Figure 4.1.7: Oxygen evolution rates of cells at $OD_{750} = 2$.
Comparison of net oxygen production (purple), oxygen consumption (red) and oxygen production (green) under high (**H**) or low (**L**) Mg^{2+} concentrations. The bars represent the amount of oxygen [µmol/L/min] calculated from the slope during the measurement. Oxygen consumption was significantly reduced under Mg^{2+} deficiency. Experimental error bars indicate the means ±SDs of 5 (**H**) or 7 (**L**) biological replicates. Significant differences (two-sample t-test) are indicated as: * $p < 0.05$; ** $p < 0.01$; *** $p < 0.001$. The measurements were performed in cooperation with [redacted].

conditions, the net oxygen evolution rate significantly decreased, as seen in Figure 4.1.7. Yet, O_2 consumption was much more influenced at Mg^{2+} limitation. Thus, the apparently lower net O_2 production observed in cells grown under **L** conditions was mainly due to reduced O_2 consumption. Since the O_2 evolution seemed relatively unaffected under **L** conditions, Dual-PAM-100 measurements were performed in cooperation with [redacted] to analyse further to what extent the activity and the interaction of the two PSs and, thus, the photosynthesis machinery was

affected.

4.1.1.7. Mg^{2+} limitation led to a lower maximal quantum yield of PSII

The Dual-PAM-100 measuring system is a combined Chl fluorimeter enabling the probe of the PSII photosynthetic activity and a P_{700} measuring unit providing information about the electron transfer through PSI (Schreiber 1986; Schreiber *et al.* 1988). Importantly, rather than the intensity of fluorescence signal, which can vary over several orders of magnitude under different light conditions, the system measures fluorescent yields, a proxy for PSII characteristics, which varies on a much narrower scale (factor of 5-6) (Schreiber 2004). One of the most common approaches is to measure the so-called fluorescence induction (or Kautzky) curve, *i.e* the kinetics of the increase of fluorescence yield upon illumination combined with saturating pulse analysis (Schreiber 2004). The F_v (variable fluorescence) contribution to the fluorescence yield is highest after dark adaption. It can be measured upon application of a saturating light pulse to a dark-adapted sample which results in the maximal fluorescence yield, F_m (= F_o + F_v, where F_o represents the initial fluorescence). With this, the maximal PSII quantum yield F_v/F_m, which is broadly used to characterise the fitness of PSII in the literature, can be determined (Campbell *et al.* 1998). The pattern of the fluorescence induction curves of higher plants and cyanobacteria differ as a result of their different antenna systems, pigment ratios and, predominantly, the redox state of the PQ pool in the dark (Mullineaux *et al.* 1986; Schreiber *et al.* 1995; Campbell *et al.* 1996). Some typical signal patterns are shown in Figure 4.1.8. After dark adaptation, the PQ pool in higher plants is oxidised. Hence, PSII centres are open, and the system is in state I. Thus, the potential for photochemistry is maximal, and the fluorescence quantum yield is minimal (Campbell *et al.* 1998). This F_o is normally probed by low-intensity measuring light (ML) which is weak enough not to induce charge separation (Campbell *et al.* 1998). Upon applying a saturating light pulse, all PSII centres transiently close, and the maximal fluorescent yield, F_m (maximal fluorescence, reduced Q_A), is reached. Upon switching on the actinic light (which drives photosynthesis), the fluorescence level first increases as a result of the reaction centre closure (reduction of Q_A) and then decreases due to photochemical quenching and non-photochemical quenching (Schreiber 2004). These processes result in a decrease in the maximal ($F_{m'}$), steady-state, and minimum fluorescence ($F_{o'}$) (Figure 4.1.8 A). In cyanobacteria, the phycobilisomes and a relatively high amount of PSI result in a high level of non-variable background fluorescence (Campbell *et al.* 1996) (Figure 4.1.8 B, C).

Additionally, cyanobacterial cells are usually in state II in darkness due to a partially reduced PQ pool; hence, the initial fluorescence signal is quenched to $F_{o'}$ (Ogawa *et al.* 2016). Weak blue light, which is mainly absorbed by PSI (where most of the Chl *a* are bound), results in PQ oxidation and, hence, a state I transition, and thus, a higher fluorescence yield, and the F_o level can be determined (Ogawa *et al.* 2017). Upon illumination with actinic light, the PQ pool becomes oxidised *via* a large PSI population, and hence the fluorescence yield increases (Figure 4.1.8 B, Fm' values). To achieve a complete reaction centre closure and maximal quantum yield, an effective PSII inhibitor, DCMU, can be applied (Campbell *et al.* 1998). DCMU blocks the electron transfer between Q_A and Q_B, resulting in a complete reaction centre closure. Since the PQ pool is oxidised and cells turn to state I (Figure 4.1.8 C), F_m can be determined. Although oxygen evolution was only slightly altered,

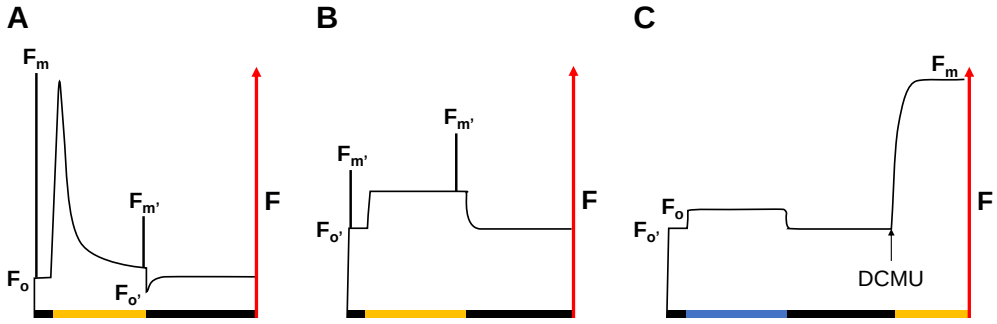

Figure 4.1.8: Typical induction curve traces of plants and cyanobacteria (adapted from (Ogawa *et al.* 2017)).
Induction curves are measured to estimate the maximal quantum yield of PSII. (A) Induction curve of a land plant. F_o is determined after the onset of the ML. Application of a saturation pulse results in F_m. After the onset of actinic light, the fluorescence transiently decreases, and applying saturation pulse results in $F_{m'}$. Switching off the light leads to a signal decrease below F_o values, and $F_{o'}$ can be determined. (B) In cyanobacteria switching on the ML results in $F_{o'}$ values, and a saturating light pulse after dark adaption is lower than under actinic light exposure (compare the two $F_{m'}$ values). (C) After the onset of ML F_o' is determined. The addition of weak blue light results in F_o. Actinic light exposure and the addition of DCMU results in F_m values.

the changes in the amount of Chl *a* plus the altered PSI:PSII ratio indicated that the activity of the photosynthetic apparatus could be affected to some extent. To examine which specific part was most influenced by limited Mg^{2+} availability, the Chl fluorescence parameter PSII maximum quantum yield F_v/F_m was determined, which is a good indicator of PSII photosynthetic performance in plants (Maxwell *et al.* 2000) and gives reliable numbers in cyanobacteria (Campbell *et al.* 1998). In F_v/F_m measurements, using induction curves according to an adapted protocol (see section 3.2.4.13 and Figure 4.1.9), blue light did not lead to a signal increase after growth at Mg^{2+} limitation. For this reason, F_v/F_m was calculated using the

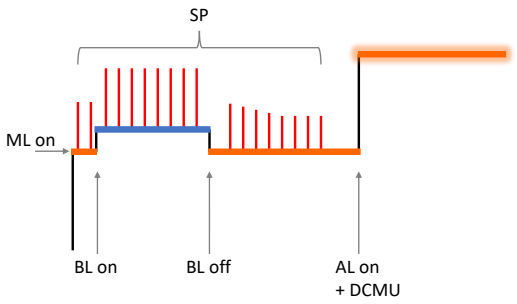

Figure 4.1.9: Schematic representation of the fluorescence trace of an induction curve measurement with dark-adapted *Synechocystis* cells.
Low-intensity ML (2 µmol photons * m^{-2} * s^{-1}) was turned on after 1000 ms to determine F_o'. After 14900 ms, low-intensity blue light (+29 µmol photons * m^{-2} * s^{-1}) was turned on to determine F_o. The blue light was switched off after 316010 ms. After 664000 ms, DCMU was added, and actinic light (+216 µmol photons * m^{-2} * s^{-1}) was turned on to determine F_m. Saturation pulses (10000 µmol photons * m^{-2} * s^{-1}) were applied throughout the measurement.

lowest signal in the dark and the highest signal in the light after adding DCMU. Clearly, the Mg^{2+} limitation resulted in a lowered maximal PSII quantum yield (Figure 4.1.10). Both the initial fluorescence signal and the intensity of the peaks

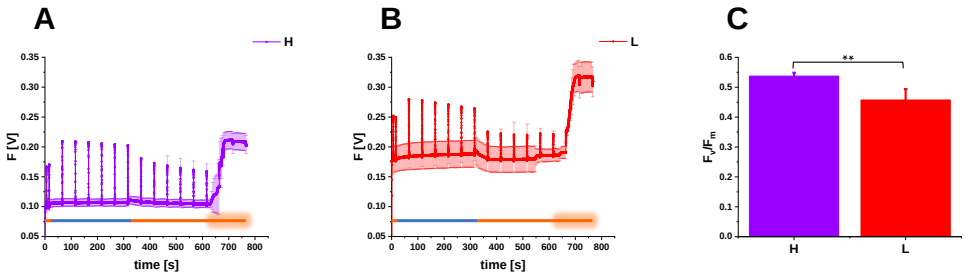

Figure 4.1.10: Fluorescence induction curves measured using *Synechocystis* cells grown under H or L conditions.
Averaged traces of PAM fluorescence induction curves of *Synechocystis* cells grown under **H** (A) or **L** (B) conditions were obtained using an adapted measuring protocol (see section 3.2.4.13). Dark incubated cells were illuminated with low-intensity ML light, and saturating light pulses were given. The weak blue light was turned on to induce state transitions. Saturation pulses were added to monitor a change in signal intensity. The blue light was turned off, and saturating light pulses were added to follow state transitions. After adding DCMU, continuous actinic light was switched on, and F_m was determined. The photosynthetic parameter F_v/F_m (C) was calculated from the lowest fluorescence in the dark and the highest fluorescence after adding DCMU in the light. Experimental error bars indicate the means ±SDs of 4 (**H**) or 6 (**L**) biological replicates. Significant differences (two-sample t-test) are indicated as: * $p < 0.05$; ** $p < 0.01$; *** $p < 0.001$. The measurements were performed in cooperation with [redacted].

observed when saturating light pulses were given were higher when *Synechocystis* cells were grown under **L** conditions. In addition, decreasing peak intensities were observed after switching off the blue light and giving saturating light pulses, indicating state transitions when cells were grown under **H** conditions. Changes between the initial fluorescence signal and the fluorescence signal under blue light illumi-

nation without the addition of saturating pulses were not observed under Mg^{2+} deficiency.

4.1.1.8. The effective quantum yields of PSI (Y(I)) and PSII (Y(II)) were altered

As the maximum quantum efficiency of PSII was lower when cells were grown under **L** conditions, next, the efficiencies of light utilisation of the PSs under different light conditions were examined (Genty *et al.* 1989). Therefore, the effective quantum yields of the PSs were measured after adaption to different light intensities. The efficiency of PSI and PSII energy conversion was measured simultaneously using a Dual-PAM-100 routine (Klughammer *et al.* 2008; Pfündel *et al.* 2008). In agreement with the observed changes in the PSI-to-PSII ratio and changes in the fluorescence yield parameter, a significant decrease in PSII quantum yield (Y(II)) (Figure 4.1.11 A), accompanied by a simultaneous increase in the PSI quantum yield (Y(I)) (Figure 4.1.11 B left **H**, right **L**) was observed. Y(I) is reduced by non-photochemical energy dissipation of the PSI reaction centres due to electron shortage at the donor side (Y(ND)) or due to a shortage of electron acceptors (Y(NA)) (Klughammer *et al.* 2008; Pfündel *et al.* 2008). The increase in Y(I) when cells were

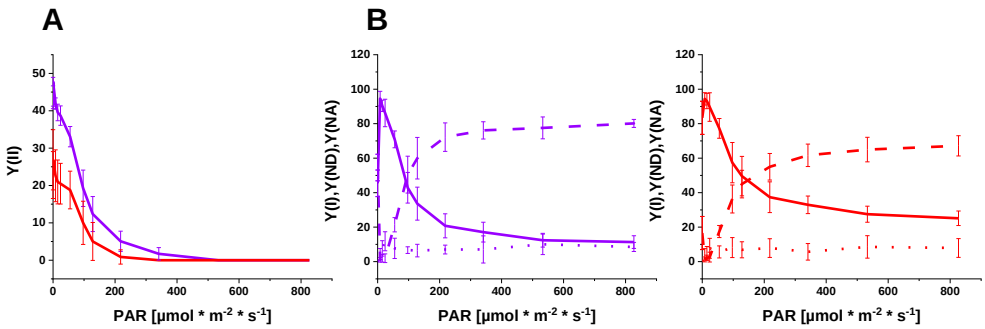

Figure 4.1.11: The effective quantum yields of PSII Y(II) and PSI Y(I).
(A) Y(II) of PSII when *Synechocystis* cells were grown under **H** (purple) or **L** (red) conditions. Y(II) appeared significantly lower at **L** conditions.(B) Y(I) (solid line), Y(ND) (dashed line) and Y(NA) (dotted line) of PSI of *Synechocystis* grown under high (purple) and low (red) Mg^{2+} conditions. A higher Y(I) at Mg^{2+} limitation was accompanied by a lower Y(ND). Experimental error bars indicate the means ±SDs of 3 (**H**) or 5 (**L**) biological replicates. The measurements were performed in cooperation with [redacted].

grown under **L** conditions was accompanied by a decrease in Y(ND), while no change in Y(NA) was observed (Figure 4.1.11). (By definition, Y(I)+Y(ND)+Y(NA) = 1 (Klughammer *et al.* 2008)).

4.1.1.9. P_{700}^+ re-reduction measurements revealed a faster re-reduction at Mg^{2+} limitation

As the donor side limitation Y(ND) was decreased when cells were grown under **L** conditions, electron transfer from the PQ pool to PSI was examined by measuring P_{700}^+ re-reduction kinetics. Changes in the light-induced P_{700} absorbance depicted the electron transfer between the two PSs. Therefore, absorbance changes were measured at 830 nm, where P_{700} redox changes can be monitored using the broad absorption band of the P_{700}^+ cation radical at 810-830 nm (Inoue *et al.* 1973; Haveman *et al.* 1975; Schreiber *et al.* 1988). The oxidation/reduction pattern of P_{700}/P_{700}^+ showed faster re-reduction of P_{700}^+ when cells were grown under **L** conditions (Figure 4.1.12 A), consistent with the afore-described increased Y(I). To

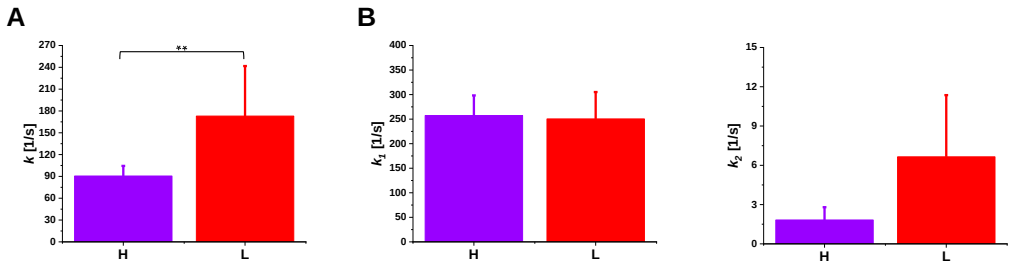

Figure 4.1.12: P_{700}^+ re-reduction kinetics.
The P_{700}^+ re-reduction kinetics were fitted with single exponential decays (A) or double exponential decays (B), and the determined rate constants (k[1/s]) were compared. P_{700}^+ re-reduction was faster when cells were grown under Mg^{2+} limitation. Experimental error bars indicate the means ±SDs of A, n=10(**H**) and n=5(**L**) and B, n=5 (**H**) and n=6 (**L**) biological replicates. Significant differences (two-sample t-test) are indicated as: * $p < 0.05$; ** $p < 0.01$; *** $p < 0.001$. The measurements were performed in cooperation with [redacted].

finally estimate the impact of cyclic electron flow on the overall PSI re-reduction kinetics, DCMU was added to the cells, which blocks PSII and thereby the linear electron flow. Although measurements with DCMU showed a faster k_2 (Figure 4.1.12 B), this was not statistically significant due to high SDs.

4.1.1.10. The ΔpH across *Synechocystis* membranes changes in response to Mg^{2+} limitation

Since both PSs were affected to some extent by the depletion of Mg^{2+}, it was finally analysed how the generation of the PMF was influenced across the TM. During photosynthesis, electron transport is accompanied by a trans-thylakoid H^+ translocation. First, protons are released into the lumen by water oxidation at the OEC. In addition, both linear and cyclic electron flow are accompanied by transmem-

brane proton transfer from the cytoplasm to the lumen. Furthermore, there is also light-dependent proton pumping at the PM. Thus, during the photosynthetic light reaction, alkalisation of the cytoplasm is caused not only by protons pumped into the thylakoid lumen but also by proton extrusion into the surrounding medium (Nitschmann *et al.* 1985; Peschek *et al.* 1985). The fluorescent dye AO, which already gave stable results in previous studies aiming at determining pH gradients across *Synechocystis* membranes, was used (Teuber *et al.* 2001; Berry *et al.* 2003; Checchetto *et al.* 2012; Miller *et al.* 2021). In brief, samples were buffered at pH 8 and incubated in the dark with AO for 15 min. Then AO fluorescence changes during a light-dark-light routine were monitored over 10 min to observe changes corresponding to the sample's acidification (decrease) or alkalisation (increase). After measuring AO fluorescence in the dark for 180 s, actinic light was switched on, followed by a rapid decrease in fluorescence signal. Subsequently, a slower biphasic increase was observed, consisting of a rapid increase transitioning into a slower increase until the fluorescence signal reached a plateau at about 350 s. When the light was turned off (480 s), the fluorescence emission rapidly increased again, followed by a slow biphasic signal decrease consisting of a rapid decrease transitioning into a slower decrease (Figure 4.1.13). When *Synechocystis* cells were grown in **L** medium,

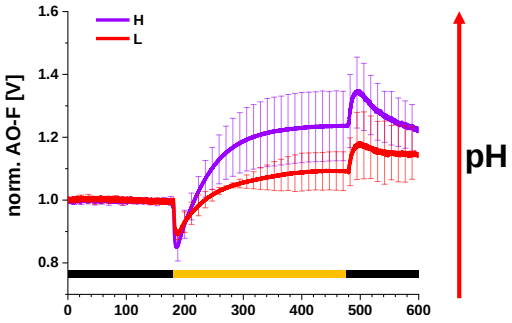

Figure 4.1.13: AO signal traces from *Synechocystis* grown under H (purple) or L (red) condition.
The cells were dark-adapted for 15 min before the measurements. After measuring fluorescence in the dark for 3 min, fluorescence changes were monitored upon exposing the cells to actinic light for 5 min. Changes in fluorescence were measured for 2 more min upon switching off the actinic light. Experimental error bars indicate the means ±SDs of n=15 (**H**) or n=4 (**L**) biological replicates. The measurements were performed in cooperation with [redacted].

the overall shape of the AO fluorescence emission trace was similar to the signal of cells grown under **H** conditions. However, altered AO fluorescence intensities were observed when cells were grown under **L** conditions compared to **H** conditions. These were a less pronounced signal decrease upon turning on the light, a lower plateau in the light, and a less pronounced signal decrease after turning off the light (Figure 4.1.13). Thus, reducing the amount of available Mg^{2+} apparently affects the

generation of a ΔpH across *Synechocystis* membranes.

4.1.2. Discussion

4.1.2.1. *Synechocystis* is able to grow at low Mg^{2+} concentrations

Mg^{2+} is vital for the normal growth and development of cyanobacterial cells. Consequently, growing *Synechocystis* cells in medium with reduced Mg^{2+} content (compared to standard BG11 growth medium) (Figure 4.1.1) resulted in a prolonged lag phase, and the cultures grown at Mg^{2+} concentrations below 30 µM no longer reached wt saturation levels during the observation time. Nevertheless, the cells could adapt to Mg^{2+} concentrations as low as 10 µM. The ability to adapt to very low Mg^{2+} concentrations was previously observed for the cyanobacterium *S. elongatus*, which can grow with only 5 µM Mg^{2+} (Utkilen 1982). The observed prolonged lag phase in *Synechocystis* cells under very low Mg^{2+} concentrations suggests that the cell metabolism adjusts to achieve adequate growth (Bertrand 2019). Since the growth of *Synechocystis* was little affected in medium containing 50 µM Mg^{2+}, this concentration was used in all further measurements. In several non-photosynthetic bacteria, Mg^{2+} limitation affects cell division (Webb 1951; Brock 1962). And also, the cyanobacterium *S. elongatus* formed "filamentous" cells under very low Mg^{2+} conditions, which were three to four times the "normal" length (Utkilen 1982). This was not observed with *Synechocystis*, indicating that the Mg^{2+} concentration was still high enough in the experiments not to affect cell division. While cell division was fairly unaffected when cells were grown under **L** conditions, the cells clearly had an enlarged EPS layer (Figure 4.1.2). Enhanced EPS production was also observed in the cyanobacterium *Cyanospira capsulata* in Mg^{2+} deficiency (De Philippis *et al.* 1991). Also *Pseudomonas aeruginosa* responds to Mg^{2+} limitation with the formation of a biofilm (Mulcahy *et al.* 2011), and a thick mucilaginous layer was observed around *Synechocystis aquatilis* f. *aquatilis* cells after Zn^{2+} exposure (De Magalhães *et al.* 2004). Thus, the enlarged EPS layer observed in *Synechocystis* under low Mg^{2+} conditions could be a protection mechanism to prevent metal poisoning. It is known that EPS play a role in chelating heavy metals, such as Co^{2+} (De Philippis *et al.* 2011), which in turn compete with Mg^{2+} for the Mg^{2+} channels binding sites (Nelson *et al.* 1971). This is of particular importance since decreasing the Mg^{2+} concentration in the growth medium could lead to competition between Mg^{2+} and Co^{2+} for the binding sites of the Mg^{2+} channel since both ions are transported by the well-known bacterial Mg^{2+} channels CorA (Affinity [µM] Mg^{2+}: 10-15; Co^{2+} 20-30 (Maguire 2006)) and MgtE (Affinity [µM] Mg^{2+}: 50; Co^{2+}: 80 (Maguire 2006)).

Additionally, in cyanobacteria, the formation of exopolysaccharides in biofilms is connected to the ability to cope with changing environmental conditions (Pereira *et al.* 2009; De Philippis *et al.* 2011; Rossi *et al.* 2015), and, in line with this, an increased formation of EPS was here observed in the EM images under Mg^{2+} deficiency stress (Figure 4.1.2). Furthermore, the chelation of metals in the EPS layer could help *Synechocystis* to accumulate and concentrate Mg^{2+} in its immediate environment under low Mg^{2+} conditions, as it has been suggested that the accumulation of Fe^{2+}/Fe^{3+} and Mn^{2+} in the polysaccharide capsule of *Microcystis flos-aquae* C3-40 may play a nutritional role (Parker *et al.* 1996). Although cells were surrounded by a huge EPS layer when grown under **L** conditions, the amount of total carbohydrates was unchanged. Therefore, the increased number of cells per mL at low Mg^{2+} concentrations when adjusting culture densities to the same OD_{750} (Figure 4.1.3) was probably due to a decreased intracellular density, as seen in EM images of cells grown under **L** conditions (Figure 4.1.2). The lower intracellular density was accompanied by a lower Chl *a* content at Mg^{2+} limitation (Figure 4.1.4 and 4.1.5) as also observed in the algae *Botryococcus braunii* when grown with $\sim$ 15 µM Mg^{2+}, where the Chl *a* content decreased with a concomitant 2.3-fold reduction in the biomass absorption coefficient (Giraldo *et al.* 2021).

4.1.2.2. Mg^{2+} limitation results in altered cell pigmentation accompanied by a reduced amount of PSI and changed energy distribution between PSI and PSII

The estimated Chl *a* content per cell was significantly lower in the cells grown under Mg^{2+} depletion compared to **H**-grown cells (Figure 4.1.4 and 4.1.5). This is a common phenomenon observed under Mg^{2+} limiting conditions in plant chloroplasts (Kobayashi *et al.* 2015) and even Chl *a* breakdown has been observed in rice to remobilise Mg^{2+} under low Mg^{2+} conditions (Peng *et al.* 2019). Low Chl *a* levels under Mg^{2+} depletion have also been observed for algae (Finkle *et al.* 1953; Ben Amor-Ben Ayed *et al.* 2015; Volgusheva *et al.* 2015; Giraldo *et al.* 2021) and in cyanobacteria (Utkilen 1982). Mg^{2+} limitation resulted in a lowered PSI:PSII ratio as judged by 77K spectra (Figure 4.1.6 A). While the number of PSII did not significantly change, the number of PSI decreased (Table 4.1.1). This has also been proposed (Hermans *et al.* 2004) and observed in plants (Farhat *et al.* 2015), and a specific reduction of PSI appears to be especially reasonable in *Synechocystis* at conditions where the formation of Chl *a* is impaired, as PSI needs about 100 molecules of Chl *a* (Jordan *et al.* 2001) whereas PSII binds only about 35 molecules (Umena *et al.* 2011). The intracellular Mg^{2+} concentration and its transport are tightly regulated, and

as free Mg^{2+} is involved in diverse cellular processes, its level is of special relevance (Maguire 1990). Thus, it is likely that the overall Chl *a* concentration decreased to keep the total free Mg^{2+} in a physiological range. While the cellular Chl *a* content decreased significantly, the number of total Car was only slightly lower under Mg^{2+} depletion. Thus, the overall Chl *a*:Car ratio was lower (Figure 4.1.4 B and 4.1.5 C). The lower Chl *a*:Car ratio might indicate oxidative stress since carotenoids provide protection against oxidative damage (Steiger *et al.* 1999; Zakar *et al.* 2016). In addition to an altered Chl *a*:Car ratio, the PC:Chl *a* ratio increased when cells were grown under **L** conditions (Figur 4.1.4 C). The altered pigment contents and ratios influenced the energy distribution between the two PSs, as observed in the 77K fluorescence emission spectra. 77K spectra after exciting PBS at 580 nm revealed an enhanced fluorescence at 685 nm and 695 nm compared to the signal at 725 nm (Figure 4.1.6 B), indicating that PBSs were bound to PSII. This is conceivable since the amount of PC:Chl *a* ratio was increased under Mg^{2+} depletion as judged from the absorption spectra (Figure 4.1.4 C), the PSI amount was decreased (Table 4.1.1), and the antenna size of PSI is rather unchanged under various light conditions (Hihara *et al.* 1998). Also, there seemed to be a difference in the ratio of the peak at 685 nm (CP43 and CP47) and the peak at 695 nm (CP47) that could indicate a favoured energy transfer *via* CP43 to PSII reaction centres or indicate immature PSII (Boehm *et al.* 2011; Spät *et al.* 2018). As CP47 binds more Chl *a* than CP43 (Guskov *et al.* 2009), the lower peak at 695 nm compared to the peak at 685 nm could also be due to the limitation of Chl *a*. A high intensity at 685 nm under **L** conditions could also be related to unbound PBSs and signals from the terminal emitter (Kłodawska *et al.* 2020). When PBSs are uncoupled or PC is not incorporated into PBSs, their excitation results in fluorescence emission at 650–665 nm (Luimstra *et al.* 2018). Since no signal increase was observed in this nm range when PBSs were excited after growth at Mg^{2+} depletion (Figure 4.1.6 B), it seems plausible that the higher signal at 685 nm is not or is not only a result of uncoupled PBS. Also, the iron stress-induced protein (IsiA) could be involved. Expression of the *isiA* gene under iron stress was first reported in 1988 (Laudenbach *et al.* 1988), and the encoded protein was, as it is a homolog of CP43, also called CP43' (Burnap *et al.* 1993). IsiA is involved in energy quenching (Ihalainen *et al.* 2005), and a supercomplex of a trimeric PSI surrounded by a ring of 18 IsiA subunits was identified in *Synechocystis* (Bibby *et al.* 2001). When IsiA is expressed, 77K fluorescence emission spectra excited at 430 nm have a higher peak at $\sim$ 685 nm (Bibby *et al.* 2001; Ma *et al.* 2017). Still, this seems unlikely since no iron stress was

induced.

4.1.2.3. A more reduced PQ pool at Mg^{2+} limitation influences the activity of both PSs

The decreased Chl *a* content per cell that was accompanied by a decreased PSI content per cell and an altered energy distribution between the two PSs influenced the electron transport in *Synechocystis*. My attempts to measure induction curves led to the difficulty that measuring F_o (minimal fluorescence, PQ pool oxidised (Ogawa *et al.* 2016; Ogawa *et al.* 2017)) under low-intensity blue light was not possible when cells were grown under **L** conditions. The signal increased under blue light when cells were grown under **H** conditions, indicating a transition to state I (Schreiber *et al.* 1995) (Figure 4.1.10 A). The gradual signal decrease during the application of saturating light pulses after switching the blue light off indicates a transition back to state II (Schreiber *et al.* 1995). Despite the fact that changes in the signal intensity upon the application of saturating light pulses could be observed when blue light was switched on and off it was not possible to distinguish between different signal intensities without light pulses when cells were grown under **L** conditions (Figure 4.1.10 B). Since the PSI:PSII ratio was changed, blue light could have excited both PSs to a similar extent, and therefore, would not induce transition to state I. Because of this, the lowest fluorescence value after dark adaption F_o (Campbell *et al.* 1998) and the highest fluorescence value under actinic light exposure in the presence of DCMU were used for F_v/F_m calculations. Calculation of F_v/F_m revealed a slightly lower PSII activity at Mg^{2+} limitation (Figure 4.1.10 C). It has already been shown for plants that the F_v/F_m value can be reduced under Mg^{2+} deficiency (Hermans *et al.* 2004; Tang *et al.* 2012; Yang *et al.* 2012; Jamali Jaghdani *et al.* 2021), and a decreased F_v/F_m is indicative of any type of stress or photoinhibition associated with PSII (Maxwell *et al.* 2000; Murchie *et al.* 2013). The F_o level was higher when cells were grown under **L** conditions compared to **H** conditions (Figure 4.1.10 A, B). The initial fluorescence signal determined after dark adaption provides information about the amount of reduced Q_A. Highly reduced Q_A leads to more recombination fluorescence, a process by which electrons in PSII are transferred back from $Pheo^-$ to $P_{680}{}^+$ (Schreiber 2004), and hence a higher initial signal. This could be the case if the PQ pool was more reduced in the dark when cells were grown under **L** conditions, consistent with the reduced PSI content. Additionally, it has been observed in *Synechococcus* sp. PCC 7942 that a high PC:Chl *a* ratio results in a higher F_o (Campbell *et al.* 1996). In O_2 evolution measurements, the

strongest observed effect was less O_2 consumption under **L** conditions, while the O_2 evolution was only slightly lowered (Figure 4.1.7). It has been shown for mitochondria that Mg^{2+} limitation induces mitochondrial oxidative stress and dysfunction (including ETC) (M. Liu *et al.* 2020). It cannot be ruled out that the PMs ETC in cyanobacteria is affected to some extent. In line with this is the unchanged amount of total carbohydrates per cell in Mg^{2+} deficiency. The EPS layer is formed from polysaccharides, which in *Synechocystis* consists of up to 12 different monosaccharides (Pereira *et al.* 2009). A high proportion of total carbohydrates measured could be caused by the huge layer of EPS, and as a result, the cell might have a lower proportion of glucose available for respiration. While the O_2 evolution was almost unchanged, the estimation of the effective quantum yields of PSI Y(I) and PSII Y(II) showed that the activity of both PSs was affected by Mg^{2+} limiting conditions, yet, to different extents. I observed a decrease in the effective PSII quantum yield Y(II) (Figure 4.1.11 A). This has also been reported for Barley chloroplasts when Barley was grown under Mg^{2+}-limiting conditions (Jamali Jaghdani *et al.* 2021) and it has been suggested that the PSII activity is lowered under Mg^{2+} deficiency due to oxidative damage (Jamali Jaghdani *et al.* 2021). A reduced activity of PSII was also observed in the cyanobacterium *Arthrospira platensis* Gomont 1892 when grown at low Mg^{2+} concentrations (Urek *et al.* 2019). Since the amount of PSII seemed unchanged (Table 4.1.1), the decrease in Y(II) was mainly a result of a reduced PSI content and a thereby more reduced PQ pool. The suggested more reduced PQ pool at low Mg^{2+} concentrations is in line with the observation that the difference between the first value of Y(II) (Figure 4.1.11 A) and F_v/F_m (Figure 4.1.10 C) is more pronounced when cells were grown under **L** conditions. This suggests that DCMU used for estimating F_m in the induction curve measurement led to a more pronounced state I transition when cells are grown under **L** conditions. The simultaneous increase in the effective quantum yields of PSI Y(I) under **L** conditions (Figure 4.1.11 B) was mainly due to a decrease in Y(ND) which is consistent with the change in PSI:PSII ratio and a more reduced PQ pool. A lower Y (ND) can be accompanied by an overall lower ΔpH (Zivcak *et al.* 2015) across the membrane, which can be suggested by the lower AO signal during illumination in the AO measurements (Figure 4.1.13). A lowered ΔpH leads to fast $P_{700}{}^+$ re-reduction kinetics as an increase in electron transport with a simultaneous decrease in ΔpH can also be observed when using an uncoupler (Evron *et al.* 2000). Thus, the faster $P_{700}{}^+$ re-reduction (Figure 4.1.12 A) under Mg^{2+} limiting growth conditions resulted from a higher Y(I) due to less donor side limitation as the number of PSI was decreased

(Table 4.1.1) and a decreased ΔpH. To investigate the cyclic electron flow around PSI, P_{700}^{+} re-reduction kinetics after the addition of DCMU were analysed. There was a trend towards faster k_2 at Mg^{2+} limitation, or at least higher variability, but based on the SDs, the differences were not statistically significant (Figure 4.1.12 B). Less or variable CEF can indicate an increased ATP requirement as CEF is needed to utilise the appropriate NADPH/ATP ratio for a functioning CBB cycle (J. F. Allen 2003; Alric *et al.* 2010).

4.1.2.4. Mg^{2+} deficiency led to a lower ΔpH across *Synechocystis* membranes

Since growth at Mg^{2+} limitation affected the photosynthetic machinery, as obvious from a lower maximal PSII quantum yield, a lower effective quantum yield of PSII, as well as an increased effective quantum yield of PSI, it was likely that the formation of a pH gradient across *Synechocystis* membranes was altered. When monitoring light-induced changes of the ΔpH across the *Synechocystis* membranes, distinct changes were observed (Figure 4.1.13). The slightly less pronounced signal decrease upon switching the light on observed when cells were grown under **L** conditions compared to **H** conditions was consistent with a reduced PSII activity Y(II) (Figure 4.1.11 A) when cells were grown under **L** conditions. The difference in signal decrease also provides a possible answer to the question as to which terminal oxidases are more affected by Mg^{2+} limitation. If the TOs of the TM were less active when cells were grown under **L** conditions, one would expect a more pronounced decrease in signal since the thylakoid lumen would be less acidified in the dark (Miller *et al.* 2021). Since the difference in signal decrease was only minor, and the amount of PSII was unchanged under both growth conditions, the observed results strongly suggest that the decreased PSII activity observed when cells were grown under **L** conditions was responsible for the observed changes. In AO measurements with a SynK (a *Synechocystis* predominantly TM-localised potassium channel) KO mutant, the decrease in AO fluorescence was less pronounced when the light was switched on (Checchetto *et al.* 2012). During the formation of a pH gradient across TMs in the light, the electric potential generated by the photosynthetic electron chain is balanced by the release of Mg^{2+} and K^{+} from the lumen and the uptake of Cl^{-} into the TM lumen (Dilley *et al.* 1965; Hind *et al.* 1974; Chow *et al.* 1976; Lyu *et al.* 2017). As a result, when cells were grown under **L** conditions, altered Mg^{2+} concentrations in the cytoplasm and/or lumen may impair proton flux across the TM. This has been observed in the SynK KO mutant, where decreased proton influx into the TM lumen was caused by impaired K^{+} transport. Therefore, in addition

to the somewhat lowered activity of PSII, impaired Mg^{2+} flux across the TM could also result in reduced AO quenching when cells were grown under **L** conditions. The subsequent increase in signal, after the initial drop, when the light was turned on, was the most dramatically affected part of the signal when comparing cells grown under **H** versus **L** conditions. Cells grown under **L** conditions reached only half the signal levels of cells grown under **H** conditions. The light-induced alkalisation of the cytoplasm is achieved by proton pumping at the TMs ETC and by proton extrusion at the PM (Teuber *et al.* 2001). Reduced activity of PSII (Figure 4.1.11 A), as well as impaired respiration (Figure 4.1.7), could have led to less alkalisation of the cytoplasm under **L** conditions. The reduced activity of PSII and the reduced PQ pool accompanied by less PSI might have resulted in less NADPH reduction at PSI and less ATP generation. Because the periplasm was buffered at pH 8, the influx of protons from the periplasm into the cytoplasm was limited to a minimum, so the observed slow acidification after the fast signal rise observed when the light was turned off could not result in a complete signal recovery to the starting AO fluorescence intensity. The slow acidification (signal decrease) observed in the dark reflects the consumption of redox equivalents in the dark (Teuber *et al.* 2001). Many enzymes of the CBB cycle require both the limited Mg^{2+} as a cofactor and alkalisation of the lumen for proper function (Lorimer *et al.* 1976; Flügge *et al.* 1980; Mott *et al.* 1986). As a result, both the possibly lower NADPH and ATP levels and an impaired CBB cycle may have resulted in slower acidification when the lights were switched off under **L** conditions. The fast AO fluorescence increase observed when the light was switched off is mainly due to a rapid decrease in acidification of the cytoplasm due to stopped water splitting at PSII. Comparing the fast signal decrease when the light is switched on with the fast signal increase when the light is switched off provides some information about the PSII activity throughout the light period. The signal increase was slightly less intense when cells were grown under **L** conditions. But compared to the signal increase when the light was switched on, the difference was less strong as observed for cells grown under **H** conditions. Thus, the difference in PSII activity appears to be less pronounced in cells grown under **L** conditions compared to cells grown under **H** conditions. In order to differentiate between effects caused directly by the Mg^{2+} limitation and effects of altered Mg^{2+} fluxes across membranes, possible Mg^{2+} channels in the membrane were examined for their function (see section 4.3). In addition, measurements with different electron transport chain inhibitors were performed to understand the AO fluorescence signal better (see section 4.2).

4.1.2.5. Conclusion

Mg^{2+} limitation leads to decreased Chl *a* levels and impaired photosynthetic apparatus function in the cyanobacterium *Synechocystis* sp. PCC 6803. In detail, I observed a reduced maximum quantum yield and a reduced effective quantum yield of PSII. The reduced PSI content per cell was in line with an increased effective quantum yield of PSI and a faster $P_{700}{}^{+}$ re-reduction. A lower pH gradient across *Synechocystis* membranes accompanied these changes. In addition, Mg^{2+} limitation leads to significant changes in the cell morphology, which could contribute to a changed ion concentration in the cell's environment. Whether these changes are due to altered Mg^{2+} fluxes across the membranes or reflect the reduction of intracellular Mg^{2+} requires further investigation. Therefore, the involvement of three predicted Mg^{2+} channels was examined (see section 4.3).

4.2. Exploration of the transmembrane proton transfer in *Synechocystis* sp. PCC 6803 using the pH sensitive fluorescent dye acridine orange

AO, like other diamines and monoamines, can be used to monitor pH changes across membranes (Palmgren 1991). As a weak base ($pK_a = 10.5$ for AO (Manente *et al.* 2008)), AO is believed to migrate freely through membranes in its unprotonated form (Palmgren 1991). When a pH gradient is established, it is accumulated in its protonated form on the side of the membrane where the pH is lower (Schuldiner *et al.* 1972; Palmgren 1991; Manente *et al.* 2008). The accumulation of AO leads to an absorption shift due to a metachromatic effect (Palmgren 1991); thus, the acidification can be followed by the signal quenching accompanying the entry of the dye (Manente *et al.* 2008). Despite its limitations in the application (Palmgren 1991), AO fluorescence can provide valuable data on the build-up of pH gradients across membranes. It has already been used for studying the electron transfer coupled ΔpH formation in cyanobacterial membranes before (Teuber *et al.* 2001; Berry *et al.* 2003; Checchetto *et al.* 2012; Miller *et al.* 2021). The signal response of AO fluorescence to various electron transport chain inhibitors in wt and mts has also been discussed (Teuber *et al.* 2001; Berry *et al.* 2003; Miller *et al.* 2021). In this work, the system introduced by Teuber *et al.* (Teuber *et al.* 2001) to monitor light-induced changes of ΔpH across *Synechocystis* membranes was used (see Section 3.2.4.16). The addition of several ETC inhibitors revealed some insights into processes affecting the AO fluorescence signal.

4.2.1. Results

4.2.1.1. Kinetics of pH gradient build-up across *Synechocystis* membranes

The light-induced generation of a ΔpH across *Synechocystis* membranes was monitored in the absence and presence of inhibitors (Figure 4.2.2). At first, light- and dark-induced changes in the AO fluorescence were recorded using wt without any addition. These measurements served as a control for subsequent measurements performed in the presence of inhibitors (Figure 4.2.1).

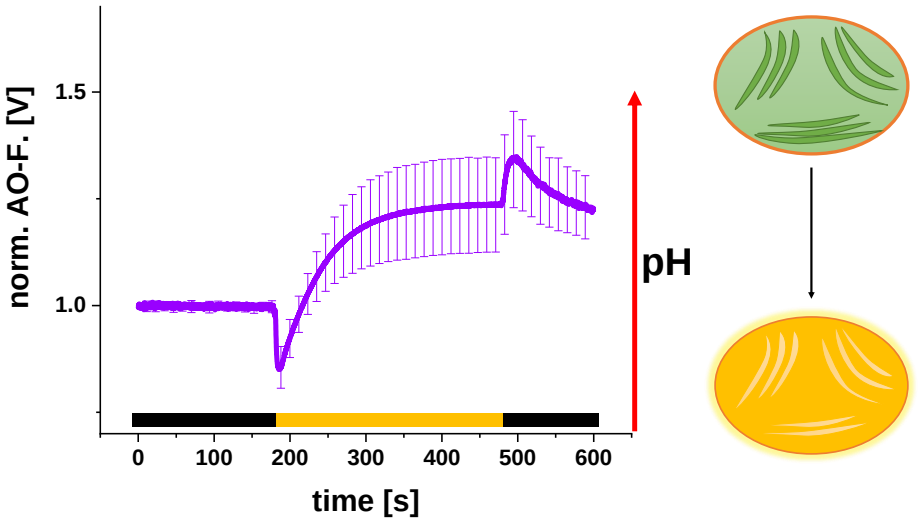

Figure 4.2.1: Light-induced changes of AO fluorescence in whole *Synechocystis* cells.
Left: The AO fluorescence signal response was recorded for ten min along a dark-light-dark pattern as indicated by the colour bar (black-yellow-black) below the plot. Switching on the actinic light resulted in a rapid signal decrease. This was followed by a biphasic increase which ended in a plateau. Switching the light off induced a rapid increase in the signal that was slightly less pronounced than the drop observed when the light was switched on. This was followed by a slower biphasic signal decrease. Right: Schematic representation of the changes in the AO fluorescence intensity upon switching on the actinic light: the intensity of AO fluorescence decreases in the lumen (light yellow) due to acidification, while it increases in the cytoplasm due to alkalisation (dark yellow). Error bars indicate the SDs of n=15 biological replicates. The measurements were performed in cooperation with [redacted].

A rapid decrease in fluorescence signal intensity within s was observed upon switching the actinic light on, followed by a slower biphasic increase over $\sim$ 2 min. Upon switching off the light, the fluorescence rapidly increased again, followed by a slow, apparently biphasic, signal decrease. To better understand the origin of these dynamic changes, comprehensive measurements were performed using selective inhibitors of various electron transport components located either in the TM and/or in the PM.

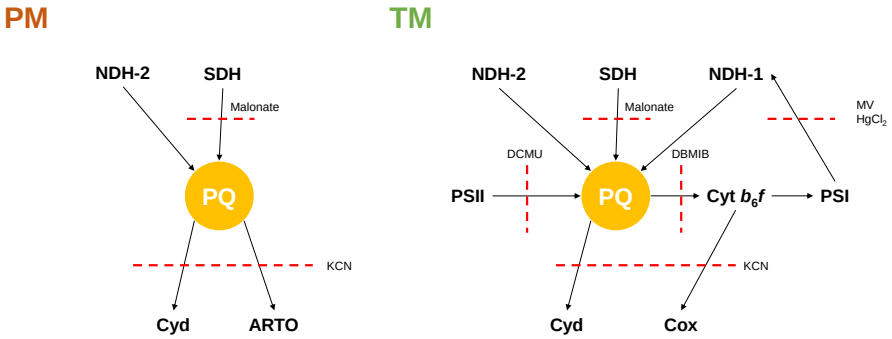

Figure 4.2.2: A schematic representation of the electron transfer pathways in the PM and the TM with sites of action of the used inhibitors.
Sites of action in the PM (left) and the TM (right) of the used inhibitors. While KCN and malonate impair the corresponding electron transport routes in both the PM and TM, DCMU, DBMIB, MV and $HgCl_2$ predominantly block specific electron transport routes in the TM. For a detailed description, see the text.

4.2.1.2. pH changes were largely impaired in the presence of DCMU

First, the contribution of PSII to the formation of trans-thylakoid pH gradient was investigated. This includes the impact of water splitting as well as linear electron flow. The PSII specific inhibitor DCMU (also known as Diuron) was used, which is a well-known algaecide and herbicide. It belongs to the group of phenylurea herbicides and was introduced in 1954 by Bayer. It binds to the Q_B binding site at D1 of PSII, disrupting the linear flow of electrons from PSII to the PQ pool (Metz *et al.* 1986; Mackay *et al.* 1993). The treated cyanobacterial cell is trapped in state I as the PQ pool becomes more and more oxidised, and phycobilisomes are transferred to PSII (Campbell *et al.* 1998). Thereby, the impact of cyclic electron flow on the overall pH changes was investigated (Figure 4.2.3). Upon switching on the light, nearly no signal decrease was observed. The subsequent signal rise was very small and did neither reach control-like AO signal levels (indicating cytoplasmic alkalisation) nor ended in a plateau. Upon switching off the light, no signal increase was observed, and instead of a subsequent signal decrease, the fluorescence stayed at a constant level. I added DCMU in combination with KCN to test which proton pumping component of the (remaining) electron transport network is responsible for the remaining AO fluorescence signal, as terminal oxidases may cause it. In the presence of both inhibitors, electron donation can only occur from the NDH-1, SDH and NDH-2 towards the PQ-pool and then to PSI. No changes in sig-

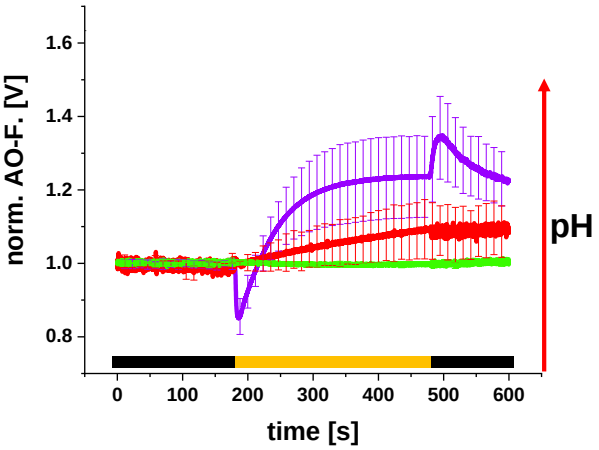

Figure 4.2.3: Changes in the AO fluorescence signal in the presence of DCMU. AO fluorescence signal of wt incubated in the dark with DCMU (red), DCMU and KCN (green) or without inhibitor (purple). When DCMU was in the sample, a regular signal increase was seen, while no signal response was seen after the addition of DCMU and KCN. Error bars indicate the SDs of n=15 (control) or n=3 (DCMU), n=3 (DCMU and KCN) biological replicates. The measurements were performed in cooperation with [redacted].

nal intensity during the dark-light-dark transition were observed after the addition of both, DCMU and KCN.

4.2.1.3. No pH changes were observed after the addition of DBMIB

Next, electron flow through the Cyt b_6f complex was inhibited by DBMIB, which results in a complete reduction of the PQ pool during illumination (Berry *et al.* 2002), and pH changes were monitored by AO fluorescence. DBMIB belongs to the 1,4-benzoquinones and inhibits electron transport between the PQ pool and the Cyt b_6f complex by binding to the Q_o site (quinol oxidation site) of the Cyt b_6f complex (Riedel *et al.* 1995). Thus, it blocks both linear and cyclic electron flow from the PQ pool to PSI. As a result, the PQ pool becomes highly reduced during illumination by electrons generated by PSII, resulting in a transition from state I to state II (Campbell *et al.* 1998). DBMIB can be kept reduced by Na-ascorbate, otherwise, it can act as an electron acceptor of PSII and a fluorescence quencher (Berry *et al.* 2002). When DBMIB was present (Figure 4.2.4), a small signal increase was observed upon switching the light on that continued in the dark. While luminal acidification was not observed, electrons could, in principle still be transported from the PSII *via* the PQ pool to Cyd in the presence of DBMIB. When DBMIB and KCN were added to wt cells in combination, electron release from PSII was fully inhibited as the PQ pool could not release any electrons to the terminal oxidases. No further signal changes compared to the signal with DBMIB were observed.

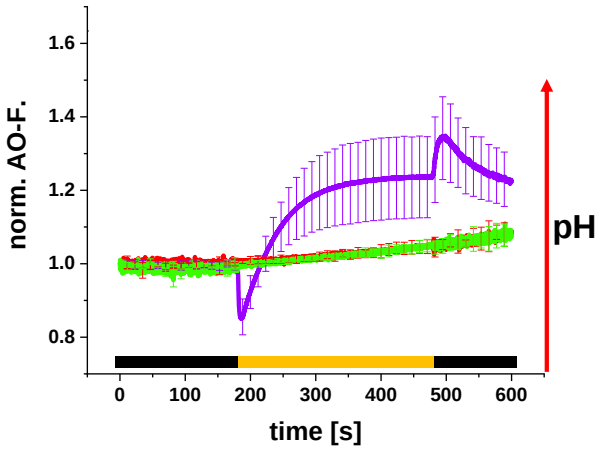

Figure 4.2.4: Changes in the AO fluorescence signal in the presence of DBMIB. AO fluorescence signal changes of wt cells incubated in the dark with DBMIB (red), DBMIB and KCN (green) or without inhibitor (purple). A slight signal increase was observed after the addition of DBMIB and DBMIB in combination with KCN. Error bars indicate SDs of n=15 (control), n=3 (DBMIB) or n=3 (DBMIB and KCN) biological replicates. The measurements were performed in cooperation with [redacted].

4.2.1.4. The SDH inhibitor malonate led to a lower AO signal in the light

In *Synechocystis*, SDH has the largest capacity to feed (respiratory) electrons into the PQ pool compared to NDH-1 and NDH-2 (Cooley *et al.* 2001). Therefore, to elucidate the influence of respiratory electron donation to the PQ pool on the formation of pH gradient across membranes, malonate was added to the sample at the beginning of a 15 min (dark) incubation period. Due to its chemical nature, malonate is a competitive inhibitor of succinate dehydrogenase (Quastel *et al.* 1928; Krebs *et al.* 1938). As SDH participates in the electron transfer processes across the PM and the TM (Lea-Smith *et al.* 2016) at a remarkable level, much fewer electrons are transferred to the PQ pool *via* the respiratory electron transport chain in the presence of malonate. Moreover, SDH is also a key enzyme in the citric acid cycle (Krebs *et al.* 1937). Therefore, in the presence of malonate, major changes in the pattern of AO fluorescence transitions are expected upon switching on and off the actinic light. These changes may reflect changes in the electron transfer processes within the thylakoid and plasma membrane, as well as metabolic changes that could alter the background signal. Figure 4.2.5 shows the formation of ΔpH in *Synechocystis* in the absence or presence of malonate followed by AO fluorescence.

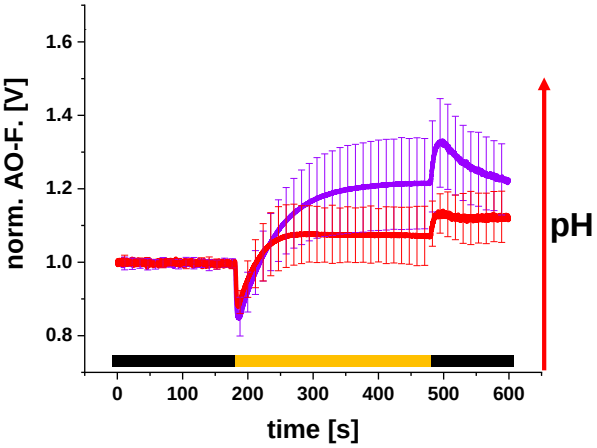

Figure 4.2.5: Changes in the AO fluorescence signal in the presence of malonate. The AO fluorescence signal of the wt after dark incubation with (red) or without malonate (purple). The signal after the addition of malonate deviated over the whole curve. In the presence of malonate, the AO signal decreased less as compared to the control and, later, reached a much lower plateau. Additionally, upon switching the light off, signal changes were less intense. Error bars indicate the SDs of n=15 (control) or n=4 (malonate) biological replicates. The measurements were performed in cooperation with [redacted].

After the addition of malonate, a less pronounced signal decrease upon switching on the light was observed. This was followed by a subsequent rise, which was initially somewhat faster compared to the control but reached a much lower plateau, indicating a less pronounced cytoplasmic alkalisation. The signal rise upon switching the light off was also less pronounced. The following phase was still biphasic but less intense than the control.

4.2.1.5. Addition of the electron acceptor MV led to a higher AO signal in the light

In cyanobacteria, SDH-mediated electron transport reduces the PQ pool in both PM and TM and thus contributes to cytoplasmic alkalisation and the formation of a ΔpH in the dark (Cooley *et al.* 2001). MV (also known as paraquat) effectively captures electrons from both PSI and Fd *in vivo* (Patrick Fuerst *et al.* 1991; Sétif 2015) and was therefore used to inhibit cyclic electron flow around PSI (Yu *et al.* 1993). Furthermore, since MV accepts electrons and transfers them to molecular oxygen, reactive oxygen species are produced in the reaction (Asada 2006). The results obtained by MV addition are shown in Figure 4.2.6. Upon switching on the actinic light, a rapid decrease in fluorescence signal intensity that seemed slightly more pronounced compared to the control was observed. This was followed by a fluorescence increase, resulting in a higher fluorescence signal without reaching a plateau. Upon switching off the light, the fluorescence signal rapidly increased again,

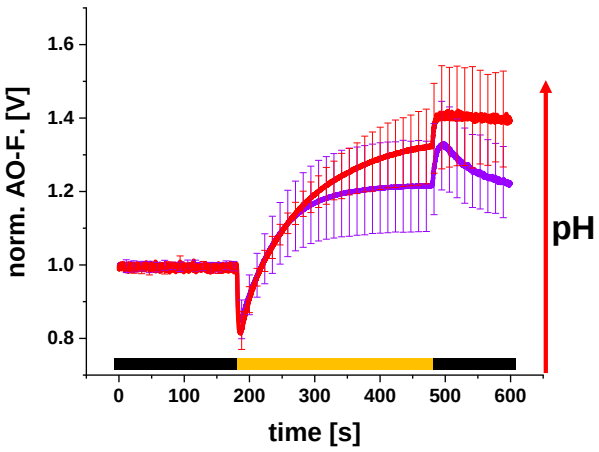

Figure 4.2.6: Changes in the AO fluorescence signal in the presence of MV. The AO fluorescence signal of wt cells incubated in the dark with (red) or without MV (purple). The signal deviated mainly from the curve's middle section after adding MV. It reached higher values and almost stayed at this level when the light was switched off. Error bars indicate the SDs of n=15 (control) or n=4 (MV) biological replicates. The measurements were performed in cooperation with [redacted].

but to a lesser extent than observed in the control. The subsequent fluorescence decrease was essentially missing, in contrast to the cells without MV.

4.2.1.6. $HgCl_2$ led to a lower AO signal in the light

Like MV, $HgCl_2$ affects the reduction and protonation of $NADP^+$. Therefore, its impact on pH and hence on the AO fluorescence signal was monitored using AO fluorescence to compare the effects of the two inhibitors. $HgCl_2$ affects NDH-mediated cyclic electron flow around PSI (Mi *et al.* 1992a; Mi *et al.* 1992b; Mi *et al.* 2000). This is rather unrelated to the function of NDH (the one mutated in M55) (Mi *et al.* 2000); however, $HgCl_2$ blocks $NADP^+$ reduction, possibly by affecting FNR activity, which results in stimulated O_2 reduction (Mi *et al.* 2000). Additionally, it is an inhibitor of PLC, which results in less electron transfer between Cyt b_6f and PSI in chloroplasts (Kimimura *et al.* 1972; Fitzpatrick *et al.* 2022). Plus, $HgCl_2$ inhibits many enzymatic reactions and therefore has several toxic effects on the cell. For example, in plants, Hg^{2+} strongly inhibits PSII (Patra *et al.* 2000). Furthermore, $HgCl_2$-treated cyanobacterial cells are shifted from state II to state I (Ivanov *et al.* 2006). Figure 4.2.7 shows the formation of the ΔpH, followed by AO fluorescence, in *Synechocystis* cells in the absence and presence of $HgCl_2$. Upon switching the light on, a signal decrease comparable to the control was observed (Figure 4.2.7). The subsequent signal increase did not reach a plateau but rather ended in a second signal increase and did not reach control-like AO signal intensities. The signal decrease upon switching the light off had two components, a short decay phase that ended in a stable fluorescence intensity.

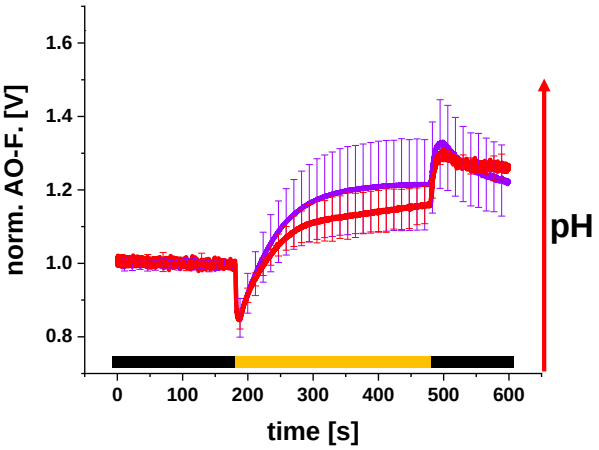

Figure 4.2.7: Changes in the AO fluorescence signal in the presence of mercury chloride.
AO fluorescence signal of wt incubated in the dark with (red) or without $HgCl_2$ (purple). The signal after the $HgCl_2$ addition had a lower plateau in the light but reached almost the same intensity when the light was switched off. The signal decrease was much less pronounced. Error bars indicate the SDs of n=15 (control) or n=3 ($HgCl_2$) biological replicates. The measurements were performed in cooperation with [redacted].

4.2.1.7. Impact of the terminal oxidase inhibitor KCN on the AO signal

Besides exploring the impact of inhibitors of SDH, NDH-1 and NDH-1-mediated cyclic electron flow on the formation of transmembrane pH gradient, signal changes were also examined when the terminal oxidases were inactivated. KCN is a potent inhibitor of complex IV (Keilin 1929; Way 1984),thereby preventing cells from utilising oxygen and generating ATP (Way 1984). Cyanobacteria possess three types of terminal oxidases: Cox, Cyd, and ARTO (Howitt *et al.* 1998; Pils *et al.* 2001; Berry *et al.* 2002), all of which are inhibited by KCN (Pils *et al.* 2001). Cox is more sensitive to KCN than Cyd. However, 100% inhibition of respiratory O_2 uptake in darkness was achieved with 100 µM KCN (Pils *et al.* 2001). Moreover, KCN can remove the copper ion from PLC (Berg *et al.* 1975). Also, KCN inhibits enzymes of the CBB cycle (Wishnick *et al.* 1969). Since KCN blocks the O_2 binding site of the terminal oxidases, electron transfer in the PM's ETC is completely blocked (compare Figure 4.2.2). The ETC in the TM remains functional in the light when PSI and FNR serve as electron acceptors. Two different measurements with KCN were performed (Figure 4.2.8). First, KCN was added during dark incubation, 2 min before measurements ($\rightarrow$ 5 min in the dark). After a 5 min incubation, the rapid decrease in fluorescence was more pronounced compared to the control. The subsequent signal increase was slower, and the signal decreased after about 200 s. Switching off the light resulted in a more pronounced signal increase compared to cells in the absence of an inhibitor, which was not followed by a slow decay, but continued to increase at a slower rate. In the second series of measurements, KCN was

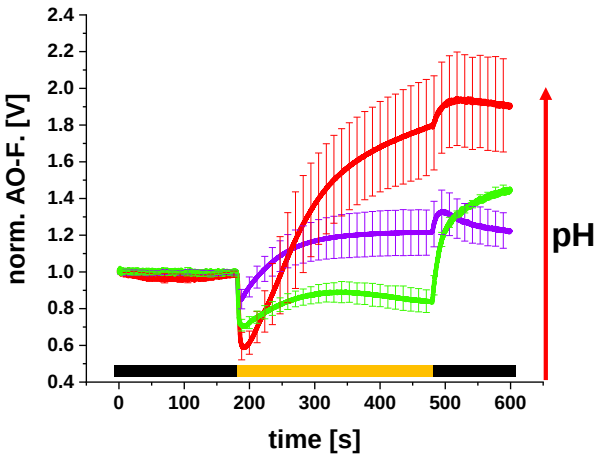

Figure 4.2.8: Changes in the AO fluorescence signal in the presence of KCN. AO fluorescence signal of wt cells incubated in the dark with (5 min (green), 18 min (red)) or without KCN (purple). The signal 5 min after KCN addition differed entirely from the signal after 18 min of incubation. Error bars indicate the SDs of n=15 (control), n=3 (KCN 5 min) or 8 (KCN 18 min) biological replicates. The measurements were performed in cooperation with [redacted].

present in the samples throughout the incubation period (→ 18 min in the dark). The resulting signal differed significantly from that observed after 5 min of incubation. The signal drop was even stronger than after 5 min of KCN incubation, and the signal increase afterwards was twice as high as in the control. Upon switching off the light, the signal increase was less pronounced compared to the control and compared to the strong signal decrease when the light was switched on. In contrast to the 5 min KCN incubation, the signal decreased slowly but without biphasic characteristics.

4.2.2. Discussion

4.2.2.1. Distinct changes in the AO fluorescence upon illumination of *Synechocystis* wt cells reflect changes in the proton translocation across membranes and cellular metabolism

The AO fluorescence signal monitored in the absence of any inhibitor (Figure 4.2.1) served as a control for all measurements performed in the presence of an inhibitor. The rapid quenching of the signal when the light was switched on has been attributed to the acidification of the thylakoid lumen (Teuber *et al.* 2001). In contrast, the subsequent slower signal that reached a plateau indicates alkalisation of the cytoplasm (Teuber *et al.* 2001). Alkalisation of the cytoplasm can occur through proton pumping across the TM into the lumen and/or proton extrusion across the PM into the surrounding medium (Nitschmann *et al.* 1985; Peschek *et al.* 1985; Katoh *et al.* 1996; Sonoda *et al.* 1998; Teuber *et al.* 2001). Upon switching off the light, a rapid signal increase was observed due to the collapse of the ΔpH across the TM (Teu-

ber *et al.* 2001), which is accompanied by the stopping of water splitting at PSII. The subsequent slow signal decrease showed the consumption of energy equivalents (Teuber *et al.* 2001). This signal decrease could be also affected by the dissipation of the pH gradients across the PM and the TM when ions are transferred back across the membranes. Since the periplasm (*i.e.* the medium) was buffered to pH 8, an decrease mainly reflects cytoplasmic re-acidification as a result of the dissipation of ΔpH across the TM. This is in line with an incomplete signal recovery, as only small amounts of protons can enter the cell from the periplasm.

4.2.2.2. PSII activity and linear electron flow are critical for the formation of a pH gradient across *Synechocystis* inner membranes

Since DCMU blocks electron transfer from PSII to the PQ pool, the electrons cannot leave PSII, and no more charge separation at P680 can occur. Therefore, the water splitting machinery of PSII stops and with this oxygen evolution (Campbell *et al.* 1998; Fitzpatrick *et al.* 2022). Thus, no signal decrease was seen when the light was switched on (Figure 4.2.3). This is in agreement with previous data that reported less luminal acidification when cells were illuminated in the presence of DCMU (Miller *et al.* 2021). The following signal increase was much less pronounced and could result from CEF and electrons fed into the PQ pool *via* respiratory processes. This decrease in signal intensity has been reported previously (Miller *et al.* 2021). Upon switching off the light, again, the signal did not change much for several reasons. First the rapid jump is missing because of the missing PSII activity and therefore less luminal acidification. Also the subsequent signal relaxation (cytoplasmic acidification) is missing due to a lack of trans-thylakoid ΔpH. Moreover, as NADPH and ATP production is likely decreased due to an impaired LEF, the postilluminal relaxation by the consumption of redox equivalents does not occur either. It has been shown that NADPH is already oxidised during illumination in the presence of DCMU (Mi *et al.* 2000). After the addition of both, DCMU and KCN, no signal response was observed. This also suggests that the observed minor alkalisation during illumination in the presence of DCMU (LEF is blocked) is rather the result of electron transport in the PM than CEF around PSI.

4.2.2.3. Blocking electron transfer at the Cyt b_6f complex inhibited the establishment of a pH gradient across membranes

DBMIB binds to the Q_o site of the Cyt b_6f complex and, thereby, inhibits the transfer of electrons from the PQ pool to the Cyt b_6f complex (Bauer *et al.* 1974). Thus,

electrons from PSII could only be transferred to Cyd (Berry *et al.* 2002). In the presence of DBMIB, a minor signal increase was observed upon switching on the actinic light, which was not the result of a Cyd-induced alkalisation of the cytoplasm since the signal did not further change when KCN was added (Figure 4.2.4). The activity of Cyd in cells grown photoautotrophically under low light intensities is relatively small (Berry *et al.* 2002). Thus, the electron transfer to Cyd is likely minor under the experimental conditions. However, since the signal continues to increase in the dark, it cannot be ruled out that the slight signal changes observed following the addition of the inhibitor(s) are artefacts.

4.2.2.4. Respiratory electron transfer to the PQ pool highly affects the generation of a ΔpH at *Synechocystis* membranes

Compared to the control, the addition of malonate resulted in a slightly reduced signal decrease upon switching on the light (Figure 4.2.5). In the presence of malonate the electron input from the SDH, and, in turn, by slowing down the TCA cycle also from the NDH-2, was expected to be reduced. Thus, mostly NADPH produced by the oxygenic pentose phosphate way can reduce the PQ pool *via* NDH-1 in the dark. This led to the assumption that the PQ pool is less reduced in the dark in the presence of malonate, as has been shown for an SDH/NDH-2 double mutant (Cooley *et al.* 2001), and hence, the TM lumen is less acidified in the dark. Therefore, a pronounced signal decrease was expected when the light-induced water splitting at PSII started to occur. As contrary a reduced signal decrease was observed, I assume that the acidification of the lumen was about to be maintained by the activity of NDH-1 in the dark. Likewise, the subsequent signal rise did not reach the signal levels of the control cells either. Thus, the reduced electron input at the ETC of both, the TM and the PM likely resulted in less proton translocation into the lumen and the periplasm and therefore in less cytoplasmic alkalisation. Furthermore, an impaired TCA cycle and changed NAD^+/NADH ratios could result in a more acidified cytoplasm compared to the control. The small rapid signal increase (alkalisation of the lumen) when the light was switched off, concurred with the less pronounced decrease (acidification of the lumen) when the light was switched on. Upon switching off the light, a reduced signal decrease, possibly as a result of impaired production/consumption of redox equivalents (as discussed below), was observed.

4.2.2.5. The production and consumption of redox equivalents strongly influences the AO fluorescence signal

The signal pattern observed after adding MV (Figure 4.2.6) revealed a slightly stronger signal decrease when the light was switched on compared to the control. In the dark, NDH-1 can utilise NADPH from the oxidative pentose phosphate way (Ogawa *et al.* 2021), which results in a partial PQ pool reduction. SDH and NDH-2 can also transfer electrons to the thylakoid PQ pool (Cooley *et al.* 2001). Still, it has been observed that MV oxidises the PQ pool in darkness (Sétif 2015), which implies that the electron transfer and with this also the proton translocation across the TM is not as efficiently as without MV. The positive charges within the thylakoid lumen increase the electrical gradient and thus impair the light-induced proton pumping (Checchetto *et al.* 2012; Miller *et al.* 2021), while a reduced proton translocation (less acidified lumen) would lead to a lower electrochemical back pressure. Thus, a less acidified lumen in the presence of MV results in a slightly stronger signal increase when the light is switched on. In contrast, the signal decrease observed when the light was switched on in the $HgCl_2$-treated cells remained unaltered compared to untreated cells (Figure 4.2.7). Therefore, it is likely that the pH in the lumen is comparable to that in the control after the dark incubation. This suggests that the PQ pool can receive electrons unimpeded through SDH, NDH-2, and NDH-1 in the dark when $HgCl_2$ is present. This is consistent with the observation of Mi *et al.* (Mi *et al.* 2000) that the transfer from FNR to NADPH is possibly influenced by $HgCl_2$, which would mainly affect CEF around PSI but might not alter NADPH-dependent PQ pool reduction in the dark. Next, a higher AO signal level in the light was reached after MV treatment (Figure 4.2.6). This result has also been observed with acridine yellow, a pH sensitive fluorescent dye that only reflects the pH of the cytoplasm (Teuber *et al.* 2001). It has been suggested that this resulted from faster linear electron transfer from PSII to PSI due to less acceptor site limitation (Teuber *et al.* 2001). In the same study, another PSI acceptor (ferricyanide) showed the same tendency but much less pronounced (Teuber *et al.* 2001). As $P_{700}{}^{+}$ re-reduction kinetics are not faster after adding MV (Bernát *et al.* 2009), the higher alkalisation might be a result of H_2O_2 production in the cell (Patrick Fuerst *et al.* 1991). In contrast, the lower level of alkalisation during illumination in the $HgCl_2$-treated sample (Figure 4.2.7) possibly indicates less CEF since NDH-1 is highly involved in proton pumping during CEF (Miller *et al.* 2021). Next, a reduced signal increase was observed in the MV-treated cells when the light was switched off (Figure 4.2.6). The signal increase reflects the collapse of the pH gradient across the TM (Teuber *et al.*

2001) and is therefore strongly influenced by the PSII activity. If the signal increase differed from the initial decrease when the light was switched on, this could indicate changes in PSII activity during the illumination period. Therefore, less increase could be a result of the high amounts of singlet oxygen being produced by MV, which could damage PSII and decrease its activity (Krieger-Liszkay *et al.* 2011). The observation of the strong signal rise observed in $HgCl_2$-treated cells when the light was switched off (Figure 4.2.7), might indicate high PSII activity which occurs under $HgCl_2$ treatment (Fitzpatrick *et al.* 2022). The signal decrease observed when the light was switched off was almost missing in the MV-treated sample, likely due to less NADPH and hence, less NADPH consumption. This could be accompanied by less ATP consumption, as the CBB cycle requires a certain NADPH/ATP ratio (J. F. Allen 2002) and ATP accumulation has been observed in chloroplasts under MV treatment (Fitzpatrick *et al.* 2022). Therefore, the signal decrease upon switching the light off was attributed to the consumption of redox equivalents by the CBB cycle (as previously reported by Teuber *et al.* (Teuber *et al.* 2001)). Compared to the MV sample, there appears to be more NADPH and ATP consumption in the $HgCl_2$-treated cells. Still, the less pronounced signal decrease upon switching the light off was probably a result of less NADPH production (Mi *et al.* 2000).

4.2.2.6. The intensity of the AO signal is highly influenced by the terminal oxidases

The pH in the thylakoid lumen is also influenced by the activity of terminal oxidases (Peschek *et al.* 1985), and for this reason, the AO fluorescence signal after the addition of KCN (Figure 4.2.8) was used to observe solely the influence of photosynthetic electron transfer on intracellular pH changes. When the sample was incubated with KCN for 5 min, a strong signal decrease was seen when the light was switched on. This was in line with a less acidified TM lumen, as previously reported by Miller *et al.* (Miller *et al.* 2021). Compared to the control, the subsequent signal increase was much smaller and fell off after about 200 s reflecting less alkalisation of the cytoplasm. Switching the light off resulted in a strong signal increase, consistent with the strong signal decrease when the light was turned on. This signal increase was likely due to the dissipation of ΔpH at the TM and the stopping of water splitting at PSII. The subsequent signal did not decrease as in the control but increased instead. This signal increase could have been due to alkalisation of the cytoplasm *via* proton translocation at the PM since postilluminal acidification of the medium has been also observed under KCN treatment (Sonoda *et al.* 1998). When KCN was present in

the sample throughout the incubation period (18 min prior illumination), the initial drop in the AO fluorescence signal was even more pronounced, suggesting an even less acidified lumen in the dark (Figure 4.2.8). The subsequent signal increase during illumination was much more pronounced compared to untreated cells, probably as a result of an overall more acidified cytoplasm (Sanders *et al.* 1982; Brummer *et al.* 1985; Maduh *et al.* 1990; Ryu *et al.* 2004) before illumination. The postillumination signal increase was less pronounced compared to the control and compared to the strong signal decrease when the light was switched on. This indicates that the PSII activity decreased during illumination, probably as a result of a more reduced PQ pool since the PQ pool cannot be relaxed by TOs. This assumption is in line with an impaired electron transfer within the TM by inhibition of PLC by KCN (Berg *et al.* 1975). After switching the light off, the signal slowly decreased without the biphasic behaviour observed in untreated cells as the proton gradients collapse.

4.2.2.7. Conclusion

Based on the here presented results, it appears to be likely that the signal decrease

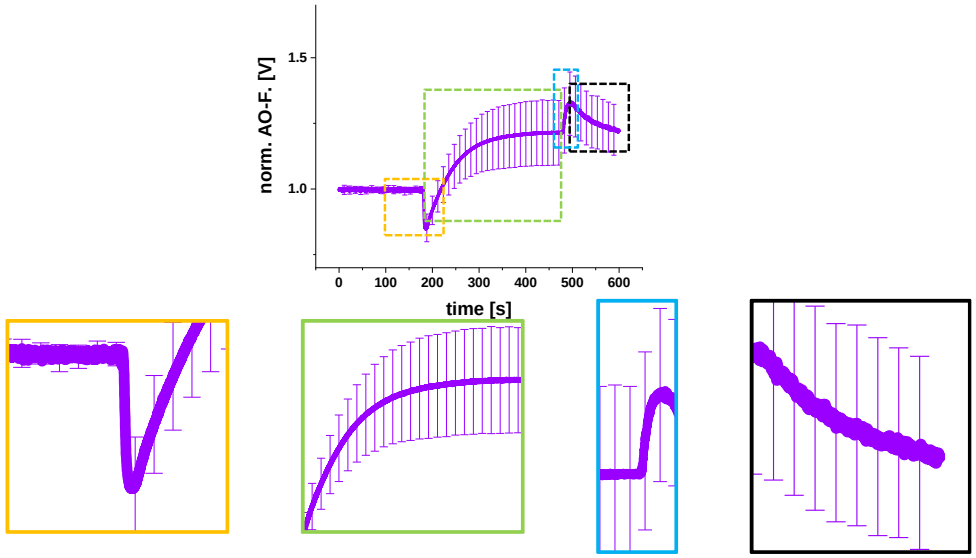

Figure 4.2.9: Interpretation of the AO fluorescence changes during dark-light-dark transition. The AO fluorescence signal has been divided into four main phases. A rapid acidification event upon switching the light on (yellow box), followed by an alkalisation event with a fast and a second slower phase (green box), a fast alkalisation event is observed upon switching the light off (blue box), followed by a subsequent biphasic acidification event (black box). Error bars indicate SDs of n=15 biological replicates.

observed when the light is switched on (Figure 4.2.9 yellow box) reflects the water

splitting at PSII and the intensity depends on the state of luminal acidification in the dark, which was previously shown by Miller *et al.* (Miller *et al.* 2021). The activity of PSII (water splitting) is the only process where electrons are not transferred across the membrane; thus, solely the pH of the lumen changes and gets more acidified. Therefore, the signal decrease upon switching on the actinic light is highly influenced by the cellular PSII amount and activity and the energy distribution towards the photosystems by the soluble antenna complexes, the PBS. And since in the presence of DCMU, no luminal acidification was observed (Figure 4.2.3), PSII is the main contributor to the signal. The biphasic signal rise is difficult to interpret with AO fluorescence due to the possibly overlapping signals of proton transfer across the PM and the TM, as proton extrusion and uptake occurs at the PM during illumination (Nitschmann *et al.* 1985; Peschek *et al.* 1985; Katoh *et al.* 1996; Sonoda *et al.* 1998; Inago *et al.* 2020) (Figure 4.2.9 green box). The PSII activity, and thus LEF, strongly influences the proton distribution across the TM and hence affects the signal rise (Teuber *et al.* 2001). Additionally, PSII activity and a functional Cyt b_6f complex are necessary for proton extrusion and uptake at the PM (Sonoda *et al.* 1998). Since no major signal change was observed after the addition of DCMU and KCN (Figure 4.2.3), it seems that the contribution of CEF to the signal changes is only minor during the dark-light-dark transition under the used conditions. This is in line with the observation that CEF contributes to a minor extent when cells were grown under photoautotrophic compared to mixotrophic conditions (Bernát *et al.* 2009). Comparing the amplitude of the initial signal decrease with that of the signal rise when the light was switched off (Figure 4.2.9 blue box) allows estimating changes in PSII activity during illumination which are potentially linked to changes in luminal acidification throughout the light period. The biphasic signal decrease observed upon switching the light off (Figure 4.2.9 black box) mainly reflects the consumption of redox equivalents (Teuber *et al.* 2001) plus, the relaxation of ΔpH across the TM while the relaxation of ΔpH across the PM is rather not significantly contributing much to the signal under the here chosen conditions.

4.3. Investigation of putative Mg^{2+} channels in the cyanobacterium *Synechocystis* sp. PCC 6803

After examining the effects of Mg^{2+} deficiency on *Synechocystis* wt cells, the influences of three putative Mg^{2+} channels encoded in the *Synechocystis* genome were studied. In bacteria, there are two families of Mg^{2+} channels that mediate Mg^{2+} influx: the CorA and MgtE family (Maguire 2006; Moomaw *et al.* 2008). Additionally, three genes (*corB*, *corC*, and *corD*) have been identified in *S. typhimurium* as being involved in Mg^{2+} efflux (M. M. Gibson *et al.* 1991). Mg^{2+} transport mediated by a CorB from *Methanoculleus thermophilus* was recently demonstrated in an *in vitro* assay (Y. S. Chen *et al.* 2021).

4.3.1. Results

4.3.1.1. Mg^{2+} channel homologs in the cyanobacterium *Synechocystis*

A cyanobacteria database, CyanoBase (Nakamura *et al.* 2000; Nakao *et al.* 2010; Fujisawa *et al.* 2017), was used to search for possible homologs of CorA and MgtE in *Synechocystis*. This yielded two hits for potential CorA homologs and one for a potential MgtE channel. The ORF *slr1216* (*mgtE*) encodes a MgtE protein (Kaneko *et al.* 1996), and it was previously proposed that MgtE is the major Mg^{2+} import system in *Synechocystis* (Pakrasi *et al.* 2006). A mt where the *mgtE* gene has been deleted showed less Chl *a* when grown under salt stress conditions (T. Li *et al.* 2016). The two CorA homologs are encoded by the ORFs *sll0507* (*corA1*) and *sll0671* (*corA2*) (Nakamura *et al.* 2000; Nakao *et al.* 2010; Fujisawa *et al.* 2017). Both genes have already been suggested to encode for Mg^{2+} channels (Pakrasi *et al.* 2006). In proteomic studies, both the CorA1 and the MgtE protein were localised in the PM (Pisareva *et al.* 2011; Liberton *et al.* 2016; Baers *et al.* 2019). Additionally, *Synechocystis* encodes possible homologs belonging to the CorC/B proteins that mediate Mg^{2+} efflux. I found two encoded CorC homologs (*sll1254*, *sll0260*) in *Synechocystis* by BLAST analysis (NCBI's BLAST search blastp, protein-protein BLAST (Sayers *et al.* 2022; NCBI 2022) Blast P0A2L4 · CORC_SALTI (CorC protein of *Salmonella typhimurium*) (UniProt 2023a)) and generated KO constructs for *slr1216*, *sll0507*, *sll0671* and *sll1254* to obtain information about the *in vivo* function of the predicted channels.

4.3.1.2. Construction of the KO strains

KO strains were generated *via* homologous recombination. The KO of the different

genes was examined with primers that bind upstream and downstream of the gene locus, plus a primer that binds inside the gene (Figure 4.3.1). The PCR products of

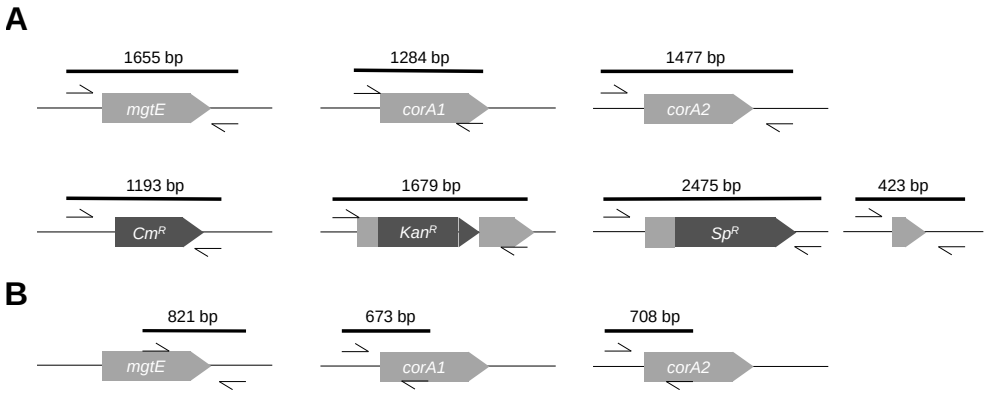

Figure 4.3.1: Primer binding sites and length of PCR product used to confirm the gene KO. (A) Primer pair used to amplify the DNA at the gene locus that binds up and downstream of the gene locus. (B) Primer pair used to amplify the DNA at the gene locus that binds within the gene and upstream or downstream of the gene locus.

the genes encoding homologs of Mg^{2+} channels in the wt and the gene loci in the mts are shown in Figure 4.3.2. A complete KO was confirmed for the *ΔcorA1* mt and *ΔcorA2* mt (Figure 4.3.2 B, C). When amplifying with a primer that binds inside the original gene, a faint band in the *ΔmgtE* mt and the *ΔcorA2ΔmgtE* mt (in the *corA2* gene) was observed (Figure 4.3.2 A, E). The same could be observed even stronger in the *ΔcorA2ΔcorA1* mt (Figure 4.3.2 F). However, these PCR products that suggested incomplete segregation could only be seen using primers that bind inside the original gene, while the antibiotic resistance cassette seemed fully integrated. Therefore, the *ΔmgtE* mt, the *ΔcorA2ΔmgtE* mt and the *ΔcorA2ΔcorA1* mt were used for further analysations. Integrating the antibiotic cassette to knock out the *corA1* gene in the *ΔmgtE* mt was impossible (Figure 4.3.2 D). Since *Synechocystis* also encodes homologs of Mg^{2+} efflux channels, a KO construct for the *sll1254* gene was made to elucidate the gene product's function. The PCR products of the gene from the wt and the generated mt and the primers used for amplification are shown in Figure 4.3.3. Although the antibiotic cassette was integrated, a strong band at the size of the corresponding gene was still observable. At an antibiotic concentration of 150 µg/mL on the agar plate, the cells stopped growing, and it was impossible to increase the antibiotic concentration any further.

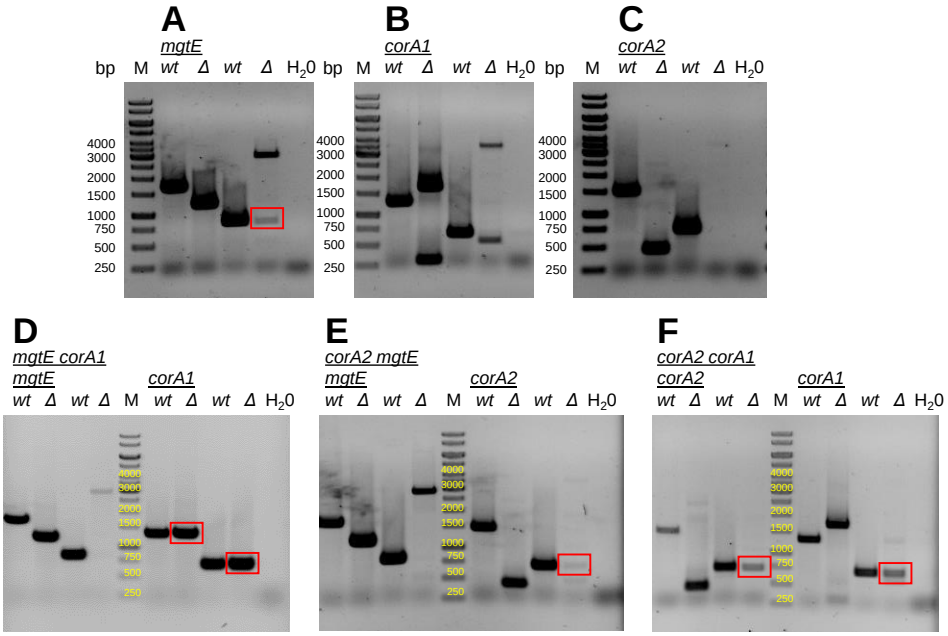

Figure 4.3.2: 1% agarose gels with the PCR products of the gene from *Synechocystis* wt and the inserted antibiotic cassette in the KO strains.
PCR products were loaded from left to right: wt and KO product amplified with the primers (Figure 4.3.1 A), wt and KO product amplified with the primers (Figure 4.3.1 B). M indicates the 1 kb marker, H_2O indicates the negative control. Bands that indicate incomplete segregation were marked with a red box.

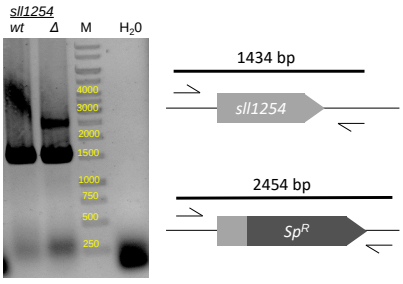

Figure 4.3.3: PCR products to check for segregation of the gene *sll1254* and the used primers.
1% agarose gel with the PCR products at the gene locus *sll1254*. The primers' binding sites and the amplified products' expected length are shown on the right. It was loaded from left to right: wt, KO product, 1 kb marker, negative control. The PCR product obtained using DNA extracted from the KO strain contains two bands, one with the length of the corresponding wt gene and one with the size of the inserted antibiotic cassette.

Thus, generating a *sll1254* KO strain was not possible; therefore, the *sll1254* gene appears to be essential in *Synechocystis*.

4.3.1.3. Growing *Synechocystis* wt and mts cells under various growth conditions

To gain more information on the mts' ability to cope with different environmental conditions, growth of the mt strains was analysed under various conditions. When grown under standard photoautotrophic Mg^{2+} replete conditions (BG11), the mts did not reveal any growth differences (Figure 4.3.4 A). Since *Synechocystis* can grow

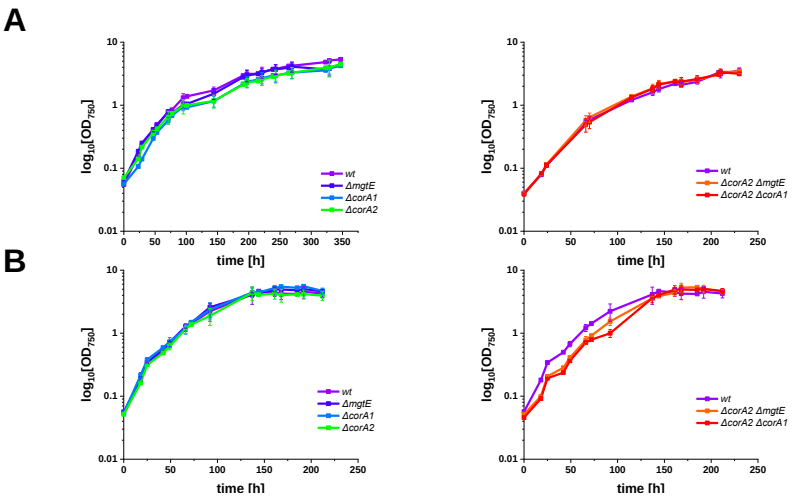

Figure 4.3.4: Growth under photoauto- and photomixotrophic conditions of wt and mt strains. *Synechocystis* wt and single mts (A left) and wt and double mts (A right) grown in BG11 under photoautotrophic conditions. No significant changes were observed during growth or upon reaching saturation. *Synechocystis* wt and single mts (B left) and wt and double mts (B right) grown in BG11 under photomixotrophic conditions. No significant changes were observed during growth or upon reaching saturation in the single mts. Experimental error bars indicate the means ±SDs for n=3.

photomixotrophically, the mts' growth properties in BG11 supplemented with 5 mM glucose were examined (Figure 4.3.4 B). While no differences in growth were observed between the wt and the single mts, the *ΔcorA2ΔmgtE* and *ΔcorA2ΔcorA1* double mts grew slower during the first 18 h. Next photoheterotrophic growth in BG11 with 5 mM glucose and in the presence of PSII inhibitor DCMU was analysed (Figure 4.3.5). DCMU is a herbicide that binds to the Q_B binding site at D1 of PSII, disrupting the linear flow of electrons from PSII to the PQ pool (Metz *et al.* 1986; Mackay *et al.* 1993). Thus, it provides information regarding growth when LEF is inhibited, the function of CEF, and glucose uptake and breakdown. No major

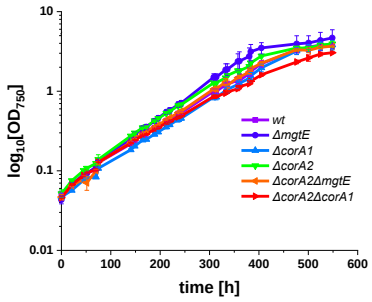

Figure 4.3.5: Growth under photoheterotrophic conditions of wt and mt strains.
Synechocystis wt and single mts were cultured in BG11 supplemented with 5 µM DCMU under photoheterotrophic conditions. No significant differences were observed. Experimental error bars indicate the means ±SDs for n=3.

changes in growth rates were observed when cells were grown photoheterotrophically. As *Synechocystis* wt can grow even at an Mg^{2+} concentration as low as 10 µM and growth appeared to be only little affected when grown with 50 µM Mg^{2+} (see section 4.1, Figure 4.1.1), the mts growth at low Mg^{2+} concentrations was examined. When cells were grown photoautotrophically under Mg^{2+} limitation (50 µM),

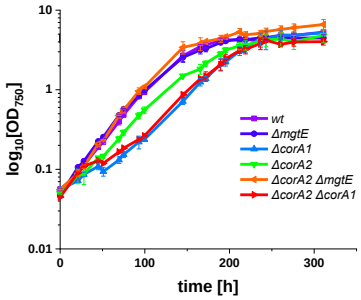

Figure 4.3.6: Growth at low Mg^{2+} concentrations of wt and mt strains.
Synechocystis wt and mts grew in BG11 containing only 50 µM Mg^{2+} under photoautotrophic conditions. The *ΔcorA1* mt, the *ΔcorA2ΔcorA1* mt and the *ΔcorA2* mt started with a prolonged slow-growing phase before they reached exponential growth. Experimental error bars are shown for n=3.

a slow-growing phase before they reached exponential growth was observed for the *ΔcorA2* mt and even more pronounced for the *ΔcorA1* mt and the *ΔcorA2ΔcorA1* mt (Figure 4.3.6). Surprisingly, the *ΔmgtE* mt had a growth advantage when grown photoautotrophically in BG11 with only 10 µM Mg^{2+} (Figure 4.3.7 A).

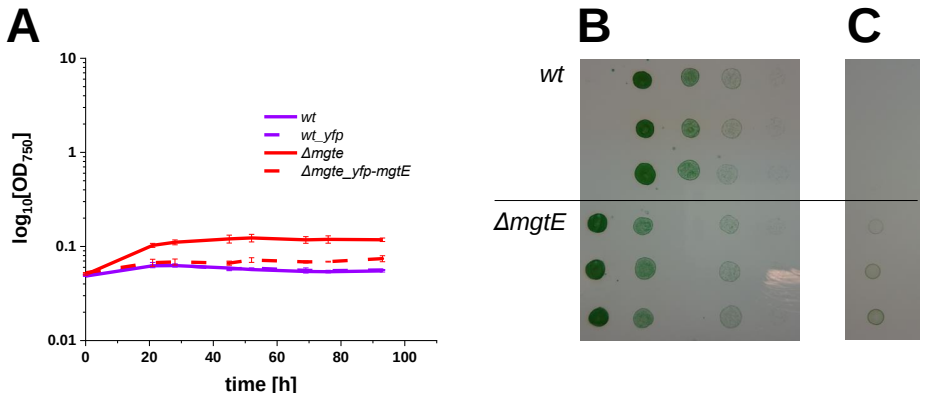

Figure 4.3.7: Growth of *Synechocystis* wt and *ΔmgtE* in the presence of 10 µM Mg^{2+}. (A) *Synechocystis* wt, *ΔmgtE* and the corresponding strains expressing a YFP (wt)/YFP-tagged MgtE (*ΔmgtE*) grown in BG11 with 10 µM Mg^{2+} under photoautotrophic conditions. The *ΔmgtE* strain had a growth advantage at very low Mg^{2+} concentrations that was complemented by expressing a YFP-tagged MgtE protein. Experimental error bars are shown for n=3. *Synechocystis* wt and *ΔmgtE* grown on BG11 agar plates with 10 µM Mg^{2+}. (B) A dilution series from 10^0 to 10^{-5} was spotted in triplicates starting with an OD_{750} of 0.2. No significant difference was observed between the wt and *ΔmgtE* when grown on BG11 agar plates with 10 µM Mg^{2+} and 0.3% $Na_2S_2O_3$. (C) When grown on BG11 agar plates with 10 µM Mg^{2+} but without $Na_2S_2O_3$, only the undiluted *ΔmgtE* could grow to some extent.

The growth advantage of the *ΔmgtE* mt was lost when an N-terminally YFP-tagged MgtE protein was expressed in the mt (Figure 4.3.7 A). Additionally, no growth difference between the mt and the wt was observed when grown photoautotrophically on BG11 agar plates supplemented with only 10 µM Mg^{2+} (Figure 4.3.7 B). $Na_2S_2O_3$ is a ROS scavenger (Stewart *et al.* 1999; Z. Wang *et al.* 2002) and was always added to BG11 agar plates. Since the growth advantage of the *ΔmgtE* mt was again observed when grown on BG11 agar plates supplemented with 10 µM Mg^{2+} without $Na_2S_2O_3$ (Figure 4.3.7 B), an influence of ROS was indicated. In plants ROS can be generated by excess Co^{2+} (Mahey *et al.* 2020). Therefore, to examine whether the growth advantage of the *ΔmgtE* mt was solely a result of the low Mg^{2+} concentrations or Co^{2+}, competing with Mg^{2+} at the MgtE channels' binding sites, growth in BG11 supplemented with additional Co^{2+} was examined (Figure 4.3.8). All mts that lack the *mgtE* gene had a growth advantage in the presence of increased Co^{2+} compared to the wt and the other mts (Figure 4.3.8 A). Yet, growth in all strains was restored in BG11 medium supplemented with Co^{2+} and excess Mg^{2+} (Figure 4.3.8 B).

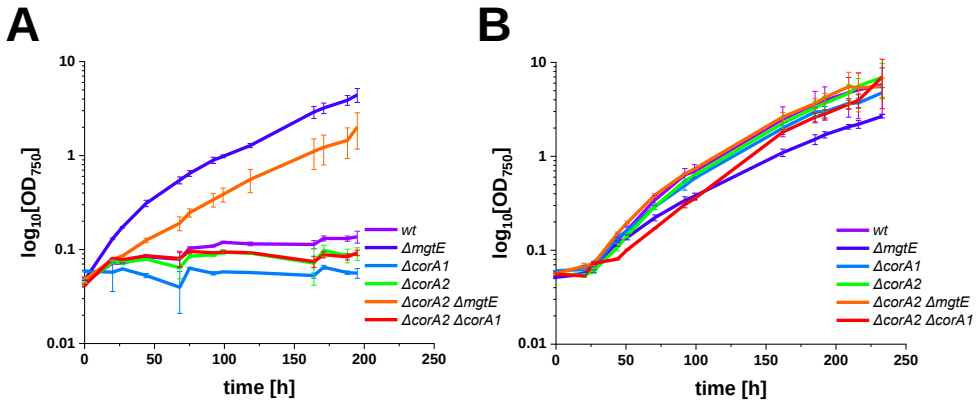

Figure 4.3.8: Growth of *Synechocystis* wt and mt strains in the presence of Co^{2+}.
(A) *Synechocystis* wt and all mts were grown in BG11 medium supplemented with 12 µM Co^{2+} under photoautotrophic conditions. All *ΔmgtE* strains displayed a growth advantage in the presence of Co^{2+}. (B) The addition of 10 mM Mg^{2+} to BG11 supplemented with 13 µM Co^{2+} restored normal growth in the strains that showed growth inhibition in (A) Experimental error bars are shown for n=3.

4.3.1.4. EM images showed differences in the cell layer when cells were grown at low Mg^{2+} concentrations

Although wt growth was not severely affected under photoautotrophic conditions when as little as 50 µM Mg^{2+} was present, the cells were surrounded by a huge EPS layer (see section 4.1, Figure 4.1.2). Since the mts were affected to different degrees when grown in BG11 with 50 µM Mg^{2+} (Figure 4.3.6), it was investigated to what extent the mts' appearance differed from the wt's. Therefore, EM images were taken after growth in a multicultivator in a turbidostatic mode at high (300 µM **H** conditions) and low (50 µM **L** conditions) Mg^{2+} concentrations. EM images taken from wt and mts cells grown under **H** conditions did not show major differences (Figure 4.3.9). Since no apparent differences were evident from EM images acquired under standard growth conditions, the following images were taken analysing *Synechocystis* wt and mt strains grown under **L** conditions (Figure 4.3.10). EM images taken under **L** conditions displayed a huge EPS layer surrounding the cell in the wt and all mts except for the mts lacking the *corA2* gene that had only little (*ΔcorA2*) or no (*ΔcorA2ΔmgtE*, *ΔcorA2ΔcorA1*) EPS layer surrounding the cell. All cells displayed a lower intracellular density (Figure 4.3.10). Furthermore, the *ΔcorA2ΔcorA1* mt, in particular, accumulated high levels of storage products (probably cyanophycin).

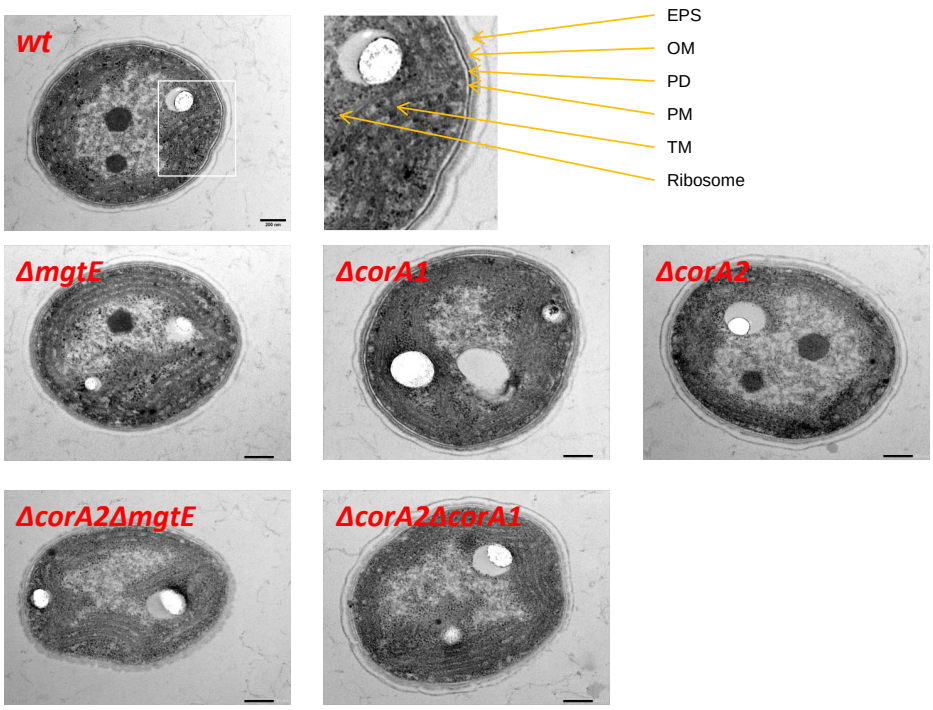

Figure 4.3.9: EM images of *Synechocystis* wt and mts which were grown in the presence of high Mg^{2+} concentrations.
The cells were surrounded by an Exopolysaccharide (EPS)-layer followed by the outer membrane (OM), a peptidoglycan layer (PD) and the plasma membrane (PM). No significant changes were observed between the wt and the mts when grown in the presence of high Mg^{2+} concentrations. The scale bar was set to 200 nm. Images were taken by [redacted] and [redacted], [redacted].

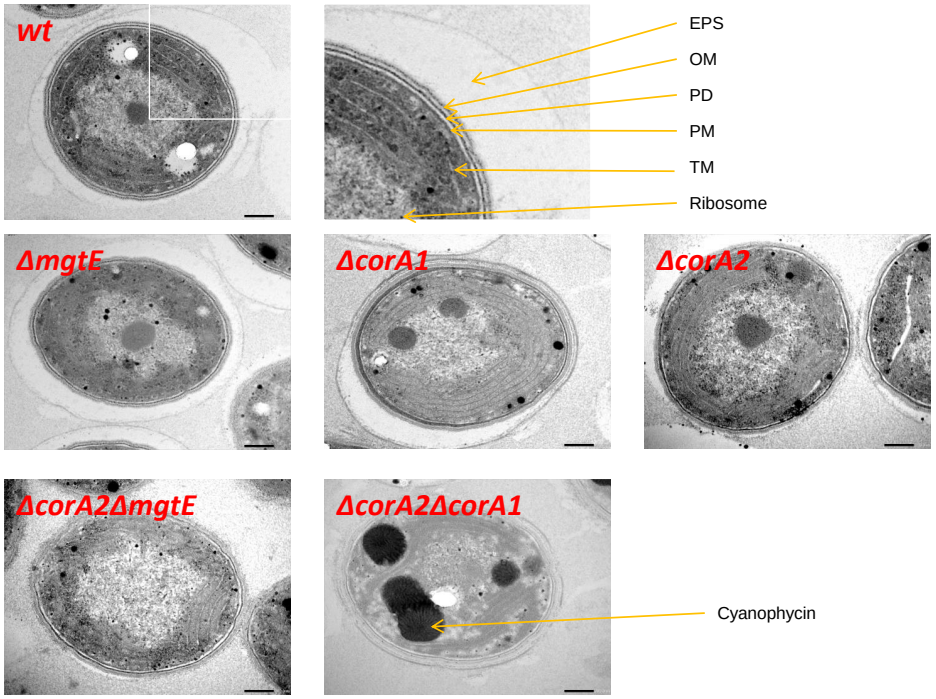

Figure 4.3.10: EM images of *Synechocystis* wt and mts which were grown in the presence of low Mg^{2+} concentrations.
The cells were surrounded by an EPS layer followed by the outer membrane (OM), a peptidoglycan layer (PD) and the plasma membrane (PM). *Synechocystis* wt and single mts developed a huge EPS layer surrounding the cells when grown at low Mg^{2+} concentrations. This was less pronounced in the *ΔcorA1* and *ΔcorA2* mt and absent in the *ΔcorA2ΔmgtE* and *ΔcorA2ΔcorA1* double mts. All cells seemed to accumulate storage products, probably cyanophycin, at low Mg^{2+} concentrations and seemed to have a reduced number of ribosomes. Additionally, the cells seemed less densely packed. The scale bar was set to 200 nm. Images were taken by [redacted] and [redacted], [redacted].

4.3.1.5. Total carbohydrates were unchanged under both growth conditions

The *Synechocystis*' EPS layer is composed of up to 12 different monosaccharides (Pereira *et al.* 2009). The amount of total carbohydrates was analysed to elucidate whether a missing EPS layer was accompanied by a decreased amount of these bio-products playing a central role in cellular bioenergetics and metabolism (Table 4.3.1). The differences observed in the abundance of an EPS layer surrounding the cells under **L** conditions (Figure 4.3.10) were not reflected by significant changes in the amount of total carbohydrates per cell. Total carbohydrates remained unaltered under either growth conditions or between the strains (Table 4.3.1).

Table 4.3.1: Amount of total carbohydrates of wt and mt strains.
The amount of total carbohydrates was measured using a phenol-sulfuric acid method after methanolic extraction of the pigments. No significant differences were observed under either growth condition or between the strains. Less than 3 replicates are marked in red.

total carbohydrates [pg/cell]			
	H	**L**	**n**
wt	0.24 ±0.06	0.32 ±0.20	3
ΔmgtE	0.25 ±0.06	0.30 ±0.15	3
ΔcorA1	0.33 ±0.09	0.28 ±0.13	3
ΔcorA2	0.23 ±0.05	0.21 ±0.08	2
ΔcorA2ΔmgtE	0.24 ±0.07	0.25 ±0.09	3
ΔcorA2ΔcorA1	0.21 ±0.07	0.28 ±0.08	3

4.3.1.6. Absorption spectra and cellular pigment content

The wt absorption spectra of cultures grown under **H** or **L** conditions differed significantly, and a reduced Chl *a* content was visible after growth in medium containing low Mg^{2+} concentrations. Additionally, EM images taken after growth under **L** conditions revealed differences between the wt and all mts lacking the *corA2* gene. The results showed impaired growth in the *ΔcorA2* mt, the *ΔcorA1* mt and the *ΔcorA2ΔcorA1* mts at low Mg^{2+} concentrations. Therefore, I further investigated to what extent the pigment ratios of the mts compared to the wt was affected under **H** and **L** conditions (Figure 4.3.11). As already observed for the wt in the whole cell (UV-Vis) spectra (see section 4.1, Figure 4.1.4), the Chl *a* content (peaks at 437 nm and 678 nm) of all *Synechocystis* mts was significantly lowered when grown in medium with low Mg^{2+} concentrations (Figure 4.3.11 A, B). The ratio of the Chl *a* peak at 437 nm and the Car shoulder at 480 nm showed a decreased Chl *a*:Car ratio for the wt and all mts under **L** conditions (Figure 4.3.11 C). The difference between the two growth conditions was most apparent in the *ΔmgtE* mt, the *ΔcorA1* mt and the *ΔcorA2* mt. Compared to high Mg^{2+} conditions, PC:Chl *a* ratio increased in all strains. The estimated PC:Chl *a* ratio increased about 2-fold in the

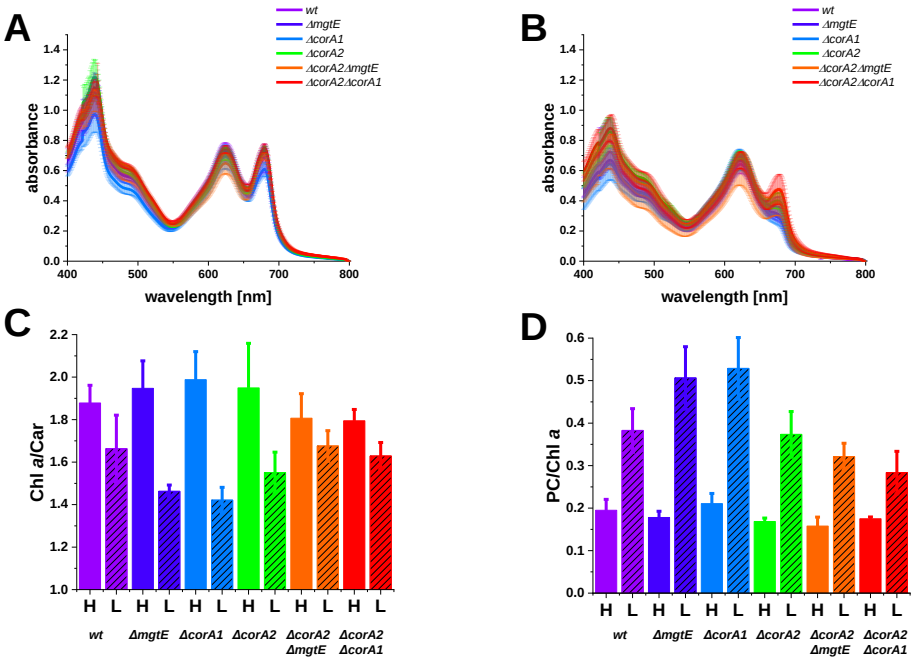

Figure 4.3.11: Absorption spectra of whole wt and mts cells.
Absorption spectra were recorded at high (A) and low (B) Mg^{2+} concentrations. The loss of Chl *a* is detectable by the decrease in the peaks at 437 nm and 678 nm. The changed ratio of Chl *a* to Car can be assumed (C), although not as clearly as in the case of the methanolic extraction (Figure 4.3.12). The increase in the PC:Chl *a* ratio is evident from the spectra (D). Experimental error bars indicate the means ±SDs of at least 3 biological replicates.

wt and all mts lacking *corA2* and almost 2.5-fold in the *ΔcorA1* and the *ΔmgtE* mts under **L** conditions (Figure 4.3.11 D). What was already apparent from the absorption spectra became even more evident after the methanolic extraction of Chl *a* and Car. All strains had less Chl *a* per cell under **L** conditions (Figure 4.3.12 A).

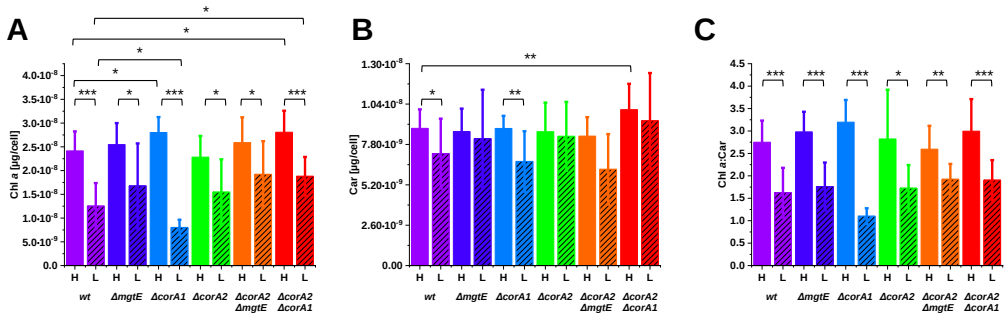

Figure 4.3.12: Estimated Chl *a* and Car content after methanolic extraction of the wt and the mts.
As already observed for the wt (see section 4.1, Figure 4.1.5), the Chl *a* amount (A) is lower under **L** conditions. (B) The amount of Car differed slightly under **L** conditions. (C) This resulted in a lower Chl *a*:Car ratio. Experimental error bars indicate the means ±SDs of at least 3 biological replicates. Significant differences (two-sample t-test) are indicated as: * $p < 0.05$; ** $p < 0.01$; *** $p < 0.001$.

Moreover, compared to the wt, the *ΔcorA1* and *ΔcorA2ΔcorA1* mts had a higher Chl *a* concentration under **H** conditions and a lower (*corA1*) or higher (*corA2corA1*) under **L** conditions (Figure 4.3.12 A). The Car content per cell was lower under **L** conditions compared to **H** conditions in the wt and the *ΔcorA1* mt, while all other strains did not show significant changes upon Mg^{2+} deficiency (Figure 4.3.12 B). The *ΔcorA2ΔcorA1* mt showed a higher Car level than the wt under **H** conditions. Overall, the lower Chl *a* content and less altered Car content resulted in a decreased Chl *a*:Car ratio in all strains (Figure 4.3.11 C).

4.3.1.7. Low-temperature fluorescence emission spectra revealed a changed PSI:PSII ratio

The observed reduced Chl *a* content in the wt was accompanied by a significantly reduced amount of PSI (see section 4.1, Table 4.1.1). Since the observed changes in Chl *a* content and pigment ratios in the mts were comparable to the wt, I hypothesised that the PSI:PSII ratio changed similarly. To compare the wt and the mts PSI:PSII ratios and to investigate the energy transfer from the PBS to the two photosystems, fluorescence emission spectra were measured at 77K after freezing whole *Synechocystis* cells in liquid nitrogen. As observed in the wt, the mts spectra showed

that Mg^{2+} limitation strongly affects the PSI:PSII ratio after Chl *a* excitation (435 nm) (Figure 4.3.13 A, B). However, the ratio decreased to different degrees

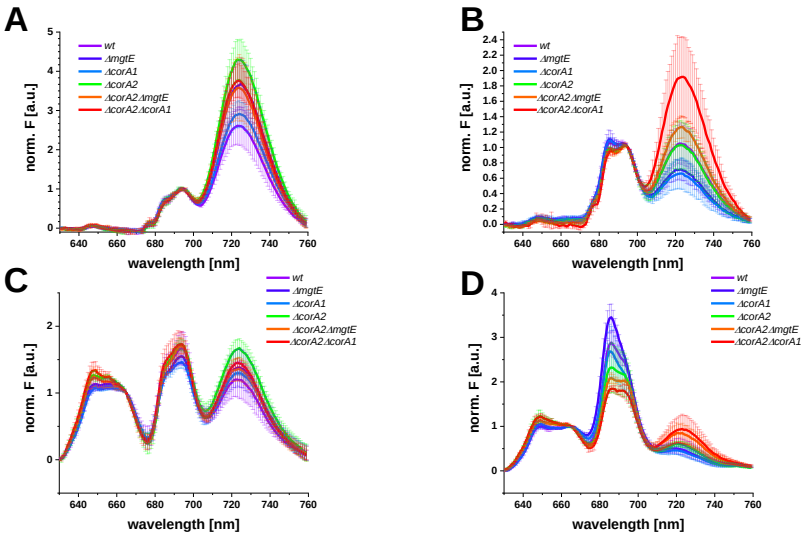

Figure 4.3.13: 77K fluorescence emission spectra of wt and mt strains.
Cells were grown under **H** (left) or **L** (right) conditions. Samples were excited at 435 nm (Chl *a*) (A, B) or 580 nm (PBS) (C, D). Spectra were normalised at 695 nm (A, B) or 669 nm (C, D). Experimental error bars indicate the means ±SDs of at least 3 biological replicates.

in all strains. While the *ΔcorA1* mt showed wt-like ratios under **H** conditions, the *ΔmgtE* mt and all mts lacking the *corA2* gene had higher PSI:PSII ratios (Figure 4.3.13 A). Under **L** conditions, the *ΔcorA2* mt showed wt-like ratios, while the *ΔmgtE* mt and *ΔcorA1* mt had lower and the *ΔcorA2* double mts higher PSI:PSII ratios (Figure 4.3.13 B). It is important to note that the signal at 685 nm not only originates from PSII (CP43 and CP47) (Andrizhiyevskaya *et al.* 2005) but can also be affected by uncoupled PBS (Luimstra *et al.* 2018) and the IsiA protein (Bibby *et al.* 2001; Ma *et al.* 2017). Differences in the ratio of the peak at 685 nm (CP43 and CP47) and the peak at 695 nm (CP47) appeared under **L** conditions. The peak at 685 nm increased while the peak at 695 nm decreased (Figure 4.3.13 B). I observed these changes in the wt, the *ΔmgtE* mt and the *ΔcorA1* mt, but not in all mts lacking the *corA2* gene. Fluorescence emission spectra after PBS excitation at 580 nm showed no significant differences between all strains under **H** conditions (Figure 4.3.13 C). Comparison of the wt and the mts spectra under **L** conditions showed differences in the number of PBSs bound to PSII (Figure 4.3.13 D). While the *ΔmgtE* mt had a tendency towards more PBSs associated with PSII, the *ΔcorA1*

mt was wt-like, and all mts lacking the *corA2* gene tended to have fewer PBSs associated with PSII (Figure 4.3.13 D). Additionally, the peak at 645 nm (PC) (Sidler 1994; Spät *et al.* 2018) was higher in these mts after PBS excitation under both conditions. I further used the data I obtained from the fluorescence emission spectra, the absorption spectra, the cellular Chl *a* content and the cell number to estimate the amount of PSI and PSII per cell (as discribed in Luimstra *et al.* (Luimstra *et al.* 2019)). As already observed in the wt under **L** conditions, the PSI popu-

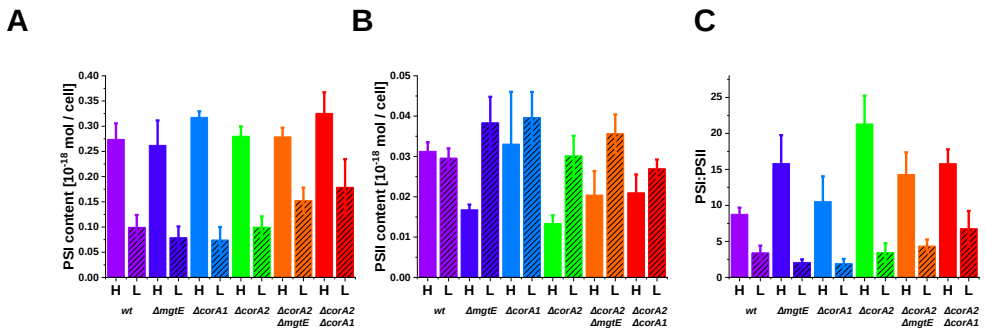

Figure 4.3.14: Estimated amount of PSI and PSII per cell.
The PSI (A) and PSII (B) content (in mol * cell^{-1}) was calculated according to Luimstra *et al.*(Luimstra *et al.* 2019), taking into account the number of cells, the results from the absorption spectra, the amount of Chl *a* and the 77K spectra (see section 5, Table A.5.2). The PSI content was slightly different in the wt and the mts and decreased in all strains at Mg^{2+} limitation. While the wt's PSII content hardly changed at high or low Mg^{2+} concentrations, the PSII content in the *ΔmgtE* and all mts lacking the *corA2* gene showed a lower PSII content at high Mg^{2+} concentrations, which increased at low Mg^{2+} concentrations. This was also reflected in higher PSI:PSII ratios at high Mg^{2+} concentrations and close to wt ratios at low Mg^{2+} concentrations (C). Experimental error bars indicate the means ±SDs of at least 3 biological replicates.

lation in all mts decreased significantly when grown at low Mg^{2+} concentrations (Figure 4.3.14 A) but was fairly unchanged among the strains. The results showed that the PSII amount hardly changed at high or low Mg^{2+} concentrations in the wt (Figure 4.3.14 B), while the *ΔmgtE* mt and all mts lacking the *corA2* gene showed a lower PSII amount than the wt under **H** conditions. The PSII levels at low Mg^{2+} concentrations were similar to the wt in all mts lacking *corA2* and slightly higher in the *ΔmgtE* mt and the *ΔcorA1* mt. The PSI:PSII were lower in all studied strains under Mg^{2+} limitation (Figure 4.3.14 C). However, this must be considered with care as the calculation only gives a rough estimation of the total abundance of PSI and PSII per cell (Luimstra *et al.* 2019). Oxygen consumption was decreased at low Mg^{2+} concentrations. The Chl *a* content was reduced, accompanied by a lowered PSI:PSII ratio and a changed energy distribution from PBS's to the two photosystems under

L conditions. These changes indicate that the activity of the photosystems was somehow affected. Therefore, first, oxygen evolution was measured to investigate possible changes in the activity of PSII. In the wt, Mg^{2+}-limitation influenced respiration much more than O_2 evolution (see section 4.1, Figure 4.1.7), while the amount of total carbohydrates in the wt at low Mg^{2+} concentrations was not affected. The amount of total carbohydrates did not change in the mts either. Surprisingly, all mts showed less respiration than the wt at high Mg^{2+} concentration (Figure 4.3.15). The respiration level in the mts did not change significantly at low Mg^{2+} concentrations compared to high Mg^{2+} concentrations. Therefore, at low Mg^{2+} concentrations, the wt and the mts had the same respiration level. Overall, O_2 evolution was less

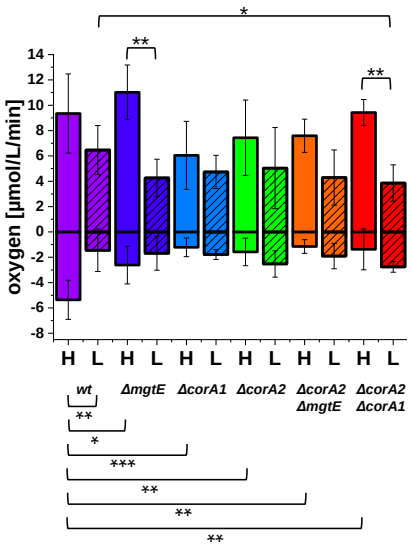

Figure 4.3.15: Oxygen evolution and consumption of wt and mt strains.
Oxygen evolution and consumption of wt and mts with the cells adjusted to an OD_{750} of 2. Measurements were performed after growth at **H** and **L** conditions. Comparison of oxygen production (+) and oxygen consumption (-) calculated from the slopes of the signal during measurements in darkness and light. Experimental error bars indicate the means ±SDs of at least 3 biological replicates. Significant differences (two-sample t-test) are indicated as: * $p < 0.05$; ** $p < 0.01$; *** $p < 0.001$. The measurements were performed in cooperation with [redacted].

affected by the different growth conditions and between the strains. O_2 evolution was significantly lower in the *ΔmgtE* mt and the *ΔcorA2ΔcorA1* mt at low Mg^{2+} concentrations compared to high Mg^{2+} concentrations, while only *ΔcorA2ΔcorA1* mt differed substantially from the wt at low Mg^{2+} concentrations.

4.3.1.8. Estimation of the maximal quantum yield (F_v/F_m) using adapted induction curves

Since O_2 evolution was relatively unchanged, the maximal quantum yield of PSII was estimated. F_v/F_m is a good indicator of PSII photosynthetic performance in plants (Maxwell *et al.* 2000) and gives reliable numbers in cyanobacteria (Campbell *et al.* 1998). Deviating from the protocol used, which defines the parameters according to the reduction state of the PQ pool, I calculated F_v/F_m using the lowest fluorescence in the dark (F_o) and the highest fluorescence after DCMU addition in actinic light (F_m) (as described in section 3.2.4.13). A reduced maximum quantum

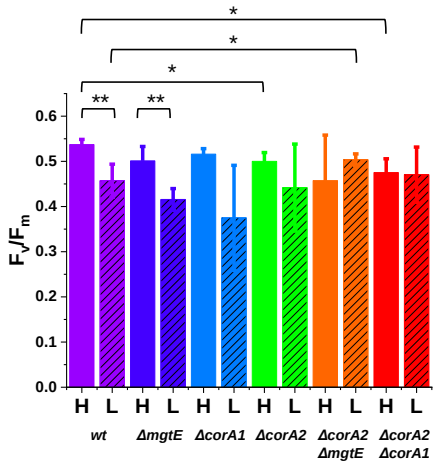

Figure 4.3.16: Maximum quantum efficiency of PSII (F_v/F_m) of wt and mt strains.
F_v/F_m was measured after growth under **H** or **L** conditions. The photosynthetic parameter F_v/F_m was calculated from the lowest fluorescence in the dark and the highest fluorescence after adding DCMU in the light (averaged traces are shown in section 5, Figure A.5.1). Experimental error bars indicate the means ±SDs of at least 3 biological replicates. Significant differences (two-sample t-test) are indicated as: * $p < 0.05$; ** $p < 0.01$; *** $p < 0.001$. The measurements were performed in cooperation with [redacted].

yield of PSII under **L** conditions compared to **H** conditions was measured in the wt and the *ΔmgtE* mt. Compared to the wt, the *ΔcorA2* and the *ΔcorA2ΔcorA1* mts showed lower values at high Mg^{2+} concentrations, and the *ΔcorA2ΔmgtE* mt reached higher values under Mg^{2+} limitation (Figure 4.3.16). Since the SDs were high, the differences between the wt and the mts were relatively small.

4.3.1.9. Estimation of the effective quantum yields of PSI and PSII

The effective quantum yields of PSI (Y(I)) and PSII (Y(II)) were estimated to provide information on the adaptability of the photosystems to different light conditions (Genty *et al.* 1989), as there were only minor differences in the maximum quantum yields of PSII. The results showed that both PSs were affected by Mg^{2+} limitation, yet, to different extents. In accordance with the changes in PSII to PSI ratios, a significant decrease in the PSII effective quantum yield (Y(II)) was observed in the wt and all mts under Mg^{2+} limitation (Figure 4.3.17).

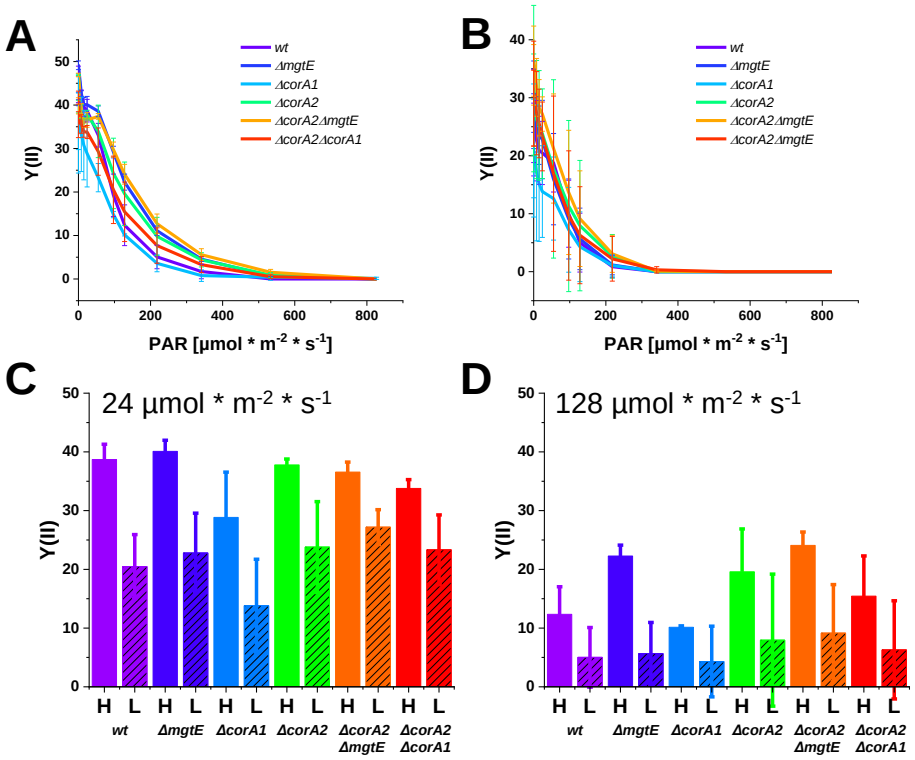

Figure 4.3.17: Effective quantum yield of PSII (Y(II) of wt and mt strains.
The effective quantum yield of PSII (Y(II) of wt and mts at high (A) and low Mg^{2+} (B) concentrations. The *ΔcorA1* mt had a lower Y(II) than the wt, especially at lower light intensities (24 µmol photons * m^{-2} * s^{-1}) (C), while the *ΔmgtE* mt and the *ΔcorA2* mts had a slightly higher Y(II) at higher light intensities (128 µmol photons * m^{-2} * s^{-1}) (D). Experimental error bars indicate the means ±SDs of at least 3 biological replicates except *ΔcorA2* n=2 (**L**). The measurements were performed in cooperation with [redacted].

The decrease in Y(II) at low Mg^{2+} concentrations (Figure 4.3.17 B) compared to high Mg^{2+} concentrations (Figure 4.3.17 A) could be observed in all studied strains. It was striking that the *ΔcorA1* mt showed already relatively lower Y(II) values at high Mg^{2+} concentrations at an intensity of 24 µmol photons * m^{-2} * s^{-1} (Figure 4.3.17 C) and 128 µmol photons * m^{-2} * s^{-1} (Figure 4.3.17 D) actinic light (notice that growth light was 30 µmol photons * m^{-2} * s^{-1}). The *ΔmgtE* and the *ΔcorA2ΔmgtE* mts reached higher values at intensities of 128 µmol photons * m^{-2} * s^{-1} actinic light at high Mg^{2+} concentrations (Figure 4.3.17 D). As already observed for the wt (see section 4.1, Figure 4.1.11), the lower effective quantum yield of PSII at low Mg^{2+} concentrations was accompanied by a concomitant increase in PSI quantum yield in all mts (see section 5, Figure A.5.2 and A.5.3). This increase was mainly due to a decrease in Y(ND) (decrease of Y(I) due to donor side limitation), while no change in Y(NA) (decrease of Y(I) due to acceptor side limitation) was observed. (By definition, Y(I)+Y(ND)+Y(NA) = 1) (Klughammer *et al.* 2008). Less Y(ND)

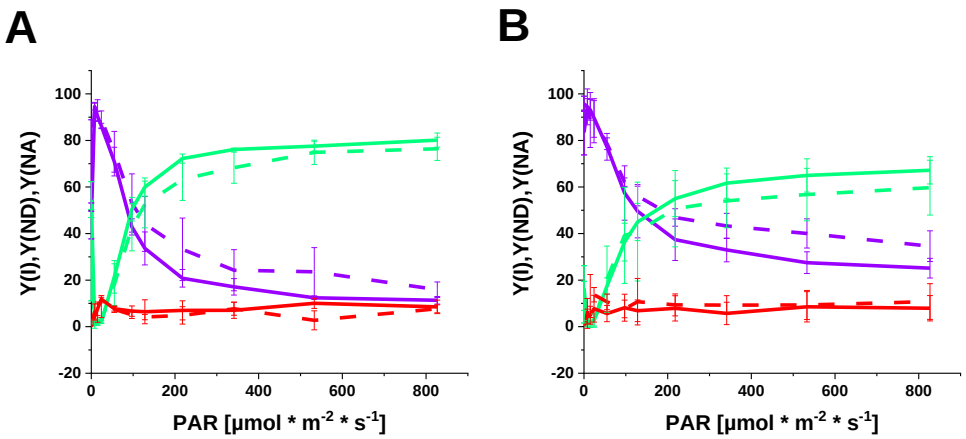

Figure 4.3.18: Effective quantum yield of PSI (Y(I) of *ΔcorA1* compared to the wt.
(A) Effective quantum yield of PSI (Y(I)) under **H** conditions of *ΔcorA1* (dashed line) compared to the wt (solid line). (B) Effective quantum yield of PSI (Y(I)) under **L** conditions of *ΔcorA1* (dashed line) compared to the wt (solid line). The wt had a higher Y(I) (purple) with lower Y(ND) (green) and unchanged Y(NA) (red) under **L** conditions compared to **H** conditions. The same was observed for the *ΔcorA1* mt under **H** conditions (A) and even more pronounced under **L** conditions (B). Experimental error bars indicate the means ±SDs of at least 3 biological replicates. The measurements were performed in cooperation with [redacted].

and a higher Y(I) were already observed in the *ΔcorA1* mt under **H** conditions

(Figure 4.3.18 A) and even more pronounced under **L** conditions (Figure 4.3.18 B). Thus, adapting photosynthesis to different light conditions appeared to be more impaired in the *ΔcorA1* mt than in the wt and the other mts.

4.3.1.10. Probing of the linear electron flow *via* P_{700}^+ re-reduction kinetics measurements

Since the effective quantum yield of both PSs was altered, the electron transfer to P_{700} was analysed by measuring P_{700}^+ re-reduction kinetics. At high Mg^{2+} concentrations, there was a tendency towards a slower P_{700}^+ re-reduction in all mts compared to the wt that was statistically significant in the *ΔcorA1* mt and the *ΔcorA2ΔmgtE* mt (Figure 4.3.19 A). Still, P_{700}^+ re-reduction kinetics measurements under **L** conditions revealed faster P_{700}^+ re-reduction for all strains compared to **H** conditions, which were statistically significant for the wt, the *ΔmgtE* mt and the *ΔcorA1* mt (Figure 4.3.19 B). The observations might be explained by a more reduced PQ pool when the cells were grown under **L** conditions. Therefore, to investigate whether this was already the case under **H** conditions and to what extent the TM-localised terminal oxidases were involved in the PQ pool relaxation, the P_{700}^+ re-reduction kinetics were measured under **H** conditions in the presence of KCN. Cells grown at high Mg^{2+} conditions were treated with KCN prior to

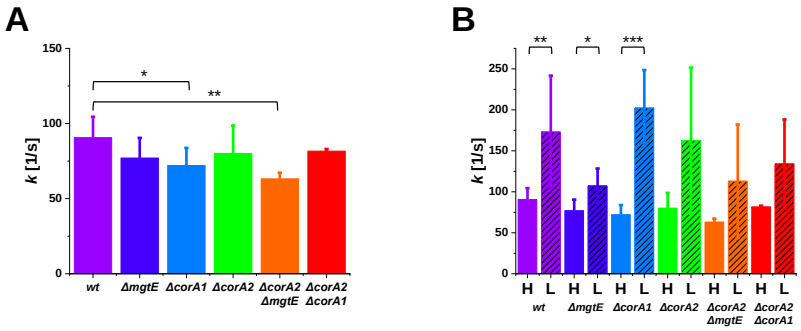

Figure 4.3.19: P_{700}^+ re-reduction kinetics of wt and mt strains.
(A) P_{700}^+ re-reduction kinetics of wt and mts determined when cells were grown under **H** conditions. The *ΔcorA1* mt and the *ΔcorA2ΔmgtE* mt had slower re-reduction kinetics compared to the wt. (B) *Synechocystis* wt, the *ΔmgtE* mt, and the *ΔcorA1* mt had significantly faster re-reduction kinetics under **L** conditions compared to **H** conditions. The trend towards faster re-reduction kinetics was also observed in the other strains, yet, the differences are not statistically significant due to the high SDs determined under **L** conditions. Experimental error bars indicate the means ±SDs of at least 3 biological replicates. Significant differences (two-sample t-test) are indicated as: * $p < 0.05$; ** $p < 0.01$; *** $p < 0.001$. The measurements were performed in cooperation with [redacted].

P_{700}^+ re-reduction measurements to prevent electron donation from the PQ pool to the TM-localised terminal oxidases. As a result, KCN treatment resulted in faster

$P_{700}{}^{+}$ re-reduction compared to untreated cells except for the *ΔmgtE* mt strain (Figure 4.3.20 A). $P_{700}{}^{+}$ re-reduction was measured repeatedly after KCN addi-

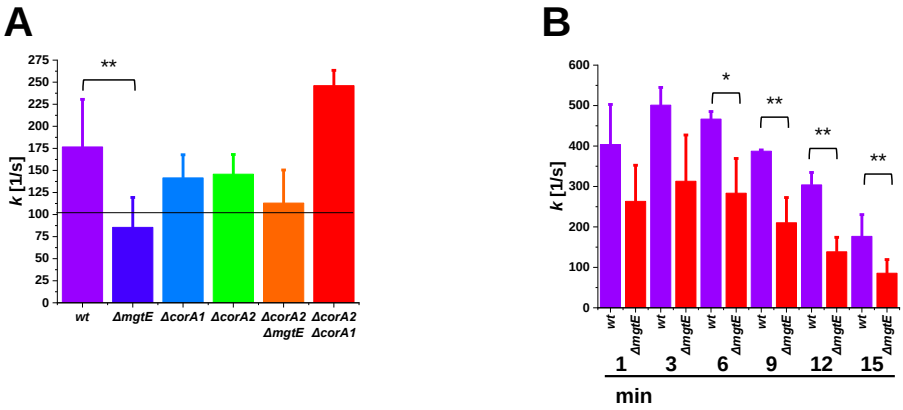

Figure 4.3.20: $P_{700}{}^{+}$ re-reduction kinetics determined in the presence of KCN.
$P_{700}{}^{+}$ re-reduction rates were measured under **H** conditions after adding KCN to assess the contribution of electron transfer to the TOs. Therefore, the samples were incubated in the presence of KCN for 15 min in the dark before the measurements. The curves were fitted with a single exponential. Compared to untreated cells, $P_{700}{}^{+}$ re-reduction rates were faster in the wt and all mts except the *ΔmgtE* mt (black line ∼ k[1/s] without KCN) (A). This difference was also observed when comparing the wt and the *ΔmgtE* mt after different incubation times (1-15 min) with KCN in the dark. Experimental error bars indicate the means ±SDs of at least 3 biological replicates (B).

tion (Figure 4.3.20 B) to determine whether this phenomenon was time-dependent. Again, the $P_{700}{}^{+}$ re-reduction in the *ΔmgtE* strain was slower than the wt's at each time point measured. The decrease in $P_{700}{}^{+}$ re-reduction seen in the wt and the *ΔmgtE* mt over the incubation time likely resulted from impaired PLC by KCN (Berg *et al.* 1975).

4.3.1.11. All mts differed from the wt in the pH gradient build-up across the membranes

The observed alterations regarding the photosynthetic parameters and the respiration observed in the mts compared to the wt could influence the proton gradients across *Synechocystis* membranes. Since growth under Mg^{2+} limitation also affected the proton gradient across the membranes in the wt (see section 4.1, Figure 4.1.13), the observed effects could be even more pronounced in the mts. Additionally, Mg^{2+} was identified long ago as a counterion for the protons pumped across the TM in the light (Dilley *et al.* 1965; Barber *et al.* 1974; Hind *et al.* 1974; Chow *et al.* 1976; Portis *et al.* 1976; Lyu *et al.* 2017). Thus, channels located in the

TM could further alter the signal. Therefore, possible changes in the generation of a pH gradient across the TM were analysed using the pH sensitive fluorescent dye acridine orange (AO) (Teuber *et al.* 2001). I monitored the light-induced generation of a ΔpH in whole *Synechocystis* wt and mts cells. The cells were dark incubated with AO for 15 min prior to the measurement. Then, AO fluorescence was monitored in a dark-light-dark transition over 10 min. At high Mg^{2+} concentrations, a rapid drop in fluorescence (acidification) was observed within seconds when the light was switched on, followed by a much slower biphasic increase (alkalisation) in the minute scale. When the light was switched off, the fluorescence rapidly increased again, followed by a signal decrease (wt Figure 4.3.21 A). While the initial drop in signal intensities upon switching the light on did only reveal minor differences between the wt and the *ΔmgtE* mt (Figure 4.3.22 A), there were clear differences in the subsequent signal increase. Especially the 2nd phase showed significant dif-

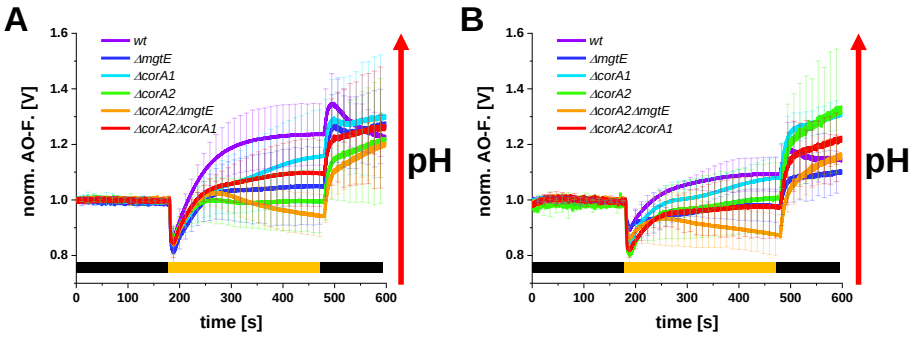

Figure 4.3.21: Light-induced changes in AO fluorescence in whole wt and mts cells.
AO measurements under **H** (A) and **L** conditions (B) during the transition from dark (black bar) to light (yellow bar) to dark (black bar). Under **H** conditions, the mts' signal decrease was wt-like when the light was switched on. The subsequent signal increase ended in a lower plateau and appeared biphasic in all mts compared to the wt. Upon switching the light off, the signal increase in the mts was stronger, and the subsequent signal decrease ended in a signal increase in all mts. Under **L** conditions, the overall signal shape of the wt and the mts was comparable to the signal under **H** conditions. The amplitude was reduced in all strains compared to **H** conditions. Experimental error bars indicate the means ±SDs of at least 3 biological replicates. The measurements were performed in cooperation with [redacted].

ferences. None of the mts could reach the AO fluorescence signal level observed in the wt. After the rapid increase in fluorescence intensity upon switching the light off, all but two mts showed a subsequent slow signal increase, while the *ΔcorA1* and *ΔmgtE* mts showed a transient signal decrease before a slow increase. These changes were even more pronounced after growing the cells at low Mg^{2+} concentrations (Figure 4.3.21 B). In general, wt and mts did not reach as high AO signals indi-

cating cytoplamic alkalisation as before when the lights were switched on. There were also differences between the signal decrease when the light was switched on and the signal increase after the light was switched off. Details are shown in Figure 4.3.22, which shows signal decrease and signal increase at the beginning and end of the light period under **H** and **L** conditions. Under **L** conditions, the

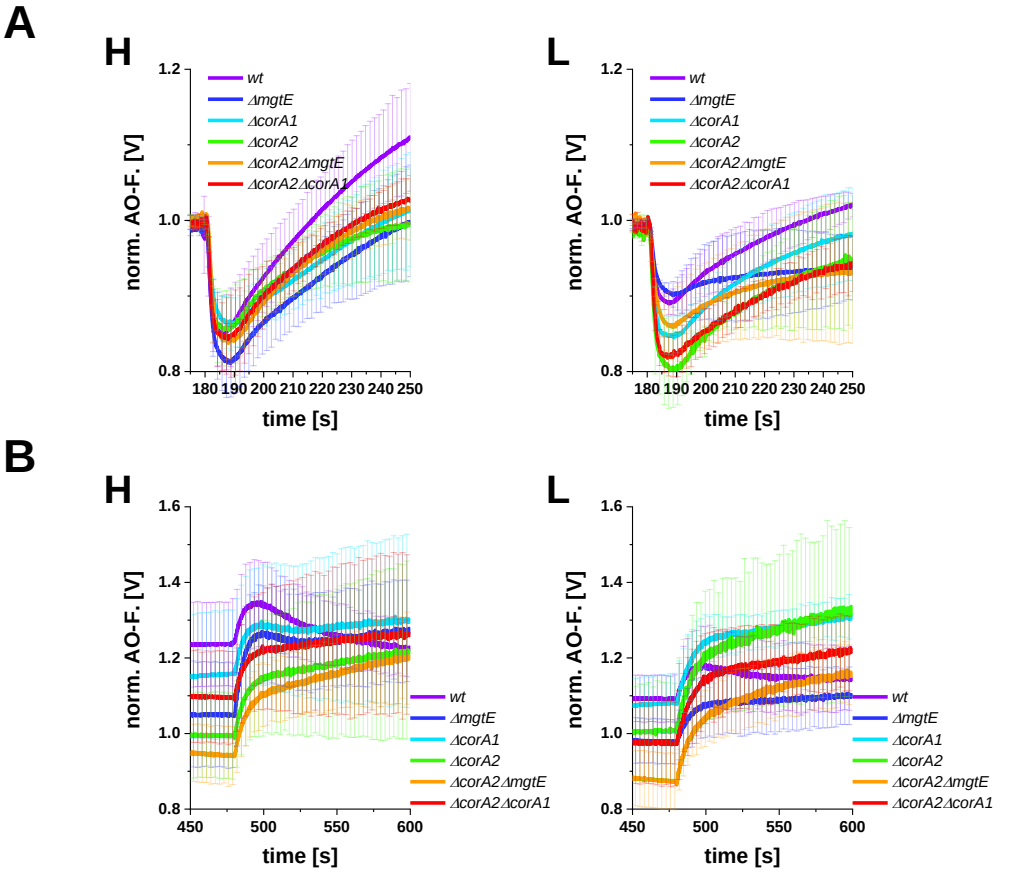

Figure 4.3.22: AO fluorescence changes observed when the light was switched on or off. The rapid signal decrease when the light was switched on (A) under **H** and **L** conditions was compared. Also, the rapid signal increase (B) upon switching the light off and the subsequent signal change under both conditions was compared. The level of acidification when the light was switched on, and the level of alkalisation in the light changed. This was most evident in the wt. Experimental error bars indicate the means ±SDs of at least 3 biological replicates. The measurements were performed in cooperation with [redacted].

ΔcorA1 mt and the *ΔcorA2ΔmgtE* mt showed a signal decrease as under **H** conditions, while the wt and the *ΔmgtE* mt had a less pronounced signal decrease, and the *ΔcorA2* mt and the *ΔcorA2ΔcorA1* mt had a more pronounced signal decrease (Figure 4.3.22 A). The AO signal level reached during light exposure was lower at low

Mg^{2+} concentrations than at high Mg^{2+} concentrations. At low Mg^{2+} concentrations, the rapid signal increase observed when switching off the light was followed by a subsequent signal increase in all mts, while the wt showed a slight signal decrease and remained at this level (Figure 4.3.22 B). Light-induced AO fluorescence changes were additionally monitored after adding KCN during dark incubation (a total of 18 min before the light was switched on) (Figure 4.3.23). Adding KCN during dark

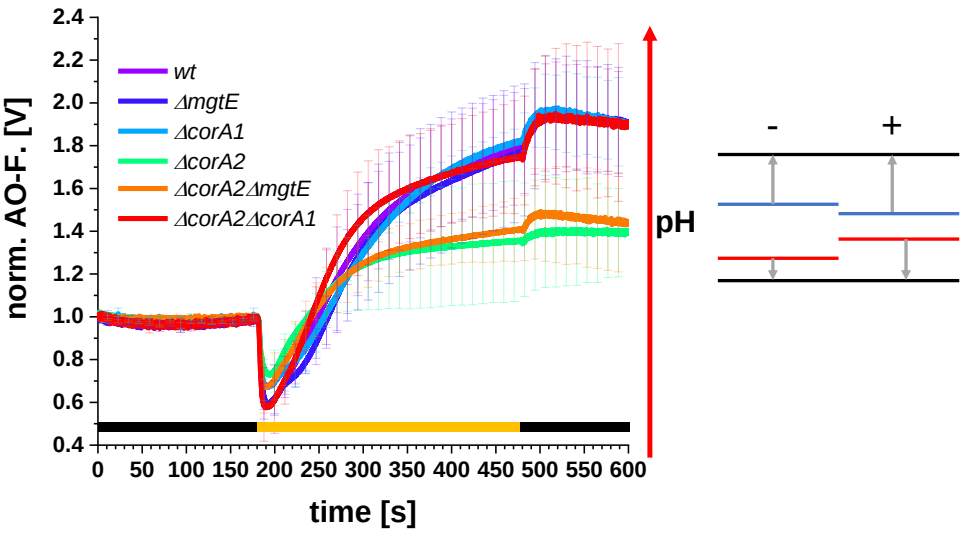

Figure 4.3.23: Light-induced changes in AO fluorescence determined in whole wt and mts cells upon addition of KCN.
AO fluorescence signals after 18 min incubation with KCN in the dark. Cells were grown under **H** conditions. All strains had a more pronounced signal drop when the light was switched on compared to untreated cells (Figure 4.3.21). This was followed by a strong signal increase. A rapid increase was observed when the light was switched off, followed by a slow decrease, or stay at the signal level (*ΔcorA2*). The scheme on the right represents the schematic view of the expected level of acidification and alkalisation in the cytoplasm (blue) and the thylakoid lumen (red) without (-) or with KCN (+). Experimental error bars indicate the means ±SDs of at least 3 biological replicates.

adaption prevents respiration by blocking the terminal oxidases. Thus, acidification of the thylakoid lumen in the dark is inhibited. Additionally, the electron transport chain localised in the PM is blocked. Monitoring the signal traces in the presence of KCN resulted in a strong signal decrease when the light was switched on and a strong subsequent signal increase (Figure 4.3.23). The *ΔcorA2* mt and the *ΔcorA2ΔmgtE* mt reached lower AO fluorescence signal levels in the light than all other strains. The scheme on the right in Figure 4.3.23 shows the expected level of acidification of the lumen (red) and the expected level of alkalisation of the cytoplasm (blue) without KCN (-) and after the addition of KCN in the dark (+). The lumen was

expected to be more alkalised due to less proton transfer across the TM in the dark (Miller *et al.* 2021), and the cytoplasm was expected to be more acidified (Sanders *et al.* 1982; Brummer *et al.* 1985; Maduh *et al.* 1990; Ryu *et al.* 2004).

4.3.1.12. Cellular localisation of the Mg^{2+} channels and analysis of the intracellular Mg^{2+} concentration

After the *in vivo* analysis of the mts where genes coding for the three predicted Mg^{2+} channels were deleted, the question remained in which membrane the respective channels are localised, the TM or the PM? Since knowing the channels' localisation would lead to a better interpretation of the obtained results, the channels were tagged with XFPs. In the first approach, the MgtE and CorA2 proteins were C-terminally tagged with a mTurqouise2 or GFP protein and the corresponding genes were under the control of their native promoters. Integration of the gene construct was confirmed by PCR (Figure 4.3.24). No fluorescence signal was observed

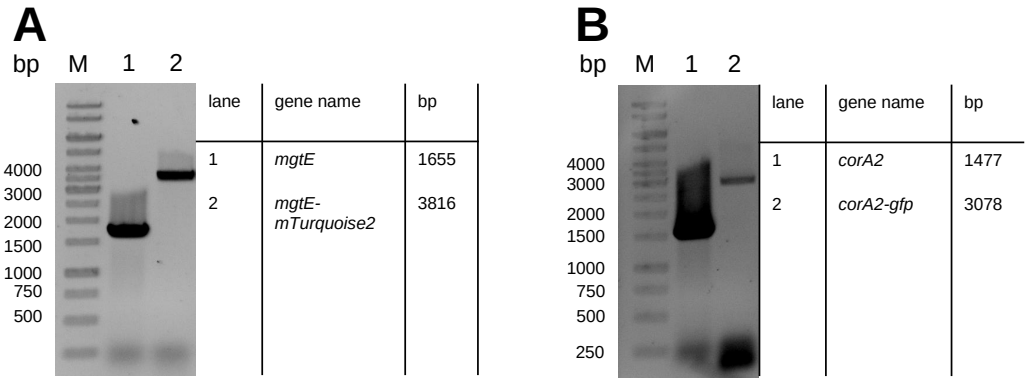

Figure 4.3.24: 1% agarose gels showing the products obtained after PCR of *Synechocystis* wt genes and the modified *mgtE* and *corA2* genes coding for XFP-tagged channels under the control of their native promoters.
(A) 1% agarose gel containing the PCR products of the *mgtE* gene from *Synechocystis* wt and the *mgtE* gene coding for a protein with a C-terminal mTurqouise2. (B) 1% agarose gels containing the PCR products of the *corA2* gene from *Synechocystis* wt and the *corA2* gene coding for a protein with a C-terminal GFP.

for both the C-terminally mTurqouise2 or the C-terminally GFP-tagged protein version. Either the expression levels were too low, or the position at the C-terminus was causing problems. Therefore, genes coding for a protein with an N-terminal YFP were next constructed and integrated into the genome of the wt and the corresponding mts under the control of a rhamnose-inducible promoter, using the

pCK306 plasmid (C. L. Kelly *et al.* 2018). Sequencing revealed a duplication region around the DNA coding for a glycine-serine (GS) linker between the channel protein and the YFP protein in the *yfp-corA1* construct (see section 5, Figure A.5.5). The integration of the gene constructs was confirmed by PCR for the wt, the *ΔmgtE* mt and the *ΔcorA2* mt, while integration into the *ΔcorA1* mt was not achieved (Figure 4.3.25 A). Therefore, the N-terminally tagged YFP version of CorA1 was analysed while maintaining antibiotic pressure. Before taking images using a fluorescence

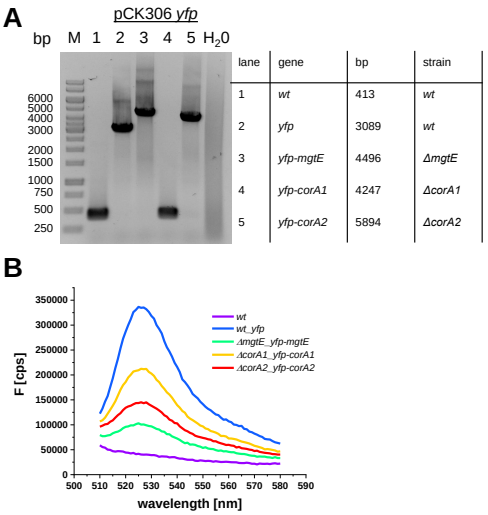

Figure 4.3.25: PCR products of genes coding for the YFP and YFP-tagged channels and the fluorescence signal observed after their expression.
(A) A 1% agarose gel with the PCR products of the pCK306 flanking region in the wt and the inserted YFP or YFP-tagged channel in the wt and the mt strains. The expected lengths of the constructs are listed in the table. (B) Before taking pictures with the fluorescence microscope, the expression of the YFP protein was checked with a fluorimeter. For this purpose, 200 µL of whole cells were filled into a cuvette, and YFP was excited at 495 nm. The recorded spectra showed a typical peak at 525 nm, the emission maximum of YFP. Wt was used as a control, and YFP expression in wt was used to verify the YFP signal.

microscope, YFP expression in whole cells was confirmed using a fluorimeter ∼ 24 h after induction of gene expression with 1 mg/mL rhamnose (Figure 4.3.25 B). The localisation of the expressed channels was checked with a fluorescence microscope equipped with a Zeiss ApoTome.2 to remove out-of-focus light (Figure 4.3.26 C, D, E). Chl *a* autofluorescence is depicted in red, and YFP fluorescence in green. *Synechocystis* wt showed faint green spots co-localised with Chl *a* autofluorescence (Figure 4.3.26 A). The wt expressing a YFP protein had a strong YFP fluorescence in the centre of the cell (Figure 4.3.26 B). *ΔmgtE* expressing YFP-MgtE showed YFP fluorescence around and co-localising with the Chl *a* autofluorescence (Figure 4.3.26 C). *ΔcorA1* expressing YFP-CorA1 showed mainly YFP fluorescence co-localising with the Chl *a* autofluorescence (Figure 4.3.26 D), and *ΔcorA2* expressing YFP-CorA2 cells showed YFP fluorescence clustered around the Chl *a* autofluorescence (Figure 4.3.26 E).

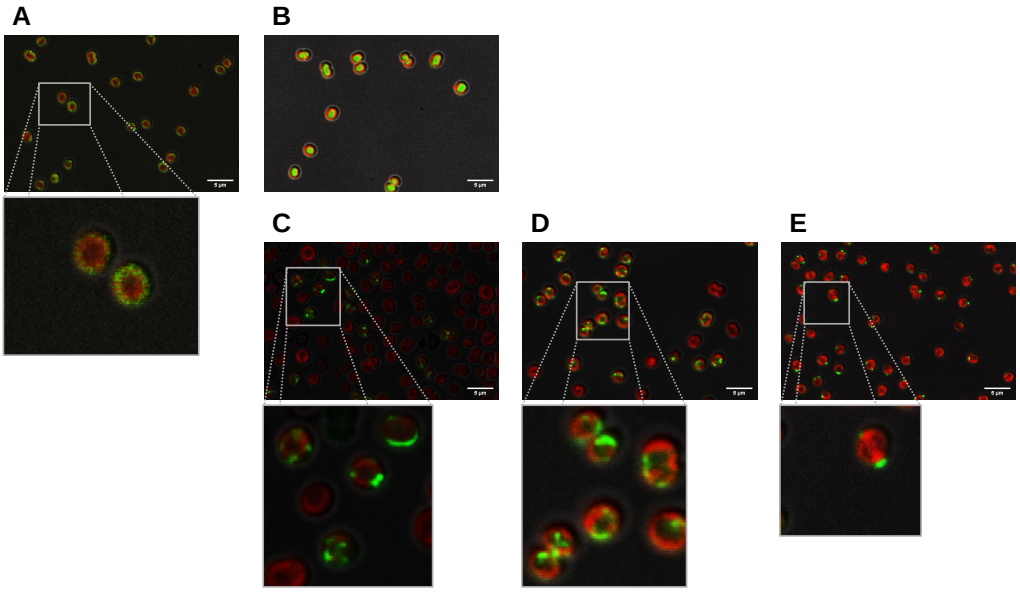

Figure 4.3.26: Cellular localisation of the YFP-tagged predicted Mg^{2+} channels. Overlay of bright field, Chl *a* fluorescence (red) and YFP fluorescence (yellow). Fluorescence images of *wt*, *wt_yfp*, *ΔmgtE_yfp-mgtE*, *ΔcorA1_yfp-corA1*, and *ΔcorA2_yfp-corA2* after induction with rhamnose. Chl *a* fluorescence was visible as a red ring near the PM, which was seen as a faint ring around the cell. A potential YFP signal caused by the fluorescence of the phycobilisomes was also observed in the wt. The YFP signal was visible in the cytoplasm of the YFP-expressing wt. The *ΔmgtE_yfp-mgtE* strain had a YFP signal that was outside of the thylakoids (at the PM) and co-localising with the thylakoids; the same was visible in the *ΔcorA1_yfp-corA1* cells. The *ΔcorA2_yfp-corA2* strain only showed fluorescence on the outside of the thylakoids.

4.3.1.13. Genomic integration of the genetically encoded Mg^{2+} sensor MARIO

It is known from experiments with intact chloroplasts that the stromal Mg^{2+} concentration increases when thylakoids are illuminated, possibly by Mg^{2+} from the thylakoid lumen acting as a counterion for the protons pumped into the thylakoid lumen across the TM (Dilley *et al.* 1965; Barber *et al.* 1974; Hind *et al.* 1974; Chow *et al.* 1976; Portis *et al.* 1976; Lyu *et al.* 2017). Therefore, changes in the Mg^{2+} concentration in *Synechocystis*' cytoplasm during the dark-to-light transition as a consequence of the generated ΔpH across the TMs were expected. Based on the fluorescence images (Figure 4.3.26), the MgtE and the CorA1 channels appeared to be localised in the TM and were of particular interest. To assess differences in the concentration in the free cytoplasmic Mg^{2+} between dark-adapted and light-exposed cells in the wt and mts, a plasmid containing an Mg^{2+} sensitive FRET sensor (MARIO (Maeshima *et al.* 2018)) under the control of the rhamnose-inducible promoter encoded by the pCK306 plasmid (C. L. Kelly *et al.* 2018) was constructed. The construct was in-

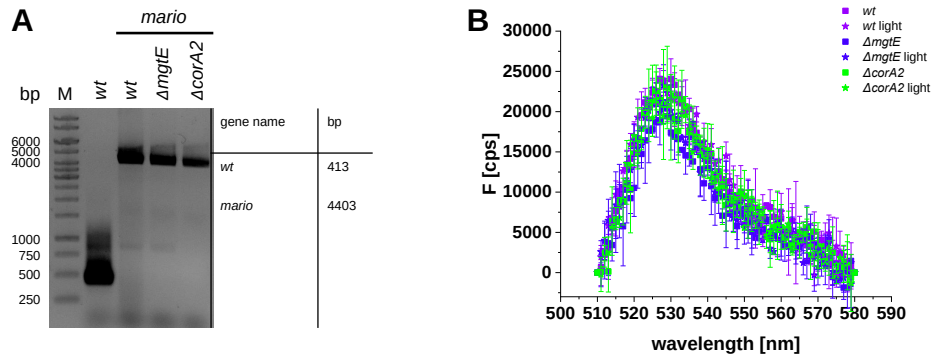

Figure 4.3.27: Genomic integration of the gene coding for the Mg^{2+} sensor MARIO and the YFP fluorescence measured in whole cells.
(A) The pKC306 plasmid was used to insert a rhamnose-inducible gene coding for MARIO into the *Synechocystis* genome. The 1% agarose gel confirms the successful integration of the DNA encoding the gene for the Mg^{2+} sensor MARIO into the genome of the wt, *ΔmgtE* and *ΔcorA2*. (B) YFP fluorescence was measured in whole cells containing the *mario* gene after induction with rhamnose. Fluorescence was measured after dark adaptation and after 10 min light exposure.

tegrated into the wt's, the *ΔmgtE* and the *ΔcorA2* mts' genome *via* homologues recombination (Figure 4.3.27 A). The expression of the constructs was verified by observation of the YFP emission in whole cells (Figure 4.3.27 B). YFP emission did not show any differences after dark adaption or light adaption. FRET signals have yet to be analysed. The construct for integration into the *ΔcorA1* mt still has to be constructed.

4.3.2. Discussion

4.3.2.1. All strains show Mg^{2+} concentration-dependent growth differences compared to the wt

Figure 4.3.2 shows the agarose gel with the PCR products, amplified with the different primer pairs shown in Figure 4.3.1. The *Synechocystis* wt genes and the inserted antibiotic cassettes in the KO strains integrated at the respective gene locus were amplified to verify the complete segregation of the mutant strains. Both, the *ΔcorA1* and the *ΔcorA2* single KO mt did not show any additional bands in the corresponding agarose gels (Figure 4.3.2 B, C), suggesting complete segregation. The expected band of the spectinomycin resistance cassette integrated into the genome at the *corA2* gene locus was not at 2475 bp. As the spectinomycin resistance is part of an Omega fragment (Prentki *et al.* 1984), it was probably lost by homologous recombination when cells were grown in the absence of Sp. After DNA amplification with the primers listed in Figure 4.3.1 B, there was still a faint band at 821 bp, the size of the wt PCR product, observable in the *ΔmgtE* KO mt, although the antibiotic cassette appeared to be fully integrated into the genome (Figure 4.3.2 A). The band at 821 bp was not observed in the *ΔcorA2ΔmgtE* double mt (Figure 4.3.2 E), implying that a complete KO of the *mgtE* gene was possible. As the *mgtE* gene had been knocked out before (T. Li *et al.* 2016), the segregation process in the *ΔmgtE* mt might have been incomplete. Still, a strong phenotype in the *ΔmgtE* mt was observed, and the complementation of the mt's phenotype by inserting a *yfp-mgtE* variant at another gene locus was possible (Figure 4.3.7 A). Thus, the observed strong phenotype was probably a consequence of the depletion of the *mgtE* gene and, consequently, the encoded protein. After DNA amplification of the *corA2* gene locus with the primers listed in Figure 4.3.1 B, a very weak band at 708 bp, the size of the wt PCR product, could be observed in the *ΔcorA2ΔmgtE* double mt. Since this band was not observed in the *ΔcorA2* mt, which was used to generate the double mt, the observed band might have resulted from primer annealing to incorrect template sites. Yet, knocking out the *mgtE* gene in combination with the *corA1* gene failed (Figure 4.3.2 D), implying that this double KO strain has a lethal phenotype and no other channel or transporter can take over the function of both channels. Since both YFP-tagged channels co-localise with the TMs autofluorescence (Figure 4.3.26 C, D), likely, the transport function of at least one channel in the TM is required for cell survival. Also, complete segregation of the *ΔcorA2ΔcorA1* double mt in combination failed. When the primers listed in Figure 4.3.1 B were used, PCR products of the genes coding for the two channels (673 bp (*corA1*) and 708 bp (*corA2*)) were visible in the agarose gel

(Figure 4.3.2 F). Since this was not the case for the single mts, the most likely explanation is that the segregation process for the first gene was still ongoing when segregation for the second gene was started or that persister cells (Samuilov *et al.* 2008) still encoding the gene grew when *ΔcorA2ΔcorA1* cells were grown in the absence of antibiotics. Although segregation appeared incomplete, the *ΔcorA2ΔcorA1* double mt showed a phenotype and was further analysed as a depletion mt. Knocking out the *sll1254* gene encoding a potential Mg^{2+} efflux channel failed, suggesting that the encoded protein is essential under the chosen growth conditions (Figure 4.3.3). When *Synechocystis* wt and mts cells were grown photoautotrophically (Figure 4.3.4 A) or photomixotrophically (Figure 4.3.4 B) at standard Mg^{2+} concentrations, no significant differences were observed between the growth rates of the wt and the mts. This has been previously observed for growth in BG11 for the *Δslr1216* KO strain (T. Li *et al.* 2016). Only the *ΔcorA2ΔmgtE* and the *ΔcorA2ΔcorA1* double mts grew slightly slower during the first 18 h under photomixotrophic conditions but reached wt-like saturation (Figure 4.3.4 B). None of the two mts showed altered growth rates under photoheterotrophic conditions (Figure 4.3.5), and the mts did not show significant changes in the amount of total carbohydrates under **H** conditions (Table 4.3.1). Additionally, respiration was not impaired to a higher degree than in the other mts under **H** conditions (Figure 4.3.15). No major differences were observed when the growth of *Synechocystis* wt and mt strains was analysed in the presence of DCMU (photoheterotrophic). Thus, wt and all mts appear to be able to compensate for the loss of LEF through the activity of respiratory complexes to the same extent. Moreover the mt strains appear unaffected in their ability to take up or break down glucose from the external medium. The lower respiration observed for all mts compared to the wt under **H** conditions (Figure 4.3.15) was, therefore, likely the result of impaired glucose production. When *Synechocystis* wt and mts were grown photoautotrophically in BG11 with 50 µM Mg^{2+}, the *ΔcorA1* mt and the *ΔcorA2ΔcorA1* mt and, to a lesser extent, the *ΔcorA2* mt showed an extended slow-growing phase before the log phase than the wt (Figure 4.3.6). The same was observed when *Synechocystis* wt was grown at low Mg^{2+} concentrations compared to high Mg^{2+} concentrations (see section 4.1, Figure 4.1.1). Thus, these three mts were more impaired by low Mg^{2+} concentrations than the wt. Since the growth of the *ΔcorA2* mt and the *ΔcorA2ΔcorA1* double mt, but not the *ΔcorA2ΔmgtE* double mt, was impaired under low Mg^{2+} concentrations, it seemed that knocking out the *mgtE* gene restored growth at low Mg^{2+} concentrations in the medium. Indeed, when grown photoautotrophically in BG11 with 10 µM Mg^{2+}, the *ΔmgtE* mt had

a growth advantage compared to the wt (Figure 4.3.7 A). The growth advantage of the *ΔmgtE* mt compared to the wt was not observed in the *ΔmgtE*_yfp-*mgtE* strain (Figure 4.3.7 B), indicating that the *mgtE* gene product was responsible for the observed difference. Since the growth advantage of *ΔmgtE* was not observed on BG11 agar plates supplemented with 10 µM Mg^{2+}, I assumed that the reason for this might be related to reactive oxygen species (ROS) rather than a better uptake or lower requirement for Mg^{2+}. Note that $Na_2S_2O_3$, which is always added to BG11 agar plates, is a ROS scavenger (Stewart *et al.* 1999; Z. Wang *et al.* 2002). Indeed, when grown on BG11 agar plates without $Na_2S_2O_3$, only the *ΔmgtE* mt could grow to some extent (Figure 4.3.7 C). Excess Co^{2+} is toxic to cells as it can impair the formation of iron-sulfur clusters as observed in *E. coli* (Ranquet *et al.* 2007), and excess Co^{2+} can result in the production of ROS in plants (Mahey *et al.* 2020). Therefore, the effect of excess Co^{2+} on *Synechocystis* wt and mts growth was examined. Again, all *ΔmgtE* mts had a growth advantage (Figure 4.3.8 A) suggesting that the gene product of *mgtE* can transport Co^{2+} as known for other CorA and MgtE channels (Hmiel *et al.* 1986; Smith *et al.* 1995). The addition of excess Mg^{2+} restored the growth of all strains (Figure 4.3.8 B). Thus, I conclude that the *mgtE* gene in *Synechocystis* encodes an ion channel transporting both Co^{2+} and Mg^{2+} that compete for the channel's binding sites. The channel is probably localised in the PM, as previously shown in proteomic analysis (Pisareva *et al.* 2011; Liberton *et al.* 2016). The CorA2 channel possibly also mediates Co^{2+} flux, yet to a lesser extent than the MgtE channel, since the *ΔcorA1* mt was more affected when grown in the presence of additional Co^{2+} (Figure 4.3.8 A) than the *ΔcorA2ΔcorA1* mt. Additionally, CorA2 might mediate Mg^{2+} flux since the *ΔmgtE* mt grew better than the *ΔcorA2ΔmgtE* mt when grown in the presence of additional Co^{2+}, and this difference was cancelled out when additional Mg^{2+} was added (Figure 4.3.8). The CorA1 channel appeared not to be involved in Co^{2+} flux, as the *ΔcorA1* mt grew worse than the *ΔcorA2ΔcorA1* mt in the presence of additional Co^{2+}. But CorA1 might be involved in Mg^{2+} flux as the *ΔcorA2* mt grew slightly better than the *ΔcorA2ΔcorA1* mt when grown at concentrations of 50 µM Mg^{2+} (Figure 4.3.6). Thus, it is likely that the growth defect observed in the *ΔcorA1* mt compared to the wt at 50 µM Mg^{2+} concentrations was not only due to Mg^{2+} limitation but may have additionally resulted from Co^{2+} intoxication.

4.3.2.2. *Synechocystis* wt and mts form different EPS layers when grown at low Mg^{2+} concentrations

When grown under **H** conditions, no differences were observed in EM images between the wt and the mts (Figure 4.3.9). Yet, some mts had an enlarged EPS layer when cells were grown under **L** conditions (Figure 4.3.10). The formation of an increased EPS layer was observed for the *ΔmgtE* mt and the *ΔcorA1* mt but was much less pronounced in the *ΔcorA2* mt and absent in the *ΔcorA2ΔmgtE* and *ΔcorA2ΔcorA1* mt (Figure 4.3.10). As already stated in section 4.1.2.1, the formation of a biofilm might help cyanobacteria to accumulate Mg^{2+} in the environment while avoiding heavy metal intoxication (De Magalhães *et al.* 2004; Pereira *et al.* 2009) and is connected to coping with changing environmental conditions (De Philippis 1998; Pereira *et al.* 2009; Rossi *et al.* 2015). Since *Synechocystis* EPS consists of up to 12 different monosaccharides (Pereira *et al.* 2009), the absence of an enlarged EPS layer under Mg^{2+} limitation could result from limited CO_2 assimilation since Mg^{2+} limitation results in poor CO_2 assimilation in plants (Jamali Jaghdani *et al.* 2021). While a missing EPS layer could indicate biased CO_2 assimilation in these three mts, this seemed to be reflected by less respiration in all mts (Figure 4.3.15). Although the amount of carbohydrates in the wt and mts was unchanged under both growth conditions (Table 4.3.1) and comparable among all studied strains, the respiration rate was already lower in all mts under **H** conditions (Figure 4.3.15), implying that all mts could be impaired in carbon fixation and unable to produce enough glucose for respiration. In addition to the observation that *ΔcorA2ΔcorA1* mt did not establish an enlarged EPS layer, the double mt also seemed to accumulate large amounts of storage products (probably cyanophycin). Cyanophycin is a nitrogen/carbon reserve polymer typically occurring under unbalanced growth conditions, including nutrient limitation (sulfate, phosphate, or potassium deficiency) (Watzer *et al.* 2018). Since Mg^{2+} limitation was accompanied by ribosome degradation in *E. coli* (McCarthy 1962), the accumulation of cyanophycin could correlate with impaired ribosome function under Mg^{2+} limitation, such that the cell has a reduced protein synthesis and stores the available nitrogen. Under Mg^{2+} deficiency, the cyanobacteria *Cyanothece* strain 16Som2 and *Cyanospira capsulata* showed lower total protein levels (De Philippis *et al.* 1991; De Philippis *et al.* 1993).

4.3.2.3. Mg^{2+} limitation results in altered pigmentation accompanied by less PSI and changed energy distribution between PSI and PSII

The Chl *a* amount under **H** conditions was slightly but significantly higher in the

ΔcorA1 mt and the *ΔcorA2ΔcorA1* mt than in the wt (Figure 4.3.12 A), which was accompanied by an apparently increased PSI amount in these mts (Figure 4.3.14 A). An unaltered Chl *a* content has been previously observed for growth in standard BG11 for the *Δslr1216* KO strain (T. Li *et al.* 2016). Yet, as with wt, Mg^{2+} limitation resulted in a lower Chl *a* content in all studied strains, most obvious in the *ΔcorA1* mt (Figure 4.3.12 A). The decrease in Chl *a* is common under Mg^{2+}-limiting conditions in plant chloroplasts (Kobayashi *et al.* 2015). Since Co^{2+} intoxication in plants also leads to reduced Chl *a* levels (Mahey *et al.* 2020), the more pronounced Chl *a* reduction in the *ΔcorA1* mt may have been the result of higher Co^{2+} levels under **L** conditions (as discussed in section 4.3.2.1 for growth inhibition at low Mg^{2+} concentration, Figure 4.3.6). While the number of Chl *a* decreased significantly in all strains under **L** conditions, the number of total Car was less affected. Still, it significantly decreased in the wt and the *ΔcorA1* mt but was only marginally lower or unchanged under Mg^{2+} depletion in all other mts (Figure 4.3.12 B). Thus, the overall Chl *a*:Car ratio was lower, which was most pronounced in the *ΔcorA1* mt (Figure 4.3.12 C). It was visible that Mg^{2+} limitation resulted in a lowered PSI:PSII ratio as judged from 77K spectra (Figure 4.3.13 A, B) yet to different extents in the respective mts. Overall the changed ratio was the result of a decreased number of PSI per cell (Figure 4.3.14 A) in all studied strains under **L** conditions. As discussed in section 4.1.2.2, a decrease of PSI reaction centres under Mg^{2+} limiting conditions has been proposed (Hermans *et al.* 2004) and observed in plants (Farhat *et al.* 2015), and reduction of PSI at low Mg^{2+} concentrations seems particularly reasonable in *Synechocystis* since PSI consumes more than three times more Chl *a* molecules than PSII (Jordan *et al.* 2001; Umena *et al.* 2011). In addition to an altered PSI:PSII ratio, the PC:Chl *a* ratio increased in all studied strains when cells were grown under **L** conditions (Figure 4.3.11 D). The altered pigment contents (Figure 4.3.12) and ratios (Figure 4.3.11) influenced the energy distribution between the two photosystems, as evident from 77K emission spectra (Figure 4.3.13 C, D). 77K spectra after exciting PBSs at 580 nm under **L** conditions revealed an enhanced fluorescence at 685 nm and 695 nm compared to the emission at 725 nm (Figure 4.3.13 D), indicating that PBSs were more associated with PSII when cells were grown at low Mg^{2+} concentrations. Yet, this was less pronounced in all mts lacking *corA2*. Still, it reflects the lower PSI:PSII ratio under Mg^{2+} depletion in all strains as judged from the 77K spectra after Chl *a* excitation (Figure 4.3.13 A, B), mainly because of a reduced PSI amount (Figure 4.3.14). When Chl *a* was excited under **L** conditions, the ratio of the peaks at 685 nm (CP43 and CP47) and

695 nm (CP47) (Andrizhiyevskaya *et al.* 2005) was altered compared to **H** conditions (Figure 4.3.13 A, B). The 685 nm peak was higher than the 695 nm peak in the wt, the *ΔmgtE* mt and the *ΔcorA1* mt but not in the case in all mts lacking *corA2*. These mts had a higher peak at 645 nm (PC (Sidler 1994; Spät *et al.* 2018)) after PBS excitation under **H** and **L** conditions (Figure 4.3.13 C, D). Since the PC amount per cell was comparable between the wt and all mts lacking *corA2* (Table 4.3.1), the changed PC:APC ratio might indicate impaired electron transfer between PC and APC (Biswas *et al.* 2020). Changes in PSs contents and energy distribution also altered the PSs' activity. Figure 4.3.16 shows that F_v/F_m values varied little, if at all, between the two growth conditions and among the strains. Still, the PQ pool appeared to be more reduced under **L** conditions in all mts and the wt, as evident by comparing the F_v/F_m value measured with DCMU (Figure 4.3.16) and the initial Y(II) value (Figure 4.3.17 A, B). If the F_v/F_m level is much higher when measured with DCMU than the Y(II) value, one can assume that the PQ pool is in a more reduced state. Although the F_v/F_m value was not drastically altered, Y(II) decreased in all observed strains under **L** conditions compared to **H** conditions, yet to different extents. Thus, the efficiencies of light utilisation of the PSs under different light conditions (Genty *et al.* 1989) was decreased in all studied strains under Mg^{2+} limitation. The decrease in Y(II) under **L** conditions was mainly a result of less PSI and therefore a more reduced PQ pool, as already discussed for the wt (see section 4.3.2.3). A decrease in PSII activity under Mg^{2+} depletion was also observed in the cyanobacterium *Arthrospira platensis* (Urek *et al.* 2019). Although Y(II) decreased significantly in all studied strains, the rate of O_2 evolution was less affected. Still, it somewhat decreased under **L** conditions compared to **H** conditions in all strains (Figure 4.3.15).

4.3.2.4. CorA1 and MgtE apparently influence the energy transduction at the TM

Despite having a slightly higher PSI amount per cell than the wt strain (Figure 4.3.14) , the *ΔcorA1* mt had a lower Y(II) (Figure 4.3.17), a higher Y(I), and a lower Y(ND) (Figure 4.3.18 A) under **H** conditions than any other strain. The higher Y(I) and lower Y(ND) in the *ΔcorA1* mt were not accompanied by faster $P_{700}{}^+$ re-reduction kinetics (Figure 4.3.19 A) when compared to the wt and the other mts probably as a result of the higher PSI content in that mt (Figure 4.3.14). Also, $P_{700}{}^+$ re-reduction kinetics in the presence of DCMU were not significantly faster compared to the wt (see section 5, Figure A.5.4), thus that respiratory elec-

tron input does not appear to reduce the PQ pool to a higher rate in the *ΔcorA1* mt. Still loss of the CorA1 protein, in line with the observed localisation of YFP-CorA1 in the TM (Figure 4.3.26 D) somehow alters the electron transport along the TM as observed in the wt only under **L** conditions. But since the localisation of YFP-CorA1 was only observed once and under antibiotic pressure, this must be considered with care. As for CorA1 also MgtE seems to alter the electron transfer properties at the TM. In spite of the fact that $P_{700}{}^{+}$ re-reduction kinetics measured in the presence of KCN were faster than those measured without KCN in all examined strains, this was not the case in the *ΔmgtE* mt and seemed less pronounced in the *ΔcorA2ΔmgtE* double mt (Figure 4.3.20 A). Thus, the *ΔmgtE* mt appears to have less respiration *via* the TOs localised in the TM. This implies that the need for PQ pool relaxation *via* the TOs was lower than in the wt, which is in good agreement with the lower amount of PSII under **H** conditions in the *ΔmgtE* mt (Figure 4.3.14). A stronger signal decrease upon switching the light on under **H** conditions (Figure 4.3.21) in the AO measurements (Figure 4.3.21) agrees well with the assumed lower rate of electron transfer to the TOs in the TM. The dual localisation of YFP-MgtE in the TM and the PM (Figure 4.3.26 C) is consistent with the influence of MgtE on electron transfer along the TM. In conclusion, both TM-localised tagged proteins (Figure 4.3.26 C,D) appear to influence electron transfer at the TM. The inability to generate a double KO mt (Figure 4.3.2 D) may be explained by this.

4.3.2.5. Mg^{2+} deficiency apparently reduces both the production and consumption of energy equivalents

Measuring alkalisation events with AO in cyanobacteria revealed one alkalisation event (Teuber *et al.* 2001), which could not be further divided into several peaks but appeared to be biphasic (see section 4.2). Although the photosynthetic machinery of all mts was affected to different extents, all seemed impaired in the formation of a wt-like pH gradient across the membranes under both growth conditions (Figure 4.3.21). As discussed in section 4.2, the intensity of the initial AO signal decrease when the light is switched on is mainly influenced by the PSII activity and the acidification of the lumen in the dark. Compared to **H** conditions, the wt and the *ΔmgtE* mt showed a less pronounced signal decrease under **L** conditions in line with a reduced Y(II) (Figure 4.3.22 A). Since a reduced Y(II) was observed under **L** conditions in all studied strains and the number of PSII was comparable among all strains, the stronger luminal acidification when the light was switched on in the *ΔcorA1* mt, the *ΔcorA2* mt and both double mts compared to the wt

could result from less luminal acidification in the dark or less proton extrusion at the PM. To address this question, one could compare the AO signal with the acridine yellow (AY) signal, which provides information on cytoplasmic alkalisation (Teuber *et al.* 2001) and additionally, measure the pH of the surrounding medium. Likewise a changed volume of the thylakoid volume cannot be precluded, albeit significant changes between the wt and the mts were not seen in EM images under **L** conditions (Figure 4.3.10). Alkalisation of the cytoplasm appeared to be biphasic in the mts, with the most significant difference compared to the wt after 250 s. While in the *ΔcorA1* mt, the signal increase indicated a strong but late alkalisation of the cytoplasm in the second phase, the signals observed in the *ΔmgtE* mt, the *ΔcorA2* mt, and the *ΔcorA2ΔcorA1* mt remained at a lower level compared to the wt. In the *ΔcorA2ΔmgtE* mt, the signal declined, starting at 250 s. These differences between the wt and all mts in the AO signal that reflected cytoplasmic alkalisation in the light were observed under both growth conditions. Thus, it appears that all mts have a reduced AO signal in the light (Figure 4.3.21) as a result of impaired respiration (Figure 4.3.15) already under **H** conditions. The further reduced AO signal in the light under **L** conditions likely results from additionally reduced activities of PSII and, therefore, less proton pumping into the lumen along the ETC of the TM. The fast AO fluorescence increase observed when the light was switched off is mainly caused by the rapid decrease in acidification of the TM lumen caused by stopped water splitting at PSII. Comparing the fast-decreasing AO signal observed when the light was switched on with the fast signal increase observed when the light was switched off provides some information about the activity of PSII in the light. A slightly reduced PSII activity was observed, probably because of increased luminal acidification in the wt, which was less pronounced in the mts and not seen in the *ΔmgtE* mt under **H** conditions (Figure 4.3.22 A, B). This difference between the AO signal increase and decrease when the light was switched on/off was less pronounced in all strains when the cells were grown under **L** conditions (compared to **H** conditions). Thus, the ability to acidify the lumen seems decreased when cells are grown under **L** conditions. After the rapid increase upon switching the light off, the AO signal decreased in the wt. This AO signal decrease was less pronounced under **L** conditions. The mts showed less or no signal decrease or even a signal increase under **H** conditions, and all mts showed only a signal increase under **L** conditions (Figure 4.3.22). The decrease in the AO signal when the light was switched off has been previously attributed to the consumption of energy equivalents (Teuber *et al.* 2001). Many CBB cycle enzymes require both (the here limited) Mg^{2+} as a cofactor

plus alkalisation of the TM lumen for proper function (Lorimer *et al.* 1976; Flügge *et al.* 1980; Mott *et al.* 1986; Mangan *et al.* 2016). Therefore, impaired production and consumption of redox equivalents in the mts under **H** conditions and the wt and the mts under **L** conditions might result in a smaller signal decrease. The signal increase in the mts might be caused by proton extrusion from the cytoplasm into the medium in the dark (Inago *et al.* 2020), which was probably only visible when there was less consumption of energy equivalents, seen as cytoplasmic acidification.

4.3.2.6. The CorA2 channel seems to influence proton translocation across the PM

AO signals determined under **H** conditions after incubating 18 min with KCN in the dark gave information about proton transfer across membranes without the interference of terminal oxidases. When the light was switched on, the AO signal decrease was steeper in all strains compared to the signal without KCN. That is because the TOs in the TM cannot attribute to luminal acidification in the dark. Thus, when cells were incubated with KCN in the dark, the lumen was overall more alkalised and when the light was switched on protons could be pumped into the lumen to a higher extent which results in a more pronounced decrease of the AO fluorescence signal (Miller *et al.* 2021). This was observed in the wt and all mts yet to different extends. After 18 min of KCN incubation, the cytoplasm was expected to be rather acidified (Sanders *et al.* 1982; Brummer *et al.* 1985; Maduh *et al.* 1990; Ryu *et al.* 2004). Indeed, the subsequently observed AO signal rise was very strong, and only the *ΔcorA2* mt and the *ΔcorA2ΔmgtE* mt did not reach wt-like AO signal levels. The lower level of the AO signal observed in the *ΔmgtE* mt, the *ΔcorA1* mt and the *ΔcorA2ΔcorA1* mt without KCN during illumination are therefore likely linked to impaired respiration. At the same time, respiratory independent processes seemed to be the reason for a lower AO signal during illumination in the presence of KCN in the *ΔcorA2* mt and the *ΔcorA2ΔmgtE* mt. The apparently less alkalised cytoplasm in these mts could result from less proton pumping along the ETC in the TMs and/or altered proton transfer at the PM. Since the $P_{700}{}^{+}$ re-reduction was wt-like in *ΔcorA2* and *ΔcorA2ΔmgtE* under KCN treatment (Figure 4.3.20), the electron transfer along the ETC in the TMs seems relatively unaffected. Eventually, there is less proton extrusion at the PM. Although lowered alkalisation of the cytoplasm in the presence of KCN during illumination was not observed in *ΔcorA2ΔcorA1* mt (probably due to incomplete segregation (Figure 4.3.2 F)), it is well possible that CorA2-mediated Mg^{2+} flux across the PM

is indirectly coupled to proton transfer across the PM. Proton transfer across the PM is influenced by the Na^+ concentration of the surrounding medium (Kaplan *et al.* 1989; Katoh *et al.* 1996; Sonoda *et al.* 1998), and Mg^{2+} dependent Na^+ extrusion has been observed in rice (Z. C. Chen *et al.* 2017). Thus altered Mg^{2+} and Na^+ flux across the PM could affect proton extrusion at the PM, resulting in less alkalisation during illumination in the *ΔcorA2* and the *ΔcorA2ΔmgtE* mt. The expression of the *sll0671* gene was connected to salt stress (Qiao *et al.* 2013). Although no salt sensitivity was observed in a previous analysis of an *sll0672-sll0671* KO (H. L. Wang *et al.* 2002) I suggest testing the growth of the mts lacking *corA2* in the presence of high and low Na^+ concentrations. In line with NaCl stress is a decreased excitation energy delivery to PSII and increased excitation delivery to PSI under **L** conditions compared to the wt (Figure 4.3.13 D). A decrease in excitation energy transfer from PBS to PSII but an increase to PSI has been observed in the cyanobacterium *Spirulina platensis* under NaCl stress (Sudhir *et al.* 2005; T. Zhang *et al.* 2010).

4.3.2.7. Conclusion

All mts were impaired in respiration already under **H** conditions (Figure 4.3.15), while respiration of the wt was only affected under **L** conditions. Lower respiration rates seem to contribute to a lower pH gradient across *Synechocystis* membranes. A reduced pH gradient across the TM could have resulted in less NADPH and ATP production or impaired NADPH and ATP utilisation in the CCB cycle in all mts. To test this hypothesis, NADPH and ATP levels in the wt and the mts should be determined in future experiments. CorA1 appears to influence photosynthetic electron transport. In the KO strain either decreased intracellular Mg^{2+} concentrations and/or altered Mg^{2+} fluxes across the TM result in altered photosynthetic electron transport. Although YFP-CorA1 was observed in the TM it cannot be ruled out that the channel has a dual localisation in the PM and the TM. It is clear that an Mg^{2+} import system is needed in the PM, and MgtE and CorA2 are two likely candidates. Based on the here presented analyses, MgtE clearly transports Co^{2+} across the PM, and since an excess of Mg^{2+} compensated for this, MgtE very likely is an Mg^{2+} channel in the PM. CorA2, in line with the observed localisation of YFP-CorA2 in the PM, also seems to enable Co^{2+} and Mg^{2+} flux across the PM. The loss of the MgtE and the CorA2 channel results in less EPS, and CorA2 in contrast to CorA1 and MgtE appears to influence proton transport across membranes despite respiraton. Still, a complementation assay is required for the *ΔcorA1* and the *ΔcorA2* KO

strain. The generated mts expressing the genetically encoded Mg^{2+} sensor MARIO could be a nice tool to investigate how far Mg^{2+} concentrations in the cytoplasm are altered between the wt and the mts, especially during dark-light transitions. This might be helpful to answer the question of whether the predicted localisations and functions of the three Mg^{2+} channels are correct, and under which conditions the three channels transport Mg^{2+} ions across *Synechocystis* membranes.

4.4. *In vitro* studies of Mg^{2+} channel homologs from the cyanobacterium *Synechocystis* sp. PCC 6803

To elucidate the activity of the predicted MgtE and the two predicted CorA channels *in vitro*, the three encoding genes were heterologously expressed in *E. coli*. Although there is no sequence homology between CorA and MgtE (Smith *et al.* 1995), the basic principles of the channel functions are similar. Both channels have a high amount of charged amino acid residues in the N-terminal region (Smith *et al.* 1995) (see section 5, Table A.5.1) and share a comparable Mg^{2+}-regulated transport mechanism, as they both function as ligand-gated ion channels with Mg^{2+}-binding resulting in channel closure (Payandeh *et al.* 2013). Mg^{2+} influx through both channels is driven by the membrane potential (Maguire 2006). So far, there are no experimentally derived structures of the *Synechocystis* channels available.

4.4.1. Results

4.4.1.1. Putative Mg^{2+} channels in *Synechocystis* and their predicted structure

Based on solved structures of similar proteins, the structures of *Synechocystis* MgtE, CorA1 and CorA2 were predicted by the AlphaFold server (Jumper *et al.* 2021; Varadi *et al.* 2022) (Figure 4.4.1). Most parts of the predicted *Synechocystis* structures showed a high confidence value, *i.e.* the probability that structures predicted by the AlphaFold sever represent the actual structures of the three proteins is high. Based on these structures, I next compared these with solved structures of CorA of *Thermotoga maritima* (Figure 4.4.4) and MgtE of *Thermus thermophilus* (Figure 4.4.2). Therefore, the predicted structures were aligned to solved crystal structures of the corresponding channel with PyMOL (Schrödinger, LLC 2021). First, the amino acids at the positions of the putative Mg^{2+} binding sites of *Thermus thermophilus* MgtE were compared to the respective amino acid positions of the aligned *Synechocystis* MgtE structure (Table 4.4.1, Figure 4.4.2). MgtE of *Thermus thermophilus* has 7 putative Mg^{2+}-binding sites (MG1-MG7), formed by 1-3 amino acids (Table 4.4.1).

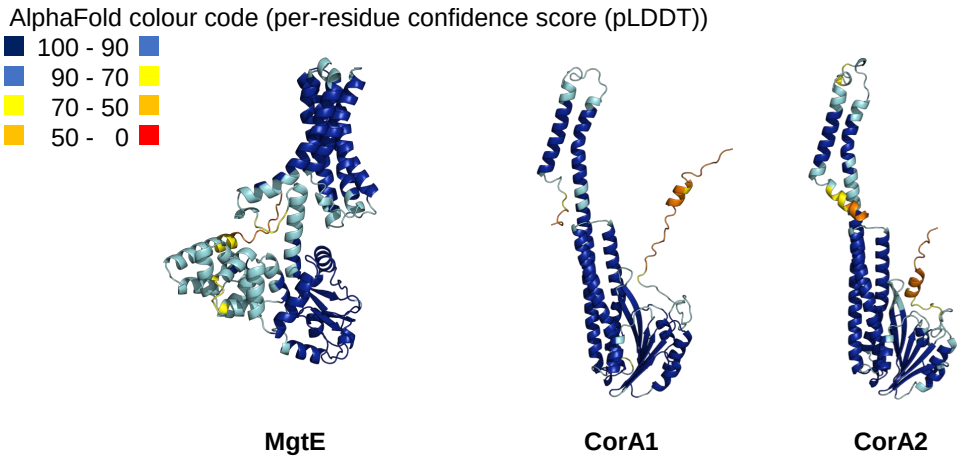

Figure 4.4.1: AlphaFold structures of the predicted MgtE and CorA proteins of *Synechocystis*. The predicted structures of the three monomers forming Mg^{2+} channels are shown in cartoon presentation, coloured according to their predicted local-distance difference test (pLDDT) value (Jumper *et al.* 2021). While most parts of the structures were at a high confidence level, all three structures also showed areas with a low confidence level. In MgtE (left), this was the case for the N domain of the cytoplasmic domain, while in the CorA (middle, right) channels, the helices at the N- and C-termini were affected. Graphics were created with PyMOL (Schrödinger, LLC 2021).

Table 4.4.1: Mg^{2+} binding sites in the MgtE channel.
Comparison of the amino acids forming the putative Mg^{2+} binding sites (Hattori *et al.* 2007; Hattori *et al.* 2009) in the *Thermus thermophilus* MgtE protein (PDB 2ZY9) (Hattori *et al.* 2009) with the amino acids at the same position of the aligned predicted *Synechocystis* MgtE structure. Amino acids that differ from the amino acids at the binding site positions of the solved structure are marked in red and amino acids that are unlikely to be involved in Mg^{2+} binding are marked in bold red. While the amino acids at the MG1-MG4 binding sites are very similar, the amino acids at the MG5-MG7 binding sites differ.

Mg^{2+} binding site	***Thermus thermophilus*** MgtE	***Synechocystis*** MgtE
MG1	Asp432, Ala428	Asp446, Thr442
MG2	Glu258, Glu255, Asp214	Glu271, Glu268, Asp227
MG3	Glu259, Asp418, Glu216	Glu272, Asp432 Glu229,
MG4	Asp91, Asp247	Asp107, Asp260
MG5	Asp226, Ala223	Glu239, Gln236
MG6	Gly136, Asp95	**Arg149**, **Arg111**
MG7	Glu59	Asp75

The respective amino acids of the *Synechocystis* MgtE Mg^{2+} binding sites are also listed in Table 4.4.1. 60% of the predicted amino acids match the actual Mg^{2+}

binding sites in *Thermus thermophilus*. While the same amino acids were in the position of the binding sites MG2-MG4, the amino acids differ in MG1 and MG5-MG7. In MG1, Thr442 is in the position of Ala428. In MG5, the acidic residue of Glu239 is in the position of the acidic residues Asp226 and Gln236 at the position of Ala223. In MG6, two arginines are in the position of the potential binding site Gly136 and Asp95. Since it is doubtful that two arginines are involved in Mg^{2+} binding, it is questionable to what extent the prediction at this position is correct, although both arginines had a pLDDT score of at least 90. In MG7, the acidic residue Asp75 is in the position of the acidic Glu59. While MG1-MG5 are structurally well

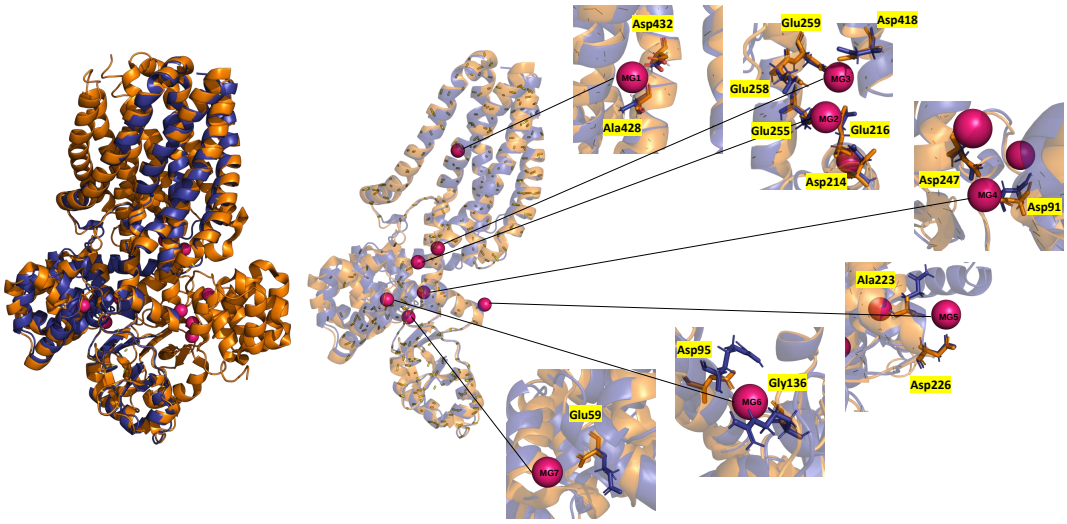

Figure 4.4.2: Mg^{2+} binding sites MG1-MG7 in the MgtE channel.
Positions of the putative Mg^{2+} (pink) binding sites (Hattori *et al.* 2007; Hattori *et al.* 2009) in the crystal structure of *Thermus thermophilus* MgtE (PDB 2ZY9) (Hattori *et al.* 2009) (orange) compared with the amino acids of the predicted *Synechocystis* MgtE structure (blue) after aligning both structures using PyMOL (Schrödinger, LLC 2021). While the orientation of the amino acids at the MG1-MG5 binding sites are very similar, the orientation and the amino acids at the MG6-MG7 binding sites differ. Amino acids are labelled in three letter code.

aligned and the amino acids replacement can be classified as "conservative", MG6-MG7 differ not only in their amino acids but also in their orientation within the two structures. Overall, the predicted MgtE structure of *Synechocystis* is mainly comparable with the resolved crystal structure of *Thermus thermophilus* MgtE, and the binding sites of MG1-MG4 could well be at the same positions as identified in the *Thermus thermophilus* structure (Figure 4.4.2). Comparing the crystal structure of *Thermotoga maritima* CorA (PDB 4I0U) (Nordin *et al.* 2013) with the two predicted

Synechocystis CorA structures, an overall comparable monomer structure can be observed. The amino acids at the predicted Mg^{2+} binding sites differ only slightly (Table 4.4.2).

Table 4.4.2: Mg^{2+} binding sites in CorA channels.
Comparison of the amino acids of the putative binding Mg^{2+} sites (Eshaghi *et al.* 2006) in the crystal structure of *Thermotoga maritima* CorA (PDB 4I0U) (Nordin *et al.* 2013) with the amino acids at the same position of the aligned predicted *Synechocystis* CorA channel structures after aligning both structures using PyMOL (Schrödinger, LLC 2021). Amino acids that differ from the amino acids at the binding site positions of the solved structure are marked in red. While the amino acids at the MG1 binding site are identical, the amino acids at the MG2 binding sites differ to some extent.

Mg^{2+} binding site	***Thermotoga maritima*** CorA	***Synechocystis*** CorA1	***Synechocystis*** CorA2
MG1	Asp89, Ala253	Asp114, Asp280	Asp100, Asp265
MG2	Leu12, Glu88, Asp253 Asp175	Ser38, Glu113, Asp280 Asp201	Ser24, Glu99, Asp265 Asp187

80% of the amino acids predicted to form the Mg^{2+} binding sites match the ac-

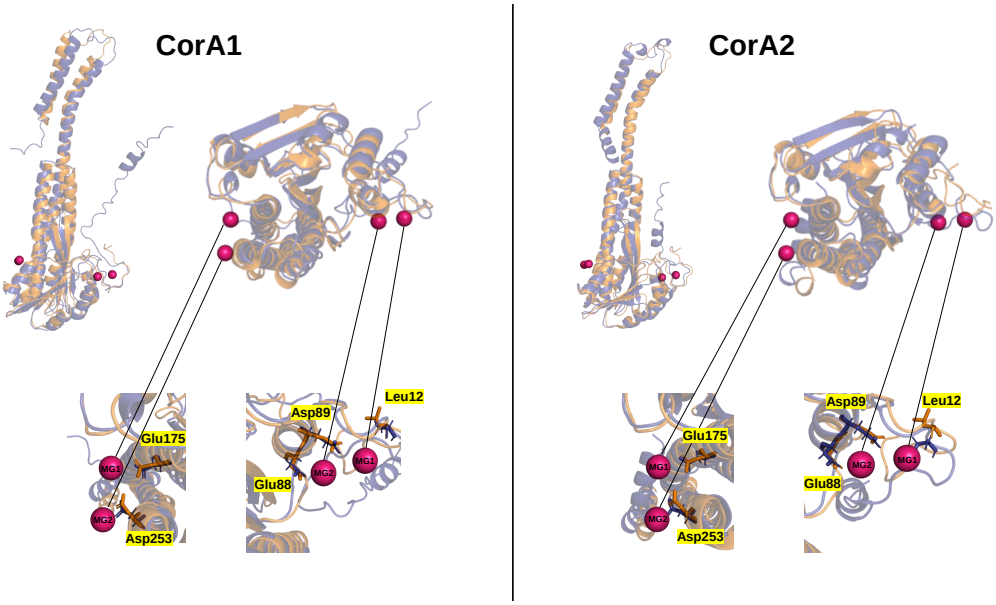

Figure 4.4.3: Mg^{2+} binding sites MG1-MG2 identified in the CorA channel structure.
Positions at the putative Mg^{2+} (pink) binding sites (Eshaghi *et al.* 2006) in the crystal structure of *Thermotoga maritima* CorA (PDB 4I0U) (Nordin *et al.* 2013) (orange) and the corresponding amino acids of the predicted *Synechocystis* CorA (left: CorA1, right: CorA2) channels after aligning both structures using PyMOL (Schrödinger, LLC 2021). While the position of the amino acids at the MG1 binding sites are very similar, the amino acids found in the MG2 binding sites differ to some extent. Amino acids are labelled in three letter code.

tual Mg^{2+} binding sites found in the *Thermotoga maritima*'s cytoplasmic domain

structure. While in MG1, all amino acids are identical and align very well in the structures (Table 4.4.2, Figure 4.4.3), the binding sites of MG2 have a serine at the Leu12 position. The overlay of the amino acids in this more flexible area did not match at all positions. Still, the acidic amino acids in the MG2 binding again matched very well. The conserved Gly-Met-Asn (GMN) motif sandwiched between two conserved transmembrane helices at the C-terminus (Knoop *et al.* 2005) was found at the entrance of the ion conducting pore (Figure 4.4.4). There were differences in the two predicted transmembrane-spanning helices and the N-terminal cytoplasmic domain of CorA1 and CorA2 compared to the structure of *Thermotoga maritima* CorA. CorA1 and CorA2 showed an elongated unstructured region at the N-terminus containing an additional helix within this region. CorA1 had an elongated unstructured region at the C-terminus, while CorA2 showed an additional helix at the C-terminus (Figure 4.4.4). The amino acids and their respective

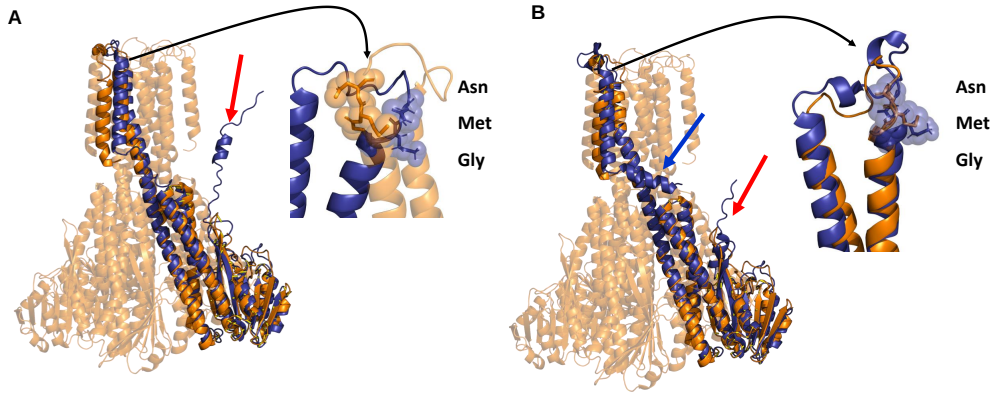

Figure 4.4.4: Comparison of the *Synechocystis* CorA channel structures predicted by AlphaFold with CorA from *Thermotoga maritima*.
Left: The predicted CorA1 monomer (blue) aligned to one monomer of the pentameric *Thermotoga maritima* CorA (PDB:4I0U) (Nordin *et al.* 2013) (orange) and the position of the conserved GMN motif (spheres). While the N-terminal cytoplasmic domains are structurally very similar, the transmembrane helices do not overlay perfectly. In addition, CorA1 had an elongated N-terminal region, including an additional helix (red arrow) which is absent in the *Thermotoga maritima* structure. Right: The predicted CorA2 monomer (blue) aligned to one monomer of the homo-pentameric *Thermotoga maritima* CorA (PDB:4I0U) (Nordin *et al.* 2013) (orange) and the position of the conserved GMN motif (spheres). Also, here, the N-terminal cytoplasmic domains are highly similar, while the transmembrane helices do not perfectly match. Just like CorA1, CorA2 had an extra N-terminal helix (red arrow).In addition, CorA2 also had an extra helix at the C-terminus (black arrow).

orientations in the predicted Mg^{2+} binding sites matched quite well (Figure 4.4.3). As with MgtE, the structural similarities between the predicted *Synechocystis* CorA structures and the solved crystal structure of *Thermotoga maritima* CorA were high.

This suggests that all three proteins could be bona fide Mg^{2+} channels. I note that the assumptions should be interpreted with care and provide only a rough idea of the protein structures and the amino acids possibly involved in Mg^{2+} binding.

4.4.1.2. Cloning of plasmids for heterologous expression

To investigate the function of the three channels and the predicted cytosolic domain (AA1-271 (AA271 end of CBS domain, Uniprot (The UniProt Consortium 2017; UniProt 2023b)) of MgtE (cytMgtE), the genes or gene regions coding for the respective proteins/domains were cloned into expression vectors (Table 4.4.3) *via* Gibson assembly cloning (D. G. Gibson *et al.* 2009), and the final expression plasmids were transformed into *E. coli* XL1-Blue cells. Since *sll0507* was cloned in frame with the *srtA* gene encoded by pET30b, *srtA* was later removed using the restriction enzymes NdeI and XhoI. The molecular mass of the encoded proteins/domains was calculated from the amino acid sequence using the ProtParam tool (Gasteiger *et al.* 2005).

Table 4.4.3: Vectors encoding the genes for protein expression and features of the produced proteins.

gene homolog	*ORF*	vector	Cleavage side	His-tag	Strep-tag	Molecular mass [kDa]
corA	*sll0507*	pET30b	TEV	C-terminal		47
corA	*sll0671*	pET30b	TEV	C-terminal		46.9
corA	*sll0671*	2HR-T	TEV	N-terminal	N-terminal	47.9
mgtE	*slr1216*	2HR-T	TEV	N-terminal	N-terminal	54.8
mgtE cytosolic domain	*slr1216 (AA1-271)*	pET30b	TEV	C-terminal		32.5

The vectors used for cloning contained a Tobacco Etch Virus nuclear-inclusion-a endopeptidase (TEV) site to allow cleavage of the genetically fused purification tag after expression. MgtE was produced with an N-terminal His-tag since the C-terminus is likely inaccessible (UniProt 2023c). CorA was produced with either an N- or C-terminal His-tag to test whether the tag's position affects the binding of the protein to the Ni-NTA column. The sequence for the N-terminal His-tag is encoded on the 2HR-T vector, which also encodes the sequence for a streptavidin (Strep) tag, providing a second opportunity for purification using a Strep-Tactin column. Successful cloning of all genes was confirmed *via* DNA sequencing, and the expression plasmids (Figure 4.4.5) were next transformed into *E. coli* expression strains for protein production.

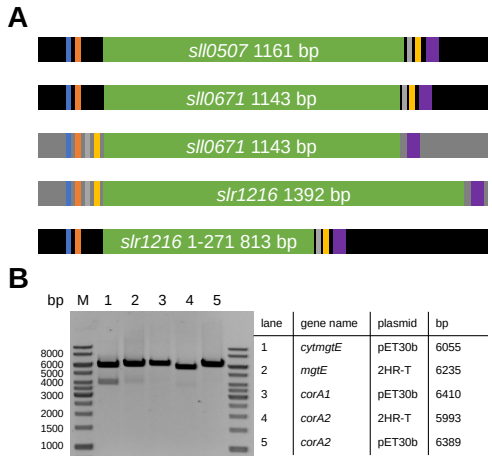

Figure 4.4.5: Transformed DNA constructs and their analysis.
A) Schematic view of the cloned DNA constructs used for expression. Colour code: black: pET30b, dark grey: 2HR-T, blue: T7 promoter, red: ribosome binding site (RBS), grey: TEV cleavage side, yellow: 6 His-tag, purple: T7 terminator. (B) Restriction digested plasmids containing the respective genes were loaded onto a 1% agarose gel. The expected sizes of the cloned constructs, which can be seen from the legend next to the gel, agreed with the band size seen on the gel.

4.4.1.3. Heterologous expression of the three potential Mg^{2+} channels CorA1, CorA2 and MgtE in *E. coli*

Since the genes were cloned downstream of a T7 promoter, the constructs were transformed into *E. coli* carrying a chromosomal copy of the phage T7 RNA polymerase gene, and expression was induced with IPTG (Studier *et al.* 1990). Figure 4.4.6 shows WBs after inducing the expression of the MgtE, CorA1 and CorA2 proteins with IPTG. Several *E. coli* strains were tested to identify the best expression strain for the membrane proteins. The expression of CorA2 was tested from two different vectors (see Table 4.4.3). MgtE was best expressed in *E. coli* C43 and *E. coli* HMS cells, with *E. coli* C43 reaching higher OD_{600} after induction. In the *E. coli* C43 strain also, both CorA channels were well expressed. Additionally, CorA1 showed a signal in the WB, which was stronger after expression in *E. coli* Rosetta2 than in *E. coli* C43 cells. CorA2 could be expressed from pET30b and 2HR-T in *E. coli* C43. Therefore, *E. coli* C43 was subsequently used as strain for expressions of MgtE and CorA2. CorA1 expression and purification were further examined in collaboration with a bachelor student ([redacted]) (Flecks 2021).

4.4.1.4. Solubilisation of the membrane proteins CorA2 and MgtE

Detergents are used to extract proteins from membranes, as they properly mimic the environment of a bilayer due to their amphiphilic character (Seddon *et al.* 2004). The strong denaturing ionic detergent SDS was used as a control, as it very effectively dissolves membrane proteins (Seddon *et al.* 2004). Triton X-100, OG, and DDM were

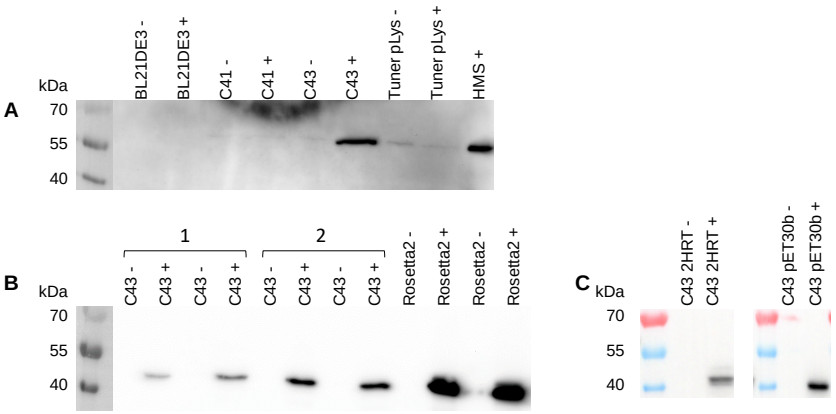

Figure 4.4.6: Identification of suitable expression strains and vectors.
WBs of whole cells from several tested *E. coli* strains before (-) and after (+) induction with IPTG. Detected His-Tag signal after (A) the expression of MgtE in *E. coli* BL21DE3, *E. coli* C41, *E. coli* C43, *E. coli* Tuner pLys and *E. coli* HMS at 37°C for 5 h; (B) the expression of CorA1 in *E. coli* C43 at 30°C overnight (1) or 37°C for 4 h (2) and *E. coli* Rosetta2 at 32°C for 5 h; (C) the expression of CorA2 in *E. coli* C43 from 2HR-T or pET30b at 37°C for 4 h.

chosen as non-ionic detergents and CHAPS and LDAO as zwitterionic detergents. Triton X-100 consists of a mixture with different headgroup lengths (on average, it has 9.5 ethylene oxide units (Sigma Product Information Sheet 2003)), yet it has the disadvantage of absorbing in the UV range. The glucoside OG and the maltoside DDM are commonly chosen mild detergents (Seddon *et al.* 2004). OG, LDAO and CHAPS have the advantage of forming small micelles; thus, the detergents can be removed *via* dialyses (Coligan 1998; Arachea *et al.* 2012). The membrane fraction was split, mixed with a detergent, and solubilised overnight at 4°C (except in the case of SDS). The solubilised membranes were ultracentrifuged, and samples of the supernatants and pellets obtained after centrifugation were loaded onto an SDS-PAGE gel. In the corresponding WB of membranes containing the produced CorA2 protein, a protein band was visible in the supernatant when Triton X-100, LDAO or DDM were used as detergents (Figure 4.4.7). The most significant difference between the protein band in the supernatant and the pellet on the WB was observed with LDAO; therefore, this detergent was subsequently used for CorA2 solubilisation. When membranes containing the produced MgtE protein were solubilised, a protein band was seen only in the supernatant fraction when DDM was used as detergent (Figure 4.4.8). Therefore, DDM was chosen for MgtE solubilisation.

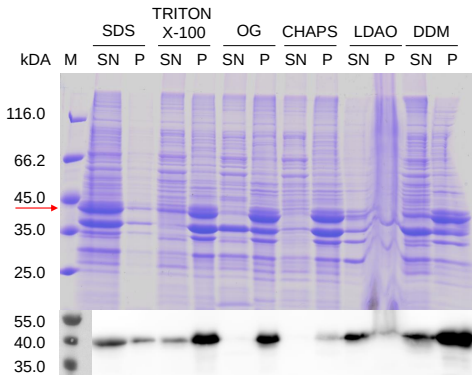

Figure 4.4.7: Solubilisation screening of CorA2.
Membranes from *E. coli* cells producing CorA2 were prepared as described in section 3.2.2.2, and proteins were extracted using the detergents specified in the main text. A CBB stained SDS-PAGE gel and the corresponding WB of the solubilised (SN) and non-solubilised (P) part of the membrane fraction are shown. SDS was used as a positive control. To solubilise CorA2, the detergents, Triton-X 100, OG, CHAPS, LDAO and DDM were used. The red arrow indicates the mass of CorA2.

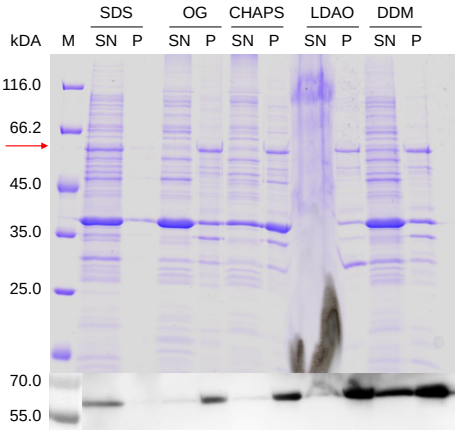

Figure 4.4.8: Solubilisation screening of MgtE.
Membranes from *E. coli* cells producing MgtE gene were prepared as described in section 3.2.2.2, and proteins were extracted using the detergents specified in the main text. A CBB stained SDS-PAGE gel and the corresponding WB of the solubilised (SN) and non-solubilised (P) part of the membrane fraction are shown. SDS was used as a positive control. To solubilise MgtE, the detergents OG, CHAPS, LDAO and DDM were used. The red arrow indicates the mass of MgtE.

4.4.1.5. Purification of CorA2 and MgtE

Since CorA2 could be successfully expressed from two different vectors, purification of the two respective proteins was compared to decide which vector is subsequently used finally. Both produced proteins contained either a C- or N-terminal His-tag. Hence a Ni-NTA column was used for purification. Figure 4.4.9 compares the SDS-PAGE gels and WBs of the purification steps when *corA2* was expressed from pET30b or 2HR-T, respectively. The broken *E. coli* cells were centrifuged at

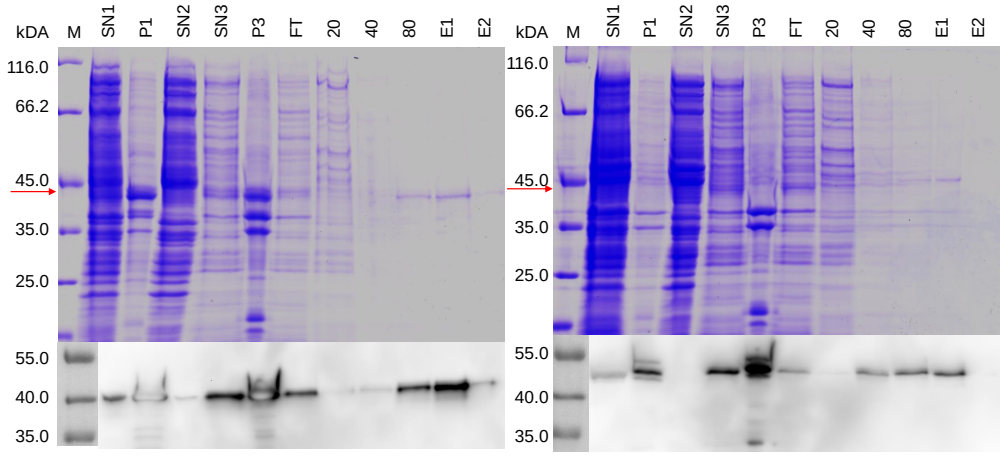

Figure 4.4.9: Purification of heterologously produced CorA2.
CBB stained SDS-PAGE gel and the corresponding WB showing purification of CorA2 when expressed from either pET30b (A) or 2HR-T (B). Lanes from left to right: Molecular mass markers (M); *E. coli* lysate after centrifugation at 10000 g (supernatant (SN1), pellet (P1)); SN2 after centrifugation at 117000 g; SN3 and P3 after detergent solubilisation and centrifugation at 117000 g; protein not binding to the Ni-NTA agarose gravity column (flow through (FT)); Washing steps with buffer containing increasing imidazole (mM) concentrations (20, 40, 80); fractions obtained upon protein elution with buffer containing 300 mM (E1) and 1000 mM (E2) imidazole. The red arrow indicates the mass of CorA2.

10000 g, and a protein band was seen in the SN1 as well as in the P1. The P1 band seemed to be more pronounced after expression from the plasmid 2HR-T. A pronounced band corresponding in size to CorA2 was observed again in P3, and this band was more pronounced after expression from 2HR-T. After eluting the protein with 300 mM imidazole, essentially a single band was observed after gene expression from the plasmid pET30b, while there were additional bands when the gene had been expressed from 2HR-T. Thus, *E. coli* C43 pET30b was used, which resulted in high yields of up to $\sim$ 1.8 mg purified CorA2 protein per litre culture, as can be assumed from the elution fractions in Figure 4.4.10. To remove the imidazole in the elution fractions, purified CorA2 was finally dialysed overnight. Since a large fraction of CorA2 precipitated during the overnight dialysis, the process was accel-

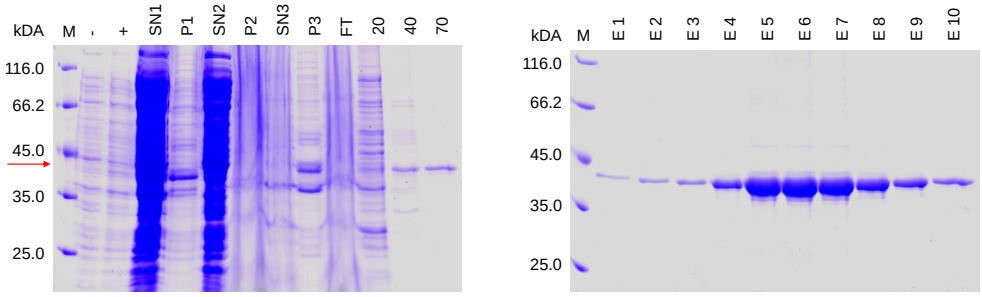

Figure 4.4.10: Purification of CorA2 when the gene was expressed from the pET30b plasmid. CBB stained SDS-PAGE gel of the samples from different steps during protein purification. The *E. coli* lysate was centrifuged at 10000 g to remove cell debris and unbroken cells (P1). The supernatant (SN1) was centrifuged at 117000 g to pellet the membranes, and the soluble proteins (SN2) were discarded. Membranes were solubilised by detergent and centrifuged again at 117000 g to remove non-solubilised proteins (P3). The supernatant (SN3) was loaded onto a Ni-NTA matrix, the flow through (FT) containing unbound proteins was discarded, and the matrix was washed with buffer containing different imidazole concentrations (mM) (20, 40, 80). CorA2 was eluted with 300 mM (E1-7) and 1000 mM (E8-10) imidazole. The red arrow indicates the mass of CorA2

erated by desalting with a PD10 column. However, the protein had a high tendency to precipitate within hours when stored at 4°C. When LDAO was exchanged against Triton X-100, the protein could be kept solubilised, and therefore after purification, the imidazole was removed, and LDAO was exchanged against Triton X-100 *via* dialysis overnight. While CorA2 purification resulted in high protein yields, the purification of MgtE needs further optimisation. Figure 4.4.11 shows the CBB stained SDS-PAGE gel and the corresponding WB from the Ni-NTA purification of MgtE ($\sim$ 54.8 kDA). As in P3, non-solubilised protein is visible, detergent treatment did only insufficiently solubilise the protein. Additionally, the protein did not properly bind to the Ni-NTA column, as distinct bands were seen in the FT and protein eluted during the washing steps. This insufficient protein binding and purification resulted in very low purification yields (8 µg protein per 100 mL of culture). In addition, the SDS-PAGE gel showed the presence of multiple additional proteins between the 66.2 and the 116 kDa band, indicating insufficient purification (Figure 4.4.11 red square). Therefore, the expression and purification of MgtE clearly need to be further optimised.

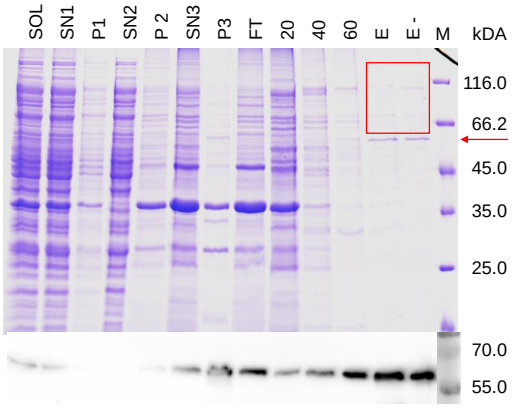

Figure 4.4.11: Purification of MgtE. CBB stained SDS-PAGE gel and the corresponding WB of samples from different steps during protein purification. Lanes from left to right: *E. coli* lysate before (SOL) and after centrifugation at 10000 g (supernatant (SN1), pellet (P1)); SN2 and P2 after centrifugation at 117000 g; SN3 and P3 after detergent solubilisation and centrifugation at 117000 g; Protein not binding to the Ni-NTA Agarose gravity column (Flow through (FT)); Washing steps with buffer containing increasing imidazole concentration (mM) (20, 40, 60); Elution with 300 mM imidazole with (E) and without SDS and DTT (E-); Molecular mass markers (M). The red arrow indicates the mass of MgtE and the red square frames protein impurities.

4.4.1.6. The lipid environment induces CorA2 oligomerisation

Further analysis of the CorA2 channel was examined in collaboration with [redacted]. Since CorA2 could be purified in high yields, its oligomerisation propensity was next tested since the functional channel is a pentamer (Lunin *et al.* 2006). The protein was integrated into destabilised liposomes (EPL:DOPC in a 3:1 (v/v) ratio) preloaded with FluoZin™-3 upon destabilisation of the liposomes with 0.1% Triton X-100. After 30 minutes of incubation, BioBeads were added to the mixture to remove the detergent. The BioBeads were exchanged several times, and after overnight incubation, the mixture was loaded onto a PD10 column to remove (most of) the not incorporated fluorescent dye. Proteoliposomes were concentrated by ultracentrifugation, washed with buffer, and dissolved in fresh buffer. Empty liposomes were treated the same way and used as a control. Besides protein monomers, additional proteins were observed when loaded onto an 8% SDS-PAGE gel (Figure 4.4.12). Possible dimer, trimer and even a faint band representing the pentameric protein (Figure 4.4.12) could be distinguished (comparable results were observed by [redacted] (Flecks 2021)). Since the protein could be successfully integrated into liposomes, next its ability to facilitate Mg^{2+} transport across an artificial lipid bilayer was examined.

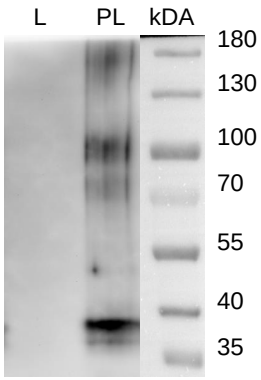

Figure 4.4.12: Analysis of CorA2-containing proteoliposomes.
Oligomeric states of CorA2 in EPL-DOPC liposomes. Empty liposomes (L) and Proteoliposomes (PL) were loaded on an 8% SDS-PAGE gel, and the samples were run under semi native conditions without any addition of DTT or SDS to the loading buffer. One can observe a strong band below 40 kDa, representing the monomeric protein, plus three fainter bands at around 75 kDa, 100 kDa and at 180 kDa.

4.4.1.7. Transport assay using the fluorescent dye FluoZin™-3

Proteoliposomes and empty liposomes, which served as control, were used immediately after preparation. After the addition of Mg^{2+} to the proteoliposomes and the empty liposomes, the kinetics of Mg^{2+} transport were recorded immediately for 400 s. Transport of Mg^{2+} across the artificial lipid bilayer will increase the encapsulated fluorophore's fluorescence. The transport kinetics are shown in Figure 4.4.13. While the signal of the control decreased over time, most likely due to photobleach-

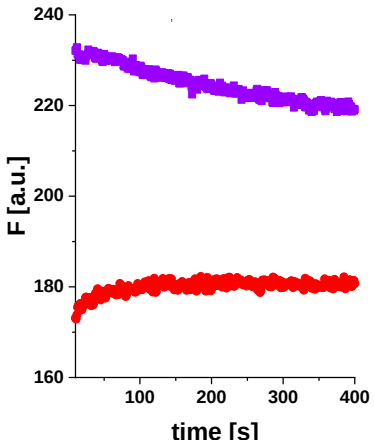

Figure 4.4.13: Mg^{2+} transport monitored using FluoZin™-3 preloaded proteoliposomes.
A change in FluoZin™-3 fluorescence was observed upon the addition of 0.8 mM Mg^{2+} to the proteoliposomes. While the signal in the empty liposomes decreased over time, most likely due to photobleaching, the signal in the proteoliposomes increased and reached a plateau indicative of Mg^{2+} uptake.

ing of the dye, the proteoliposomes showed a small signal increase that reached a plateau after $\sim$ 150 s (comparable results were observed by [redacted] (Flecks 2021)). Thus, the isolated CorA2 protein appears to assemble into pentameric units, which form a functional Mg^{2+} channel in liposomal membranes.

4.4.1.8. Expression, purification, and analysis of the cytoplasmic MgtE domain

Since only low amounts of the entire MgtE channel were purified, its cytoplasmic domain (cytMgtE) was cloned and heterologously expressed in order to characterise it further. This is of particular interest since channel opening and closing are accompanied by large changes in the orientation of the N-terminal cytoplasmic domains, which show high flexibility (Hattori *et al.* 2007; Moomaw *et al.* 2008; Hattori *et al.* 2009; Maruyama *et al.* 2018; Jin *et al.* 2021). Thus, the cytosolic domain functions as a sensor for the intracellular Mg^{2+} concentration (Hattori *et al.* 2007; Hattori *et al.* 2009). CytMgtE could be easily expressed in *E. coli* Rosetta2 cells, and the soluble domain could be purified in high amounts (Figure 4.4.14). As can be seen on

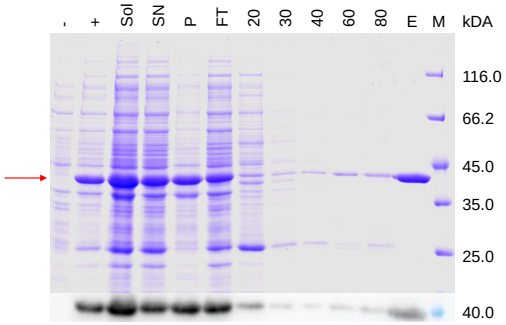

Figure 4.4.14: Purification of the cytosolic domain of MgtE.
CBB stained SDS-PAGE gel and the corresponding WB of samples from different steps during protein purification. Lanes from left to right: *E. coli* whole cells with the OD_{600} set to 1.5 before (-) and after (+) induction with 1 mM IPTG. *E. coli* lysate before (SOL) and after centrifugation at 10000 g (supernatant (SN), pellet (P); Protein not binding to the Ni-NTA Agarose gravity column (Flow through (FT)); Washing steps with buffer containing increasing imidazole concentration (mM) (20, 30, 40, 60, 80); Elution with 300 mM imidazole (E); Molecular mass markers (M). The red arrow indicates the mass of cytMgtE.

the SDS-PAGE, the expression and purification of cytMgtE were successful. Some protein was found in the pellet after centrifugation of the cell lysate, indicating the formation of inclusion bodies. Nevertheless, the protein was bound to the Ni-NTA column and, after five washing steps, was eluted with 300 mM imidazole. No other bands were visible on the gel, indicating successful purification of the isolated domain (electrophoretically pure) with high protein yields.

4.4.1.9. Mg^{2+} has an impact on the thermal stability of cytMgtE

CD spectra of cytMgtE were recorded to analyse the secondary structure in its predicted open state when no Mg^{2+} is bound to the protein plus in the predicted closed state, *i.e.* in the presence of 5 or 10 mM Mg^{2+} (Hattori *et al.* 2007; Hattori *et al.* 2009; Tomita *et al.* 2017). The spectra are dominated by the minima at $\sim$ 220 nm and at $\sim$ 208 nm, typical for α-helical structures (Holzwarth *et al.* 1965). Analysis of

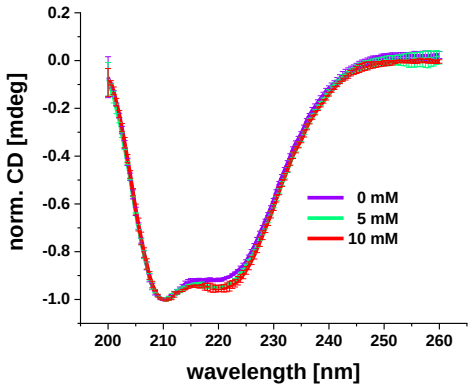

Figure 4.4.15: CD spectra of cytMgtE. Cd spectra of cytMgtE were measured in 1 mm quartz cuvettes. Spectra were normalised at 210 nm. First spectra were taken in the absence of Mg^{2+} (purple line). After the addition of 5 (green line) or 10 (red line) mM Mg^{2+} slight changes at 222 nm were observed. Error bars represent the SDs of 3 technical replicates.

the spectra (Figure 4.4.15) revealed only slight differences concerning the secondary structure of cytMgtE when 5 mM Mg^{2+} was added and no additional changes after the addition of 10 mM Mg^{2+}. Yet, in stark contrast, huge differences in the thermostability of the protein were observed (Figure 4.4.16). Samples were heated from 25-99°C, and a CD spectrum was taken at each 2°C step. While the cytMgtE

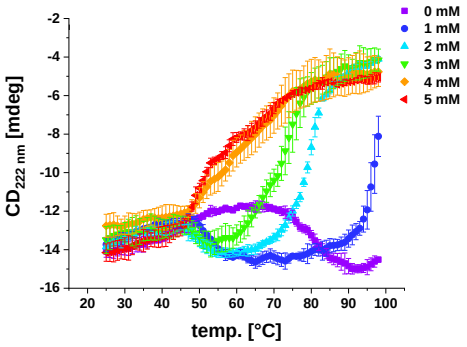

Figure 4.4.16: Thermal denaturation of cytMgtE in the absence versus presence of Mg^{2+}. Changes in the secondary structure of cytMgtE were measured in a 1 mm quartz cuvettes at 25-99°C. The signal intensity at 222 nm was plotted against the temperature. After the addition of 0-5 mM Mg^{2+}, distinct signal changes occurred with two main characteristics. Numbers next to the colour bars indicate the Mg^{2+} concentration in mM. Error bars represent the SDs of 3 technical replicates.

structure was affected only minorly up to 99 °C when no Mg^{2+} was present, striking changes became obvious in the presence of Mg^{2+} with a much faster decrease of the signal intensity at 222 nm. Two main characteristics were observed during the denaturation process of the protein in the presence and the absence of Mg^{2+}: Without Mg^{2+}, signal values increased until $\sim$ 65°C, subsequently decreased until $\sim$ 95°C and seemed to increase again at higher temperatures. The first increase "peak" shifted from $\sim$ 65°C without Mg^{2+} towards lower temperatures of $\sim$ 45°C after the addition of 1-3 mM Mg^{2+} and was not observed anymore after the addition of 4-5 mM Mg^{2+}. The second change observed was the shift of the transition

midpoint of the signal increase upon sample heating towards lower temperatures. The more Mg^{2+} was added, the earlier the signal increased. The online tool BeStSel (Micsonai *et al.* 2015; Micsonai *et al.* 2018; Micsonai *et al.* 2021) provides the opportunity to analyse a series of spectra as a function of temperature in a multiple spectra analysis. Here, the secondary structure components: parallel and antiparallel β-strands (anti1, anti2, anti3), regular parts of helices (helix1) and the distorted ends (helix2), turns, and others were analysed. The most prominent changes were

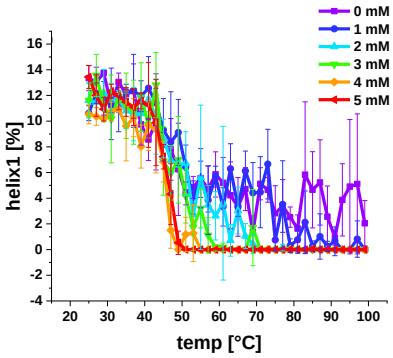

Figure 4.4.17: The multiple spectra analysis revealed Mg^{2+} induced changes in helix1.
Comparison of the CD spectra with BeStSel after thermal denaturation of cytMgtE with and without Mg^{2+}. The analysis revealed major changes in the stability of helix1. The more Mg^{2+} was added to the sample, the sooner the helix1 signal turned to 0. Numbers next to the colour bars indicate the Mg^{2+} concentration in mM. Error bars represent the SDs of 3 technical replicates.

distinguished in the helix1 (Figure 4.4.17), a region representing the regular α-helices in each protein (Micsonai *et al.* 2015; Micsonai *et al.* 2018; Micsonai *et al.* 2021).

4.4.1.10. ANS measurements revealed changes in the tertiary structure after the addition of Mg^{2+}

As cytMgtE lacks any intrinsic tryptophan, the dye ANS was used to get an idea about changes within the tertiary structure in the presence and absence of Mg^{2+} upon thermal denaturation in a fluorescence-based thermal shift assay (FTSA). Since the measurement also provides information on changes in the quaternary structure, the oligomeric state of the protein needs to be further analysed. Changes observed in ANS fluorescence, like a blue shift of the fluorescence maximum and/or an increase in the fluorescence intensity, are generally attributed to the hydrophobicity of a binding site and the restricted mobility of ANS (Gasymov *et al.* 2007; Cimmperman *et al.* 2011; Ota *et al.* 2021). Therefore, ANS has been widely used to study protein unfolding (Cimmperman *et al.* 2011). In contrast to thermal denaturation followed by CD-spectroscopy (Figure 4.4.18), ANS measurements showed a weak stabilising effect of Mg^{2+} on the protein structure at increasing temperatures. Overall, it was observed that Mg^{2+} induces structural changes in both the secondary and tertiary/quaternary structures, clearly indicating ion binding to the cytosolic

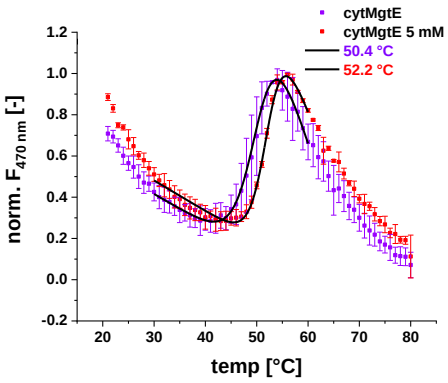

Figure 4.4.18: Thermal shift assay of cytMgtE with ANS upon thermal denaturation in the presence end absence of Mg^{2+}.
ANS-FTSA measurements of cytMgtE in the absence (purple) and presence (red) of 5 mM Mg^{2+}. ANS fluorescence intensities at 470 nm were plotted against the temperature and normalised (minimum set to 0, main peak set to 1). The temperature range that captured the transition phase was fitted with an adapted Boltzmann fit. Fit curves are shown as lines. Error bars represent the SDs of 3 technical replicates.

domain of *Synechocystis* MgtE.

4.4.2. Discussion

4.4.2.1. *Synechocystis* encodes three potential Mg^{2+} channels

Using the CyanoBase database (Nakamura *et al.* 2000; Nakao *et al.* 2010; Fujisawa *et al.* 2017), three potential Mg^{2+} channels were identified in the *Synechocystis* proteome, two of which belong to the CorA family and one likely is a MgtE family member. Thus, *Synechocystis* appears to encode both types of Mg^{2+} channels, as rather common in cyanobacteria (Pohland *et al.* 2019). It is worth mentioning that no MgtE homolog has been identified in plants thus far (Yan *et al.* 2018), which is relevant as cyanobacteria and chloroplast share a common ancestor (Schimper 1883; Mereschkowsky 1905; Lynn 1967; Gray 1989; McFadden 2001; De Clerck *et al.* 2012). Several CorA homologs were identified in plants and have been characterised as Mg^{2+} channels (Yan *et al.* 2018), and one of these has been localised at the chloroplasts envelope (Drummond *et al.* 2006). All three predicted protein structures of the Mg^{2+} channels agreed well with the experimentally solved structures of the two different channels (Figures 4.4.2, 4.4.4). Although the amino acids in the predicted Mg^{2+} binding sites differ to some extent (Tables 4.4.1, 4.4.2), it seems likely that the *Synechocystis* genes encode three Mg^{2+} channels. Amino acids forming the putative Mg^{2+} binding sites MG1–MG5 in the *Synechocystis* MgtE protein are similar to *Thermus thermophilus* MgtE regarding the amino acids as well as their orientations and MG7 also had an acidic amino acid in the same orientation. The two arginines at the MG6 position are unlikely to be involved in Mg^{2+} binding. Since ATP is recognised by the CBS domain of *Thermus thermophilus* MgtE (Tomita *et al.* 2017) and MG6 is located in the N domain, a subdomain of the cytoplasmic

domain, it is unlikely that the two arginines are relevant for the binding of ATP or other nucleotides. Thus, the prediction of the MG6 binding site of *Synechocystis*' MgtE is likely incorrect, showing the used method's limitations. In both predicted *Synechocystis* CorA channels, all amino acids, except Leu12, were identical to the amino acids identified in the solved structure at the putative Mg^{2+} binding sites. The structures did not align well in this unstructured region. Still, serine, instead of leucine, might also function as a binding site. Although the predicted binding sites in *Synechocystis* CorA1 and CorA2 have to be considered with care, the stated amino acids might be good candidates for mutational analysis to analyse the binding sites and transport across membranes of *Synechocystis* CorA1 and CorA2.

4.4.2.2. All three predicted Mg^{2+} channels can be heterologously expressed in *E. coli*

While it was possible to clone and transform all three genes into suitable expression systems (Figure 4.4.5), only MgtE and CorA2 could be purified (close) to homogeneity. In collaboration with [redacted], we identified *E. coli* C43 being a better choice for CorA1 expression than *E. coli* Rosetta2, plus CHAPS is better suited for protein solubilisation (Flecks 2021). Still, there is no purification protocol established until now that results in high yields of pure protein. Since the inefficient binding of CorA1 to the Ni-NTA column was a major problem, the His-tag should be moved from the C- to the N-terminus. The observation that *E. coli* C43 works best for the expression of all here analysed channels was not unexpected since *E. coli* C43 is widely used as a host for membrane protein expression (Hattab *et al.* 2015). *E. coli* C43 was generated in 1996 when *E. coli* BL21(DE3) strains were selected for their efficiency in expressing membrane proteins (Miroux *et al.* 1996). Later, two mutations in the lacUV5 promoter were identified as the main cause for the increased membrane protein expression levels. These mutations turned the promoter back into the wild-type lac promoter. This allows the expressed protein to be better incorporated into the membrane since protein production that leads to oversaturation of the Sec translocon capacity will result in protein aggregation (Wagner *et al.* 2008).

4.4.2.3. A protocol for the purification of MgtE still needs to be established

Purification of heterologously expressed MgtE resulted in very low protein yields. This could have several reasons based on the WB analyses (Figure 4.4.11). First, the protein solubilisation using DDM was inefficient, with high amounts of protein

not solubilised and remaining in the membrane (Figure 4.4.8). Additionally, the His-tagged protein did not completely bind to the Ni-NTA column, and a large fraction of unbound protein can be seen as a strong protein signal in the WB in the FT (Figure 4.4.11). Additionally, the bound protein eluted already at low imidazole concentrations. As the construct also contains a Strep-tag, a second purification step might improve protein purification. To check whether the His-tag is not accessible in the folded protein, one could purify the protein under denaturing conditions. If the denatured protein binds better to the Ni-NTA column, *i.e.* the His-tag is better accessible under these conditions, it might be worth to introduce an additional linker between the tag and the protein.

4.4.2.4. CorA2 oligomerises in artificial membranes

CorA2 expression resulted in the isolation of up to 1.8 mg electrophoretically pure protein per litre culture. As the protein tended to precipitate during overnight dialysis, the buffer was exchanged using a PD10 column. Yet, the protein tended to precipitate quickly when stored at 4°C. LDAO (critical micelle concentration (cmc) 1-2 mM/0.023% (Stetsenko *et al.* 2017)) was shown to induce protein precipitation when used at concentrations 10-20x higher than its cmc (Arachea *et al.* 2012). Thus, lowering the detergent concentration in the storage buffer might result in reduced protein precipitation. An impact of LDAO became apparent, as the purified protein can be stored at 4°C when LDAO is exchanged for Triton X-100. Liposomes were destabilised for reconstituting CorA2 into lipid membranes with 0.1% Triton X-100. CorA is a homo-pentamer (Lunin *et al.* 2006), and to investigate the oligomeric state of the protein, the proteoliposomes were analysed *via* semi native SDS-PAGE. The appearance of bands having different sizes on the WB suggested the successful integration of CorA2 into proteoliposomes and the formation of oligomeric structures (Figure 4.4.12) (see also (Flecks 2021)). The band at $\sim$ 180 kDa could well represent a tetramer or a pentamer. Yet, whether CorA really forms a pentamer when incorporated into liposomes needs further verification, *i.e. via* size exclusion chromatography.

4.4.2.5. CorA2 seems to facilitate Mg^{2+} flux across model membranes

The fluorophores MagFura2 and FluoZin™-3 were both previously successfully used to demonstrate CorA-mediated Mg^{2+} influx into proteoliposomes when the proteins of *Thermotoga maritima* (Payandeh *et al.* 2008; Stetsenko *et al.* 2020) or *Arabidopsis thaliana* (MRS2/MGT/CorA-type) (Ishijima *et al.* 2018) were analysed.

Although a fluorescence signal increase was observed with the Mg^{2+} sensitive dye FluoZin™-3 (Figure 4.4.13) when Mg^{2+} was added to the proteoliposomes, indicating Mg^{2+} transport, the assay was not constantly reproducible. In some cases, a signal increase was observed in the control sample (see section 5, Figure A.5.6). This was particularly evident when higher Mg^{2+} concentrations (> 6 mM) were used. Such Mg^{2+} concentrations can lead to fusion processes and leaky liposomes (Düzgünes *et al.* 1981). If dye leaked out of the liposomes or Mg^{2+} entered the liposomes, an increase in the fluorescence signal would be the result. An additional size exclusion chromatography step might help to remove any remaining Mg^{2+} bound to the sample to ensure that the positive result was not due to Mg^{2+} copurified with the protein. In addition, this would ensure that no free fluorophore is present outside the liposomes. Another problem of the transport assay was the use of a very concentrated liposome solution, resulting in significant light scattering. To overcome this, encapsulation of the dye must become more efficient. Encapsulation was achieved by adding the fluorophore during the rehydration of the lipid film. After destabilising the liposomes and adding BioBeads, a high amount of the fluorophore was bound to the BioBeads, *i.e.* removed from the proteoliposomes. Therefore, the fluorophore should be added after detergent removal, and encapsulation might be performed by freeze-thaw cycles (Stetsenko *et al.* 2020). The additional steps and analyses proposed here to improve the test set could help to detect *Synechocystis* CorA2-mediated Mg^{2+} transport across membranes reliably.

4.4.2.6. The isolated cytosolic domain of MgtE interacts with Mg^{2+}

The results obtained with cytMgtE clearly indicated that Mg^{2+} affects the proteins' structure. This was observed on the secondary structure as well as the tertiary/quaternary structure level (Figure 4.4.18). While almost no structural changes were observed at RT in the CD spectra (Figure 4.4.15) in the absence versus presence of Mg^{2+}, structural alterations were clearly seen upon heating the protein solution to 99°C (Figure 4.4.16). While the CD spectrum of the protein without Mg^{2+} only changed little upon heating, the protein structure clearly changed with increasing temperature when 5 mM Mg^{2+} was present (see section 5, Figure A.5.7). The more Mg^{2+} was added to the protein solution, the earlier the protein denatured. The observed changes at 222 nm during heat denaturation in the presence vs absence of Mg^{2+} showed a striking similarity to the changes during heat denaturation in the presence vs absence of DTT of a CBS protein from the hyperthermophilic archaeon *Pyrobaculum aerophilum* (PDB: 2RIH) (King *et al.* 2008). There, thermal denatura-

tion was followed in the presence vs absence of DTT since the homodimeric protein was linked *via* a cysteine bridge (King *et al.* 2008). The denaturation curve without Mg^{2+} of the *Synechocystis* cytMgtE was comparable to the curve without DTT in the *Pyrobaculum aerophilum* CBS protein. The denaturation curve in the presence of 2 mM Mg^{2+} was comparable to the curve in the presence of DTT in the *Pyrobaculum aerophilum* CBS protein. Surprisingly, Mg^{2+} seemed not to stabilise the cytMgtE domain but led to changes of the secondary structure resulting in a lowered melting point (Figure 4.4.16). To further investigate the oligomeric state of the protein, size exclusion chromatography should be performed in the absence versus presence of increasing Mg^{2+} concentrations. This would also allow for the interpretation of changes in the quaternary structure in the thermal shift assay. The thermal shift assay performed to monitor changes in the cytMgtE tertiary/quaternary structure showed a different effect of Mg^{2+} binding to cytMgtE. The tertiary/quaternary structure appeared to be stabilised by Mg^{2+}-binding, observed as an $\sim 2°C$ increase in the melting temperature (Figure 4.4.18). Thus, it could be clearly shown that Mg^{2+} influences the conformation of cytMgtE both on the secondary as well as the tertiary/quaternary structure level. The observed differences in the thermal stability of cytMgtE in the absence versus presence of Mg^{2+} clearly suggest binding of Mg^{2+} to the isolated cytMgtE domain. Since *Synechocystis* MgtE has been shown to bind cyclic di-adenosine monophosphate (Selim *et al.* 2021), future experiments should be performed in the presence of these to show the influence of adenonucleotides on the proteins' interaction with Mg^{2+}. In addition, the determination of the cytMgtE protein structure in the presence and absence of Mg^{2+} is required to define the expected conformational changes of cytMgtE.

4.4.2.7. Conclusion

CorA2 has been successfully purified, but a method for the purification of MgtE and CorA1 has yet to be established. Albeit this cannot be said with certainty, CorA2 appears to mediate Mg^{2+} flux across artificial membranes and thus seems to be an Mg^{2+} channel. Additionally, differences in protein stability that were dependent on Mg^{2+} were discovered in studies using the cytoplasmic domain of MgtE. Since Mg^{2+} binding to the soluble MgtE domain is Mg^{2+}-dependent (Hattori *et al.* 2009), these changes could be a first direct indication that Mg^{2+} binding regulates *Synechocystis*' MgtE channel activity.

5. Appendix

Amino acid sequences of the analysed proteins. The sequences were obtained from "CyanoBase"(Nakamura *et al.* 2000; Nakao *et al.* 2010; Fujisawa *et al.* 2017).

Table A.5.1: Amino acid sequences of the analysed proteins.
Charged amino acids are underlined (−/+).

Protein	Amino acid sequence
Sll1216 (MgtE)	MTEVTTTVRLNPDREELQKLVRAQIETLLETSQFDAAKTILTPVQPAD
Sll1216 AA1-271	IADVIESLPSRLQVLAFRLLSKNEAIDVYEHLAPPVQESLLEDFKHPE
(cytMgtE)	VLEIFNQMSPDDRVRLLDELPAKVVRQLFKHLSNEERKATSLLLGYKP
	ETAGRIMTTEYVSLKEDYTASQALDHIRHIATSFETIYVLYVTNESRR
	LTGTLSLRNLVMAKPEEYIGQIMVPDVVSVHTNTDQEEVARTIQHYDF
	LAVPVVDSEQRLVGIVTVDDVIDILEEEATEDIYTAGGVQSQGDDYFK
	SSLMTVARKRVVWLFILLVTNTLTSQVIHSQEDVLQKTIALAAFIPLL
	IDAGGNVGAQSSTVVIRGLNTEDVRLTQVLPVIAREGGAGALLGLMLG
	IVVTVWAYFLQGDWLVAITVGSSLFIISLLAAFAGGGLPFLFKSMKLD
	PALMSAPFITTAVDVLGVAIYLLIARSLLGI
Sll0507 (CorA1)	MPQTQPGIEDFLLRQLRHPQEEEEEEDYFDYFYDEPGSEPGTLSIEPD
	APPSRIVLVDYSPSHAVRKSDISPNALRPYLGTNTVSWMDIEGLGSEE
	VLKEVGEIFKLHPLLLEDIVNVPQRAKVEDYNDHVMVIAHRVRPNREE
	DGFESEQVSFVLGKRYLLTFQEGHIIDCFNPLRERIRTNQGKVCQQGA
	DYLCYLLIDMLIDEYFPLLEDYEERIEALEDTIIRNPNSSLMEEIYHI
	RRELLALRRLIWPLRHVMNVLLRDTTNSIVTADVRIYFRDCYDHIIQV
	LDIIEAYRELASSLMEVYMTAMSNKMNEVMKFLTVISTIFIPLTFIAG
	VYGMNFKEMPELNSRWGYYITWIVMLLIAGGSLYFFWRKGWLSPSYDL
	GEK
Sll0671 (CorA2)	MPNKPQFRQSNLVSHFNYFNSPESIPGTLNLSPNAPPPRIILIDYNKN
	QATKIELKNPLDCEAYVDTESVSWINIDGLGNHTTWEQLGEVFKLHPV
	ALEDIVNVPQRPKVVEYENHLIFISRMVTLDQSSQTFISEQISFILGK
	HYLLTIQEEPKYDCLFSVRERIRTKKGAIRQKNADYLFYALIDAIIDG
	FFPVMEVYGELVQSLQSEIISCPTNKSLAKIHQLQQDLLIMRRAIWPQ
	RDAINSLLRDGSDLISDEVRVFLRDCYDHTIQILDMIETYRDLASNLT
	DIYLSSVSNRMNEIMKTLTVISSIFIPLTFIAGIYGMNFNPDKSPWNM
	PELNWYWGYPVIWMVMLTVGGMMLYFFWRKGWFRNLNDVEKGNR

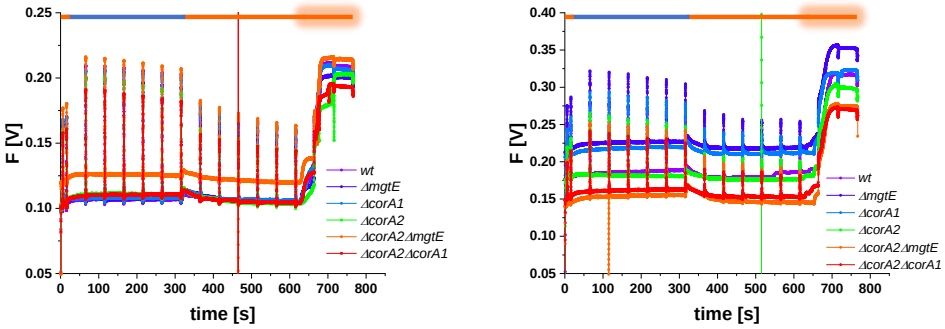

Figure A.5.1: Averaged traces of PAM fluorescence induction curves from *Synechocystis* cells grown under high (left) or low (right) Mg^{2+} concentrations.
Dark incubated cells were illuminated with low-intensity ML light ($F_{o'}$), and saturation pulses were added ($F_{m'}$). Weak blue light was turned on to induce a state transition (F_o). Saturation pulses were added to monitor a change in signal strength. Blue light was turned off and saturation pulses were added to follow the state transition. After the addition of DCMU, continuous actinic light was switched on, and F_m was determined. The photosynthetic parameter F_v/F_m was calculated from the lowest fluorescence in the dark and the highest fluorescence after the addition of DCMU in the light. Experimental error bars indicate the means ±SDs of at least 3 biological replicates. The measurements were performed in cooperation with [redacted].

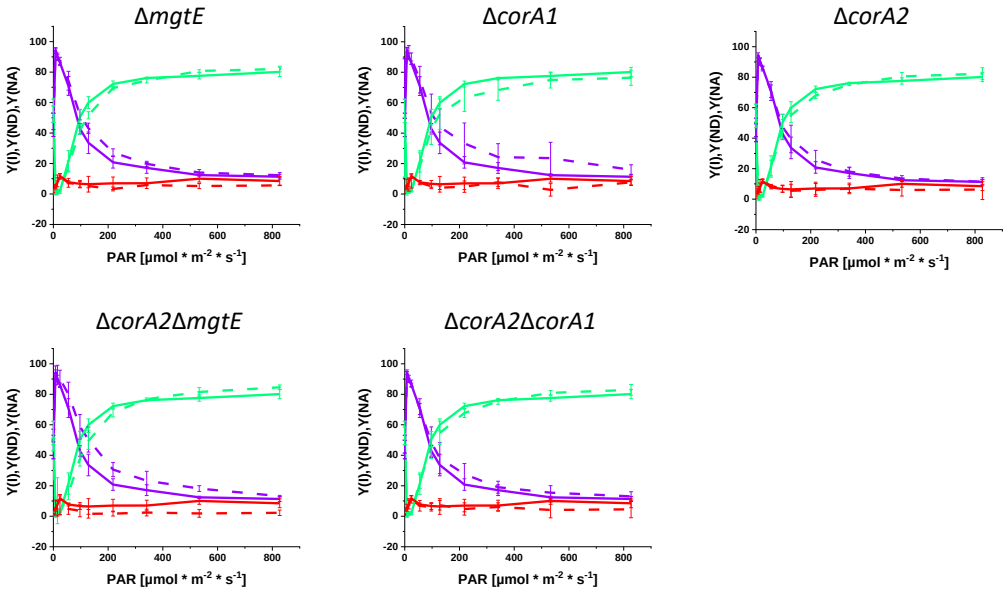

Figure A.5.2: PSI quantum yield, acceptor and donor side limitations of wt and mts under H conditions.
Effective quantum yield of PSI (Y(I)) of the mts (dashed line) compared to the wt (solid line) at high Mg^{2+} concentrations. While most mts showed wt-like levels of the three parameters, the *ΔcorA1* mt had a higher Y(I), and a lower Y(ND) compared to the wt. Experimental error bars indicate the means ±SDs of at least 3 biological replicates. The measurements were performed in cooperation with [redacted].

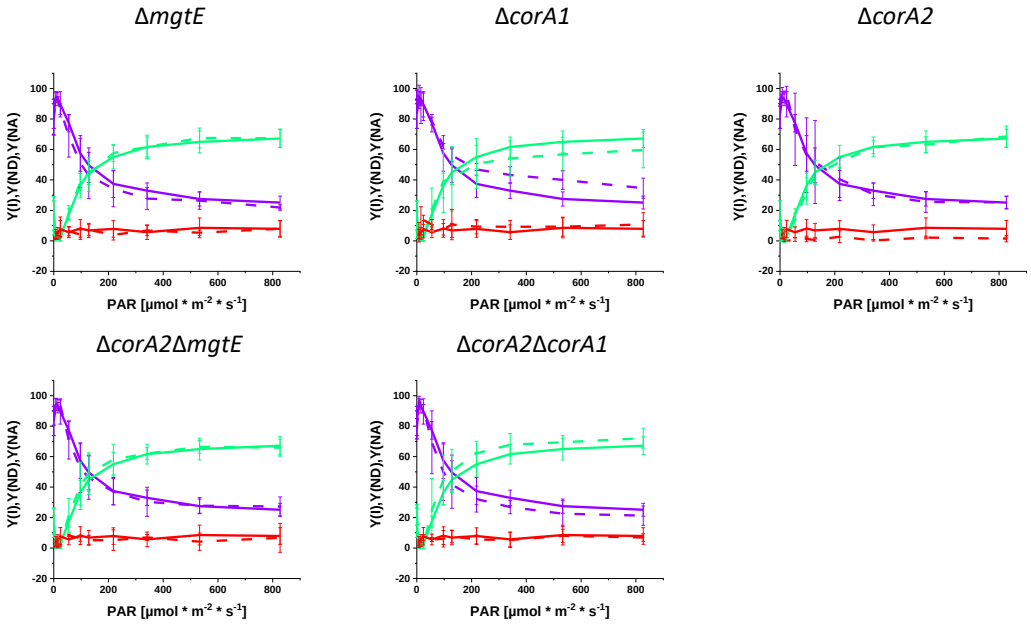

Figure A.5.3: PSI quantum yield, acceptor, and donor side limitations of wt and mts under L conditions.
Effective quantum yield of PSI (Y(I)) of the mts (dashed line) compared to the wt (solid line) at low Mg^{2+} concentrations. As for **H** conditions, most mts showed wt-like levels of the three parameters, while the *ΔcorA1* mt had a higher Y(I) and a lower Y(ND) compared to the wt. Experimental error bars indicate the means ±SDs of at least 3 biological replicates except *ΔcorA2* n=2 (**L**). The measurements were performed in cooperation with [redacted].

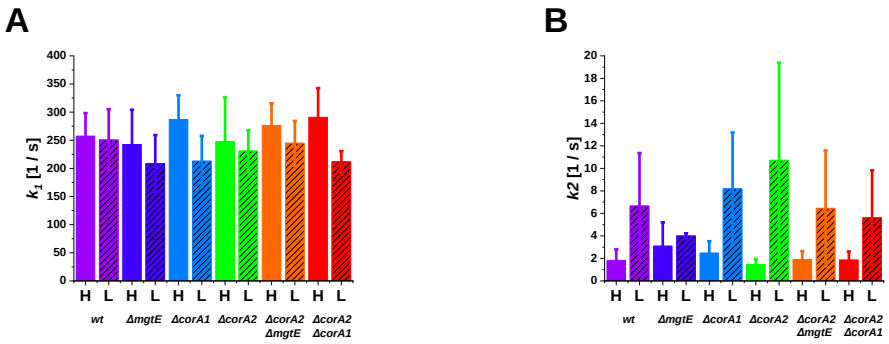

Figure A.5.4: P_{700}^{+} re-reduction kinetics in the presence of DCMU.
To assess the influence of cyclic electron flow around PSI, P_{700}^{+} re-reduction rates were measured at high and low Mg^{2+} concentrations in the presence of DCMU. The curves were fitted with two exponentials. The fast component (k_1) showed no differences between the wt and the mts or between the two Mg^{2+} concentrations (A). Overall, k_2 seemed faster under low Mg^{2+} concentrations, with no significant differences between the strains (B).Experimental error bars indicate the means ±SDs of at least 3 biological replicates. The measurements were performed in cooperation with [redacted].

Table A.5.2: Cellular pigment contents and ratios of wt and mts cells.
Contents [10^{-18} mol/cell] and ratios of Chl *a*, PSI, PSII and PC of wt and mts cells grown under high **H**) and low (**L**) Mg^{2+} conditions. Numbers were obtained as described in Luimstra et al. 2019 Luimstra *et al.* 2019. Less than 3 biological replicates are marked in red.

	H						units
	wt	*ΔmgtE*	*ΔcorA1*	*ΔcorA2*	*ΔcorA2ΔmgtE*	*ΔcorA2ΔcorA1*	
Chl *a* content	28.7 ±4.8	28.5 ±6.2	31.5 ±3.9	28.3 ±1.6	30.3 ±5.2	33.9 ±3.9	10^{-18} mol/cell
n	8	7	7	7	7	8	
PSI content	0.27 ±0.03	0.26 ±0.05	0.32 ±0.01	0.28 ±0.02	0.28 ±0.02	0.33 ±0.04	10^{-18} mol/cell
n	4	3	3	3	4	4	
PSII content	0.031 ±0.002	0.017 ±0.001	0.033 ±0.013	0.013 ±0.002	0.020 ±0.006	0.021 ±0.005	10^{-18} mol/cell
n	4	3	3	3	4	4	
PSI:PSII ratio	8.8 ±0.9	15.8 ±3.9	10.5 ±3.5	21.3 ±3.9	14.3 ±3.1	15.8 ±2.0	
n	4	3	3	3	4	4	
PC content	5.8 ±1.1	5.1 ±0.6	6.3 ±0.1	4.9 ±0.5	4.3 ±0.5	6.0 ±0.9	10^{-18} mol/cell
n	3	2	2	2	3	3	
PC:Chl *a* ratio	0.19 ±0.03	0.18 ±0.01	0.21 ±0.02	0.17 ±0.01	0.16 ±0.02	0.17 ±0.00	
n	6	5	5	5	4	5	
PC:PSII ratio	182.8 ±26.5	319.0 ±41.8	184.3 ±76.0	402.6 ±52.4	215.3 ±48.1	276.4 ±47.2	
n	3	2	2	2	3	3	
	L						units
	wt	*ΔmgtE*	*ΔcorA1*	*ΔcorA2*	*ΔcorA2ΔmgtE*	*ΔcorA2ΔcorA1*	
Chl *a* content	11.0 ±2.4	9.2 ±2.4	8.8 ±2.6	11.0 ±2.0	16.5 ±2.6	18.8 ±5.5	10^{-18} mol/cell
n	3	3	3	3	3	3	
PSI content	0.10 ±0.02	0.08 ±0.02	0.07 ±0.03	0.10 ±0.02	0.15 ±0.03	0.18 ±0.06	10^{-18} mol/cell
n	3	3	3	3	3	3	
PSII content	0.030 ±0.002	0.038 ±0.006	0.040 ±0.006	0.030 ±0.005	0.036 ±0.005	0.027 ±0.002	10^{-18} mol/cell
n	3	3	3	3	3	3	
PSI:PSII ratio	3.4 ±1.0	2.1 ±0.4	1.9 ±0.7	3.4 ±1.3	4.3 ±0.9	6.7 ±2.5	
n	3	3	3	3	3	3	
PC content	4.1 ±0.7	4.5 ±0.6	4.5 ±0.6	4.0 ±0.2	5.3 ±0.6	5.2 ±0.7	10^{-18} mol/cell
n	3	3	3	3	3	3	
PC:Chl *a* ratio	0.38 ±0.05	0.51 ±0.07	0.53 ±0.07	0.37 ±0.05	0.32 ±0.03	0.28 ±0.05	
n	3	3	3	3	3	3	
PC:PSII ratio	140. ±22.6	119.4 ±7.9	115.5 ±21	137.1 ±27.3	148.4 ±15.6	193.3 ±35.5	
n	3	3	3	3	3	3	

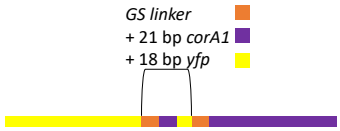

Figure A.5.5: Region of duplication in *yfp-corA1*.
Between the *yfp* and the *corA1* gene was a duplication of the DNA coding for a GS linker, the first 21 bp of *corA1* and the last 18 bp *yfp*.

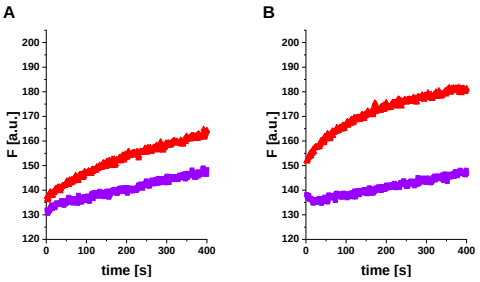

Figure A.5.6: Mg^{2+} transport monitored using FluoZin™-3 preloaded proteoliposomes.
Change of the FluoZin™-3 fluorescence upon the addition of 2 mM Mg^{2+} (A) or 6 mM Mg^{2+} (B). The signal in the empty liposomes (purple), as well as the signal in the proteoliposomes (red), increased after Mg^{2+} addition.

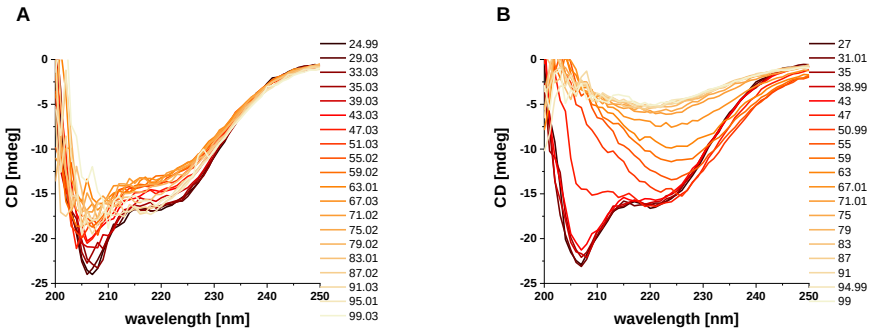

Figure A.5.7: Mg^{2+}-binding affects the CD spectra of cytMgtE.
Changes in the secondary structure of cytMgtE in the absence of Mg^{2+} (A) or presence (B) of 5 mM Mg^{2+} (B) were determined at increasing temperatures. While the signal at 222 nm changed only to a minor extent with increasing temperatures when Mg^{2+} was absent, the signal intensity decreased in the presence of Mg^{2+}.

Acknowledgement

Curriculum vitae

References

Akanuma, G., A. Kobayashi, S. Suzuki, F. Kawamura, Y. Shiwa, S. Watanabe, H. Yoshikawa, R. Hanai, and M. Ishizuka (2014). "Defect in the formation of 70S ribosomes caused by lack of ribosomal protein L34 can be suppressed by magnesium". In: *Journal of Bacteriology* 196.22, pp. 3820–3830.

Alatossava, T., H. Jütte, A. Kuhn, and E. Kellenberger (1985). "Manipulation of intracellular magnesium content in polymyxin B nonapeptide-sensitized Escherichia coli by ionophore A23187". In: *Journal of Bacteriology* 162.1, pp. 413–419.

Allen, J. F. (2002). "Photosynthesis of ATP—Electrons, Proton Pumps, Rotors, and Poise". In: *Cell* 110.3, pp. 273–276.

— (2003). "Cyclic, pseudocyclic and noncyclic photophosphorylation: New links in the chain". In: *Trends in Plant Science* 8.1, pp. 15–19.

— (1992). "Protein phosphorylation in regulation of photosynthesis". In: *Biochimica et Biophysica Acta - Bioenergetics* 1098.3, pp. 275–335.

Allen, J. F., W. B. de Paula, S. Puthiyaveetil, and J. Nield (2011). "A structural phylogenetic map for chloroplast photosynthesis". In: *Trends in Plant Science* 16.12, pp. 645–655.

Allen, M. M. (1968). "Photosynthetic Membrane System in Anacystis nidulans". In: *Journal of Bacteriology* 96.3, pp. 836–841.

Alric, J., J. Lavergne, and F. Rappaport (2010). "Redox and ATP control of photosynthetic cyclic electron flow in Chlamydomonas reinhardtii (I) aerobic conditions". In: *Biochimica et Biophysica Acta - Bioenergetics* 1797.1, pp. 44–51.

Anastassopoulou, J. (2003). "Metal–DNA interactions". In: *Journal of Molecular Structure* 651, pp. 19–26.

Anderson, J. M. and E.-M. Aro (1994). "Grana stacking and protection of Photosystem II in thylakoid membranes of higher plant leaves under sustained high irradiance: An hypothesis". In: *Photosynthesis Research* 41, pp. 315–326.

Anderson, S. L. and L. McIntosh (1991). "Light-activated heterotrophic growth of the cyanobacterium Synechocystis sp. strain PCC 6803: a blue-light-requiring process". In: *Journal of Bacteriology* 173.9, pp. 2761–2767.

Andersson, B. and J. M. Anderson (1980). "Lateral heterogeneity in the distribution of chlorophyll-protein complexes of the thylakoid membranes of spinach chloroplasts". In: *Biochimica et Biophysica Acta - Bioenergetics* 593.2, pp. 427–440.

Andrizhiyevskaya, E. G., A. Chojnicka, J. A. Bautista, B. A. Diner, R. van Grondelle, and J. P. Dekker (2005). "Origin of the F685 and F695 fluorescence in photosystem II". In: *Photosynthesis Research* 84.1-3, pp. 173–180.

Arachea, B. T., Z. Sun, N. Potente, R. Malik, D. Isailovic, and R. E. Viola (2012). "Detergent selection for enhanced extraction of membrane proteins". In: *Protein Expression and Purification* 86.1, pp. 12–20.

Armitano, J., P. Redder, V. A. Guimarães, and P. Linder (2016). "An essential factor for high Mg2+ tolerance of Staphylococcus aureus". In: *Frontiers in microbiology* 7, p. 1888.

Asada, K. (2006). "Production and scavenging of reactive oxygen species in chloroplasts and their functions". In: *Plant physiology* 141.2, pp. 391–396.

Baers, L. L., L. M. Breckels, L. A. Mills, L. Gatto, M. J. Deery, T. J. Stevens, C. J. Howe, K. S. Lilley, and D. J. Lea-Smith (2019). "Proteome Mapping of a Cyanobacterium Reveals Distinct Compartment Organization and Cell-Dispersed Metabolism 1[CC-BY]". In: *Plant Physiology* 181.4, pp. 1721–1738.

Balakrishnan, K., C. Rajendran, and G. Kulandaivelu (2000). "Differential Responses of Iron, Magnesium, and Zinc Deficiency on Pigment Composition, Nutrient Content, and Photosynthetic Activity in Tropical Fruit Crops". In: *Photosynthetica* 38.3, pp. 477–479.

Barber, J. (1980). "Membrane surface charges and potentials in relation to photosynthesis". In: *Biochimica et Biophysica Acta - Reviews on Bioenergetics* 594.4, pp. 253–308.

Barber, J. and M. Archer (2001). "P680, the primary electron donor of photosystem II". In: *Journal of Photochemistry and Photobiology A: Chemistry* 142.2-3, pp. 97–106.

Barber, J., J. Mills, and J. Nicolson (1974). "Studies with cation specific ionophores show that within the intact chloroplast Mg ++ acts as the main exchange cation for H + pumping". In: *FEBS Letters* 49.1, pp. 106–110.

Barrick, J. E., K. A. Corbino, W. C. Winkler, A. Nahvi, M. Mandal, J. Collins, M. Lee, A. Roth, N. Sudarsan, I. Jona, J. K. Wickiser, and R. R. Breaker (2004). "New RNA motifs suggest an expanded scope for riboswitches in bacterial genetic control". In: *Proceedings of the National Academy of Sciences* 101.17, pp. 6421–6426.

Barten, R. and H. Lill (1995). "DNA-uptake in the naturally competent cyanobacterium, Synechocystis sp. PCC 6803". In: *FEMS Microbiology Letters* 129.1, pp. 83–87.

Bateman, A. (1997). "The structure of a domain common to archaebacteria and the homocystinuria disease protein". In: *Trends in Biochemical Sciences* 22.1, pp. 12–13.

Battchikova, N., M. Eisenhut, and E. M. Aro (2011a). "Cyanobacterial NDH-1 complexes: Novel insights and remaining puzzles". In: *Biochimica et Biophysica Acta - Bioenergetics* 1807.8, pp. 935–944.

Battchikova, N., L. Wei, L. Du, L. Bersanini, E. M. Aro, and W. Ma (2011b). "Identification of novel Ssl0352 protein (NdhS), essential for efficient operation of cyclic electron transport around photosystem I, in NADPH:plastoquinone oxidoreductase (NDH-1) complexes of Synechocystis sp. PCC 6803". In: *Journal of Biological Chemistry* 286.42, pp. 36992–37001.

Bauer, R. and M. J. Wijnands (1974). "The inhibition of photosynthetic electron transport by DBMIB and its restoration by p-phenylenediamines; studied by

means of prompt and delayed chlorophyll fluorescence of green algae". In: *Zeitschrift für Naturforschung C* 29.11-12, pp. 725–732.

Baykov, A. A., H. K. Tuominen, and R. Lahti (2011). "The CBS domain: A protein module with an emerging prominent role in regulation". In: *ACS Chemical Biology* 6.11, pp. 1156–1163.

Belkin, S., R. J. Mehlhorn, and L. Packer (1987). "Proton Gradients in Intact Cyanobacteria". In: *Plant Physiology* 84.1, pp. 25–30.

Ben Amor-Ben Ayed, H., B. Taidi, H. Ayadi, D. Pareau, and M. Stambouli (2015). "Effect of magnesium ion concentration in autotrophic cultures of Chlorella vulgaris". In: *Algal Research* 9, pp. 291–296.

Berg, S. P. and D. Krogmann (1975). "Mechanism of KCN inhibition of photosystem I". In: *Journal of Biological Chemistry* 250.23, pp. 8957–8962.

Bernát, G., N. Waschewski, and M. Rögner (2009). "Towards efficient hydrogen production: The impact of antenna size and external factors on electron transport dynamics in Synechocystis PCC 6803". In: *Photosynthesis Research* 99.3, pp. 205–216.

Berry, S., Y. V. Bolychevtseva, M. Rögner, and N. V. Karapetyan (2003). "Photosynthetic and respiratory electron transport in the alkaliphilic cyanobacterium Arthrospira (Spirulina) platensis". In: *Photosynthesis research* 78, pp. 67–76.

Berry, S., D. Schneider, W. F. Vermaas, and M. Rögner (2002). "Electron transport routes in whole cells of Synechocystis sp. Strain PCC 6803: The role of the cytochrome bd-type oxidase". In: *Biochemistry* 41.10, pp. 3422–3429.

Bertrand, R. L. (2019). "Lag phase is a dynamic, organized, adaptive, and evolvable period that prepares bacteria for cell division". In: *Journal of Bacteriology* 201.7, e00697–18.

Bibby, T. S., J. Nield, and J. Barber (2001). "Iron deficiency induces the formation of an antenna ring around trimeric photosystem I in cyanobacteria". In: *Nature* 412.6848, pp. 743–745.

Billini, M., K. Stamatakis, and V. Sophianopoulou (2008). "Two Members of a Network of Putative Na + /H + Antiporters Are Involved in Salt and pH Tolerance of the Freshwater Cyanobacterium Synechococcus elongatus". In: *Journal of Bacteriology* 190.19, pp. 6318–6329.

Birch, N. J. (1990). "Magnesium in Biology and Medicine: An Overview". In: *Metal Ions in Biological Systems: Volume 26: Compendium on Magnesium and Its Role in Biology: Nutrition and Physiology*. Ed. by H. Sigel and A. Sigel. New York: CRC Press. Chap. 6, pp. 105–117.

Biswas, A., X. Huang, P. H. Lambrev, and I. H. van Stokkum (2020). "Modelling excitation energy transfer and trapping in the filamentous cyanobacterium Anabaena variabilis PCC 7120". In: *Photosynthesis research* 144, pp. 261–272.

Boehm, M., E. Romero, V. Reisinger, J. Yu, J. Komenda, L. A. Eichacker, J. P. Dekker, and P. J. Nixon (2011). "Investigating the early stages of photosystem II assembly in Synechocystis sp. PCC 6803: Isolation of CP47 and CP43 complexes". In: *Journal of Biological Chemistry* 286.17, pp. 14812–14819.

Bonaventura, C. and J. Myers (1969). “Fluorescence and oxygen evolution from Chlorella pyrenoidosa”. In: *Biochimica et Biophysica Acta - Bioenergetics* 189.3, pp. 366–383.

Brändén, G., R. B. Gennis, and P. Brzezinski (2006). “Transmembrane proton translocation by cytochrome c oxidase”. In: *Biochimica et Biophysica Acta - Bioenergetics* 1757.8, pp. 1052–1063.

Brock, T. D. (1962). “Effects of magnesium ion deficiency on Escherichia coli and possible relation to the mode of action of novobiocin”. In: *Journal of Bacteriology* 84.4, pp. 679–682.

Brummer, B., A. Bertl, I. Potrykus, H. Felle, and R. W. Parish (1985). “Evidence that fusicoccin and indole-3-acetic acid induce cytosolic acidification of Zea mays cells”. In: *FEBS letters* 189.1, pp. 109–114.

Burnap, R. L., T. Troyan, and L. A. Sherman (1993). “The Highly Abundant Chlorophyll-Protein Complex of Iron-Deficient Synechococcus sp. PCC7942 (CP43’) Is Encoded by the isiA Gene”. In: *Plant Physiology* 103.3, pp. 893–902.

Cakmak, I., C. Hengeler, and H. Marschner (1994). “Changes in phloem export of sucrose in leaves in response to phosphorus, potassium and magnesium deficiency in bean plants”. In: *Journal of Experimental Botany* 45.9, pp. 1251–1257.

Calzadilla, P. I. and D. Kirilovsky (2020). “Revisiting cyanobacterial state transitions”. In: *Photochemical & Photobiological Sciences* 19.5, pp. 585–603.

Campbell, D., D. Bruce, C. Carpenter, P. Gustafsson, and G. Öquist (1996). “Two forms of the photosystem II D1 protein alter energy dissipation and state transitions in the cyanobacterium Synechococcus sp. PCC 7942”. In: *Photosynthesis Research* 47.2, pp. 131–144.

Campbell, D., V. Hurry, A. K. Clarke, P. Gustafsson, G. Öquist, and G. Oquist (1998). “Chlorophyll Fluorescence Analysis of Cyanobacterial Photosynthesis and Acclimation”. In: *Microbiology and Molecular Biology Reviews* 62.3, pp. 667–683.

Carrillo, N. and E. A. Ceccarelli (2003). “Open questions in ferredoxin-NADP+ reductase catalytic mechanism”. In: *European Journal of Biochemistry* 270.9, pp. 1900–1915.

Casella, S., F. Huang, D. Mason, G. Y. Zhao, G. N. Johnson, C. W. Mullineaux, and L. N. Liu (2017). “Dissecting the Native Architecture and Dynamics of Cyanobacterial Photosynthetic Machinery”. In: *Molecular Plant* 10.11, pp. 1434–1448.

Checchetto, V., A. Segalla, G. Allorent, N. La Rocca, L. Leanza, G. M. Giacometti, N. Uozumi, G. Finazzi, E. Bergantino, I. Szabo, and I. Szabò (2012). “Thylakoid potassium channel is required for efficient photosynthesis in cyanobacteria”. In: *Proceedings of the National Academy of Sciences* 109.27, pp. 11043–11048.

Chen, Y. S., G. Kozlov, B. E. Moeller, A. Rohaim, R. Fakih, B. Roux, J. E. Burke, and K. Gehring (2021). “Crystal structure of an archaeal CorB magnesium transporter”. In: *Nature Communications* 12.1, p. 4028.

Chen, Z. C., N. Yamaji, T. Horie, J. Che, J. Li, G. An, and J. F. Ma (2017). "A magnesium transporter OsMGT1 plays a critical role in salt tolerance in rice". In: *Plant Physiology* 174.3, pp. 1837–1849.

Chow, W., A. Wagner, and A. Hope (1976). "Light-dependent Redistribution of Ions in Isolated Spinach Chloroplasts". In: *Functional Plant Biology* 3.6, pp. 853–861.

Chung, C. T., S. L. Niemela, and R. H. Miller (1989). "One-step preparation of competent Escherichia coli: transformation and storage of bacterial cells in the same solution". In: *Proceedings of the National Academy of Sciences* 86.7, pp. 2172–2175.

Cimmperman, P. and D. Matulis (2011). "Chapter 8. Protein Thermal Denaturation Measurements via a Fluorescent Dye". In: *RSC Biomolecular Sciences*. 22, pp. 247–274.

Cogdell, R. J. and A. T. Gardiner (2015). "Activated OCP unlocks nonphotochemical quenching in cyanobacteria". In: *Proceedings of the National Academy of Sciences* 112.41, pp. 12547–12548.

Coligan, J. E. (1998). "Commonly Used Detergents". In: *Current Protocols in Protein Science*, Appendix 1l1–Appendix 1l3.

Cooley, J. W. and W. F. J. Vermaas (2001). "Succinate Dehydrogenase and Other Respiratory Pathways in Thylakoid Membranes of Synechocystis sp. Strain PCC 6803: Capacity Comparisons and Physiological Function". In: *Journal of Bacteriology* 183.14, pp. 4251–4258.

DalCorso, G., P. Pesaresi, S. Masiero, E. Aseeva, D. Schünemann, G. Finazzi, P. Joliot, R. Barbato, and D. Leister (2008). "A Complex Containing PGRL1 and PGR5 Is Involved in the Switch between Linear and Cyclic Electron Flow in Arabidopsis". In: *Cell* 132.2, pp. 273–285.

Dann, C. E., C. A. Wakeman, C. L. Sieling, S. C. Baker, I. Irnov, and W. C. Winkler (2007). "Structure and Mechanism of a Metal-Sensing Regulatory RNA". In: *Cell* 130.5, pp. 878–892.

De Baaij, J. H., F. J. Arjona, M. Van Den Brand, M. Lavrijsen, A. L. Lameris, R. J. Bindels, and J. G. Hoenderop (2016). "Identification of SLC41A3 as a novel player in magnesium homeostasis". In: *Scientific Reports* 6, p. 28565.

De Clerck, O., K. A. Bogaert, and F. Leliaert (2012). "Diversity and evolution of algae: primary endosymbiosis". In: *Genomic Insights into the Biology of Algae*. Ed. by G. Piganeau. Vol. 64. Academic Press. Chap. 2, pp. 55–86.

De Magalhães, C. C., D. Cardoso, C. P. Dos Santos, and R. M. Chaloub (2004). "Physiological and photosynthetic responses of Synechocystis aquatilis f. aquatilis (Cyanophyceae) to elevated levels of zinc". In: *Journal of Phycology* 40.3, pp. 496–504.

De Philippis, R., C. Sili, G. Tassinato, M. Vincenzini, and R. Materassi (1991). "Effects of growth conditions on exopolysaccharide production by Cyanospira capsulata". In: *Bioresource Technology* 38.2-3, pp. 101–104.

De Philippis, R. (1998). "Exocellular polysaccharides from cyanobacteria and their possible applications". In: *FEMS Microbiology Reviews* 22.3, pp. 151–175.

De Philippis, R., G. Colica, and E. Micheletti (2011). "Exopolysaccharide-producing cyanobacteria in heavy metal removal from water: Molecular basis and practical applicability of the biosorption process". In: *Applied Microbiology and Biotechnology* 92.4, pp. 697–708.

De Philippis, R., M. C. Margheri, E. Pelosi, and S. Ventura (1993). "Exopolysaccharide production by a unicellular cyanobacterium isolated from a hypersaline habitat". In: *Journal of Applied Phycology* 5, pp. 387–394.

De Rosa, E., V. Checchetto, C. Franchin, E. Bergantino, P. Berto, I. Szabò, G. M. Giacometti, G. Arrigoni, and P. Costantini (2015). "[NiFe]-hydrogenase is essential for cyanobacterium Synechocystis sp. PCC 6803 aerobic growth in the dark". In: *Scientific Reports* 5.1, pp. 1–12.

Dekker, J. P. and E. J. Boekema (2005). "Supramolecular organization of thylakoid membrane proteins in green plants". In: *Biochimica et Biophysica Acta - Bioenergetics* 1706.1-2, pp. 12–39.

Depège, N., S. Bellafiore, and J.-D. Rochaix (2003). "Role of Chloroplast Protein Kinase Stt7 in LHCII Phosphorylation and State Transition in Chlamydomonas". In: *Science* 299.5612, pp. 1572–1575.

Dervaux, J., A. Mejean, and P. Brunet (2015). "Irreversible collective migration of cyanobacteria in eutrophic conditions". In: *PLoS ONE* 10.3, e0120906.

Dilley, R. and L. Vernon (1965). "Ion and water transport processes related to the light-dependent shrinkage of spinach chloroplasts". In: *Archives of Biochemistry and Biophysics* 111.2, pp. 365–375.

Doello, S., M. Burkhardt, and K. Forchhammer (2021). "The essential role of sodium bioenergetics and ATP homeostasis in the developmental transitions of a cyanobacterium". In: *Current Biology* 31.8, pp. 1606–1615.

Dörrich, A. K. and A. Wilde (2015). "Spot assays for viability analysis of cyanobacteria". In: *Bio-protocol* 5.17, e1574.

Drummond, R., A. Tutone, Y.-C. Li, and R. Gardner (2006). "A putative magnesium transporter AtMRS2-11 is localized to the plant chloroplast envelope membrane system". In: *Plant Science* 170.1, pp. 78–89.

Dual-PAM-100 (2006). *Measuring System for Simultaneous Assessment of P700 and Chlorophyll Fluorescence*. Heinz Walz GmbH. Effeltrich, Germany, pp. 1–87. URL: `https://www.walz.com/files/downloads/manuals/dual-pam-100/Dual-PAM_1e.pdf` (visited on Mar. 21, 2023).

Düzgünes, N., J. Wilschut, R. Fraley, and D. Papahadjopoulos (1981). "Studies on the mechanism of membrane fusion. Role of head-group composition in calcium- and magnesium-induced fusion of mixed phospholipid vesicles". In: *Biochimica et Biophysica Acta - Biomembranes* 642.1, pp. 182–195.

Eaton-Rye, J. J. (2011). "Construction of Gene Interruptions and Gene Deletions in the Cyanobacterium Synechocystis sp. Strain PCC 6803". In: *Photosynthesis Research Protocols*. Ed. by R. Carpentier. Humana Press. Chap. 22, pp. 295–312.

Elsässer, M., E. Feitosa-Araujo, S. Lichtenauer, S. Wagner, P. Fuchs, J. Giese, F. Kotnik, M. Hippler, A. J. Meyer, V. G. Maurino, *et al.* (2020). "Photosynthetic

activity triggers pH and NAD redox signatures across different plant cell compartments". In: *BioRxiv*. doi:10.1101/2020.10.31.363051.

Ereño-Orbea, J., I. Oyenarte, and L. A. Martínez-Cruz (2013). "CBS domains: Ligand binding sites and conformational variability". In: *Archives of Biochemistry and Biophysics* 540.1-2, pp. 70–81.

Ermakova, M., T. Huokko, P. Richaud, L. Bersanini, C. J. Howe, D. J. Lea-Smith, G. Peltier, and Y. Allahverdiyeva (2016). "Distinguishing the roles of thylakoid respiratory terminal oxidases in the cyanobacterium Synechocystis sp. PCC 6803". In: *Plant Physiology* 171.2, pp. 1307–1319.

Eshaghi, S., D. Niegowski, A. Kohl, D. M. Molina, S. A. Lesley, and P. Nordlund (2006). "Crystal structure of a divalent metal ion transporter CorA at 2.9 angstrom resolution". In: *Science* 313.5785, pp. 354–357.

Evron, Y. and R. E. McCarty (2000). "Simultaneous measurement of ΔpH and electron transport in chloroplast thylakoids by 9-aminoacridine fluorescence". In: *Plant Physiology* 124.1, pp. 407–414.

Fagerbakke, K. M., S. Norland, and M. Heldal (1999). "The inorganic ion content of native aquatic bacteria". In: *Canadian Journal of Microbiology* 45.4, pp. 304–311.

Falkner, G., F. Horner, K. Werdan, and H. W. Heldt (1976). "pH Changes in the Cytoplasm of the Blue-Green Alga Anacystis nidulans Caused by Light-dependent Proton Flux into the Thylakoid Space". In: *Plant Physiology* 58.6, pp. 717–718.

Farhat, N., A. G. Ivanov, M. Krol, M. Rabhi, A. Smaoui, C. Abdelly, and N. P. Hüner (2015). "Preferential damaging effects of limited magnesium bioavailability on photosystem I in Sulla carnosa plants". In: *Planta* 241.5, pp. 1189–1206.

Feord, H. K., F. E. Dear, D. J. Obbard, and G. Van Ooijen (2019). "A magnesium transport protein related to mammalian SLC41 and bacterial MgtE contributes to circadian timekeeping in a unicellular green alga". In: *Genes* 10.2, p. 158.

Fernández-González, B., I. M. Martínez-Férez, and A. Vioque (1998). "Characterization of two carotenoid gene promoters in the cyanobacterium Synechocystis sp. PCC 6803". In: *Biochimica et Biophysica Acta-Gene Structure and Expression* 1443.3, pp. 343–351.

Finkle, B. J. and D. Appleman (1953). "The effect of magnesium concentration on chlorophyll and catalase development in Chlorella". In: *Plant Physiology* 28.4, p. 652.

Fitzpatrick, D., E. M. Aro, and A. Tiwari (2022). "True oxygen reduction capacity during photosynthetic electron transfer in thylakoids and intact leaves". In: *Plant Physiology* 189.1, pp. 112–128.

Flecks, F. (2021). "Expression, Reinigung und Charakterisierung cyanobakterieller CorA-Homologe". Bachelor thesis. Johannes Gutenberg-Universität Mainz, pp. 1–43.

Flügge, U. I., M. Freisl, and H. W. Heldt (1980). "The mechanism of the control of carbon fixation by the pH in the chloroplast stroma". In: *Planta* 149.1, pp. 48–51.

Foster, A. W., D. Osman, and N. J. Robinson (2014). "Metal preferences and metallation". In: *Journal of Biological Chemistry* 289.41, pp. 28095–28103.

Franken, G. A. C., M. A. Huynen, L. A. Martínez-Cruz, R. J. M. Bindels, and J. H. F. de Baaij (2022). "Structural and functional comparison of magnesium transporters throughout evolution". In: *Cellular and Molecular Life Sciences* 79.8, p. 418.

Fujisawa, T., R. Narikawa, S.-I. Maeda, S. Watanabe, Y. Kanesaki, K. Kobayashi, J. Nomata, M. Hanaoka, M. Watanabe, S. Ehira, E. Suzuki, K. Awai, and Y. Nakamura (2017). "CyanoBase: a large-scale update on its 20th anniversary". In: *Nucleic Acids Research* 45, pp. D551–D554.

Funato, Y. and H. Miki (2019). "Molecular function and biological importance of CNNM family Mg 2+ transporters". In: *Journal of Biochemistry* 165.3, pp. 219–225.

Gasteiger, E., C. Hoogland, A. Gattiker, S. Duvaud, M. Wilkins, R. Appel, and A. Bairoch (2005). "Protein Identification and Analysis Tools on the ExPASy Server". In: *The Proteomics Protocols Handbook*. Ed. by J. M. Walker. Humana Press, pp. 571–607.

Gasymov, O. K. and B. J. Glasgow (2007). "ANS fluorescence: potential to augment the identification of the external binding sites of proteins". In: *Biochimica et Biophysica Acta-Proteins and Proteomics* 1774.3, pp. 403–411.

Gebert, M., K. Meschenmoser, S. Svidová, J. Weghuber, R. Schweyen, K. Eifler, H. Lenz, K. Weyand, and V. Knoop (2009). "A root-expressed magnesium transporter of the MRS2/MGT gene family in Arabidopsis thaliana allows for growth in low-Mg2+ environments". In: *The Plant Cell* 21.12, pp. 4018–4030.

Genty, B., J. M. Briantais, and N. R. Baker (1989). "The relationship between the quantum yield of photosynthetic electron transport and quenching of chlorophyll fluorescence". In: *Biochimica et Biophysica Acta - General Subjects* 990.1, pp. 87–92.

Gibson, D. G., L. Young, R. Y. Chuang, J. C. Venter, C. A. Hutchison, and H. O. Smith (2009). "Enzymatic assembly of DNA molecules up to several hundred kilobases". In: *Nature Methods* 6.5, pp. 343–345.

Gibson, M. M., D. A. Bagga, C. G. Miller, and M. E. Maguire (1991). "Magnesium transport in Salmonella typhimurium: the influence of new mutations conferring Co 2+ resistance on the CorA Mg 2+ transport system". In: *Molecular Microbiology* 5.11, pp. 2753–2762.

Giménez-Mascarell, P., I. González-Recio, C. Fernández-Rodríguez, I. Oyenarte, D. Müller, M. L. Martínez-Chantar, and L. A. Martínez-Cruz (2019). "Current structural knowledge on the CNNM family of magnesium transport mediators". In: *International Journal of Molecular Sciences* 20.5, p. 1135.

Giraldo, N. D., S. M. Correa, A. Arbeláez, F. L. Figueroa, R. Ríos-Estepa, and L. Atehortúa (2021). "Reducing self-shading effects in Botryococcus braunii cultures: effect of Mg2+ deficiency on optical and biochemical properties, photosynthesis and lipidomic profile". In: *Bioresources and Bioprocessing* 8, p. 33.

Goytain, A. and G. A. Quamme (2005). “Functional characterization of human SLC41A1, a Mg2+ transporter with similarity to prokaryotic MgtE Mg2+ transporters”. In: *Physiological Genomics* 21, pp. 337–342.

Gray, M. W. (1989). “The evolutionary origins of organelles”. In: *Trends in Genetics* 5, pp. 294–299.

Grossman, A. R., D. Bhaya, K. E. Apt, and D. M. Kehoe (1995). “Light-harvesting complexes in oxygenic photosynthesis: Diversity, Control, and Evolution”. In: *Annual Review of Genetics* 29.1, pp. 231–288.

Guliyeva, A. J. and O. K. Gasymov (2020). “ANS fluorescence: Potential to discriminate hydrophobic sites of proteins in solid states”. In: *Biochemistry and Biophysics Reports* 24, p. 100843.

Guskov, A., J. Kern, A. Gabdulkhakov, M. Broser, A. Zouni, and W. Saenger (2009). “Cyanobacterial photosystem II at 2.9-Å resolution and the role of quinones, lipids, channels and chloride”. In: *Nature Structural and Molecular Biology* 16.3, pp. 334–342.

Gutu, A., F. Chang, and E. K. O’Shea (2018). “Dynamical localization of a thylakoid membrane binding protein is required for acquisition of photosynthetic competency”. In: *Molecular Microbiology* 108.1, pp. 16–31.

Harada, K., T. Arizono, R. Sato, M. D. L. Trinh, A. Hashimoto, M. Kono, M. Tsujii, N. Uozumi, S. Takaichi, and S. Masuda (2019). “DAY-LENGTH-DEPENDENT DELAYED-GREENING1, the Arabidopsis Homolog of the Cyanobacterial H+-Extrusion Protein, Is Essential for Chloroplast pH Regulation and Optimization of Non-Photochemical Quenching”. In: *Plant and Cell Physiology* 60.12, pp. 2660–2671.

Hattab, G., D. E. Warschawski, K. Moncoq, and B. Miroux (2015). “Escherichia coli as host for membrane protein structure determination: A global analysis”. In: *Scientific Reports* 5, p. 12097.

Hattori, M., N. Iwase, N. Furuya, Y. Tanaka, T. Tsukazaki, R. Ishitani, M. E. Maguire, K. Ito, A. Maturana, and O. Nureki (2009). “Mg2+-dependent gating of bacterial MgtE channel underlies Mg2+ homeostasis”. In: *The EMBO Journal* 28.22, pp. 3602–3612.

Hattori, M., Y. Tanaka, S. Fukai, R. Ishitani, and O. Nureki (2007). “Crystal structure of the MgtE Mg2+ transporter”. In: *Nature* 448.7157, pp. 1072–1075.

Haveman, J., P. Mathis, and A. Vermeglio (1975). “Light-induced absorption changes in the near ultraviolet of the primary electron acceptor of photosystem II at liquid nitrogen temperature”. In: *FEBS Letters* 58.1-2, pp. 259–261.

Heaton, F. W. (1990). “Role of Magnesium in Enzyme Systems”. In: *Metal Ions in Biological Systems: Volume 26: Compendium on Magnesium and Its Role in Biology: Nutrition and Physiology*. Ed. by H. Sigel and A. Sigel. New York: CRC Press. Chap. 7, pp. 119–133.

Hermans, C., G. N. Johnson, R. J. Strasser, and N. Verbruggen (2004). “Physiological characterisation of magnesium deficiency in sugar beet: Acclimation to low magnesium differentially affects photosystems I and II”. In: *Planta* 220.2, pp. 344–355.

Hermans, C. and N. Verbruggen (2005). “Physiological characterization of Mg deficiency in Arabidopsis thaliana”. In: *Journal of Experimental Botany* 56.418, pp. 2153–2161.

Hertle, A. P., T. Blunder, T. Wunder, P. Pesaresi, M. Pribil, U. Armbruster, and D. Leister (2013). “PGRL1 Is the Elusive Ferredoxin-Plastoquinone Reductase in Photosynthetic Cyclic Electron Flow”. In: *Molecular Cell* 49.3, pp. 511–523.

Hihara, Y., K. Sonoike, and M. Ikeuchi (1998). “A Novel Gene, pmgA , Specifically Regulates Photosystem Stoichiometry in the Cyanobacterium Synechocystis Species PCC 6803 in Response to High Light1”. In: *Plant Physiology* 117.4, pp. 1205–1216.

Hind, G., H. Y. Nakatani, and S. Izawa (1974). “Light-Dependent Redistribution of Ions in Suspensions of Chloroplast Thylakoid Membranes”. In: *Proceedings of the National Academy of Sciences* 71.4, pp. 1484–1488.

Hmiel, S. P., M. D. Snavely, C. G. Miller, and M. E. Maguire (1986). “Magnesium transport in Salmonella typhimurium: Characterization of magnesium influx and cloning of a transport gene”. In: *Journal of Bacteriology* 168.3, pp. 1444–1450.

Holzwarth, G. and P. Doty (1965). “The Ultraviolet Circular Dichroism of Polypeptides 1”. In: *Journal of the American Chemical Society* 87.2, pp. 218–228.

Howitt, C. A. and W. F. J. Vermaas (1998). “Quinol and Cytochrome Oxidases in the Cyanobacterium Synechocystis sp. PCC 6803”. In: *Biochemistry* 37.51, pp. 17944–17951.

Huang, S., L. Chen, R. Te, J. Qiao, J. Wang, and W. Zhang (2013). “Complementary iTRAQ proteomics and RNA-seq transcriptomics reveal multiple levels of regulation in response to nitrogen starvation in Synechocystis sp. PCC 6803”. In: *Molecular BioSystems* 9.10, pp. 2565–2574.

Huang, Y., F. Jin, Y. Funato, Z. Xu, W. Zhu, J. Wang, M. Sun, Y. Zhao, Y. Yu, H. Miki, and M. Hattori (2021). “Structural basis for the Mg2+ recognition and regulation of the CorC Mg2+ transporter”. In: *Science Advances* 7.7, eabe6140.

Ihalainen, J. A., S. D’Haene, N. Yeremenko, H. Van Roon, A. A. Arteni, E. J. Boekema, R. Van Grondelle, H. C. Matthijs, and J. P. Dekker (2005). “Aggregates of the chlorophyll-binding protein IsiA (CP43’) dissipate energy in cyanobacteria”. In: *Biochemistry* 44.32, pp. 10846–10853.

Inago, H., R. Sato, and S. Masuda (2020). “Regulation of light-induced H+ extrusion and uptake by cyanobacterial homologs of the plastidial FLAP1, DLDG1, and Ycf10 in Synechocystis sp. PCC6803”. In: *Biochimica et Biophysica Acta - Bioenergetics* 1861.10, p. 148258.

Inoue, Y., T. Ogawa, and K. Shibata (1973). “Light-induced spectral changes of P700 in the 800-nm region in Anacystis and spinach lamellae”. In: *Biochimica et Biophysica Acta-Bioenergetics* 305.2, pp. 483–487.

Irving, H. and R. J. Williams (1948). “Order of stability of metal complexes”. In: *Nature* 162.4123, pp. 746–747.

Ishijima, S., Y. Manabe, Y. Shinkawa, A. Hotta, A. Tokumasu, M. Ida, and I. Sagami (2018). “The homologous Arabidopsis MRS2/MGT/CorA-type Mg2+ channels,

AtMRS2-10 and AtMRS2-1 exhibit different aluminum transport activity". In: *Biochimica et Biophysica Acta - Biomembranes* 1860.11, pp. 2184–2191.

Ivanov, A. G., M. Krol, D. Sveshnikov, E. Selstam, S. Sandström, M. Koochek, Y. I. Park, S. Vasil'ev, D. Bruce, G. Öquist, and N. P. Huner (2006). "Iron deficiency in cyanobacteria causes monomerization of photosystem I trimers and reduces the capacity for state transitions and the effective absorption cross section of photosystem I in vivo". In: *Plant Physiology* 141.4, pp. 1436–1445.

Jamali Jaghdani, S., P. Jahns, and M. Tränkner (2021). "Mg deficiency induces photo-oxidative stress primarily by limiting CO2 assimilation and not by limiting photosynthetic light utilization". In: *Plant Science* 302, p. 110751.

Jin, F., M. Sun, T. Fujii, Y. Yamada, J. Wang, A. D. Maturana, M. Wada, S. Su, J. Ma, H. Takeda, T. Kusakizako, A. Tomita, Y. Nakada-Nakura, K. Liu, T. Uemura, Y. Nomura, N. Nomura, K. Ito, O. Nureki, K. Namba, S. Iwata, Y. Yu, and M. Hattori (2021). "The structure of MgtE in the absence of magnesium provides new insights into channel gating". In: *PLoS Biology* 19.4, e3001231.

Jokinen, R. (1990). "Magnesium in the Environment". In: *Metal Ions in Biological Systems: Volume 26: Compendium on Magnesium and Its Role in Biology: Nutrition and Physiology*. Ed. by H. Sigel and A. Sigel. New York: CRC Press. Chap. 2, pp. 15–32.

Joliot, P., G. Barbieri, and R. Chabaud (1969). "Un nouveau modele des centres photochimiques du systeme II". In: *Photochemistry and Photobiology* 10.5, pp. 309–329.

Joliot, P. (1968). "Kinetic Studies of Photosystem II in Photosynthesis". In: *Photochemistry and Photobiology* 8.5, pp. 451–463.

Jordan, P., P. Fromme, O. Klukas, H. T. Witt, W. Saenger, and N. Krauß (2001). "X-Ray crystallographic structure analysis of cyanobacterial photosystem I at 2.5 Å resolution". In: *Nature* 411.June, pp. 909–917.

Jumper, J., R. Evans, A. Pritzel, T. Green, M. Figurnov, O. Ronneberger, K. Tunyasuvunakool, R. Bates, A. Žídek, A. Potapenko, A. Bridgland, C. Meyer, S. A. Kohl, A. J. Ballard, A. Cowie, B. Romera-Paredes, S. Nikolov, R. Jain, J. Adler, T. Back, S. Petersen, D. Reiman, E. Clancy, M. Zielinski, M. Steinegger, M. Pacholska, T. Berghammer, S. Bodenstein, D. Silver, O. Vinyals, A. W. Senior, K. Kavukcuoglu, P. Kohli, and D. Hassabis (2021). "Highly accurate protein structure prediction with AlphaFold". In: *Nature* 596.7873, pp. 583–589.

Jürgens, U. and J. Weckesser (1985). "Carotenoid-containing outer membrane of Synechocystis sp. strain PCC6714". In: *Journal of Bacteriology* 164.1, pp. 384–389.

Kaňa, R. and Govindjee (2016). "Role of Ions in the Regulation of Light-Harvesting". In: *Frontiers in Plant Science* 7, p. 1849.

Kaneko, T., S. Sato, H. Kotani, A. Tanaka, E. Asamizu, Y. Nakamura, N. Miyajima, M. Hirosawa, M. Sugiura, S. Sasamoto, T. Kimura, T. Hosouchi, A. Matsuno, A. Muraki, N. Nakazaki, K. Naruo, S. Okumura, S. Shimpo, C. Takeuchi, T. Wada, A. Watanabe, M. Yamada, M. Yasuda, and S. Tabata (1996). "Sequence Analysis of the Genome of the Unicellular Cyanobacterium Synechocystis sp. Strain

PCC6803. II. Sequence Determination of the Entire Genome and Assignment of Potential Protein-coding Regions". In: *DNA Research* 3.3, pp. 109–136.

Kaplan, A., S. Scherer, and M. Lerner (1989). " Nature of the Light-Induced H + Efflux and Na + Uptake in Cyanobacteria ". In: *Plant Physiology* 89.4, pp. 1220–1225.

Katoh, A., M. Sonoda, H. Katoh, and T. Ogawa (1996). "Absence of light-induced proton extrusion in a cotA-less mutant of Synechocystis sp. Strain PCC6803". In: *Journal of Bacteriology* 178.18, pp. 5452–5455.

Keilin, D. (1929). "Cytochrome and respiratory enzymes". In: *Proceedings of the Royal Society of London. Series B, Containing Papers of a Biological Character* 104.730, pp. 206–252.

Kelly, C. L., G. M. Taylor, A. Hitchcock, A. Torres-Méndez, and J. T. Heap (2018). "A Rhamnose-Inducible System for Precise and Temporal Control of Gene Expression in Cyanobacteria". In: *ACS Synthetic Biology* 7.4, pp. 1056–1066.

Kelly, S. M., T. J. Jess, and N. C. Price (2005). "How to study proteins by circular dichroism". In: *Biochimica et Biophysica Acta - Proteins and Proteomics* 1751.2, pp. 119–139.

Kemp, B. E. (2004). "Bateman domains and adenosine derivatives form a binding contract". In: *Journal of Clinical Investigation* 113.2, pp. 182–184.

Kerfeld, C. A., M. R. Sawaya, V. Brahmandam, D. Cascio, K. K. Ho, C. C. Trevithick-Sutton, D. W. Krogmann, and T. O. Yeates (2003). "The crystal structure of a cyanobacterial water-soluble carotenoid binding protein". In: *Structure* 11.1, pp. 55–65.

Kimimura, M. and S. Katoh (1972). "Studies on electron transport associated with Photosystem I. I. Functional site of plastocyanin: Inhibitory effects of HgCl2 on electron transport and plastocyanin in chloroplasts". In: *Biochimica et Biophysica Acta - Bioenergetics* 283.2, pp. 279–292.

Kimura, T., V. A. Lorenz-Fonfria, S. Douki, H. Motoki, R. Ishitani, O. Nureki, M. Higashi, and Y. Furutani (2018). "Vibrational and Molecular Properties of Mg2+ Binding and Ion Selectivity in the Magnesium Channel MgtE". In: *Journal of Physical Chemistry B* 122.42, pp. 9681–9696.

King, N. P., T. M. Lee, M. R. Sawaya, D. Cascio, and T. O. Yeates (2008). "Structures and Functional Implications of an AMP-Binding Cystathionine β-Synthase Domain Protein from a Hyperthermophilic Archaeon". In: *Journal of Molecular Biology* 380.1, pp. 181–192.

Kirilovsky, D., R. Kaňa, and O. Prášil (2014). "Mechanisms Modulating Energy Arriving at Reaction Centers in Cyanobacteria". In: *Non-Photochemical Quenching and Energy Dissipation in Plants, Algae and Cyanobacteria*. Ed. by B. Demmig-Adams, G. Garab, W. Adams III, and Govindjee. Vol. 40. Advances in Photosynthesis and Respiration. Dordrecht: Springer Netherlands. Chap. 22.

Kłodawska, K., L. Kovács, R. Vladkova, A. Rzaska, Z. Gombos, H. Laczkó-Dobos, and P. Malec (2020). "Trimeric organization of photosystem I is required to maintain the balanced photosynthetic electron flow in cyanobacterium Synechocystis sp. PCC 6803". In: *Photosynthesis Research* 143.3, pp. 251–262.

Klughammer, C. and U. Schreiber (1994). “An improved method, using saturating light pulses, for the determination of photosystem I quantum yield via P700+-absorbance changes at 830 nm”. In: *Planta* 192, pp. 261–268.

— (2008). “Saturation Pulse method for assessment of energy conversion in PS I”. In: *PAM Application Notes* 1, pp. 11–14.

Knoop, V., M. Groth-Malonek, M. Gebert, K. Eifler, and K. Weyand (2005). “Transport of magnesium and other divalent cations: evolution of the 2-TM-GxN proteins in the MIT superfamily”. In: *Molecular Genetics and Genomics* 274.3, pp. 205–216.

Kobayashi, N. I. and K. Tanoi (2015). “Critical issues in the study of magnesium transport systems and magnesium deficiency symptoms in plants”. In: *International Journal of Molecular Sciences* 16.9, pp. 23076–23093.

Kolisek, M., A. Nestler, J. Vormann, and M. Schweigel-Röntgen (2012). “Human gene SLC41A1 encodes for the Na + /Mg 2+ exchanger”. In: *American Journal of Physiology-Cell Physiology* 302.1, pp. C318–C326.

Krasikov, V. (2012). “Dynamic changes in gene expression of the cyanobacterium Synechocystis sp. PCC 6803 in response to nitrogen starvation”. PhD thesis. Universiteit van Amsterdam, p. 196.

Krebs, H. A. and W. A. Johnson (1937). “Metabolism of ketonic acids in animal tissues”. In: *Biochemical Journal* 31.4, pp. 645–660.

Krebs, H. A., E. Salvin, and W. A. Johnson (1938). “The formation of citric and α-ketoglutaric acids in the mammalian body”. In: *Biochemical Journal* 32.1, pp. 113–117.

Krieger-Liszkay, A., P. B. Kós, and É. Hideg (2011). “Superoxide anion radicals generated by methylviologen in photosystem I damage photosystem II”. In: *Physiologia Plantarum* 142.1, pp. 17–25.

Kucharski, L. M., W. J. Lubbe, and M. E. Maguire (2000). “Cation hexaammines are selective and potent inhibitors of the CorA magnesium transport system”. In: *Journal of Biological Chemistry* 275.22, pp. 16767–16773.

Laemmli, U. K. (1970). “Cleavage of Structural Proteins during the Assembly of the Head of Bacteriophage T4”. In: *Nature* 227.5259, pp. 680–685.

Latowski, D., J. Grzyb, and K. Strzałka (2004). “The xanthophyll cycle - molecular mechanism and physiological significance”. In: *Acta Physiologiae Plantarum* 26.2, pp. 197–212.

Laudenbach, D. E. and N. A. Straus (1988). “Characterization of a cyanobacterial iron stress-induced gene similar to psbC”. In: *Journal of Bacteriology* 170.11, pp. 5018–5026.

Lea-Smith, D. J., P. Bombelli, R. Vasudevan, and C. J. Howe (2016). “Photosynthetic, respiratory and extracellular electron transport pathways in cyanobacteria”. In: *Biochimica et Biophysica Acta - Bioenergetics* 1857.3, pp. 247–255.

Lehigh University, L. E. I. at (2011). *Calcium and Water Hardness*. URL: `https://ei.lehigh.edu/envirosci/watershed/wq/wqbackground/calciumbg.html` (visited on Mar. 21, 2023).

Li, L., A. F. Tutone, R. S. Drummond, R. C. Gardner, and S. Luan (2001). "A novel family of magnesium transport genes in Arabidopsis". In: *The Plant Cell* 13.12, pp. 2761–2775.

Li, T., Y. Zhang, M. Shi, G. Pei, L. Chen, and W. Zhang (2016). "A putative magnesium transporter Slr1216 involved in sodium tolerance in cyanobacterium Synechocystis sp. PCC 6803". In: *Algal Research* 17, pp. 202–210.

Li, X. P., O. Björkman, C. Shih, A. R. Grossman, M. Rosenquist, S. Jansson, and K. K. Niyogi (2000). "A pigment-binding protein essential for regulation of photosynthetic light harvesting". In: *Nature* 403.6768, pp. 391–395.

Liberton, M., R. Saha, J. M. Jacobs, A. Y. Nguyen, M. A. Gritsenko, R. D. Smith, D. W. Koppenaal, and H. B. Pakrasi (2016). "Global Proteomic Analysis Reveals an Exclusive Role of Thylakoid Membranes in Bioenergetics of a Model Cyanobacterium". In: *Molecular & Cellular Proteomics* 15.6, pp. 2021–2032.

Liu, D., V. M. Johnson, and H. B. Pakrasi (2020). "A Reversibly Induced CRISPRi System Targeting Photosystem II in the Cyanobacterium Synechocystis sp. PCC 6803". In: *ACS Synthetic Biology* 9.6, pp. 1441–1449.

Liu, L. N. (2016). "Distribution and dynamics of electron transport complexes in cyanobacterial thylakoid membranes". In: *Biochimica et Biophysica Acta - Bioenergetics* 1857.3, pp. 256–265.

Liu, M. and S. C. Dudley (2020). "Magnesium, oxidative stress, inflammation, and cardiovascular disease". In: *Antioxidants* 9.10, p. 907.

Lorimer, G. H., M. R. Badger, and T. J. Andrews (1976). "The Activation of Ribulose-1,5-bisphosphate Carboxylase by Carbon Dioxide and Magnesium Ions. Equilibria, Kinetics, a Suggested Mechanism, and Physiological implications". In: *Biochemistry* 15.3, pp. 529–536.

Luimstra, V. M., J. M. Schuurmans, C. F. de Carvalho, H. C. P. Matthijs, K. J. Hellingwerf, and J. Huisman (2019). "Exploring the low photosynthetic efficiency of cyanobacteria in blue light using a mutant lacking phycobilisomes". In: *Photosynthesis Research* 141.3, pp. 291–301.

Luimstra, V. M., J. M. Schuurmans, A. M. Verschoor, K. J. Hellingwerf, J. Huisman, and H. C. P. Matthijs (2018). "Blue light reduces photosynthetic efficiency of cyanobacteria through an imbalance between photosystems I and II". In: *Photosynthesis Research* 138.2, pp. 177–189.

Lunin, V. V., E. Dobrovetsky, G. Khutoreskaya, R. Zhang, A. Joachimiak, D. A. Doyle, A. Bochkarev, M. E. Maguire, A. M. Edwards, and C. M. Koth (2006). "Crystal structure of the CorA Mg2+ transporter". In: *Nature* 440.7085, pp. 833–837.

Lynn, S. (1967). "On the origin of mitosing cells". In: *Journal of Theoretical Biology* 14.3, pp. 255–74.

Lyu, H. and D. Lazár (2017). "Modeling the light-induced electric potential difference $\Delta\Psi$ across the thylakoid membrane based on the transition state rate theory". In: *Biochimica et Biophysica Acta - Bioenergetics* 1858.3, pp. 239–248.

Ma, F., X. Zhang, X. Zhu, T. Li, J. Zhan, H. Chen, C. He, and Q. Wang (2017). "Dynamic Changes of IsiA-Containing Complexes during Long-Term Iron Deficiency in Synechocystis sp. PCC 6803". In: *Molecular Plant* 10.1, pp. 143–154.

Mackay, S. P. and P. J. O'Malley (1993). "Molecular modelling of the interaction between DCMU and QB-binding site of photosystem II". In: *Zeitschrift für Naturforschung. C* 48.3-4, pp. 191–198.

Maduh, E. U., J. L. Borowitz, and G. E. Isom (1990). "Cyanide-induced alteration of cytosolic pH: Involvement of cellular hydrogen ion handling processes". In: *Toxicology and Applied Pharmacology* 106.2, pp. 201–208.

Maeshima, K., T. Matsuda, Y. Shindo, H. Imamura, S. Tamura, R. Imai, S. Kawakami, R. Nagashima, T. Soga, H. Noji, K. Oka, and T. Nagai (2018). "A Transient Rise in Free Mg2+ Ions Released from ATP-Mg Hydrolysis Contributes to Mitotic Chromosome Condensation". In: *Current Biology* 28.3, 444–451.e6.

Maguire, M. E. (2006). "Magnesium Transporters: Properties, Regulation and Structure". In: *Frontiers in Bioscience* 11.1, pp. 3149–3163.

— (1990). "Magnesium: A Regulated and Regulatory Cation". In: *Metal Ions in Biological Systems: Volume 26: Compendium on Magnesium and Its Role in Biology: Nutrition and Physiology*. Ed. by H. Sigel and A. Sigel. 26th ed. CRC Press. Chap. 8, pp. 135–153.

Maguire, M. E. and J. A. Cowan (2002). "Magnesium chemistry and biochemistry". In: *Biometals* 15.3, p. 203.

Mahey, S., R. Kumar, M. Sharma, V. Kumar, and R. Bhardwaj (2020). "A critical review on toxicity of cobalt and its bioremediation strategies". In: *SN Applied Sciences* 2.7, p. 1279.

Manente, S., S. De Pieri, A. Iero, C. Rigo, and M. Bragadin (2008). "A comparison between the responses of neutral red and acridine orange: Acridine orange should be preferential and alternative to neutral red as a dye for the monitoring of contaminants by means of biological sensors". In: *Analytical Biochemistry* 383.2, pp. 316–319.

Mangan, N. M., A. Flamholz, R. D. Hood, R. Milo, and D. F. Savage (2016). "PH determines the energetic efficiency of the cyanobacterial CO2 concentrating mechanism". In: *Proceedings of the National Academy of Sciences* 113.36, E5354–E5362.

Mareš, J., O. Strunecký, L. Bučinská, and J. Wiedermannová (2019). "Evolutionary patterns of thylakoid architecture in Cyanobacteria". In: *Frontiers in Microbiology* 10, p. 277.

Martin, R. B. (1990). "Bioinorganic chemistry of Magnesium". In: *Metal Ions in Biological Systems: Volume 26: Compendium on Magnesium and Its Role in Biology: Nutrition and Physiology*. Ed. by H. Sigel and A. Sigel. New York: CRC Press. Chap. 1, pp. 1–13.

Martin, W., T. Rujan, E. Richly, A. Hansen, S. Cornelsen, T. Lins, D. Leister, B. Stoebe, M. Hasegawa, and D. Penny (2002). "Evolutionary analysis of Arabidopsis, cyanobacterial, and chloroplast genomes reveals plastid phylogeny and

thousands of cyanobacterial genes in the nucleus". In: *Proceedings of the National Academy of Sciences* 99.19, pp. 12246–12251.

Maruyama, T., S. Imai, T. Kusakizako, M. Hattori, R. Ishitani, O. Nureki, K. Ito, A. D. Maturana, I. Shimada, and M. Osawa (2018). "Functional roles of Mg2+ binding sites in ion-dependent gating of a Mg2+ channel, MgtE, revealed by solution NMR". In: *eLife* 7, e31596.

Matthies, D., O. Dalmas, M. J. Borgnia, P. K. Dominik, A. Merk, P. Rao, B. G. Reddy, S. Islam, A. Bartesaghi, E. Perozo, and S. Subramaniam (2016). "Cryo-EM Structures of the Magnesium Channel CorA Reveal Symmetry Break upon Gating". In: *Cell* 164.4, pp. 747–756.

Maxwell, K. and G. N. Johnson (2000). "Chlorophyll fluorescence—a practical guide". In: *Journal of Experimental Botany* 51.345, pp. 659–668.

McCarthy, B. (1962). "The effects of magnesium starvation on the ribosome content of Escherichia coli". In: *Biochimica et Biophysica Acta - Specialized Section on Nucleic Acids and Related Subjects* 55.6, pp. 880–889.

McDonald, A. E., A. G. Ivanov, R. Bode, D. P. Maxwell, S. R. Rodermel, and N. P. Hüner (2011). "Flexibility in photosynthetic electron transport: The physiological role of plastoquinol terminal oxidase (PTOX)". In: *Biochimica et Biophysica Acta - Bioenergetics* 1807.8, pp. 954–967.

McFadden, G. I. (2001). "Primary and secondary endosymbiosis and the origin of plastids". In: *Journal of Phycology* 37.6, pp. 951–959.

Mereschkowsky, C. (1905). "Über Natur und Ursprung der Chromatophoren im Pflanzenreiche". In: *Biologisches Centralblatt* 25, pp. 293–604.

Merhaut, D. J. (2007). "Magnesium". In: *Handbook of Plant Nutrition*. Ed. by A. V. Barker and D. J. Pilbeam. 1st. CRC Press. Chap. 6, pp. 146–172.

Metz, J. G., H. B. Pakrasi, M. Seibert, and C. J. Arntzer (1986). "Evidence for a dual function of the herbicide-binding D1 protein in photosystem II". In: *FEBS Letters* 205.2, pp. 269–274.

Mewes, A., G. Langer, L. J. de Nooijer, J. Bijma, and G. J. Reichart (2014). "Effect of different seawater Mg2+ concentrations on calcification in two benthic foraminifers". In: *Marine Micropaleontology* 113, pp. 56–64.

Mi, H., T. Endo, U. Schreiber, and K. Asada (1992a). "Donation of electrons from cytosolic components to the intersystem chain in the cyanobacterium synechococcus sp. PCC 7002 as determined by the reduction of P700". In: *Plant and Cell Physiology* 33.8, pp. 1099–1105.

Mi, H., T. Endo, U. Schreiber, T. Ogawa, and K. Asada (1992b). "Electron donation from cyclic and respiratory flows to the photosynthetic intersystem chain is mediated by pyridine nucleotide dehydrogenase in the cyanobacterium synechocystis PCC 6803". In: *Plant and Cell Physiology* 33.8, pp. 1233–1237.

Mi, H., C. Klughammer, and U. Schreiber (2000). "Light-induced dynamic changes of NADPH fluorescence in Synechocystis PCC 6803 and its ndhB-defective mutant M55". In: *Plant and Cell Physiology* 41.10, pp. 1129–1135.

Micsonai, A., É. Bulyáki, and J. Kardos (2021). "BeStSel: From Secondary Structure Analysis to Protein Fold Prediction by Circular Dichroism Spectroscopy". In: *Methods in Molecular Biology* 2199, pp. 175–189.

Micsonai, A., F. Wien, É. Bulyáki, J. Kun, É. Moussong, Y. H. Lee, Y. Goto, M. Réfrégiers, and J. Kardos (2018). "BeStSel: A web server for accurate protein secondary structure prediction and fold recognition from the circular dichroism spectra". In: *Nucleic Acids Research* 46.W1, W315–W322.

Micsonai, A., F. Wien, L. Kernya, Y. H. Lee, Y. Goto, M. Réfrégiers, and J. Kardos (2015). "Accurate secondary structure prediction and fold recognition for circular dichroism spectroscopy". In: *Proceedings of the National Academy of Sciences* 112.24, E3095–E3103.

Mikkat, S., C. Milkowski, and M. Hagemann (2000). "The gene sll 0273 of the cyanobacterium Synechocystis sp. strain PCC6803 encodes a protein essential for growth at low Na + /K + ratios". In: *Plant, Cell & Environment* 23.6, pp. 549–559.

Miller, N. T., M. D. Vaughn, and R. L. Burnap (2021). "Electron flow through NDH-1 complexes is the major driver of cyclic electron flow-dependent proton pumping in cyanobacteria". In: *Biochimica et Biophysica Acta - Bioenergetics* 1862.3, p. 148354.

Mirkovic, T., E. E. Ostroumov, J. M. Anna, R. Van Grondelle, Govindjee, and G. D. Scholes (2017). "Light absorption and energy transfer in the antenna complexes of photosynthetic organisms". In: *Chemical Reviews* 117.2, pp. 249–293.

Miroux, B. and J. E. Walker (1996). "Over-production of proteins in Escherichia coli: mutant hosts that allow synthesis of some membrane proteins and globular proteins at high levels". In: *Journal of Molecular Biology* 260.3, pp. 289–298.

Mitchell, P. (1961). "Coupling of Phosphorylation to Electron and Hydrogen Transfer by a Chemi-Osmotic type of Mechanism". In: *Nature* 191.4784, pp. 144–148.

— (1976). "Possible molecular mechanisms of the protonmotive function of cytochrome systems". In: *Journal of Theoretical Biology* 62.2, pp. 327–367.

Mohamed, H. E., A. M. Van De Meene, R. W. Roberson, and W. F. Vermaas (2005). "Myxoxanthophyll is required for normal cell wall structure and thylakoid organization in the cyanobacterium Synechocystis sp. strain PCC 6803". In: *Journal of Bacteriology* 187.20, pp. 6883–6892.

Moncany, M. L. and E. Kellenberger (1981). "High magnesium content of Escherichia coli B". In: *Experientia* 37.8, pp. 846–847.

Moomaw, A. S. and M. E. Maguire (2008). "The Unique Nature of Mg 2+ Channels". In: *Physiology* 23.5, pp. 275–285.

Mott, K. A. and J. A. Berry (1986). "Effects of pH on Activity and Activation of Ribulose 1,5-Bisphosphate Carboxylase at Air Level CO 2". In: *Plant Physiology* 82.1, pp. 77–82.

Mulcahy, H. and S. Lewenza (2011). "Magnesium limitation is an environmental trigger of the Pseudomonas aeruginosa biofilm lifestyle". In: *PLoS One* 6.8, e23307.

Mullineaux, C. W. and J. F. Allen (1986). “The state 2 transition in the cyanobacterium Synechococcus 6301 can be driven by respiratory electron flow into the plastoquinone pool”. In: *Febs Letters* 205.1, pp. 155–160.

Mullineaux, C. W. (2014). “Co-existence of photosynthetic and respiratory activities in cyanobacterial thylakoid membranes”. In: *Biochimica et Biophysica Acta - Bioenergetics* 1837.4, pp. 503–511.

Mullineaux, C. W. and J. F. Allen (1990). “State 1-State 2 transitions in the cyanobacterium Synechococcus 6301 are controlled by the redox state of electron carriers between Photosystems I and II”. In: *Photosynthesis Research* 23.3, pp. 297–311.

Mullineaux, C. W. and L. N. Liu (2020). “Membrane Dynamics in Phototrophic Bacteria”. In: *Annual Review of Microbiology* 74, pp. 633–654.

Murakami, A. (1997). “Quantitative analysis of 77K fluorescence emission spectra in Synechocystis sp. PCC 6714 and Chlamydomonas reinhardtii with variable PS I/PS II stoichiometries”. In: *Photosynthesis Research* 53, pp. 141–148.

Murata, N. (1969). “Control of excitation transfer in photosynthesis I. Light-induced change of chlorophyll a fluoresence in Porphyridium cruentum”. In: *Biochimica et Biophysica Acta - Bioenergetics* 172.2, pp. 242–251.

Murchie, E. H. and T. Lawson (2013). “Chlorophyll fluorescence analysis: A guide to good practice and understanding some new applications”. In: *Journal of Experimental Botany* 64.13, pp. 3983–3998.

Mustila, H., D. Muth-Pawlak, E. M. Aro, and Y. Allahverdiyeva (2021). “Global proteomic response of unicellular cyanobacterium Synechocystis sp. PCC 6803 to fluctuating light upon CO2 step-down”. In: *Physiologia Plantarum* 173.1, pp. 305–320.

Nakamura, Y., T. Kaneko, and S. Tabata (2000). “CyanoBase, the genome database for Synechocystis sp. strain PCC6803: Status for the year 2000”. In: *Nucleic Acids Research* 28.1, p. 72.

Nakao, M., S. Okamoto, M. Kohara, T. Fujishiro, T. Fujisawa, S. Sato, S. Tabata, T. Kaneko, and Y. Nakamura (2010). “CyanoBase: the cyanobacteria genome database update 2010”. In: *Nucleic Acids Research* 38.suppl_1, pp. D379–D381.

NCBI (2022). *BLAST:Basic Local Alignment Search Tool*. URL: `https://blast.ncbi.nlm.nih.gov/Blast.cgi` (visited on Oct. 22, 2022).

Nelson, D. L. and E. P. Kennedy (1971). “Magnesium transport in Escherichia coli. Inhibition by cobaltous ion”. In: *The Journal of biological chemistry* 246.9, pp. 3042–3049.

Nickelsen, J. and B. Rengstl (2013). “Photosystem II assembly: from cyanobacteria to plants”. In: *Annual review of Plant Biology* 64, pp. 609–635.

Niegowski, D. and S. Eshaghi (2007). “The CorA family: Structure and function revisited”. In: *Cellular and Molecular Life Sciences* 64.19-20, pp. 2564–2574.

Nikkanen, L., D. Solymosi, M. Jokel, and Y. Allahverdiyeva (2021). “Regulatory electron transport pathways of photosynthesis in cyanobacteria and microalgae: Recent advances and biotechnological prospects”. In: *Physiologia Plantarum* 173.2, pp. 514–525.

Nitschmann, W. H. and G. A. Peschek (1985). “Modes of proton translocation across the cell membrane of respiring cyanobacteria”. In: *Archives of Microbiology* 141.4, pp. 330–336.

Nordin, N., A. Guskov, T. Phua, N. Sahaf, Y. Xia, S. Lu, H. Eshaghi, and S. Eshaghi (2013). “Exploring the structure and function of Thermotoga maritimaCorA reveals the mechanism of gating and ion selectivity in Co2+/Mg2+ transport”. In: *Biochemical Journal* 451.3, pp. 365–374.

Ogawa, T., M. Misumi, and K. Sonoike (2017). “Estimation of photosynthesis in cyanobacteria by pulse-amplitude modulation chlorophyll fluorescence: problems and solutions”. In: *Photosynthesis Research* 133.1-3, pp. 63–73.

Ogawa, T. and K. Sonoike (2016). “Effects of Bleaching by Nitrogen Deficiency on the Quantum Yield of Photosystem II in Synechocystis sp. PCC 6803 Revealed by Chl Fluorescence Measurements”. In: *Plant and Cell Physiology* 57.3, pp. 558–567.

Ogawa, T., K. Suzuki, and K. Sonoike (2021). “Respiration Interacts With Photosynthesis Through the Acceptor Side of Photosystem I, Reflected in the Dark-to-Light Induction Kinetics of Chlorophyll Fluorescence in the Cyanobacterium Synechocystis sp. PCC 6803”. In: *Frontiers in Plant Science* 12, p. 717968.

Ota, C., S.-i. Tanaka, and K. Takano (2021). “Revisiting the Rate-Limiting Step of the ANS–Protein Binding at the Protein Surface and Inside the Hydrophobic Cavity”. In: *Molecules* 26.2, p. 420.

Pakrasi, H., T. Ogawa, and M. Bhattacharrya-Pakrasi (2006). “Transport of Metals: A Key Process in Oxygenic Photosynthesis”. In: *Regulation of Photosynthesis*. Ed. by E.-M. Aro and B. Andersson. Vol. 11. Advances in Photosynthesis and Respiration 1986. Dordrecht: Kluwer Academic Publishers. Chap. 14, pp. 253–264.

Palmgren, M. G. (1991). “Acridine orange as a probe for measuring pH gradients across membranes: Mechanism and limitations”. In: *Analytical Biochemistry* 192.2, pp. 316–321.

Parker, D. L., B. R. Schram, J. L. Plude, and R. E. Moore (1996). “Effect of metal cations on the viscosity of a pectin-like capsular polysaccharide from the cyanobacterium Microcystis flos-aquae C3-40”. In: *Applied and Environmental Microbiology* 62.4, pp. 1208–1213.

Patra, M. and A. Sharma (2000). “Mercury toxicity in plants”. In: *The Botanical Review* 66, pp. 379–422.

Patrick Fuerst, E. and M. Norman (1991). “Interactions of Herbicides with Photosynthetic Electron Transport”. In: *Weed Science* 39.3, pp. 458–464.

Payandeh, J., C. Li, M. Ramjeesingh, E. Poduch, C. E. Bear, and E. F. Pai (2008). “Probing structure-function relationships and gating mechanisms in the CorA Mg2+ transport system”. In: *Journal of Biological Chemistry* 283.17, pp. 11721–11733.

Payandeh, J. and E. F. Pai (2006). “A structural basis for Mg2+ homeostasis and the CorA translocation cycle”. In: *The EMBO Journal* 25.16, pp. 3762–3773.

Payandeh, J., R. Pfoh, and E. F. Pai (2013). "The structure and regulation of magnesium selective ion channels". In: *Biochimica et Biophysica Acta - Biomembranes* 1828.11, pp. 2778–2792.

Pelletier, J. and J. Caventou (1818). "Sur la Matière verte des Feuilles". In: *Annales de chimie et de physique* 9, pp. 194–196.

Peng, Y. Y., L. L. Liao, S. Liu, M. M. Nie, J. Li, L. D. Zhang, J. F. Ma, and Z. C. Chen (2019). "Magnesium deficiency triggers sgr-mediated chlorophyll degradation for magnesium remobilization". In: *Plant Physiology* 181.1, pp. 262–275.

Pereira, S., A. Zille, E. Micheletti, P. Moradas-Ferreira, R. De Philippis, and P. Tamagnini (2009). "Complexity of cyanobacterial exopolysaccharides: Composition, structures, inducing factors and putative genes involved in their biosynthesis and assembly". In: *FEMS Microbiology Reviews* 33.5, pp. 917–941.

Peschek, G. A., T. Czerny, G. Schmetterer, and W. H. Nitschmann (1985). "Transmembrane Proton Electrochemical Gradients in Dark Aerobic and Anaerobic Cells of the Cyanobacterium (Blue-Green Alga) Anacystis nidulans". In: *Plant Physiology* 79.1, pp. 278–284.

Pfoh, R., A. Li, N. Chakrabarti, J. Payandeh, R. Pomes, and E. F. Pai (2012). "Structural asymmetry in the magnesium channel CorA points to sequential allosteric regulation". In: *Proceedings of the National Academy of Sciences* 109.46, pp. 18809–18814.

Pfündel, E., C. Klughammer, and U. Schreiber (2008). "Monitoring the effects of reduced PS II antenna size on quantum yields of photosystems I and II using the Dual-PAM-100 measuring system". In: *PAM Application Notes* 1, pp. 21–24.

Pils, D. and G. Schmetterer (2001). "Characterization of three bioenergetically active respiratory terminal oxidases in the cyanobacterium Synechocystis sp. strain PCC 6803". In: *FEMS Microbiology Letters* 203.2, pp. 217–222.

Pisareva, T., J. Kwon, J. Oh, S. Kim, C. Ge, Å. Wieslander, J.-S. Choi, and B. Norling (2011). "Model for Membrane Organization and Protein Sorting in the Cyanobacterium Synechocystis sp. PCC 6803 Inferred from Proteomics and Multivariate Sequence Analyses". In: *Journal of Proteome Research* 10.8, pp. 3617–3631.

Pohland, A.-C. and D. Schneider (2019). "Mg2+ homeostasis and transport in cyanobacteria – at the crossroads of bacterial and chloroplast Mg2+ import". In: *Biological Chemistry* 400.10, pp. 1289–1301.

Porra, R., W. Thompson, and P. Kriedemann (1989). "Determination of accurate extinction coefficients and simultaneous equations for assaying chlorophylls a and b extracted with four different solvents: verification of the concentration of chlorophyll standards by atomic absorption spectroscopy". In: *Biochimica et Biophysica Acta - Bioenergetics* 975.3, pp. 384–394.

Portis, A. R. and H. W. Heldt (1976). "Light-dependent changes of the Mg2+ concentration in the stroma in relation to the Mg2+ dependency of CO2 fixation in intact chloroplasts". In: *Biochimica et Biophysica Acta - Bioenergetics* 449.3, pp. 434–446.

Pottosin, I. and G. Schönknecht (1996). "Ion Channel Permeable for Divalent and Monovalent Cations in Native Spinach Thylakoid Membranes". In: *Journal of Membrane Biology* 152.3, pp. 223–233.

Pottosin, I. and S. Shabala (2016). "Transport Across Chloroplast Membranes: Optimizing Photosynthesis for Adverse Environmental Conditions". In: *Molecular Plant* 9.3, pp. 356–370.

Prentki, P. and H. M. Krisch (1984). "In vitro insertional mutagenesis with a selectable DNA fragment". In: *Gene* 29.3, pp. 303–313.

Qiao, J., S. Huang, R. Te, J. Wang, L. Chen, and W. Zhang (2013). "Integrated proteomic and transcriptomic analysis reveals novel genes and regulatory mechanisms involved in salt stress responses in Synechocystis sp. PCC 6803". In: *Applied Microbiology and Biotechnology* 97, pp. 8253–8264.

Quastel, J. H. and W. R. Wooldridge (1928). "Some properties of the dehydrogenating enzymes of bacteria". In: *Biochemical Journal* 22.3, pp. 689–702.

Rakhimberdieva, M. G., D. V. Vavilin, W. F. Vermaas, I. V. Elanskaya, and N. V. Karapetyan (2007). "Phycobilin/chlorophyll excitation equilibration upon carotenoid-induced non-photochemical fluorescence quenching in phycobilisomes of the cyanobacterium Synechocystis sp. PCC 6803". In: *Biochimica et Biophysica Acta - Bioenergetics* 1767.6, pp. 757–765.

Rangl, M., N. Schmandt, E. Perozo, and S. Scheuring (2019). "Real time dynamics of gating-related conformational changes in CorA". In: *eLife* 8, e47322.

Ranquet, C., S. Ollagnier-de-Choudens, L. Loiseau, F. Barras, and M. Fontecave (2007). "Cobalt stress in Escherichia coli: The effect on the iron-sulfur proteins". In: *Journal of Biological Chemistry* 282.42, pp. 30442–30451.

Rast, A., S. Heinz, and J. Nickelsen (2015). "Biogenesis of thylakoid membranes". In: *Biochimica et Biophysica Acta - Bioenergetics* 1847.9, pp. 821–830.

Rexroth, S., C. W. Mullineaux, D. Ellinger, E. Sendtko, M. Rögner, and F. Koenig (2011). "The plasma membrane of the cyanobacterium Gloeobacter violaceus contains segregated bioenergetic domains". In: *The Plant Cell* 23.6, pp. 2379–2390.

Reynolds, E. S. (1963). "The use of lead citrate at high pH as an electron-opaque stain in electron microscopy". In: *Journal of Cell Biology* 17.1, pp. 208–212.

Riedel, A., D. M. Kramer, and W. Nitschke (1995). "The inhibitor DBMIB and its influence on the EPR and redox properties of the Rieske-2FE2S-centre of the cytochrome b6f complex". In: *Journal of Inorganic Biochemistry* 59.2-3, p. 545.

Rippka, R., J. Waterbury, and G. Cohen-Bazire (1974). "A cyanobacterium which lacks thylakoids". In: *Archives of Microbiology* 100.1, pp. 419–436.

Rippka, R., J. Deruelles, J. B. Waterbury, M. Herdman, and R. Y. Stanier (1979). "Generic Assignments, Strain Histories and Properties of Pure Cultures of Cyanobacteria". In: *Journal of General Microbiology* 111.1, pp. 1–61.

Rossi, F. and R. De Philippis (2015). "Role of Cyanobacterial Exopolysaccharides in Phototrophic Biofilms and in Complex Microbial Mats". In: *Life* 5.2, pp. 1218–1238.

Ruban, A. V. (2018). “Light harvesting control in plants”. In: *FEBS Letters* 592.18, pp. 3030–3039.

Ryu, J. Y., J. Y. Song, J. M. Lee, S. W. Jeong, W. S. Chow, S. B. Choi, B. J. Pogson, and Y. I. Park (2004). “Glucose-induced expression of carotenoid biosynthesis genes in the dark is mediated by cytosolic pH in the cyanobacterium Synechocystis sp. PCC 6803”. In: *Journal of Biological Chemistry* 279.24, pp. 25320–25325.

Sahni, J., B. Nelson, and A. M. Scharenberg (2007). “SLC41A2 encodes a plasma-membrane Mg2+ transporter”. In: *Biochemical Journal* 401.2, pp. 505–513.

Saito, T., N. I. Kobayashi, K. Tanoi, N. Iwata, H. Suzuki, R. Iwata, and T. M. Nakanishi (2013). “Expression and functional analysis of the CorA-MRS2-ALR-type magnesium transporter family in rice”. In: *Plant and Cell Physiology* 54.10, pp. 1673–1683.

Sakurai, I., J. R. Shen, J. Leng, S. Ohashi, M. Kobayashi, and H. Wada (2006). “Lipids in oxygen-evolving photosystem II complexes of cyanobacteria and higher plants”. In: *Journal of Biochemistry* 140.2, pp. 201–209.

Samuel Miller Lab UW, S. (2011). *Gibson Assembly*. URL: `https://pengxulab.weebly.com/uploads/7/9/3/5/79359982/gibson_assembly_%E2%80%93_samuel_miller_lab_uw_seattle.pdf` (visited on Dec. 6, 2022).

Samuilov, V. D., A. V. Bulakhov, D. B. Kiselevsky, Y. E. Kuznetsova, D. V. Molchanova, S. V. Sinitsyn, and A. A. Shestak (2008). “Tolerance to antimicrobial agents and persistence of Escherichia coli and cyanobacteria”. In: *Biochemistry (Moscow)* 73.7, pp. 833–838.

Sanders, D. and C. L. Slayman (1982). “Control of intracellular pH: Predominant role of oxidative metabolism, not proton transport, in the eukaryotic microorganism Neurospora”. In: *Journal of General Physiology* 80.3, pp. 377–402.

Santana-Sanchez, A., D. Solymosi, H. Mustila, L. Bersanini, E. M. Aro, and Y. Allahverdiyeva (2019). “Flavodiiron proteins 1–to-4 function in versatile combinations in O2 photoreduction in cyanobacteria”. In: *eLife* 8, e45766.

Sarpong, K. and R. Bose (2017). “Efficient sortase-mediated N-terminal labeling of TEV protease cleaved recombinant proteins”. In: *Analytical Biochemistry* 521, pp. 55–58.

Sasaki, Y., K. Sekiguchi, Y. Nagano, and R. Matsuno (1993). “Chloroplast envelope protein encoded by chloroplast genome”. In: *FEBS Letters* 316.1, pp. 93–98.

Sayers, E. W., E. E. Bolton, J. R. Brister, K. Canese, J. Chan, D. C. Comeau, R. Connor, K. Funk, C. Kelly, S. Kim, T. Madej, A. Marchler-Bauer, C. Lanczycki, S. Lathrop, Z. Lu, F. Thibaud-Nissen, T. Murphy, L. Phan, Y. Skripchenko, T. Tse, J. Wang, R. Williams, B. W. Trawick, K. D. Pruitt, and S. T. Sherry (Jan. 2022). “Database resources of the national center for biotechnology information”. In: *Nucleic Acids Research* 50.D1, pp. D20–D26.

Schimper, A. F. W. (1883). “Über die entwicklung der Chlorophyllkörner und Farbkörper”. In: *Botanische Zeitung* 41, pp. 105–112.

Schock, I., J. Gregan, S. Steinhauser, R. Schweyen, A. Brennicke, and V. Knoop (2000). “A member of a novel Arabidopsis thaliana gene family of candidate

Mg2+ ion transporters complements a yeast mitochondrial group II intron-splicing mutant". In: *Plant Journal* 24.4, pp. 489–501.

Schreiber, U. (1986). "Detection of rapid induction kinetics with a new type of high-frequency modulated chlorophyll fluorometer". In: *Current topics in photosynthesis: Dedicated to Professor LNM Duysens on the occasion of his retirement* 1-2, pp. 261–272.

Schreiber, U. (2004). "Pulse-Amplitude-Modulation (PAM) Fluorometry and Saturation Pulse Method: An Overview". In: ed. by G. C. Papageorgiou. Vol. 19. Advances in Photosynthesis and Respiration. Dordrecht: Springer, pp. 279–319.

Schreiber, U., T. Endo, H. Mi, and K. Asada (1995). "Quenching analysis of chlorophyll fluorescence by the saturation pulse method: Particular aspects relating to the study of eukaryotic algae and cyanobacteria". In: *Plant and Cell Physiology* 36.5, pp. 873–882.

Schreiber, U., C. Klughammer, and C. Neubauer (1988). "Measuring P700 absorbance changes around 830 nm with a new type of pulse modulation system". In: *Zeitschrift für Naturforschung C* 43.9-10, pp. 686–698.

Schrödinger, LLC (2021). *The PyMOL Molecular Graphics System, Version 2.5.0.*

Schuldiner, S., H. Rottenberg, and M. Avron (1972). "Determination of DeltapH in Chloroplasts. 2. Fluorescent Amines as a Probe for the Determination of DeltapH in Chloroplasts". In: *European Journal of Biochemistry* 25.1, pp. 64–70.

Schweyen, R. J. and E. M. Froschauer (2007). "New perspectives in magnesium research: Nutrition and health". In: *New Perspectives in Magnesium Research: Nutrition and Health*. Ed. by Y. Nishizawa, H. Morii, and J. Durlach. London: Springer. Chap. 5, pp. 46–54.

Scott, J. W., S. A. Hawley, K. A. Green, M. Anis, G. Stewart, G. A. Scullion, D. G. Norman, and D. G. Hardie (2004). "CBS domains form energy-sensing modules whose binding of adenosine ligands is disrupted by disease mutations". In: *Journal of Clinical Investigation* 113.2, pp. 274–284.

Seddon, A. M., P. Curnow, and P. J. Booth (2004). "Membrane proteins, lipids and detergents: Not just a soap opera". In: *Biochimica et Biophysica Acta - Biomembranes* 1666.1-2, pp. 105–117.

Selim, K. A., M. Haffner, M. Burkhardt, O. Mantovani, N. Neumann, R. Albrecht, R. Seifert, L. Krüger, J. Stülke, M. D. Hartmann, M. Hagemann, and K. Forchhammer (2021). "Diurnal metabolic control in cyanobacteria requires perception of second messenger signaling molecule c-di-AMP by the carbon control protein SbtB". In: *Science Advances* 7.50, eabk0568.

Sétif, P. (2015). "Electron-transfer kinetics in cyanobacterial cells: Methyl viologen is a poor inhibitor of linear electron flow". In: *Biochimica et Biophysica Acta - Bioenergetics* 1847.2, pp. 212–222.

Shen, G., S. Boussiba, and W. Vermaas (1993). "Synechocystis sp PCC 6803 strains lacking photosystem I and phycobilisome function." In: *The Plant Cell* 5.12, pp. 1853–1863.

Sidler, W. A. (1994). "Phycobilisome and Phycobiliprotein Structures". In: *The Molecular Biology of Cyanobacteria*. Ed. by D. A. Bryant. Dordrecht: Springer Netherlands. Chap. 7, pp. 139–216.

Sigma Product Information Sheet (2003). *TRITON X - 100*. URL: `https://www.sigmaaldrich.com/deepweb/assets/sigmaaldrich/product/documents/160/855/t8532pis.pdf` (visited on Mar. 21, 2023).

Silver, S. (1969). "Active transport of magnesium in Escherichia coli". In: *Proceedings of the National Academy of Sciences* 62.3, pp. 764–771.

Smith, R. L., L. J. Thompson, and M. E. Maguire (1995). "Cloning and characterization of MgtE, a putative new class of Mg2+ transporter from Bacillus firmus OF4". In: *Journal of Bacteriology* 177.5, pp. 1233–1238.

SnapGene (2022). *SnapGene Viewer 6.1.2*. URL: `https://www.snapgene.com/snapgene-viewer` (visited on Dec. 6, 2022).

Sonoda, M., H. Katoh, W. Vermaas, G. Schmetterer, and T. Ogawa (1998). "Photosynthetic electron transport involved in PxcA-dependent proton extrusion in Synechocystis sp. strain PCC6803: Effect of pxcA inactivation on CO2, HCO3-, and NO3- uptake". In: *Journal of Bacteriology* 180.15, pp. 3799–3803.

Spät, P., A. Klotz, S. Rexroth, B. Maček, and K. Forchhammer (2018). "Chlorosis as a developmental program in cyanobacteria: The proteomic fundament for survival and awakening". In: *Molecular and Cellular Proteomics* 17.9, pp. 1650–1669.

Stamatakis, K., M. Tsimilli-Michael, and G. C. Papageorgiou (2014). "On the question of the light-harvesting role of β-carotene in photosystem II and photosystem I core complexes". In: *Plant Physiology and Biochemistry* 81, pp. 121–127.

Stanier, R. Y., R. Kunisawa, M. Mandel, and G. Cohen-Bazire (1971). "Purification and properties of unicellular blue-green algae (order Chroococcales)". In: *Bacteriological reviews* 35.2, pp. 171–205.

Steiger, S., L. Schäfer, and G. Sandmann (1999). "High-light-dependent upregulation of carotenoids and their antioxidative properties in the cyanobacterium Synechocystis PCC 6803". In: *Journal of Photochemistry and Photobiology B: Biology* 52.1-3, pp. 14–18.

Stetsenko, A. and A. Guskov (2017). "An Overview of the Top Ten Detergents Used for Membrane Protein Crystallization". In: *Crystals* 7.7.

— (2020). "Cation permeability in CorA family of proteins". In: *Scientific Reports* 10.1, p. 840.

Stewart, P. S., W. Wattanakaroon, L. Goodrum, S. M. Fortun, and B. R. McLeod (1999). "Electrolytic Generation of Oxygen Partially Explains Electrical Enhancement of Tobramycin Efficacy against Pseudomonas aeruginosa Biofilm". In: *Antimicrobial Agents and Chemotherapy* 43.2, pp. 292–296.

Strand, D. D., N. Fisher, and D. M. Kramer (2017). "The higher plant plastid NAD(P)H dehydrogenase-like complex (NDH) is a high efficiency proton pump that increases ATP production by cyclic electron flow". In: *Journal of Biological Chemistry* 292.28, pp. 11850–11860.

Strašková, A., G. Steinbach, G. Konert, E. Kotabová, J. Komenda, M. Tichý, and R. Kaňa (2019). "Pigment-protein complexes are organized into stable microdomains in cyanobacterial thylakoids". In: *Biochimica et Biophysica Acta - Bioenergetics* 1860.12, p. 148053.

Studier, W. F., A. H. Rosenberg, J. J. Dunn, and J. W. Dubendorff (1990). "Use of T7 RNA polymerase to direct expression of cloned genes". In: *Methods in Enzymology* 185, pp. 60–89.

Sudhir, P. R., D. Pogoryelov, L. Kovács, G. Garab, and S. D. Murthy (2005). "The effects of salt stress on photosynthetic electron transport and thylakoid membrane proteins in the cyanobacterium Spirulina platensis". In: *Journal of Biochemistry and Molecular Biology* 38.4, pp. 481–485.

Sun, Y., R. Yang, L. Li, and J. Huang (2017). "The Magnesium Transporter MGT10 Is Essential for Chloroplast Development and Photosynthesis in Arabidopsis thaliana". In: *Molecular Plant* 10.12, pp. 1584–1587.

Takahashi, H. (2022). "Cyclic electron flow A to Z". In: *Journal of Plant Research* 135.4, pp. 539–541.

Takaichi, S. and M. Mochimaru (2007). "Carotenoids and carotenogenesis in cyanobacteria: unique ketocarotenoids and carotenoid glycosides". In: *Cellular and molecular life sciences* 64, pp. 2607–2619.

Takaichi, S., T. Maoka, and K. Masamoto (2001). "Myxoxanthophyll in Synechocystis sp. PCC 6803 is myxol 2-dimethyl-fucoside,(3 R, 2 S)-myxol 2-(2, 4-di-O-methyl-α-l-fucoside), not rhamnoside". In: *Plant and Cell Physiology* 42.7, pp. 756–762.

Takeda, H., M. Hattori, T. Nishizawa, K. Yamashita, S. T. Shah, M. Caffrey, A. D. Maturana, R. Ishitani, and O. Nureki (2014). "Structural basis for ion selectivity revealed by high-resolution crystal structure of Mg2+ channel MgtE". In: *Nature Communications* 5.May, p. 5374.

Tang, N., Y. Li, and L.-S. Chen (2012). "Magnesium deficiency–induced impairment of photosynthesis in leaves of fruiting Citrus reticulata trees accompanied by up-regulation of antioxidant metabolism to avoid photo-oxidative damage". In: *Journal of Plant Nutrition and Soil Science* 175.5, pp. 784–793.

Teuber, M., M. Rögner, and S. Berry (2001). "Fluorescent probes for non-invasive bioenergetic studies of whole cyanobacterial cells". In: *Biochimica et Biophysica Acta - Bioenergetics* 1506.1, pp. 31–46.

The UniProt Consortium (2017). "UniProt: the universal protein knowledgebase". In: *Nucleic Acids Research* 45.D1, pp. D158–D169.

Tissières, A. and J. Watson (1958). "Ribonucleoprotein particles from Escherichia coli". In: *Nature* 182, pp. 778–780.

Tomita, A., M. Zhang, F. Jin, W. Zhuang, H. Takeda, T. Maruyama, M. Osawa, K.-i. I. Hashimoto, H. Kawasaki, K. Ito, N. Dohmae, R. Ishitani, I. Shimada, Z. Yan, M. Hattori, and O. Nureki (2017). "ATP-dependent modulation of MgtE in Mg2+homeostasis". In: *Nature Communications* 8.1, p. 148.

Trachsel, E., P. Redder, P. Linder, and J. Armitano (2019). "Genetic screens reveal novel major and minor players in magnesium homeostasis of Staphylococcus aureus". In: *PLoS Genetics* 15.8, e1008336.

Tsujii, M., E. Tanudjaja, and N. Uozumi (2020). "Diverse physiological functions of cation proton antiporters across bacteria and plant cells". In: *International Journal of Molecular Sciences* 21.12, p. 4566.

Tsunekawa, K., T. Shijuku, M. Hayashimoto, Y. Kojima, K. Onai, M. Morishita, M. Ishiura, T. Kuroda, T. Nakamura, H. Kobayashi, M. Sato, K. Toyooka, K. Matsuoka, T. Omata, and N. Uozumi (2009). "Identification and characterization of the Na+/H+ antiporter Nhas3 from the thylakoid membrane of Synechocystis sp. PCC 6803". In: *Journal of Biological Chemistry* 284.24, pp. 16513–16521.

Umena, Y., K. Kawakami, J. R. Shen, and N. Kamiya (2011). "Crystal structure of oxygen-evolving photosystem II at a resolution of 1.9Å". In: *Nature* 473.7345, pp. 55–60.

UniProt (2023a). *UniProt: the universal protein knowledgebase*. URL: `https://www.uniprot.org/uniprotkb/P0A2L4/entry` (visited on Mar. 21, 2023).

— (2023b). *UniProt: the universal protein knowledgebase*. URL: `https://www.uniprot.org/uniprotkb/P73368/entry` (visited on Mar. 21, 2023).

— (2023c). *UniProt: the universal protein knowledgebase*. URL: `https://www.uniprot.org/uniprotkb/P73368/feature-viewer` (visited on Mar. 21, 2023).

Urek, R. O. and Y. Kerimoglu (2019). "Evaluation of Effects of Mg2+and Cu2+on Pigment-Metabolite Production and Photosystem II Activity of Arthrospira platensis Gomont 1892". In: *Turkish Journal of Fisheries and Aquatic Sciences* 19.10, pp. 873–883.

Utkilen, H. C. (1982). "Magnesium-limited Growth of the Cyanobacterium Anacystis nidulans". In: *Microbiology* 128.8, pp. 1849–1862.

Vajravel, S., M. Kis, K. Kłodawska, H. Laczko-Dobos, P. Malec, L. Kovács, Z. Gombos, and T. N. Toth (2017). "Zeaxanthin and echinenone modify the structure of photosystem I trimer in Synechocystis sp. PCC 6803". In: *Biochimica et Biophysica Acta - Bioenergetics* 1858.7, pp. 510–518.

Van De Meene, A. M., W. P. Sharp, J. H. McDaniel, H. Friedrich, W. F. Vermaas, and R. W. Roberson (2012). "Gross morphological changes in thylakoid membrane structure are associated with photosystem I deletion in Synechocystis sp. PCC 6803". In: *Biochimica et Biophysica Acta - Biomembranes* 1818.5, pp. 1427–1434.

Vanoye, C. G. and A. L. George (2002). "Functional characterization of recombinant human CIC-4 chloride channels in cultured mammalian cells". In: *Journal of Physiology* 539.2, pp. 373–383.

Varadi, M., S. Anyango, M. Deshpande, S. Nair, C. Natassia, G. Yordanova, D. Yuan, O. Stroe, G. Wood, A. Laydon, A. Zídek, T. Green, K. Tunyasuvunakool, S. Petersen, J. Jumper, E. Clancy, R. Green, A. Vora, M. Lutfi, M. Figurnov, A. Cowie, N. Hobbs, P. Kohli, G. Kleywegt, E. Birney, D. Hassabis, and S. Velankar (2022). "AlphaFold Protein Structure Database: Massively expanding

the structural coverage of protein-sequence space with high-accuracy models". In: *Nucleic Acids Research* 50.D1, pp. D439–D444.

Vermaas, W. F. (2001). "Photosynthesis and Respiration in Cyanobacteria". In: *eLS*. March. Wiley.

Vermass, W. F. J., A. W. Rutherford, and Ö. Hansson (1988). " Site-directed mutagenesis in photosystem II of the cyanobacterium Synechocystis sp. PCC 6803: Donor D is a tyrosine residue in the D2 protein ". In: *Proceedings of the National Academy of Sciences* 85.22, pp. 8477–8481.

Vicente, J. B., C. M. Gomes, A. Wasserfallen, and M. Teixeira (2002). "Module fusion in an A-type flavoprotein from the cyanobacterium Synechocystis condenses a multiple-component pathway in a single polypeptide chain". In: *Biochemical and Biophysical Research Communications* 294.1, pp. 82–87.

Volgusheva, A., G. Kukarskikh, T. Krendeleva, A. Rubin, and F. Mamedov (2015). "Hydrogen photoproduction in green algae Chlamydomonas reinhardtii under magnesium deprivation". In: *RSC Advances* 5.8, pp. 5633–5637.

Wabakken, T., E. Rian, M. Kveine, and H. C. Aasheim (2003). "The human solute carrier SLC41A1 belongs to a novel eukaryotic subfamily with homology to prokaryotic MgtE Mg2+ transporters". In: *Biochemical and Biophysical Research Communications* 306.3, pp. 718–724.

Wacker, W. E. C. (1969). "The Biochemistry of Magnesium". In: *Annals of the New York Academy of Sciences* 162.2, pp. 717–726.

Wagner, S., M. M. Klepsch, S. Schlegel, A. Appel, R. Draheim, M. Tarry, M. Högbom, K. J. van Wijk, D. J. Slotboom, J. O. Persson, and J.-W. de Gier (2008). "Tuning Escherichia coli for membrane protein overexpression". In: *Proceedings of the National Academy of Sciences* 105.38, pp. 14371–14376.

Waldo, G. S., B. M. Standish, J. Berendzen, and T. C. Terwilliger (1999). "Rapid protein-folding assay using green fluorescent protein". In: *Nature Biotechnology* 17.7, pp. 691–695.

Waldron, K. J. and N. J. Robinson (2009). "How do bacterial cells ensure that metalloproteins get the correct metal?" In: *Nature Reviews Microbiology* 7.1, pp. 25–35.

Wang, C. Y., J. D. Shi, P. Yang, P. G. Kumar, Q. Z. Li, Q. G. Run, Y. C. Su, H. S. Scott, K. J. Kao, and J. X. She (2003). "Molecular cloning and characterization of a novel gene family of four ancient conserved domain proteins (ACDP)". In: *Gene* 306, pp. 37–44.

Wang, H. L., B. L. Postier, and R. L. Burnap (2002). "Polymerase chain reaction-based mutageneses identify key transporters belonging to multigene families involved in Na+ and ph homeostasis of Synechocystis sp. PCC 6803". In: *Molecular Microbiology* 44.6, pp. 1493–1506.

Wang, Z., Y. Xu, Z. Yang, H. Hou, G. Jiang, and T. Kuang (2002). "Effect of sodium thiosulfate on the depletion of photosynthetic apparatus in cyanobacterium Synechocystis sp. PCC 6803 cells grown in the presence of glucose". In: *Photosynthetica* 40.3, pp. 383–387.

Watzer, B. and K. Forchhammer (2018). “Cyanophycin Synthesis Optimizes Nitrogen Utilization in the Unicellular Cyanobacterium Synechocystis sp. Strain PCC 6803”. In: *Applied and Environmental Microbiology* 84.20. Ed. by C. Vieille, e01298–18.

Way, J. L. (1984). “Cyanide intoxication and its mechanism of antagonism”. In: *Annual Review of Pharmacology and Toxicology* 24.1, pp. 451–481.

Webb, M. (1951). “The influence of magnesium on cell division: 4. The specificity of magnesium”. In: *Journal of General Microbiology* 5.3, pp. 480–484.

Werdan, K., H. W. Heldt, and M. Milovancev (1975). “The role of pH in the regulation of carbon fixation in the chloroplast stroma. Studies on CO2 fixation in the light and dark”. In: *Biochimica et Biophysica Acta - Bioenergetics* 396.2, pp. 276–292.

Willstätter, R. (1906). “Zur Kenntniss der Zusammensetzung des Chlorophylls”. In: *Justus Liebig’s Annalen der Chemie* 350.1-2, pp. 48–82.

Willstätter, R. and A. Stoll (1913). Berlin: Verlag von Julius Springer.

Wilson, A., G. Ajlani, J. M. Verbavatz, I. Vass, C. A. Kerfeld, and D. Kirilovsky (2006). “A soluble carotenoid protein involved in phycobilisome-related energy dissipation in cyanobacteria”. In: *The Plant Cell* 18.4, pp. 992–1007.

Wishnick, M. and M. D. Lane (1969). “Inhibition of Ribulose Diphosphate Carboxylase by Cyanide. Inactive ternary complex of enzyme, ribulose diphosphate,and cyanide”. In: *Journal of Biological Chemistry* 244.1, pp. 55–59.

Wojdyr, M. (2010). “Fityk: a general-purpose peak fitting program”. In: *Journal of Applied Crystallography* 43.5, p. 1126.

Wollman, F.-A. and C. Lemaire (1988). “Studies on kinase-controlled state transitions in Photosystem II and b6f mutants from Chlamydomonas reinhardtii which lack quinone-binding proteins”. In: *Biochimica et Biophysica Acta - Bioenergetics* 933.1, pp. 85–94.

Yamamoto, H., T. Nakayama, and C. Chichester (1962). “Studies on the light and dark interconversions of leaf xanthophylls”. In: *Archives of Biochemistry and Biophysics* 97.1, pp. 168–173.

Yan, Y. W., D. D. Mao, L. Yang, J. L. Qi, X. X. Zhang, Q. L. Tang, Y. P. Li, R. J. Tang, and S. Luan (2018). “Magnesium transporter MGT6 plays an essential role in maintaining magnesium homeostasis and regulating high magnesium tolerance in Arabidopsis”. In: *Frontiers in Plant Science* 9.March, p. 274.

Yang, G. H., L. T. Yang, H. X. Jiang, Y. Li, P. Wang, and L. S. Chen (2012). “Physiological impacts of magnesium-deficiency in Citrus seedlings: Photosynthesis, antioxidant system and carbohydrates”. In: *Trees* 26.4, pp. 1237–1250.

Yeremenko, N., R. Jeanjean, P. Prommeenate, V. Krasikov, P. J. Nixon, W. F. Vermaas, M. Havaux, and H. C. Matthijs (2005). “Open reading frame ssr2016 is required for antimycin A-sensitive photosystem I-driven cyclic electron flow in the cyanobacterium Synechocystis sp. PCC 6803”. In: *Plant and Cell Physiology* 46.8, pp. 1433–1436.

Young, A. J. and H. A. Frank (1996). "Energy transfer reactions involving carotenoids: Quenching of chlorophyll fluorescence". In: *Journal of Photochemistry and Photobiology B: Biology* 36.1, pp. 3–15.

Yu, L., J. Zhao, U. Mühlenhoff, D. A. Bryant, and J. H. Golbeck (1993). "PsaE is required for in vivo cyclic electron flow around photosystem I in the cyanobacterium Synechococcus sp. PCC 7002". In: *Plant Physiology* 103.1, pp. 171–180.

Zakar, T., H. Laczko-Dobos, T. N. Toth, and Z. Gombos (2016). "Carotenoids assist in cyanobacterial photosystem II assembly and function". In: *Frontiers in Plant Science* 7, p. 295.

Zavřel, T., J. Červený, and M. A. Sinetova (2015). "Measurement of Chlorophyll". In: *Bio-protocol* 5.9, e1467.

Zavřel, T., P. Očenášová, M. Sinetova, and J. Červený (2018). "Determination of Storage (Starch/Glycogen) and Total Saccharides Content in Algae and Cyanobacteria by a Phenol-Sulfuric Acid Method". In: *Bio-Protocol* 8.15, e2966.

Zhang, B., C. Zhang, R. Tang, X. Zheng, F. Zhao, A. Fu, W. Lan, and S. Luan (2022). "Two magnesium transporters in the chloroplast inner envelope essential for thylakoid biogenesis in Arabidopsis". In: *New Phytologist* 236.2, pp. 464–478.

Zhang, T., H. Gong, X. Wen, and C. Lu (2010). "Salt stress induces a decrease in excitation energy transfer from phycobilisomes to photosystem II but an increase to photosystem I in the cyanobacterium Spirulina platensis". In: *Journal of Plant Physiology* 167.12, pp. 951–958.

Zhu, Y., J. E. Graham, M. Ludwig, W. Xiong, R. M. Alvey, G. Shen, and D. A. Bryant (2010). "Roles of xanthophyll carotenoids in protection against photoinhibition and oxidative stress in the cyanobacterium Synechococcus sp. strain PCC 7002". In: *Archives of Biochemistry and Biophysics* 504.1, pp. 86–99.

Zivcak, M., M. Brestic, K. Kunderlikova, O. Sytar, and S. I. Allakhverdiev (2015). "Repetitive light pulse-induced photoinhibition of photosystem i severely affects CO2 assimilation and photoprotection in wheat leaves". In: *Photosynthesis Research* 126.2-3, pp. 449–463.

Zlenko, D. V., I. V. Elanskaya, E. P. Lukashev, Y. V. Bolychevtseva, N. E. Suzina, E. S. Pojidaeva, I. A. Kononova, A. V. Loktyushkin, and I. N. Stadnichuk (2019). "Role of the PB-loop in ApcE and phycobilisome core function in cyanobacterium Synechocystis sp. PCC 6803". In: *Biochimica et Biophysica Acta - Bioenergetics* 1860.2, pp. 155–166.